Engineered Silicon and Germanium for Quantum Technology

Stehouwer, L.E.A.

DOI
10.4233/uuid:7422dbc3-60b3-4c03-83d2-b132eb877312

Publication date
2025

Document Version
Final published version

Citation (APA)
Stehouwer, L. E. A. (2025). *Engineered Silicon and Germanium for Quantum Technology*. [Dissertation (TU Delft), Delft University of Technology]. https://doi.org/10.4233/uuid:7422dbc3-60b3-4c03-83d2-b132eb877312

Important note
To cite this publication, please use the final published version (if applicable).
Please check the document version above.

Engineered Silicon and Germanium for Quantum Technology

Lucas Erik Adriaan Stehouwer

ENGINEERED SILICON AND GERMANIUM FOR QUANTUM TECHNOLOGY

ENGINEERED SILICON AND GERMANIUM FOR QUANTUM TECHNOLOGY

Proefschrift

ter verkrijging van de graad van doctor
aan de Technische Universiteit Delft,
op gezag van de Rector Magnificus prof. dr. ir. T.H.J.J. van der Hagen,
voorzitter van het College voor Promoties,
in het openbaar te verdedigen op woensdag 17 december 2025 om 12:30 uur

door

Lucas Erik Adriaan STEHOUWER

Master of Science in Applied Physics,
Technische Universiteit Delft, Delft, Nederland,
geboren te Amsterdam, Nederland.

Dit proefschrift is goedgekeurd door de

Promotor: dr. G. Scappucci
Promotor: Prof. dr. ir. M. Veldhorst

Samenstelling promotiecommissie:

Rector Magnificus	voorzitter
Dr. G. Scappucci	Technische Universiteit Delft
Prof. dr. ir. M. Veldhorst	Technische Universiteit Delft
Onafhankelijke leden:	
Prof. dr. ir. L.M.K. Vandersypen	Technische Universiteit Delft
Prof. dr. G. Capellini	Università Roma Tre
Prof. dr. D. Bougeard	Universität Regensburg
Dr. P. Scarlino	École Polytechnique Fédérale de Lausanne
Reservelid:	
Prof. dr. R. Hanson	Technische Universiteit Delft

Printed by: Gilde Print

Front & Back: Visual impression of the epitaxial process for the deposition of low-disorder strained germanium quantum wells.

ISBN 978-94-6496-507-0

An electronic version of this dissertation is available at
http://repository.tudelft.nl/.

I am sure that the projected device, or rather the species of devices of which it is to be the first representative, is so radically new that many of its uses will become clear only after it has been put into operation.

John von Neumann

CONTENTS

SUMMARY

Quantum computers hold the promise of vastly increased computing power with expected applications in areas such as health care and the energy transition. Spin qubits in semiconductor quantum dots are a promising candidate as the building block for a large scale quantum computer, due to their small footprint, long coherence times, and compatibility with advanced semiconductor manufacturing. In this thesis we study ^{28}Si/SiGe and Ge/SiGe heterostructures, two material platforms that have been developed to host single electron and hole spin qubits respectively. Each heterostructure is grown by chemical vapor deposition and subsequently characterised by structural and electronic measurement techniques to verify the design and development of each material platform. The first three experiments focus on the development of the Ge/SiGe heterostructure, while the last two experiments study the ^{28}Si/SiGe heterostructure.

Developing Ge/SiGe heterostructures, we first explore the growth on a Ge wafer instead of the commonly used Si wafer. We find a less disordered crystal structure and observe significant improvements of measured disorder properties in two-dimensional transport experiments. We then further study the Ge/SiGe heterostructure grown from a Ge wafer by exploring disorder properties when using a thick SiGe barrier layer. We find that the disorder from the semiconductor-dielectric interface is mitigated resulting in a record high mobility. We identify interface roughness and background impurities as the remaining dominant sources of disorder. Finally, we explore whether the improved Ge/SiGe heterostructure from the first experiment also results in a lower noise environment for hole spin qubits. We extensively probe charge noise and magnetic noise using multiple characterisation techniques and find that charge noise is reduced when using qubit devices fabricated on Ge/SiGe heterostructures grown from a Ge wafer.

Developing ^{28}Si/SiGe heterostructures, we first study the energy splitting of the nearly degenerate conduction band valleys (valley splitting) in ^{28}Si/SiGe heterostructures. We combine atomic level characterisation, theoretical modeling, and measurements of valley splitting in quantum dots to attribute valley splitting variations to random Ge and Si compositions at the ^{28}Si/SiGe interfaces. We propose methods to increase valley splitting by introducing Ge into the Si quantum well. In the last experiment, we grow several ^{28}Si/SiGe heterostructures where we intentionally introduce Ge into the ^{28}Si quantum well for increased valley splitting. We characterise valley splitting and disorder properties with two-dimensional transport experiments. We find increased valley splitting energies at the cost of increased disorder and stress the need for a delicate balance between the two.

These results have advanced state-of-the-art material platforms for spin qubits by providing improvements in terms of crystal quality and electrical disorder. In the last chapter, we highlight the need for further progress by reducing magnetic noise through isotopic purification, and addressing the impact of the dielectric oxide on electrical noise, in the pursuit of a large-scale quantum computer.

SAMENVATTING

Quantumcomputers bieden vooruitzicht op een aanzienlijk grotere rekenkracht, met verwachte toepassingen in gebieden zoals de gezondheidszorg en de energietransitie. Spin-qubits in halfgeleider quantum dots zijn een veelbelovende kandidaat als bouwsteen voor een grootschalige quantumcomputer, vanwege hun kleine formaat, lange coherentietijden en compatibiliteit met geavanceerde halfgeleiderproductie.

In dit proefschrift bestuderen we ^{28}Si/SiGe en Ge/SiGe heterostructuren, twee materiaalplatformen die zijn ontwikkeld om qubits te huisvesten, repectievelijk op basis van enkele elektronen en elektrongaten. Elke heterostructuur wordt gegroeid door middel van een chemisch opdampproces en vervolgens gekarakteriseerd met structurele en elektronische meetmethoden om het ontwerp en de ontwikkeling van elk materiaalplatform te verifiëren. De eerste drie experimenten richten zich op de ontwikkeling van de Ge/SiGe heterostructuur, terwijl de laatste twee experimenten het ^{28}Si/SiGe platform onderzoeken.

Bij de ontwikkeling van Ge/SiGe heterostructuren onderzoeken we eerst de groei op een Ge substraat in plaats van het gangbare Si substraat. We constateren een minder wanordelijke kristalstructuur en observeren aanzienlijke verbeteringen in de gemeten wanorde-eigenschappen in tweedimensionale transporteigenschappen. Vervolgens bestuderen we de Ge/SiGe heterostructuur verder, wederom gegroeid vanaf een Ge substraat, door de elektronische eigenschappen te onderzoeken bij gebruik van een dikke SiGe barrièrelaag. We stellen vast dat hierdoor de wanorde van het halfgeleider-oxide grensvlak wordt verminderd, wat resulteert in een recordhoge mobiliteit. We identificeren ruwheid van het Ge/SiGe grensvlak en achtergrondverontreinigingen als de overblijvende dominante bronnen van wanorde.

Tot slot onderzoeken we of de verbeterde Ge/SiGe heterostructuur uit het eerste experiment ook resulteert in een omgeving met minder ruis voor elektrongat spin-qubits. We onderzoeken uitgebreid ladingsruis en magnetische ruis met meerdere karakteriseringstechnieken en constateren dat ladingsruis afneemt bij gebruik van qubit-apparaten die zijn vervaardigd op Ge/SiGe heterostructuren gegroeid vanaf een Ge substraat.

Bij de ontwikkeling van ^{28}Si/SiGe heterostructuren bestuderen we eerst de energie splitsing van de bijna gelijke energieniveau's in de geleidingsbanddalen (dal-splitsing) in ^{28}Si/SiGe heterostructuren. We combineren karakterisering op atomaire schaal, theoretische modellering en metingen van dal-splitsing in quantum dots om variaties in dal-splitsing toe te schrijven aan willekeurige Ge en Si samenstellingen bij de ^{28}Si/SiGe grensvlakken. We stellen methoden voor om de dal-splitsing te vergroten door Ge toe te voegen aan de Si quantum put. In het laatste experiment groeien we meerdere ^{28}Si/SiGe heterostructuren waarin we bewust Ge introduceren in de ^{28}Si quantum put om de dal-splitsing te vergroten. We karakteriseren de dal-splitsing en wanorde-eigenschappen met tweedimensionale transportmetingen. We vinden verhoogde dal-splitsing energieën ten

koste van toegenomen wanorde, en benadrukken de noodzaak van een delicate balans tussen beide.

Deze resultaten hebben twee geavanceerde materiaalplatformen voor spin-qubits verder ontwikkeld door meerdere verbeteringen te bieden op het gebied van kristalkwaliteit en elektrische wanorde. In het laatste hoofdstuk benadrukken we de noodzaak van verdere vooruitgang door het verminderen van magnetische ruis via isotopische zuivering, en het aanpakken van de invloed van het diëlektrische oxide op elektrische ruis, in de zoektocht naar een grootschalige quantumcomputer.

1

INTRODUCTION

Technology uses results from scientific research, but with a delay.
Scientific research uses results of technology without delay.

Hendrik Casimir

1

1.1. AGES OF MATERIAL

On the 19th of September 1991, while hiking in the Ötztal Alps, Erika and Helmut Simon discovered the well-preserved remains of a Stone-Age man dating back to 3300 B.C. The man, better known as Ötzi, lived during the European Chalcolithic period. Among his possessions was an axe with a blade made of copper and several flint-tipped arrows. It is, in fact, these two materials—stone (*lithos* in Greek) and copper (*chalcos* in Greek)—that define the Chalcolithic period in which Ötzi lived.

Materials are considered so important to human development that historians and scholars have named historical periods based on the dominant material used[1]. Examples include the *Stone Age*, *Copper-Stone (Chalcolithic) Age*, *Bronze Age*, and *Iron Age*. The transition from one period to another is accompanied by humanity's increasing ability to create, shape, and manipulate materials. For example, the Stone Age is characterised by 'percussion flaking', the ability to detach smaller pieces of stone (flakes) from larger rocks. These flakes could then be sharpened and used as tools.

Stones, however, are not known for their ability to deform. Gradually, interest increased in materials such as gold, silver, and copper which could be shaped more easily. In particular, the smelting of copper can be considered one of the major technological advancements of the Chalcolithic Age. Copper smelting is a highly non-trivial process, requiring the heating of copper ore to temperatures exceeding 1000 °C in an oxygen-deprived environment. It is still not fully understood how the process was discovered, but it is believed to have evolved from pottery-making techniques.

Copper proved useful for Chalcolithic humans like Ötzi, but it was generally too soft to be used for strong weapons and tools. Eventually, a more robust material had to be found. The innovation that led to this was the mixing of pure copper with impurities such as arsenic, lead, or iron, creating an *alloy*. The most widely used alloy was a combination of copper and tin, which we now call bronze. Bronze possesses greater hardness than pure copper and could be used more easily in casting processes, making it a highly popular material to work with.

Eventually, iron became the dominant working material. However, the transition from bronze to iron was not straightforward. Pure iron is actually softer than bronze and therefore needed to be alloyed with carbon (to form steel) to surpass bronze in hardness. Importantly, iron ore was more abundant and easier to acquire than copper and tin. Tin, in particular, was not readily available in the Mediterranean region and had to be imported via far Eastern trade routes. Scholars believe that interruptions in these trade routes spurred the increased use of iron in the Mediterranean region. The production of iron and steel has evolved over the centuries and remains crucial to this day.

Materials have accompanied mankind from the beginning of its existence and as societies advanced so did the usage, invention, and engineering of ever more advanced materials. So, Which material dominates modern times? Arguably, consumer electronics such as the radio, television, and computer have had a major impact on people's daily lives. However, the electrons that power these devices require a medium in which to operate. Silicon has been the dominant material for electronics since the late 20th century, and as such, this era is often referred to as the *Silicon Age*.

[1] Section 1.1 is based on chapters 1, 4, 7, and 10 of Ref. [1]

1.2. THE SILICON AGE

The computer has arguably been the most influential device on human development over the last seven decades. The first electrical, programmable, and general-purpose computer was the Electrical Integrator And Computer (ENIAC) [2]. It was completed in 1945 and consisted of 18,000 vacuum tubes, weighed 27 tons and occupied a 28 m^2 room. The vacuum tube that the ENIAC used is a device in which the flow of electric current between two electrodes through a vacuum is controlled. The physical states off the vacuum tube, namely 'on' and 'off', are used as binary digits (bits) — usually represented as 0 and 1 —, the smallest unit of data that a computer can process and store.

In contrast, a modern microprocessor contains about 0.1 trillion (100,000,000,000) transistors, in a device that can easily fit in your pocket. Obviously, a lot of technological development and breakthroughs were needed to get to this point. We will highlight some of the key material developments that were made.

Modern computers use semiconductor transistors. The earliest semiconductor transistor was invented in 1947 and was the germanium point-contact transistor [3]. It consists of three terminals where the current through the material is controlled by one of the terminals. Compared to vacuum tubes, semiconductor transistors were more reliable, faster, and generated less heat. However, these early germanium-based devices were still hard to control and strongly dependent on the purity of the sample, limiting the commercial use of these early devices [4].

Silicon transistors initially lagged behind germanium transistors due to limited electrical conductivity from unstable surface states [5]. Silicon became more popular than germanium once silicon dioxide was used to passivate the silicon surface, effectively protecting the underlying bulk silicon. Moreover, the transistors protected by a silicon oxide could be manufactured in a planar process [6], leading to the invention of the metal-oxide-semiconductor field-effect-transistor (MOSFET) in 1959. The inherent scalability of the planar manufacturing process of MOSFETs resulted in the MOSFET still being the dominant transistor type today. It has been the most produced device in human history with over 13 sextillion made.

Despite the incredible advancements that the transistor has made leading to very powerful (super)computers, there are specific problems that even the best computers struggle to solve. For these kinds of problems, a new type of computer is needed that works fundamentally different. In the next section, we will discuss this new type of computer which uses fundamental properties of quantum mechanics for its functionality.

1.3. QUANTUM MECHANICS AND TECHNOLOGY

Quantum mechanics is a fundamental physical theory describing the behaviour of Nature at the atomic scale where classical physics fails. Quantum mechanics was collectively developed in the first decades of the 20th century by a generation of scientists and, like all successful theories, it accurately explained and predicted experimental observations such as blackbody radiation [7] and the photoelectric effect [8]. The underlying principle that led to these successes is the so-called wave-particle duality, the idea that a quantum system can both behave like a wave and a particle.

Since Nature is governed by quantum systems, scientists naturally wanted to develop

simulations of quantum systems. However, the simulation of quantum systems turns out to be exponentially computationally expensive depending on the system size. This led to the idea to use a quantum computing machine instead of a classical computer to simulate quantum systems [9, 10].

A quantum computer works fundamentally different from a normal (classical) computer. The building block of a classical computer is the bit, which can either be in the 0 or in the 1 state (see Fig. 1.1(a)), and is physically realised by the transistor. The fundamental building block of a quantum computer is the quantum bit, or qubit. A qubit leverages two quantum properties: *superposition* and *entanglement*.

Superposition expresses the property of a quantum system to be in a linear combination of different states. For a qubit, this means that the quantum state $|\Psi\rangle$ of the qubit can be in a linear combination of 0 and 1, mathematically expressed as:

$$|\Psi\rangle = \alpha\,|0\rangle + \beta\,|1\rangle\,. \tag{1.1}$$

When we measure the state $|\Psi\rangle$ of the qubit, its wavefunction collapses to one of its basis states $|0\rangle$ or $|1\rangle$. The probability with which we measure the $|0\rangle$ or $|1\rangle$ state is given by $|\alpha|^2$ and $|\beta|^2$ respectively (α and β are complex numbers), and obey the relation $|\alpha|^2 + |\beta|^2 = 1$. Using trigonometric relations and Euler's equation, one can write the qubit state as:

$$|\Psi\rangle = \cos\frac{\theta}{2}\,|0\rangle + e^{i\phi}\sin\frac{\theta}{2}\,|1\rangle\,. \tag{1.2}$$

Using θ and ϕ, the qubit state is represented as an arrow on a sphere, known as the *Bloch* sphere (see Fig. 1.1(b)).

While a bit only requires the knowledge of a single binary value to describe its state (0 or 1), to describe the state of a qubit, one needs both the coefficients α and β. Now, if we have a quantum system consisting of two interacting qubits, the state describing the total system will be a superposition of four possible states, requiring four coefficients to describe. In general, a system containing N qubits requires 2^N coefficients to describe its total state.

Quantum entanglement is the second primary feature of quantum mechanics that a quantum computer takes advantage of. Two qubits are said to be entangled with each other when the global state of the two qubits cannot be written as a product of the qubits' individual states [12]. An example of an entangled state between two qubits A and B is:

$$\frac{1}{\sqrt{2}}\left(|0\rangle_A\,|1\rangle_B - |1\rangle_A\,|0\rangle_B\right)\,. \tag{1.3}$$

Due to the entanglement between the two qubits, if we measure the state of qubit A, say $|0\rangle$, we immediately know that the state of qubit B is $|1\rangle$, without having to also measure qubit B, see Fig. 1.1(c).

For certain applications, the combination of superposition and entanglement allows a quantum computer to scale its computing power more efficiently compared to a classical computer. One of the first developed algorithms where a quantum computer can be applied, is the efficient factorisation of prime numbers [13], a problem at the basis of cryptography. Other possible applications include drug design for pharmaceuticals [14],

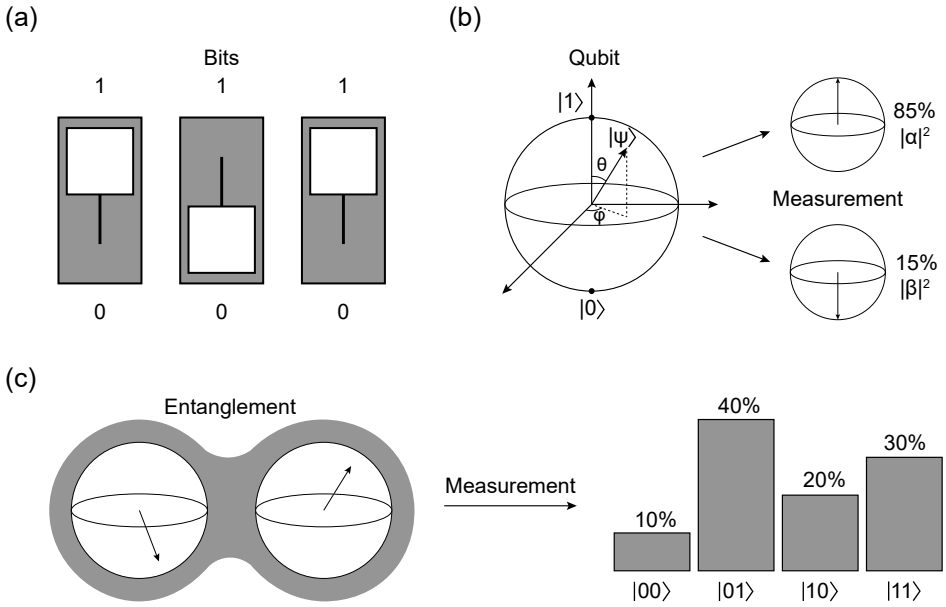

Figure 1.1: **Bits and qubits.** (a) Schematic image of three bits which can be thought of as switches that are turned on (1) or off (0) representing the two possible states they can be in. (b) Image of a qubit state represented on the Bloch sphere. A qubit state can be in a superposition of the $|0\rangle$ and $|1\rangle$ states and collapses to one of the two when measuring the state of the qubit. (c) Two qubits can become entangled, where the state of one qubit affects the total state of the system. All figures adapted from Ref. [11].

nitrogen fixation in agriculture [15], and efficient database search [16]. Perhaps most exciting are all the possible applications that have not yet been thought of, although, it is still unclear whether any of these applications can be commercially realised and what their impact on society would be. All currently existing quantum computers are not yet capable of performing any of these tasks and a lot of work is still needed to build a useful quantum computer.

1.4. MATERIAL FOR THE QUANTUM AGE

Material development has played a pivotal role in the history of mankind and it is likely going to be an essential driver of a prospective quantum era. In the same way that the transistor became the physical building block to encode bits in a classical computer, the qubits making up a quantum computer also need to be physically realised. There are multiple approaches to building a qubit, such as superconducting circuits [17–19], trapped ions [20–22], neutral atoms [23, 24], topologically protected states [25, 26], photons [27, 28], colour centres [29, 30], and spins [31–33]. All of these different approaches to making qubits have their respective advantages and disadvantages.

In this thesis, we focus on the development of silicon-germanium material platforms for spin qubits. Curiously, similar to the previous material ages, our (increased) ability to deform and control the structural and electrical properties of silicon and germanium, in

combination with the ability to alloy them, makes this system a promising candidate for a large-scale quantum computer. Spin qubits have a small footprint (< 150 nm), with the potential of integrating millions of qubits on a small chip (1 mm^2) [32, 34]. Furthermore, silicon and germanium have been used for decades by the semiconductor industry for the fabrication of classical electronics. The possibility of leveraging existing expertise and fabrication facilities by using these materials for the fabrication of spin qubits is another key motivator.

Despite these advantages, spin qubits also face serious challenges that need to be addressed. These challenges arise from various sources of noise that affect the coherence of spin qubits. More specifically, charge noise, originating from background impurities, disordered interfaces, and lattice defects, and magnetic noise, resulting from interactions between the spin qubit and nuclear spins, limit the ability to initialise, control, and read out dense arrays of spin qubits. Furthermore, non-uniformity between spin qubits necessitates the individual tuning of each qubit, which is time-intensive and not scalable to systems comprising millions of qubits.

The research presented in this thesis is motivated by the conviction that careful design and optimisation of the material host plays a key role in addressing the current pressing spin qubit challenges. We focus on feedback cycles, ideally as fast as possible, in which a material stack is grown and characterised in terms of both its structural quality and electrical performance. The findings of this characterisation are then used to inform the design of the next iteration of the material platform. Using this approach, we incrementally improve our material platforms, enabling the development of increasingly coherent and uniform spin qubits.

1.5. ENGINEERED SILICON AND GERMANIUM FOR QUANTUM TECHNOLOGY

In this thesis we explore advancements in Ge/SiGe and ^{28}Si/SiGe heterostructures. For both material platforms, the goal is to improve the qubits' host environment to allow for more uniform and longer-lived qubits. For this purpose, in the Ge/SiGe heterostructure we focus on characterising and reducing disorder. In the ^{28}Si/SiGe heterostructure we concentrate our efforts on the study and enhancement of valley splitting, a main limitation for spin qubits in silicon [33], while maintaining a low disorder environment. An overview of the chapters in this thesis is provided in the following.

Chapter 2 discusses the theoretical framework and employed methods that underlie this thesis. We first focus on the band gap engineering of silicon and germanium and how we use these materials to grow ^{28}Si/SiGe and Ge/SiGe heterostructures. We discuss several types of disorder present in the heterostructures such as electrical noise and magnetic noise. We end by discussing the devices and methods that we employ to characterise the material platforms both structurally and electrically.

In chapter 3 we challenge the mainstream approach to grow Ge/SiGe heterostructures on a Si wafer and instead, start the epitaxial growth on a Ge wafer. This choice results in a more uniform crystalline environment with an order of magnitude less dislocations compared to when using a Si wafer. As a consequence, we observe a drastic improvement of disorder properties of the two-dimensional hole gas measured across several

heterostructure field-effect transistors.

In chapter 4 we further explore disorder properties of the two-dimensional hole gas of a Ge/SiGe heterostructure grown on a Ge wafer, by using thick SiGe barrier layers to mitigate the influence of the semiconductor-dielectric interface. The use of thick SiGe barriers results in a record-high mobility for Ge/SiGe heterostructures. We identify that the remaining dominant scattering sources are background impurities and interface roughness. Despite the thick SiGe barriers, we predict that quantum confinement of holes in gate-defined quantum dots is possible.

In chapter 5 we explore whether the improved Ge/SiGe heterostructure also provides a lower noise environment for hole spin qubits hosted in the material. We comprehensively probe the charge noise in complex two dimensional micron-scale devices and find a factor of two improvement in the average probed noise levels. We then use coherently driven spin qubits to extend our investigation from electrical to magnetic noise using spin echo measurements. We identify coherence modulations coming from the spinful ^{73}Ge isotopes as well as the ^{29}Si present in the barrier layers surrounding the Ge quantum well. The findings motivate the necessity of complete isotopic purification of the Ge/SiGe material stack.

In chapter 6 we move onto ^{28}Si/SiGe heterostructures and show statistical measurements of valley splitting in quantum dots. We advance our understanding of valley splitting in Si/SiGe heterostructures by combining atomic level characterisation, theoretical modeling of valley splitting in quantum dots, and transport measurements. We attribute the variability of valley splitting in ^{28}Si/SiGe quantum dots to random Ge and Si composition distributions at the ^{28}Si/SiGe interfaces. We propose practical methods of enhancing the valley splitting above a certain threshold by introducing a small amount of Ge into the ^{28}Si quantum well.

In chapter 7 we build upon our insights from the previous chapter and grow several ^{28}Si/SiGe where we introduce a small amount of Ge into the ^{28}Si quantum well. We achieve this by intentionally diffusing the ^{28}Si/SiGe interfaces while progressively positioning the interfaces closer together, effectively introducing Ge into the ^{28}Si quantum well. We use heterostructure field-effect transistors to characterise the disorder properties and valley splitting in the quantum Hall regime. We find that introducing Ge into the quantum well indeed increases the valley splitting as predicted by our findings in chapter 6. However, we also find a profound correlation between the increased valley splitting and increased disorder induced by the Ge atoms. We show that through precise heterostructure engineering one can find a delicate balance between increased valley splitting and increased disorder.

Lastly, in chapter 8, we conclude the main findings of this thesis and speculate on the next steps in the development of both material platforms.

2

Theory and Methods

It is nice to know that the computer understands the problem,
but I would like to understand it too.

Eugene Wigner

In this chapter we will describe the theory and methods that are employed in this thesis to grow, fabricate, and characterise silicon-germanium heterostructures. We begin by discussing the bandstructure of silicon and germanium and show how it is engineered to confine electrons in silicon and holes in germanium. We will then describe the material challenges that are present in these heterostructures, some of which we manage to address in later chapters of this thesis. We move on to show how the heterostructures are grown using chemical vapor deposition, and subsequently how we characterise them both structurally and electrically. We end the chapter with a brief description of the fabrication process and the cryogenic measurement set-ups used in experiments.

2.1. BANDSTRUCTURE

Silicon (Si) and germanium (Ge) are both group IV semiconductors that share the same diamond (zinc blende) lattice structure. Fig. 2.1(a) shows the diamond lattice structure, which consists of two interleaved face-centered cubic (fcc) lattices giving it a two-atom basis with one atom at coordinates (0,0,0) and a second atom at (1/4, 1/4, 1/4) in units of lattice constant a. The primitive unit cell (blue shaded region) is defined by a set of primitive lattice vectors given by:

$$a_1 = \frac{a}{2}(0,1,1) \qquad a_2 = \frac{a}{2}(1,0,1) \qquad a_3 = \frac{a}{2}(1,1,0)\,. \tag{2.1}$$

These lattice vectors give the crystallographic directions in which the diamond crystal is symmetric under translation.

A system that is periodic in real space is also periodic in reciprocal space (k-space), which is a useful representation to describe the physics of solids. For a diamond lattice, the primitive unit cell in k-space is defined by:

$$b_1 = \frac{2\pi}{a}(-1,1,1) \qquad b_2 = \frac{2\pi}{a}(1,-1,1) \qquad b_3 = \frac{2\pi}{a}(1,1,-1)\,. \tag{2.2}$$

Fig. 2.1(b) shows the primitive unit cell (the Brillouin zone), which has the form of a truncated octahedron. Several points of symmetry are indicated by Γ, L, and X. These high-symmetry points are used to plot the band structure starting at the L-point in the middle of the hexagonal face of the Brillioun zone in the (1,1,1)-direction, going to the Γ-point at the center of the Brillioun zone, and then towards the X-point in the (1,0,0)-direction. The band structure of bulk silicon and bulk germanium is shown in Fig. 2.1(c) and Fig. 2.1(d) respectively. In bulk silicon, the conduction band minimum (CBM), also known as the Δ-point, is at 85% of the distance from Γ towards the X-point. The maximum of the valence band is in the Γ-point, giving silicon an indirect band gap of 1.11 eV [35, 36]. In Fig. 2.1(d) the band structure of bulk germanium is shown. Here, the valence band maximum (VBM) is in the Γ-point and the conduction band mimimum is in the L-point, resulting in an indirect band gap of 0.664 eV [35, 36].

We use the band structure properties of silicon and germanium to confine electrons in the conduction band minimum of silicon and to confine electron holes in the valence band maximum of germanium. However, both the conduction band minimum of silicon and the valence band maximum in germanium suffer from multiple energy degeneracies. These energy degeneracies cause additional degrees of freedom on top of the spin degree

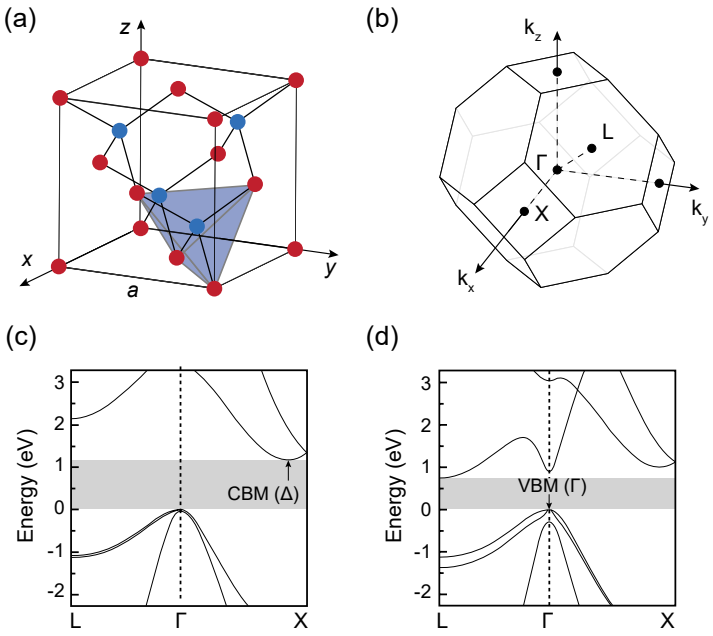

Figure 2.1: **Bandstructure of silicon and germanium.** (a) Diamond lattice structure of silicon and germanium with lattice constant a. The shaded blue region shows the 2-atom primitive unit cell. (b) Primitive unit cell in reciprocal k-space. Symmetry points are indicated by X, L, and Γ. (c) The band structure of silicon plotted along the symmetry points. Silicon has an indirect band gap (grey) of 1.11 eV. The conduction band minima, also known as valleys, are at the Δ-point. (d) The band structure of germanium plotted along the high symmetry points. Germanium has an indirect band gap (grey) of 0.664 eV. The top of the valence band is in the Γ-point.

of freedom that defines a spin qubit. This can negatively impact qubit operations such as initialisation and Pauli spin blockade (PSB) [37, 38]. In the next section, we will see how we can design silicon-germanium material platforms that make use of strain and band gap engineering to resolve these degeneracies.

2.1.1. BAND GAP ENGINEERING WITH SILICON AND GERMANIUM

Silicon and germanium are the only group IV elements that are completely miscible, giving one the ability to form any random $Si_{1-x}Ge_x$ ($0 < x < 1$) alloy of arbitrary composition [35]. One can use this ability to alter conduction and valence band energies by controlling the $Si_{1-x}Ge_x$ composition. Another way to influence the band energies, is to apply strain to $Si_{1-x}Ge_x$ crystals. Strain can be achieved by making use of the differences in lattice constants between silicon and germanium. The lattice constant of Ge ($a_{Ge} = 0.5658$ nm) is 4.2% larger than the Si lattice constant ($a_{Si} = 0.5431$ nm). Furthermore, the lattice constant of $Si_{1-x}Ge_x$ follows an empirical relation known as Vegard's law [39, 40]:

$$a_{Si_{1-x}Ge_x} = 0.5431 + 0.01992x + 0.002733x^2 \text{ nm}. \tag{2.3}$$

Now, if a sufficiently thin film of $Si_{1-x}Ge_x$ is grown on a $Si_{1-y}Ge_y$ ($x \neq y$) substrate, the $Si_{1-x}Ge_x$ film will accommodate the lattice constant of the underlying $Si_{1-y}Ge_y$ substrate.

From the difference in the lattice constant between the $Si_{1-x}Ge_x$ film and the $Si_{1-y}Ge_y$ substrate, it follows that the $Si_{1-x}Ge_x$ film will be strained. More specifically, for $x > y$ the $Si_{1-x}Ge_x$ film will compressively strained while for $x < y$ the $Si_{1-x}Ge_x$ film will be tensile strained.

The $Si_{1-x}Ge_x$ film and the $Si_{1-y}Ge_y$ substrate will not share the same band energies due to the difference in composition and strain between the two layers. At the interface where the two different layers are in contact, the band energies will bend sharply to keep the Fermi level between the two layers constant, forming a so-called heterojunction. Multiple heterojunctions can be combined to form a heterostructure, where, if engineered correctly, one can create an energy quantum well which can be used to confine holes or electrons. In this thesis, we achieve this by growing a layer of silicon or germanium between two layers of silicon-germanium. We will refer to these material platforms as Si/SiGe and Ge/SiGe heterostructures.

Fig. 2.2(a) shows a schematic of a tensile strained Si quantum well sandwiched between two SiGe layers. In such a Si/SiGe heterostructure, both the conduction band energy E_{CB} and valence band energy E_{VB} of the strained Si will be lower in energy compared to the SiGe layers, creating a type II band alignment. For example, the conduction band offset between the Si layer sandwiched between two $Si_{0.7}Ge_{0.3}$ layers is about 160 meV [33, 35]. When we apply a positive gate voltage to the heterostructure, the band energies will tilt crossing the Fermi level (dotted line) such that electrons will accumulate in the Si layer.

In bulk silicon there are six equivalent conduction band minima (also known as valleys), which need to be resolved to form a well-defined two level system for a qubit. The strain induced in the quantum well breaks the symmetry of the silicon lattice, effectively splitting the 6-fold Δ_6 energy degeneracy into an in-plane 4-fold $(+k_x, -k_x, +k_y, -k_y)$ Δ_4 degeneracy and an out-of-plane $(+k_z, -k_z)$ Δ_2 degeneracy (see Fig. 2.2(b)). The Δ_2 levels are about 200 meV [33] lower in energy compared to the Δ_4 levels. Due to additional confinement from electrostatic gates and electric fields, the Δ_2 levels are split into two non-degenerate energy levels. The energy difference between these two levels, often referred to as the valley splitting energy E_{VS}, can vary between a few tens to hundreds of μeV [41, 42]. Maximizing the valley splitting energy is a crucial aspect in Si/SiGe heterostructures, as it competes with the Zeeman energy-split spin-up and spin-down state that defines the spin qubit.

Fig. 2.2(c) shows a schematic of a compressively strained Ge quantum well sandwiched between two SiGe layers. In such a Ge/SiGe heterostructure, the valence band energy in the Ge layer is higher compared to the surrounding SiGe layers, while the opposite is true for the conduction band energies, creating a type I band alignment. As Fig. 2.2(c) shows, the difference in valence band energies between the strained Ge (sGe) layer and the SiGe layers creates a finite energy well ($\approx$ 130 meV for Ge between $Si_{0.2}Ge_{0.8}$ [43]). Under the application of a negative gate voltage, the valence band energy E_{VB} of the strained germanium (sGe) will cross the Fermi level first (dotted line), allowing for the accumulation of holes.

Like Si, bulk Ge also suffers from a six-fold energy degeneracy in the valance band maximum at the Γ-point. Because of the presence of spin-orbit interaction, the six-fold degeneracy is lifted into a four-fold degeneracy in the top most valence band and a

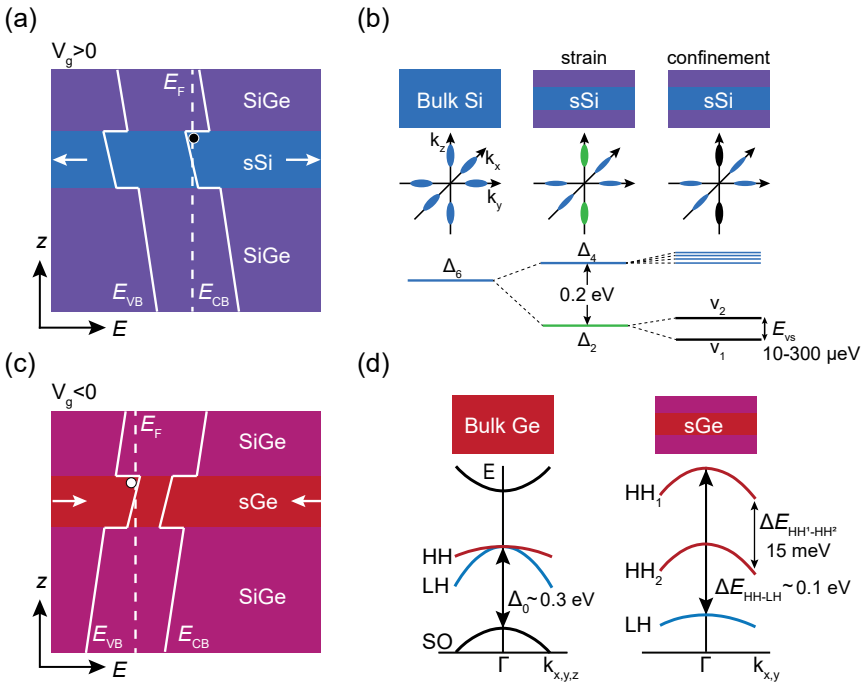

Figure 2.2: **Bandstructure under confinement.** (a) Schematic of a Si/SiGe heterostructure. In such a structure the silicon quantum well is tensile strained and both the conduction- and the valence band energy in the silicon quantum well is lower compared to the SiGe layers, creating a type II band alignment. When applying a positive gate voltage through a metal gate (not shown) the conduction band will tilt such that one can accumulate electrons in the conduction band minimum of the silicon layer. (b) The conduction band minimum (valley) in bulk silicon has a 6-fold energy degeneracy (Δ_6). The valleys can be split in energy using a combination of strain and confinement to create two energy states v_1 and v_2. The energy difference between these two states is characterised by the valley splitting energy E_{VS}. For reference, several energy splittings are indicated. (c) Schematic of a Ge/SiGe heterostructure. The germanium quantum well is compressively strained. The valence band energy in the Ge quantum well is higher compared to the surrounding SiGe layer, while the opposite happens for the conduction band energy, creating a type I band alignment. When applying a negative gate voltage to a metal gate (not shown) electron holes are accumulated in the valence band maximum of the germanium quantum well. (d) In bulk germanium the valance band maximum is 6-fold energy degenerate, which is split in energy by $\Delta_0 \approx 0.3$ eV due to the presence of spin-orbit interaction. The valence bands at the Γ-point can be grouped into heavy hole (HH) and light hole (LH) bands. These are split in energy due to the combination of strain and confinement, where the HH band is energetically favoured. For reference, several energy splittings are indicated.

two-fold degeneracy separated in the lower laying split-off (SO) band [44]. The energy difference, referred to as the spin-orbit gap Δ_0 is roughly 0.3 eV for germanium (see Fig. 2.2(d)). Near the Γ-point, the valence band can be grouped into heavy-hole (HH, red) and light-hole (LH, blue) states. In Ge/SiGe heterostructures, the holes are strongly confined in the z-direction, resulting in a quasi 2D system. The strong confinement in combination with the strain in the Ge layer will give rise to an energy splitting $\Delta E_{\mathrm{HH-LH}}$ of more than 100 meV [45] between the HH and LH states, where the HH states will be energetically favoured. Furthermore, subbands (HH_1, HH_2) will arise as shown in the

right panel of Fig. 2.2(d). These subbands are separated in energy by roughly 15 meV [43], creating a sufficiently large energy spacing for defining a spin qubit.

The creation of Si/SiGe and Ge/SiGe heterostructures is a challenging effort and although theoretically both material platforms can act as a host for spin qubits, in practice there are many challenges to overcome. In the next section we will discuss some of these challenges.

2.2. MATERIAL CHALLENGES IN SI AND GE HETEROSTRUCTURES

In this section we will discuss the material challenges present in the Si and Ge heterostructures. Improvements in spin qubits were often preceded by improvements in the heterostructure hosting the spin qubit [46–48]. Therefore, to further achieve advancements in spin qubit performance it is important to understand different types of disorder present in the heterostructures, and how to address them. With disorder we mean everything that uncontrollably interacts with the electron or hole spin qubit. We distinguish between two types of disorder: static disorder and dynamic disorder. Static disorder, such as strain fluctuations and crystal dislocations, affect the global potential landscape that confines a spin qubit. Dynamic disorder, such as charge noise and magnetic noise, fluctuates over time and can depend on device operation. In the following sections, we will describe several types of disorder including crystal dislocations, charge noise, and magnetic noise.

2.2.1. STRAIN AND DISLOCATIONS

Arguably, the most critical layer of the Ge/SiGe and Si/SiGe heterostructures is the strained quantum well. In both cases, strain in the quantum well is achieved when growing a thin layer of Ge or Si on top of a SiGe alloy that is *strain-relaxed*. If the layer of Si or Ge is thin enough, it will adopt the lattice constant of the SiGe on which it is grown. As Eq. 2.3 shows, the lattice constant for any SiGe composition is always larger than the lattice constant of Si ($a_{\mathrm{SiGe}} > a_{\mathrm{Si}}$) and always smaller than the lattice constant of Ge ($a_{\mathrm{SiGe}} < a_{\mathrm{Ge}}$). This means that a strained Ge layer grown on top of a relaxed SiGe will be compressively strained (see Fig. 2.3(a)). Similarly, a strained Si layer grown on top of a relaxed SiGe will be tensile strained (see Fig. 2.3(b)).

To achieve the growth of tensile strained Si or compressively strained Ge, we first need a strain-relaxed SiGe. As SiGe substrates of high crystalline qualities are not available, one grows the SiGe alloys starting from a high-quality silicon or germanium substrate. However, in the growth process of SiGe alloys, dislocations will form. As Fig. 2.3(c) shows, when growing a thick enough $Si_{1-x}Ge_x$ on top of $Si_{1-y}Ge_y$ ($x \neq y$), strain relaxation occurs through the formation of dislocations. We identify two types of dislocations, misfit dislocations, and threading dislocations. Upon relaxation, misfit dislocations form at the interface between the $Si_{1-y}Ge_y$ and $Si_{1-x}Ge_x$ films. For (001) oriented substrates, the misfit dislocations have line vectors along the [110] and [1$\bar{1}$0] direction [49]. Each misfit dislocation can spawn up to two threading dislocations, which thread upwards at a 60° angle along the (111) plane (see Fig. 2.3(d)) [40]. The threading dislocations could be problematic as they can travel upwards and eventually penetrate the quantum well, where they can trap charges acting as scattering centers or source of charge noise. This can be detrimental not only to the mobility of charge carriers, but also to the functioning

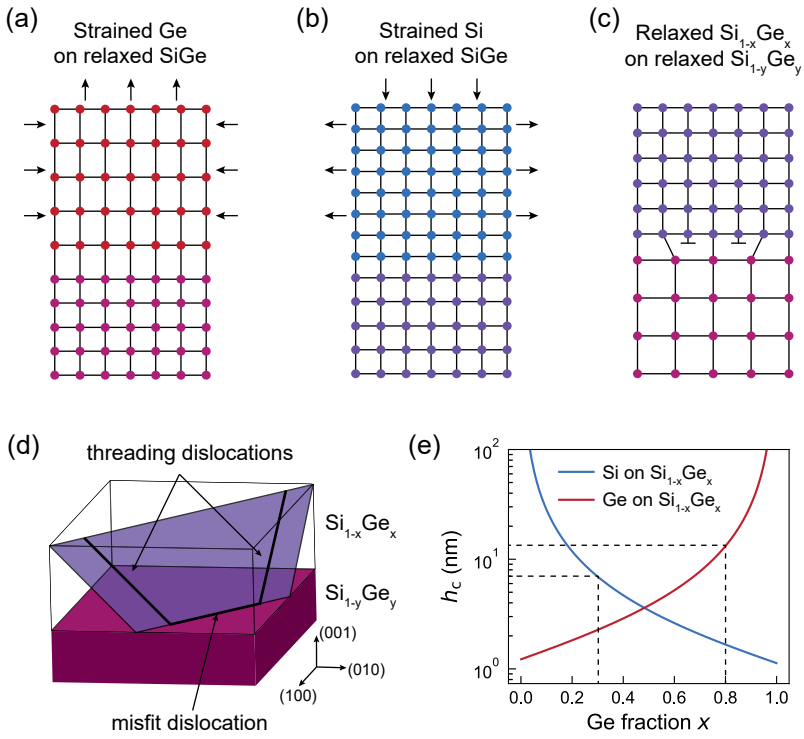

Figure 2.3: **Strain and dislocations.** (a) Schematic of a strained Ge layer grown on a strain-relaxed SiGe substrate. Arrows express that the Ge layer is compressed in-plane and is stretched out in the out of plane direction. (b) Schematic of strained Si grown on strain-relaxed SiGe. Arrows express that the Si layer is stretched in-plane while in the out of plane direction it is compressed. (c) Schematic of a strain-relaxed $Si_{1-x}Ge_x$ on top of another strain-relaxed a $Si_{1-y}Ge_y$ ($x \neq y$) layer. Since the two SiGe alloys do not share the same lattice constant, at the interface there will be a formation of dislocations. (d) Schematic of the two type of dislocations that form. Misfit dislocations will run in plane along the [110] and [1$\bar{1}$0] direction. Once misfit dislocations get blocked, threading dislocations will form traveling upwards along the (111) plane. (e) The critical thickness h_c as a function of Ge fraction x for the case of Si grown on $Si_{1-x}Ge_x$ (blue) and Ge grown on $Si_{1-x}Ge_x$ (red). Dotted lines indicate the critical thickness of Si on $Si_{0.7}Ge_{0.3}$ (6.9 nm) and Ge on $Si_{0.2}Ge_{0.8}$ (13.3 nm).

of quantum dots.

The thickness of a $Si_{1-x}Ge_x$ film grown on top of $Si_{1-y}Ge_y$ substrate for which strain-relaxation occurs is called the critical thickness h_c. The critical thickness is described by the Matthews-Blakeslee law [50]:

$$h_c = \frac{b}{8\pi f}\frac{(1-\nu\cos^2\theta)}{(1+\nu)\cos\lambda}\left[\ln\left(\frac{h_c}{b}\right)+1\right]. \tag{2.4}$$

In Eq. 2.4, $f = (a_f - a_s)/a_s$ is the misfit between a film and a substrate with lattice constant a_f and a_s respectively, ν is the Poisson ratio, and $\cos\theta = \cos\lambda = 0.5$ for 60° $a/2<110>$ type dislocations [51]. This model of the critical thickness assumes pre-existing dislocations in the $Si_{1-y}Ge_y$ substrate [52]. However, it assumes no dependence on the growth temperature or growth rate and deviations from the Eq. 2.3 have been experimentally

observed [53]. Nevertheless, we will use the Matthews-Blakeslee law as an indication at what thickness a strained layer might become likely to relax. Fig. 2.3(e) shows the critical thickness h_c as a function of Ge fraction x for a Si layer grown on a $Si_{1-x}Ge_x$ substrate (blue) and a Ge layer grown on a $Si_{1-x}Ge_x$ substrate (red). We find that the critical thickness of a Si layer grown on $Si_{0.7}Ge_{0.3}$ is 6.9 nm and the critical thickness of a Ge layer grown on a $Si_{0.2}Ge_{0.8}$ is 13.3 nm.

2.2.2. CHARGE NOISE AND MAGNETIC NOISE

Spin qubits are confined and operated by a combination of electric and magnetic fields. Any unwanted fluctuations in either of these fields cause dephasing of the quantum state of the spin qubit. Here we briefly discuss these two types of noise.

Random and uncontrolled electric field fluctuations, often referred to as charge noise, is currently seen as one of the major limitations of (any) spin qubit platform [37, 54, 55]. Although charge noise does not affect the spin state of a qubit directly, it couples to the qubit via the spin-orbit interaction and influences qubit operations such as spin-to-charge conversion, causing initialisation and readout errors. In the material stack, charge noise may be caused by different types of defects acting as two-level fluctuators (TLFs). For example, these defects can be dislocations (threading and misfit) and background contamination such as carbon and oxygen [56]. Another often mentioned source of charge noise is the interface between the heterostructure and gate dielectric where there is a high amount of interface traps [57, 58]. The semiconductor-dielectric interface is especially problematic for Si/SiGe and Ge/SiGe spin qubits since the limited thermal budget, determined by the growth temperature of these heterostructures, does not allow the use of high-quality thermally grown SiO_2 but relatively lower-quality dielectrics (e.g. Al_2O_3 or SiO_2) deposited via low-temperature atomic layer deposition.

In the presence of many two-level-fluctuators the power spectral density of charge noise follows a $1/f$ behaviour with f the switching frequency [59]. This behaviour has been experimentally observed in both Ge/SiGe [60] and in Si/SiGe heterostructures [58]. Deviations of $1/f$ have also been experimentally observed [56], where the power spectral density follows a Lorentzian $1/f^2$ shape typically associated with a single TLF [61].

Magnetic noise is one of the key reasons why the community moved from III-IV materials to group IV materials for spin qubits. Most of the pioneering work on spin qubits was done in GaAs/AlGaAs due to the high quality of growth techniques for these materials [32, 62]. However, all isotopes in Ga and As have a non-zero nuclear spin of $I = 3/2$ resulting in limited coherence times ($T_2^* \approx 10$ ns) due to the hyperfine coupling of the spin qubit to the nuclear spin bath [63]. In comparison, natural silicon and germanium contain isotopes that carry zero nuclear spin with only 4.7% of ^{29}Si ($I = 1/2$) and 7.8% of ^{73}Ge ($I = 9/2$) carrying non-zero nuclear spin respectively. Because of the reduced hyperfine interaction spin qubits in natural Si/SiGe have a longer coherence time of $T_2^* \approx 1$ µs. Moreover, both materials can be further isotopically purified to levels of a few tens of parts per million [64]. This resulted in longer coherence times $T_2^* \approx 20$ µs [48, 65] in a ^{28}Si/SiGe heterostructure with a residual ^{29}Si isotope concentration of 800 ppm. In germanium, spin qubits have only been shown in natural Ge/SiGe heterostructures with reported coherence times of around $T_2^* \approx 1$ µs [66, 67]. Recently, coherence times

in natural Ge/SiGe have been extended to 20 μs using hopping-based qubit operation [68] and 17.6 μs when operating a spin qubit in a hyperfine sweet-spot [69]. To further improve qubit coherence, the growth of fully isotopically purified Ge/SiGe and Si/SiGe material stacks is still an active area of research.

2.3. EPITAXIAL GROWTH OF SI AND GE HETEROSTRUCTURES

In the next sections, we will first describe the processing conditions that we use for the epitaxial growth of the Ge/SiGe and Si/SiGe heterostructures. We then dive into the heterostructures describing layer by layer the growth of the complete material stack.

2.3.1. ASM EPSILON 2000

The silicon and germanium heterostructures covered in this thesis are grown by reduced pressure chemical vapor deposition (RP-CVD) using an ASM Epsilon 2000 reactor at the Else Kooi Laboratory (EKL) of TU Delft. The Epsilon 2000 key features are a load-locked design, single-wafer processing, wafer rotation, and a low thermal mass susceptor. These features are designed to keep ambient air, containing oxygen and moisture, out of the process chamber.

A major benefit of the RP-CVD tool is the fact that it is the preferred tool of the semiconductor fabrication industry for the epitaxy of silicon and germanium due to its compatibility with larger wafer sizes. In contrast, in research settings other systems such as molecular beam epitaxy [70], low energy plasma enhanced chemical vapor deposition (LEPE-CVD) [71], and ultra high vacuum chemical vapor deposition (UHV-CVD) [72] are popular due to their increased flexibility allowing for the growth of novel materials. However, an RP-CVD used in a research setting can act as an excellent bridge between industry and academia. The usage of smaller and cheaper 4-inch wafers allows for cost effective exploration of different growth conditions, which subsequently could be quickly adopted into an industrial setting.

Fig. 2.4 shows a schematic of the three main wafer handling areas of the Epsilon 2000. Wafers are loaded by a user in one of the two available load locks via a cassette that can hold up to 25 wafers. The load locks are purged with N_2 and are only exposed to air during wafer loading and unloading. To remove air, the load locks on this Epsilon 2000 can be repeatedly pumped and back filled using N_2. Only after the preparation of a load lock, is it opened to the wafer handling chamber, which is also always in an N_2 atmosphere. The wafer handling chamber contains a transfer arm with a quartz wand, which is used to take the wafer from the load lock and transfer it to the quartz process chamber. The process chamber is also always purged with N_2 (at room temperature) or H_2 (during processing) and is only opened during wafer loading or unloading.

Figure 2.5(a), (b) show a detailed down- and side view of the process chamber. Process gases enter the chamber at the inlet flange and are carried with a laminar flow through the chamber toward the exhaust flange. During processing, the wafer sits on top of a silicon carbide-coated susceptor, which can rotate around its axis to promote wafer uniformity. The susceptor itself is held by a quartz support and surrounded by a silicon carbide ring, which helps to ensure the laminar flow of gases across the wafer. The susceptor is surrounded by four (front, side, rear, and center) thermocouples that monitor the

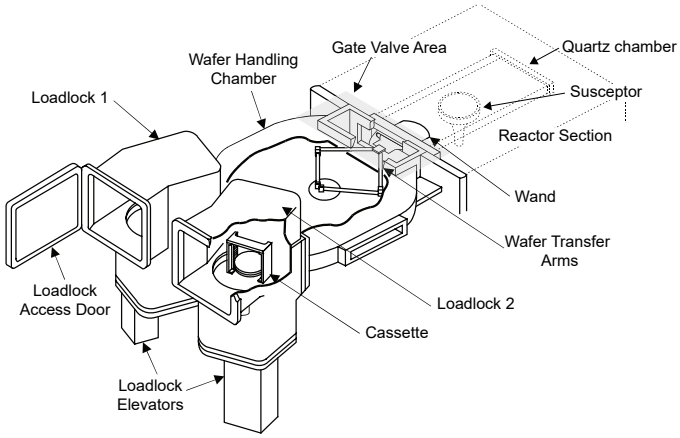

Figure 2.4: **The Epsilon 2000 RP-CVD.** Schematic image of the inside of an ASM Epsilon 2000 RP-CVD. Key features of the Epsilon 2000 are the load locks, single-wafer processing, wafer rotation, and a low thermal mass susceptor. Wafers are loaded in one of the the two load locks, which are physically separated from the process chamber by a wafer handling chamber to avoid the ingress of moisture and oxygen into the process chamber.

temperature of the chamber. The heat is provided and controlled by an array of lamps that surround the process chamber from the bottom and top. The lamps heat up the susceptor, which itself transfers the heat to the wafer. The process chamber itself stays at a cooler temperature to avoid deposition on the walls of the chamber. Lastly, as we run processes under reduced pressure, the process chamber is reinforced with ribs.

Fig. 2.5(c) shows a simplified image of the gas panel and process gases that the Epsilon 2000 at EKL is equipped with at the time of writing this thesis. To begin, there are two carrier gases, N_2 and H_2. When the Epsilon 2000 is not used, there is always a flow of 10 standard liters per minute (slm) of N_2 through the process chamber. When wafers are processed, the carrier gas is switched to H_2.

During processing, the walls of the process chamber become contaminated with silicon and germanium. To keep the chamber walls clean, and therefore facilitate efficient heat transfer from the lamps to the susceptor, we regularly clean the chamber with hydrogen chloride (HCl). However, over time HCl also degrades the parts inside the chamber such as the susceptor. We therefore also coat the susceptor(ring) with silicon after cleaning.

The Epsilon 20000 is equipped with two silicon-based precursor gases, namely dichlorosilane ($Si_2H_2Cl_2$) and an isotopically enriched silane ($^{28}SiH_4$ (1%), 1% diluted in H_2). The isotopically enriched $^{28}SiH_4$ (1%) has a residual amount of 800 ppm of ^{29}Si isotopes left carrying non-zero nuclear magnetic spin. In addition, there are three germanium-based precursor gases (germane), namely GeH_4, GeH_4 (2%), and $^{70}GeH_4$ (2%), the last two both 2% diluted in H_2. The $^{70}GeH_4$ (2%) is depleted of ^{73}Ge isotopes (residual amount of 800 ppm). The natural GeH_4 (2%) and the isotopically purified $^{70}GeH_4$ (2%) share the same process line to the process chamber, which means we cannot flow these two precursor gases at the same time. Having multiple silicon and germanium precursor gases gives the possibility to cover a wide range of growth rates and compositions required for the silicon

and germanium based heterostructures.

The precursor gases are part of the gas panel. The gas panel is further equipped with pressure regulators (row of white circles in Fig. 2.5(c)), which regulate the pressure of each precursor gas to about 1.5 bar. The flow of gases is controlled by mass flow controllers (row of white squares in Fig. 2.5(c)). This Epsilon 2000 also features a set of deposit and vent valves for each gas line. This allows us to individually let each gas flow either to a vent or to deposition inside the process chamber.

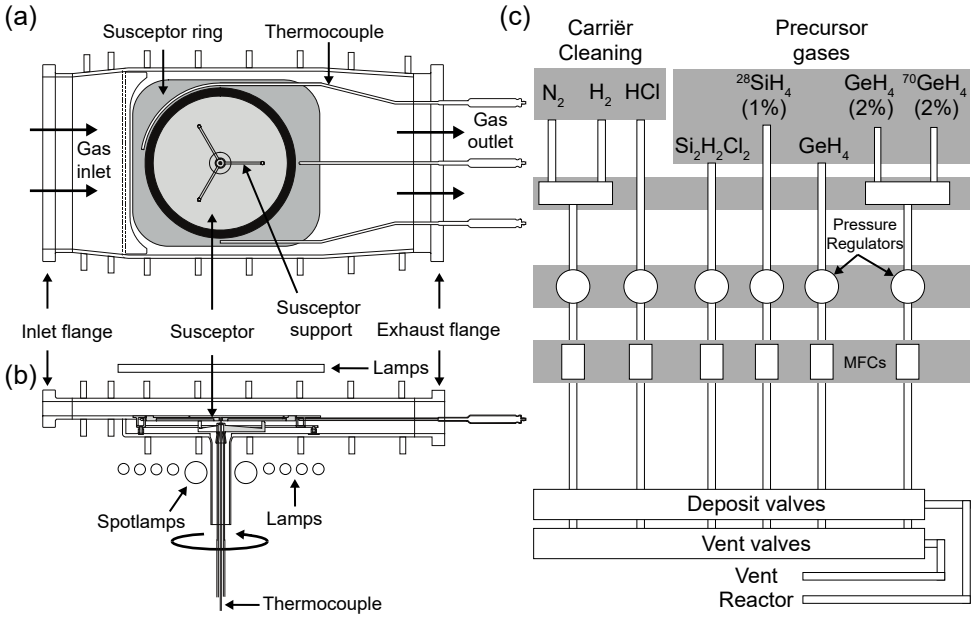

Figure 2.5: **Details of the process chamber and process gases.** (a), (b) Bottom and side on view of the quartz process chamber. Gases enter the chamber from the left, are flown over the susceptor holding a wafer and leave the chamber on the right. There is an array of lamps above and below the chamber that heats up the SiC susceptor, which in turn heats up the wafer. Temperature is controlled by four thermocouples located on the front, side, back and center of the susceptor. To promote processing uniformity, the susceptor rotates around its axis. (c) Shematic image of the gas panel of the Epsilon 2000. N_2 and H_2 are the carrier gases used at room and processing temperatures respectively. HCl is used to clean the process chamber after a wafer is processed. This Epsilon 2000 features two silicon based precursors, $Si_2H_2Cl_2$ and an isotopically enriched $^{28}SiH_4$ (1% diluted in H_2) as well as three germanium based precursors, GeH_4, GeH_4 (2%), and $^{70}GeH_4$ (2%), both 2% diluted in H_2.

2.3.2. GROWING SILICON-GERMANIUM HETEROSTRUCTURES

In this section we cover in detail the growth procedure of the ^{28}Si/SiGe and Ge/SiGe heterostructures used in this thesis. To grow silicon-germanium, a combination of silicon and germanium precursor gases enter the process chamber in a laminar flow using H_2 as the carrier gas. The chamber pressure during growth is always 20 Torr and the flow of the carrier gas is typically a few tens of standard liters per minute (slm). The heat of the chamber decomposes the precursor gases leaving Si, Ge, H, and Cl atoms. Epitaxial growth occurs when the Si and Ge atoms adhere to the heated solid substrate (see

Fig. 2.6(a)). Finally, unreacted gases and desorbed atoms are laminarly flown out of the process chamber to an exhaust.

Fig. 2.6(b) and (c) give a detailed overview of the layers for each heterostructure in terms of Si_xGe_{1-x} composition, layer thickness, and growth temperature. Below, we will address each layer of the two heterostructures.

Wafer preparation

The growth of the Si/SiGe and Ge/SiGe heterostructures starts with a 100 mm n-type silicon wafer (100) with a resistivity of 1-5 Ωcm. Additionally, in the case of the Ge/SiGe heterostructure we explore growth starting from a germanium wafer (100) with a resistivity of 1250 Ωcm. When using a germanium wafer, we first perform an HF clean followed by rinsing with water and a Marangoni drying process, prior to loading the wafer into the load lock. The silicon wafer is placed into the load lock without any precleaning treatments. Once a wafer is loaded into one of the reactor's vacuum load locks, we perform three cycles of pumping and backfilling with N_2 as a first step to remove hydrocarbon contamination during the cleaning and loading process.

Once a wafer is loaded into the process chamber, the wafer is baked at a low pressure of 20 Torr to remove the 1-2 nm native oxide from the wafer's surface. For a germanium wafer, we do this at a temperature of 800 °C for 10 minutes, while for a silicon wafer we use a temperature of 1100 °C for 90 seconds.

Virtual substrate

The virtual substrate (VS) provides a strain-relaxed substrate with a different lattice constant with respect to the underlying silicon or germanium wafer. This is done by gradually adjusting the lattice constant from the substrate to the lattice constant of the desired SiGe composition. The targeted SiGe lattice constant will only be reached once the SiGe is completely strain-relaxed. To ensure strain-relaxation, the layers in the VS are typically several microns thick, which in practice means that the growth of the VS is a time and resource consuming part of the growth process.

The VS of the ^{28}Si/SiGe heterostructure is grown by forward step-grading, where the Ge (1-x) content is increased in four layers ($1-x = 0.07, 0.14, 0.21, 0.31$) with a final Ge content of 31% (see Fig. 2.6(b)). After the growth of each layer, the substrate is annealed at 850 °C to promote the formation of misfit dislocations and hence strain relaxation.

For the Ge/SiGe heterostructure, we use reverse grading to grow the VS. In this technique, first a layer of pure Ge is grown on top of the Si wafer using an initial Ge seed layer grown at 420 °C, followed by multiple growth (625 °C) and annealing (800 °C) cycles. The Ge content is subsequently linearly reduced to 80%. This technique allows for high (70%-80%) Ge contents while keeping the threading dislocation density in the range of $10^6 - 10^7\,\mathrm{cm}^{-2}$ [73]. A downside of this technique is the fact that we grow a pure layer of germanium on top of the silicon substrate, creating an interface of maximum lattice mismatch. This can be avoided by starting the growth of the VS from a germanium substrate. This will minimise the lattice mismatch and consequently treading dislocations are reduced to $10^5\,\mathrm{cm}^{-2} - 10^6\,\mathrm{cm}^{-2}$ [74].

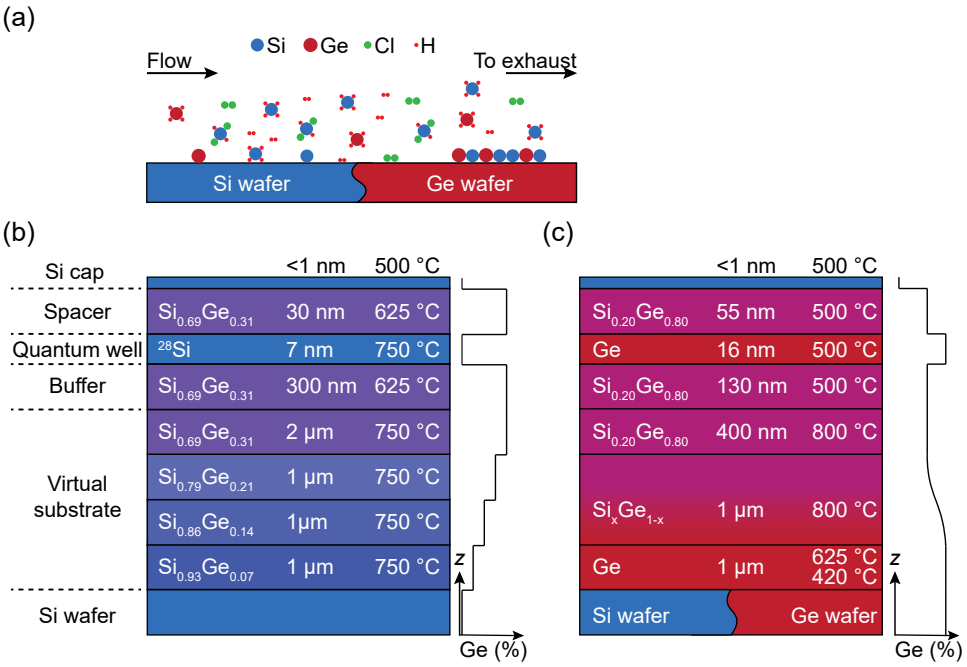

Figure 2.6: **Details of growth process.** (a) Schematic image of the growth process. Precursors and carrier gases are flown laminarly into the process chamber. The gases are decomposed into silicon and germanium atoms and byproducts. Growth happens when the silicon and germanium atoms adhere to the heated silicon or germanium substrate. Byproducts and unreacted gases are subsequently carried out of the process chamber. (b), (c) Layer by layer details of the ^{28}Si/SiGe and Ge/SiGe heterostructures showing layer composition, thickness, and growth temperature. For both heterostructures we show a schematic of the Ge concentration profile throughout the heterostructure.

Buffer layer

The buffer layer is grown to separate the quantum well from the misfit dislocation network trapped inside the VS. This is done by growing the buffer layer with the same composition as the last layer of the VS, but at a lower temperature, 625 °C for the ^{28}Si/SiGe heterostructure, and 500 °C for the Ge/SiGe heterostructure.

The quantum well

A coherently strained quantum well layer is grown on the strain-relaxed buffer layer allowing for the accumulation of electrons in the ^{28}Si quantum well and holes in the Ge quantum well. The ^{28}Si quantum well is grown using isotopically enriched $^{28}SiH_4$ at a temperature of 750 °C. At this elevated growth temperature, we maintain a precise control of the growth rate due to the use of the highly diluted $^{28}SiH_4$ in H_2 (1%). The Ge quantum well is grown using natural GeH_4 at a temperature of 500 °C. The low growth temperature is required to avoid diffusion of the SiGe/Ge and Ge/SiGe interfaces.

Spacer layer
The purpose of the spacer layer is to separate the charges accumulated in the quantum well from the wafer's surface. Typically any fabrication of devices requires the deposition of an oxide (e.g. Al_2O_3 or SiO_2) to insulate the wafer from deposited metal gate electrodes. The interface between the semiconductor and oxide is highly disordered [75] and therefore the spacer has the important job of shielding the charges in the quantum well from this disorder. This is a key feature of heterostructures.

Cap
Both heterostructures are finished with a thin (< 1nm) silicon cap. The silicon cap is grown using dichlorosilane at a temperature of 500 °C. At this temperature, silicon only grows when there are still germanium atoms exposed [75]. As soon as a first complete layer of silicon is grown, the growth will stop. This self-terminating passivation process helps to grow a very thin high-quality capping layer, which will subsequently oxidize once the wafer is exposed to air.

2.4. STRUCTURAL CHARACTERISATION

The structural characterisation is an essential part in the development of ^{28}Si/SiGe and Ge/SiGe heterostructures. In particular, it is important to understand layer thickness, silicon-germanium composition, surface roughness, interface width and roughness, dislocation count, and strain. Fig. 2.7 shows several characterisation techniques that we use to get these insights into our heterostructures.

The best atomic resolution is provided by scanning tunneling electron microscopy (STEM). Imaging is done using a 200-300 keV electron beam that is focused on a thin slice of material called the lamella, which itself is prepared using a focused ion beam (FIB). Fig. 2.7(a) shows a typical STEM image of a ^{28}Si/SiGe heterostructure where atom planes can be resolved. The intensity of the image depends on the atomic weight (Z-contrast), which allows to differentiate between Si and Ge. The intensity profile of an STEM image can be extracted to evaluate quantum well width and interface width.

Atom probe tomography (APT) is a highly specialized technique that provides the opportunity for full 3D reconstruction of the material under study. It offers high spatial resolution (0.1 nm in depth; 0.3-0.5 nm laterally) as well as chemical composition. Fig. 2.7(b) shows such a 3D reconstruction for a ^{28}Si/SiGe heterostructure. APT samples are prepared in the form of a truncated cone with a hemispherical cap. Atoms at the tip of the cap are ionised and subsequently evaporated from the cap by the use of high DC voltages, electric fields, and lasers. A detector records the time of flight and x, y coordinates of where the ions hit the detector. This information is used to build a 3D reconstruction using a dedicated software. We have used APT to study interface roughness over the size of a quantum dot.

Secondary ion mass spectroscopy (SIMS) is used to understand precise chemical compositions as well as the presence of background contaminants such as oxygen and carbon. During a SIMS measurement, a beam of primary ions is used to evaporate secondary ions from a sample which is placed in a vacuum. The secondary ions are collected by a mass spectrometer to specify detected atoms or isotopes. Fig. 2.7(c) shows a

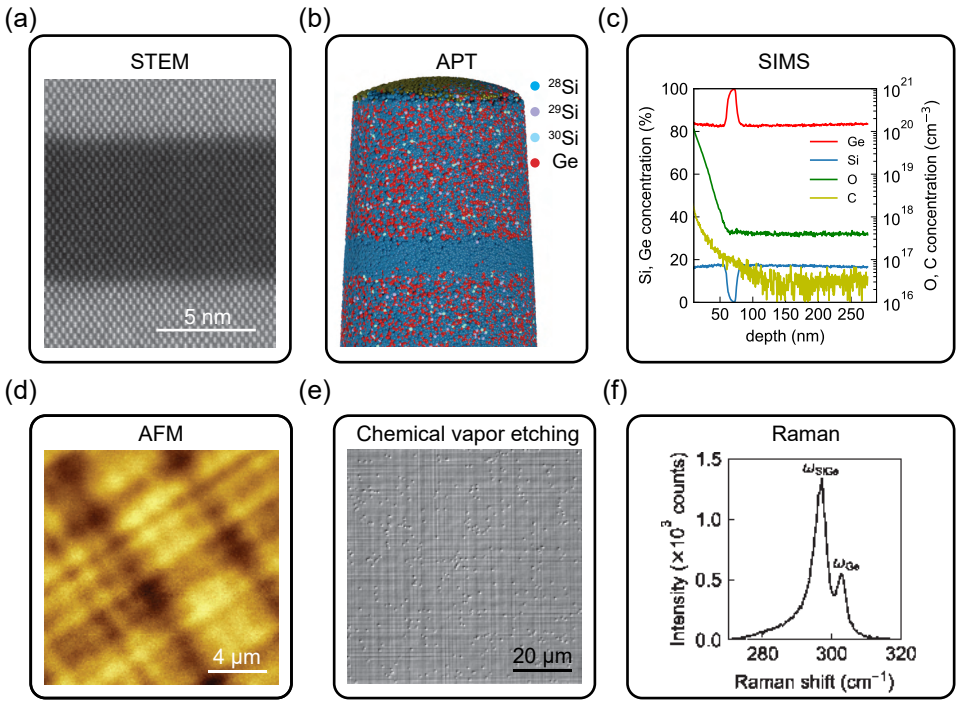

Figure 2.7: **Overview of structural characterisation techniques**. (a) Scanning tunneling electron microscopy (STEM) provides atomic-level precision in layer thickness. The intensity of the image is sensitive to atomic weight allowing to differentiate between silicon and germanium. (b) Atom probe tomography is the only technique that can provide 3D information of a heterostructure. We have used it to study interface roughness over the area of a typical quantum dot. (c) Secondary ion mass spectroscopy offers a high accuracy of chemical composition as well as the detection of background contaminants such as oxygen and carbon. (d) Atomic force microscopy is a non-destructive technique that we use to analyse the 2D surface roughness. It also can reveal the cross-hatch pattern induced by misfit dislocations in the virtual substrate. (e) Chemical vapor etching can be used to reveal threading dislocations present in a heterostructure. (f) Strain is analysed using Raman spectroscopy. It can be used to evaluate lateral strain fluctuations of the quantum well.

shows a typical SIMS profile of the first 250 nm of a Ge/SiGe heterostructure. We routinely measure oxygen and carbon background contaminants below 10^{18} and 10^{17} atoms/cm^3 respectively. SIMS is also used to understand the residual amount of isotopes carrying non-zero nuclear spin in layers grown using isotopically enriched precursor gases.

Atomic force microscopy (AFM) is a non-destructive technique to evaluate the surface of the heterostructures. Fig. 2.7(d) shows an AFM image of a sample and clearly reveals the cross-hatch pattern coming from misfit dislocations in the virtual substrate. AFM can be used to understand 2D surface roughness and the spatial frequency of misfit dislocations from 2D Fourier analysis.

Chemical vapor etching is a technique to understand the density of threading dislocations in the heterostructures. We developed this technique for our ^{28}Si/SiGe and Ge/SiGe heterostructures by etching in-situ the surface of the heterostructure using gaseous HCl [76]. The etch rate into the heterostructure is higher compared to the overall etch rate,

effectively revealing the presence of threading dislocations. In chapter 3, we have used this technique to compare the threading dislocation density in Ge/SiGe heterostructures grown on a silicon or germanium substrate.

To evaluate strain in a layer, especially important for the quantum well, Raman spectroscopy can be used. It uses laser light to evaluate vibrational modes of the crystal giving insight into chemistry and strain of the crystal. In chapter 3 we have used Raman spectroscopy to understand strain fluctuations in the Ge/SiGe heterostructure grown on a Ge substrate.

Lastly, there are several other characterisation techniques that we did not use in this thesis, but can be extremely useful for future development of silicon-germanium heterostructures. Firstly, scanning electron microscopy (SEM) can be used to evaluate layer thickness. It does not have the same spatial accuracy as STEM but it can still easily reveal layers 100 nm thick. Furthermore, it does not require the preparation of a lamella. It is especially useful for calibration of thick layers, such as the ones present in the virtual substrate. Next to this, X-ray diffraction (XRD) is commonly used to evaluate layer thickness and chemical composition. Especially when combined with chemical composition data from SIMS and spatial information from SEM/STEM, XRD can be used to develop growth conditions for new silicon-germanium compositions. Finally, ellipsometry is another non-destructive technique that can be used to evaluate chemical composition and layer thickness. It is a quick analysis technique that can be done in-line and moreover, can provide uniformity maps of chemical composition and layer thickness across the wafer.

2.5. DEVICE FABRICATION

We require the fabrication of devices to characterise the properties of the heterostructures. Two types of devices are fabricated, namely Hall bar shaped heterostructure field effect transistors (H-FETs) and quantum dot devices. The H-FETs are microscale devices that we use to assess macroscopic static disorder present in the material, which we characterise from transport properties such as mobility and percolation density. Quantum dots are nanoscale devices that allow us to assess locally dynamic disorder like charge noise relevant for spin qubits. Below we will give a brief account on the fabrication of these two types of devices on a Ge/SiGe heterostructure. For the fabrication of devices on the ^{28}Si/SiGe heterostructure, we refer the reader to Ref. [77, 78]. All Ge/SiGe heterostructure device fabrication is done in the Van Leeuwenhoek Laboratory (VLL) clean room.

The fabrication of H-FETs is done in four steps on 20x20 mm coupons diced from a 100 mm wafer. Fig. 2.8(a), (b) show a simplified side view and optical image of an H-FET respectively. Each fabrication step consists of coating with optically sensitive photoresist, a baking step to activate the resist, optical lithography with a laser writer or electron beam, and subsequent development using a developer. Photoresist, baking temperature, and developer used depend on the specific fabrication step.

We evaporate 30 nm of platinum into the top SiGe layer to create PtGeSi ohmic contacts (orange). These are annealed at 400 °C into the SiGe to reach the Ge quantum well. To be able to flow a current through the accumulated channel inside the Ge quantum well, the ohmic contacts are wire bonded to a printed circuit board (PCB). Before the Pt evaporation, the wafer's surface is cleaned with a buffered oxide etch (BOE, HF 7:1).

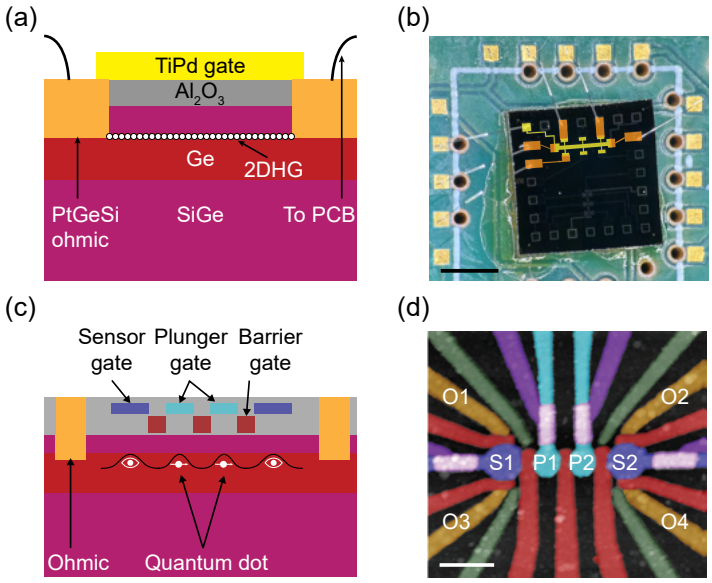

Figure 2.8: **Hall bar and quantum dot devices**. (a) Side view schematic of an H-FET fabricated on a Ge/SiGe heterostructure. We anneal Pt into the top SiGe to create PtGeSi ohmic contacts. These are used to connect to the accumulated channel in the Ge quantum well. We connect the H-FET with wire bonds to a printed circuit board (PCB). The channel in the Ge quantum well is accumulated by a TiPd gate, which is isolated from the heterostructure with an Al_2O_3 oxide. (b) Optical top view image of an H-FET bonded to a PCB. Scale bar corresponds to 1 mm. (c) Side view schematic of a quantum dot device containing two inner quantum dots and two outer sensing dots. The potential landscape is controlled by a set of plunger, barrier, and sensor gates. (d) Top view false coloured AFM image of a quantum dot device. Two inner quantum dots are defined underneath gates P1 and P2 (light blue) and two sensing quantum dots underneath gates S1 and S2 (dark blue). Barrier (green/red) and screening (purple) gates are used to tune the potential landscape around each quantum dot. Nanoscale ohmic contacts (orange) are used as a reservoir. Scale bar corresponds to 100 nm.

We subsequently deposit 30 nm of Al_2O_3 at 300 °C. The high-k dielectric oxide insulates the quantum well from the metal gate. For the metal gate we deposit 10 nm of titanium-paladium (TiPd) on top of the Al_2O_3 oxide. Fig. 2.8(c) shows a quantum dot device featuring two quantum dots defined under metallic gates P1 and P2 (light blue), and two sensing dots defined under metallic gates S1 and S2 (dark blue). The fabrication of these nanoscale devices (scale bar corresponds to 100 nm) uses the same concepts as the fabrication steps for the H-FETs, but requires multiple gate electrodes, defined by electron-beam (e-beam) lithography in order to reach the required nanoscale dimensions.

Fig. 2.8(d) shows a top view false coloured AFM image of a quantum dot device. It is fabricated using two layers of overlapping Ti:Pd gates evaporated using thickness of 3:17 and 3:27 nm respectively. The first gate layer is isolated from the heterostructure by 7 nm of Al_2O_3 and the second gate layer is isolated from the first layer by 5 nm of Al_2O_3. The first gate layer comprises the barrier (red/green) and screening (purple) gate layers, while the second gate layer defines the plunger (P1 and P2) and the sensor (S1 and S2) gates. Nanoscale Pt ohmic contacts (O1-O4, orange) are also defined by electron beam lithography.

2.6. CHARACTERISATION OF HALL BARS

To evaluate the transport properties of a heterostructure, we use Hall bar-shaped heterostructure field effect transistors (H-FETs), as shown in Fig. 2.9(a). Due to their large size (width $W = 100\,\mu m$ and length $L = 1000\,\mu m$), the fabrication requirements are less critical compared to the fabrication of quantum dots. Furthermore, we use cryogenic multiplexers, which allow us to measure multiple H-FETs during the same cool down [79]. If the H-FETs come from different parts of the wafer, this method gives us insights into the uniformity of transport metrics across the wafer. Perhaps most importantly, since H-FET measurements by now are quite standardized in the lab we can use them to evaluate and compare the transport properties from different heterostructures. The results presented in Ref. [80] (also from this lab) is a good example of this procedure where three different heterostructures were evaluated with only a 2 nm difference in the quantum well width between each heterostructure. It shows that H-FETs can be used to carefully optimise different aspects of the overall complex heterostructures.

Experimentally, we measure H-FETs using four-probe lock-in techniques at a frequency of 7.777 Hz. Fig. 2.9(a) shows a schematic image of an H-FET measurement set-up. Both in Ge/SiGe and Si/SiGe we operate the H-FETs in accumulation mode using the top gate voltage V_g to control the density n of charge carriers in the quantum well. We set an AC source-drain voltage V_{sd} across the H-FET (between 0.1-1 mV) and measure the longitudinal voltage drop V_{xx}, transverse voltage drop V_{xy}, and AC current I_{sd} using voltage amplifiers through ohmic contacts. The transverse voltage drop V_{xy} is induced by an out-of-plane magnetic field B with typical values between -0.5 and 0.5 T.

The H-FETs are cooled down in a cryogenic refrigerator and are connected to the room-temperature measurement equipment through twisted pairs of coaxial cables. We use galvanically decoupled SPI and IVVI racks that house current and voltage amplifiers as well as digital to analog converters (DACs). Since the input impedance of the voltage amplifiers $Z_{in} \approx 10\,G\Omega$ is much higher compared to the combined impedance of the ohmics and the conductive channel in the quantum well, the current in the voltage amplifier circuit is negligible. This allows us to accurately measure the drop in voltages and currents in an H-FET. We use the DAC to apply a DC gate voltage V_g to the H-FETs. For the source-drain voltage V_{sd} we use an SR830 lock-in amplifier.

2.6.1. CLASSICAL HALL EFFECT

For low ($|B|$<0.5 T) magnetic fields the transverse resistivity $\rho_{xy} = V_{xy}/I_{sd}$ will depend linearly on the applied magnetic field denoting the classical Hall regime. In this regime the motion of carriers is well described by the Drude model. With this model, we can find the carrier density n using $\rho_{xy} = B/ne$, where e is the electron charge. Once the carrier density n is known, we can use it to find the carrier mobility $\mu = 1/en\rho_{xx,0}$, where $\rho_{xx,0}$ the longitudinal resistivity ($\rho_{xx} = V_{xx}/I_{sd}(W/L)$) at zero magnetic field. We can now plot the mobility as a function of density as shown in Fig. 2.9(b). Each line in Fig. 2.9(b) represents a mobility-density curve from a different H-FET showing transport uniformity of the heterostructure. The maximum carrier mobility μ is a common metric to assess disorder in the heterostructures as it is directly related to the average scattering time τ_t ($\mu = e\tau_t/m^*$). A high mobility points towards a long time between scattering events and therefore a low amount of scattering sources present in the material stack.

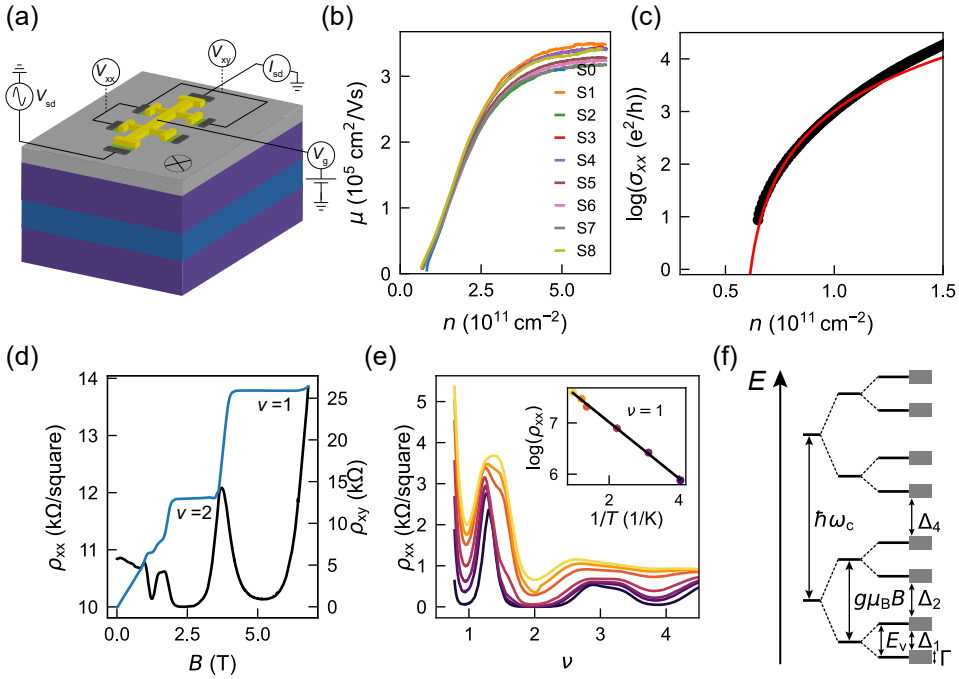

Figure 2.9: **Classical and quantum Hall transport**. (a) Schematic image of an H-FET fabricated on top of a heterostructure. The measurement set-up to characterise an H-FET is shown. (b) Mobility-density plots from multiple H-FETs measured using cryo-multiplexers during the same cooldown. Measuring multiple H-FETs allows us to understand uniformity of the heterostructure across the wafers and extract metrics with statistical significance. A typical metric from this plot is the maximum mobility μ_{max}. (c) Longitudinal conductivity σ_{xx} plotted as a function of density n. From a fit (red line) we extract the percolation density n_{p}. (d) Shubnikov-de Haas oscillations of ρ_{xx} and ρ_{xy}. Plateaus in ρ_{xy} with the associated minima in ρ_{xx} corresponding to filling factor ν are clearly visible. (e) ρ_{xx} as function of ν for different temperatures. For a given filling factor ν, the minima in ρ_{xx} follow an Arrhenius law with respect to temperature. From a fit (see inset) one can extract the mobility gap Δ of the evaluated filling factor. (f) Schematic of the energy levels in the quantum Hall regime. Landau levels are separated in energy by $\hbar\omega_{\mathrm{c}}$. Each Landau level can further split by the Zeeman energy given by $g\mu_{\mathrm{B}}B$. In the case of silicon, these levels are split again by the valley splitting energy E_{v}. Each energy level is smeared out by disorder which is captured by Γ. In practice one measured the mobility gaps Δ corresponding to a specific filling factor ν.

A downside of reporting maximum mobility is that maximum mobility is typically reached at high densities due to screening of the carriers inside the quantum well. Therefore, we also often report the percolation density n_{p}, which is the minimum density of charge carriers needed to form a conductive channel inside the quantum well [81]. At these densities the assessed disorder landscape is more similar to the disorder felt by single charges trapped inside quantum dots [60]. Fig. 2.9(c) shows how we extract the percolation density. We fit (red line) the longitudinal conductivity σ_{xx} as a function of carrier density n using the following fitting formula [82]:

$$\sigma_{\mathrm{xx}} \propto (n - n_{\mathrm{p}})^{1.31}, \tag{2.5}$$

where the percolation density n_p is the only fitting parameter.

2.6.2. THE QUANTUM HALL EFFECT

We can further understand the disorder landscape of our heterostructures by measuring tranport properties in H-FETs in the quantum Hall regime. As Fig. 2.9(d) shows, when entering the quantum Hall regime, the transverse resistivity ρ_{xy} (blue) will increase with quantised steps between resistivity plateaus according to $\rho_{xy} = 2\pi\hbar/e^2\nu$, where ν is called the filling factor. Similarly, the longitudinal resistivity ρ_{xx} (black) will start to oscillate, reaching zero whenever ρ_{xy} is at a plateau.

The oscillations in ρ_{xx} are periodic in ν and the minima occur at magnetic field values given by $B = 2\pi\hbar n/e\nu$ (see Fig. 2.9(d)). This oscillatory behaviour of the longitudinal resistivity is the result of the presence of Landau levels that arise due to the increased confinement from the increased magnetic field. The energy of the n^{th} landau level is given by:

$$E_n = \hbar\omega_c(n+1/2)\,, \tag{2.6}$$

where the cyclotron frequency ω_c is given by $\omega_c = eB/m^*$. Fig. 2.9(f) shows a schematic image of the energy splitting in the quantum hall regime for two Landau levels. In reality, the Landau levels are also spin degenerate. Therefore, each landau level is further split in energy first by the Zeeman gap given by $E_z = g\mu_B B$. In the case of silicon, where there is also the valley degeneracy, the Zeeman levels are split again in energy separated by the valley splitting energy E_v. Finally, the energy levels are smeared out due to the presence of disorder. This disorder is captured by Γ, which is related to the quantum transport lifetime via $\Gamma = \hbar/2\tau_q$.

In practice, we measure the mobility gaps Δ from doing quantum Hall transport measurements for a range of temperatures (see Fig. 2.9(e)). For a given filling factor ν the associated minima in ρ_{xx} follow an Arrhenius law given by:

$$\rho_{xx} \propto \exp(-\Delta/2k_B T)\,, \tag{2.7}$$

where k_B is the Boltzmann constant and T the temperature. Using this relation, we extract the mobility gap Δ associated with a specific filling factor ν.

2.7. CHARACTERISATION OF QUANTUM DOTS

Quantum dots are useful devices to use as local probes for the characterisation of material properties such as valley splitting and charge noise. Fig. 2.10(a) shows a top view false-coloured AFM image of a device containing two quantum dots (P1, P2) and two sensing quantum dots (S1, S2). The device is operated by connecting all sensor (dark blue), barrier (green, red), screening (purple), and plunger (light blue) gates to DACs, which apply DC gate voltages to each gate (not all shown in Fig. 2.10(a) for clarity). The ohmic contacts (orange) provide a reservoir of charge from which each quantum dot can be loaded.

We use the different gates to tune the potential landscape around a quantum dot. If done correctly, one can create discretely spaced energy levels. Fig. 2.10(b) shows a simplified image of discrete energy levels present in a quantum dot. If the chemical potential μ_N of a charge N falls within the bias window set by the source drain voltage V_{sd} a current will flow through the quantum dot. By changing the voltage of the quantum

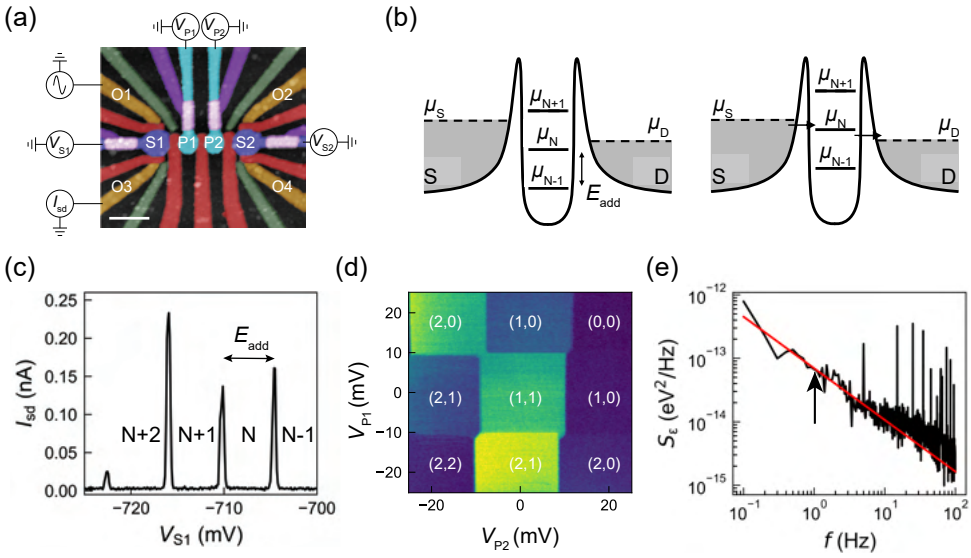

Figure 2.10: **Quantum dot characterisation**. (a) False coloured AFM image of a quantum dot device containing two quantum dots defined underneath gates P1 and P2 (light blue) and two sensing quantum dots defined underneath gates S1 and S2 (dark blue). Barrier gates (green, red) and screening gates (purple) are used to control the potential landscape around each quantum dot by applying DC voltages to each gate. Pt ohmic contacts O1-O4 (orange) act as charge reservoirs. Current through a quantum dot can be measured by applying an AC source drain voltage V_{sd} on one ohmic and measuring the current I_{sd} on another ohmic. (b) Schematic of the quantised energy levels present in a quantum dot. Current will flow through a quantum dot once the chemical potential μ_N of charge N level falls within the bias window between the chemical potentials of the source (μ_s) and drain (μ_d). Figure adapted from Ref. [77] (c) Current I_{sd} as a function of plunger gate voltage V_{S1} of sensing quantum dot S1. We observe sharp equally spaced Coulomb peaks corresponding to the equally spaced energy levels of the quantum dot. Due to the sharp flank of the Coulomb peak, quantum dots can be used as sensors to sense the charge state of capacatively coupled nearby quantum dots. In (d) we show the charge state of the double dot system defined underneath plunger gates P1 and P2, sensed by quantum dot S1. (e) The flank of the Coulomb peak can also be used to measure current fluctuations over time. This can be converted to a charge noise power spectral density S_ϵ as a function of frequency f. Charge noise at 1 Hz is often quoted to compare noise levels between different material platforms.

dot (e.g. V_{S1}) we effectively move the ladder of energy levels through the bias window resulting in a sequence of sharp Coulomb peaks (see Fig. 2.10(c)).

Since a Coulomb peak is very sharp, when we position ourselves on the flank of the Coulomb peak, we can accurately sense the charge state on a capacitively coupled nearby quantum dot. In this way, Fig. 2.10(d) shows a the charge state of the quantum dots defined underneath plunger gates P1 and P2. Such a figure is called a charge stability diagram. In this case, the charge transitions are almost perfectly straight due to the use of virtual gate matrices [83]. This is normally not the case since neigbouring quantum dots are capacatively coupled to each other.

Quantum dots are also excellent to measure noise present in the heterostructures. Charge noise is regarded as a detrimental source of noise for spin qubits. Charge noise can be measured by monitoring current fluctuations at the flank of a Coulomb peak where they are most pronounced. Current fluctuations are converted to a current noise spectral

density S_I from a Fourier transform. Current noise spectral density is converted into charge noise spectral density using

$$S_\epsilon = \frac{\alpha^2 S_I}{|\mathrm{d}I/\mathrm{d}V|^2}, \tag{2.8}$$

where α is the lever arm. Fig. 2.10(e) shows a typical charge noise spectral density S_ϵ as a function of frequency f, following a $1/f$ (red line) trend. Charge noise levels are often quoted at a frequency of 1 Hz to compare noise present in different material platforms to each other.

2.8. CRYOGENIC REFRIGERATORS

H-FETs and quantum dots need to be characterised at cryogenic temperatures (typically between 10 mK and 4 K) where the thermal energies are lower than energy scales for quantum devices. For example, typical values for valley splitting in silicon are around 100 μeV, which corresponds to 1.16 K. The measurements presented in this thesis are either performed in a Leiden MCK50-400 wet ^{3}He/^{4}He dilution refrigerator (chapters 3, 4, 5, 6, and 7) or in a BlueFors LD400 dry ^{3}He/^{4}He refrigerator (chapter 5).

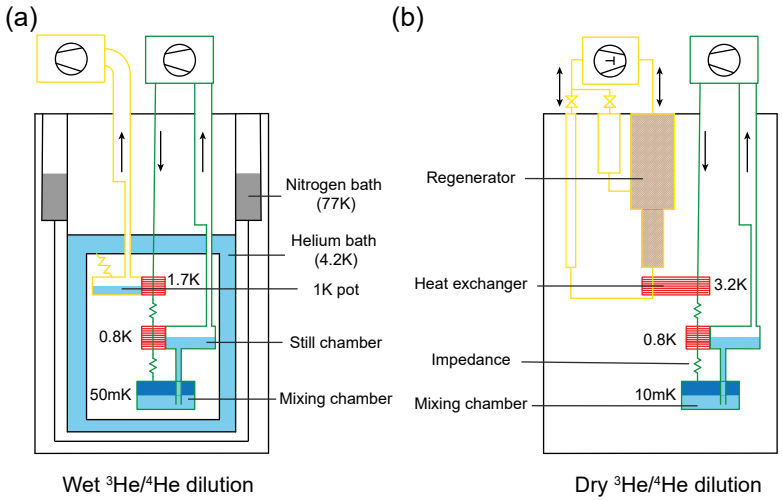

Figure 2.11: **Schematic of wet and dry ^{3}He/^{4}He dilution refrigerator**. (a) Schematic of a wet dilution refrigerator. The system makes use of liquid Nitrogen and Helium for its pre-cooling reaching a temperature of 1.7 K in the 1K pot. Major components including pumps, still chamber, and mixing chamber are indicated. (b) Schematic of a dry ^{3}He/^{4}He dilution refrigerator. This system makes use of a regenerator to do the pre-cooling to a temperature of 3.2 K. Figures adapted from [77, 84].

Fig. 2.11(a), (b) show a schematic image of both types of refrigerators. Each system can be split up into a pre-cooling circuit (yellow) and a closed main cooling circuit (green). The main cooling circuit is identical between the two systems and consists of a still chamber, a mixing chamber, and a mixture of ^{3}He and ^{4}He isotopes that is pumped around the

circuit. The isotope mixture is first pre-cooled from room temperature to 1.7 K (3.2 K) by the pre-cooling circuit in the wet (dry) system using heat exchangers. A second step of cooling is performed with heat exchangers at the still chamber where additional cooling comes from the evaporation of the Helium mixture. The Helium mixture then enters the mixing chamber as a liquid, where the mixture separates into a concentrated (dark blue) and dilute (light blue) ^{3}He phase. The mixture of the two phases provides the final cooling power where the base temperature of the refrigerator is reached.

The main difference between the wet and dry dilution refrigerators is in the pre-cooling circuit. A wet system makes use of liquid Nitrogen (77 K) and liquid Helium (4.2 K) for its pre-cooling. A part of the Helium bath is directed to the 1K pot where the evaporation of Helium results in a temperature of 1.7 K. A dry system makes use of a two-stage pulse tube that pushes and pulls ^{4}He through a regenerator, a magnetic porous material with a high specific heat. In each system the pre-cooling system is connected to the main-cooling system via a heat exchanger.

3

GERMANIUM WAFERS FOR STRAINED QUANTUM WELLS WITH LOW DISORDER

We grow strained Ge/SiGe heterostructures by reduced-pressure chemical vapor deposition on 100 mm Ge wafers. The use of Ge wafers as substrates for epitaxy enables high-quality Ge-rich SiGe strain-relaxed buffers with a threading dislocation density of $(6\pm1)\times10^5$ cm^{-2}*, nearly an order of magnitude improvement compared to control strain-relaxed buffers on Si wafers. The associated reduction in short-range scattering allows for a drastic improvement of the disorder properties of the two-dimensional hole gas, measured in several Ge/SiGe heterostructure field-effect transistors. We measure an average low percolation density of* $(1.22\pm0.03)\times10^{10}$ cm^{-2}*, and an average maximum mobility of* $(3.4\pm0.1)\times10^6$ cm^2/Vs *and quantum mobility of* $(8.4\pm0.5)\times10^4$ cm^2/Vs *when the hole density in the quantum well is saturated to* $(1.65\pm0.02)\times10^{11}$ cm^{-2}*. We anticipate immediate application of these heterostructures for next-generation, higher-performance Ge spin-qubits and their integration into larger quantum processors.*

This chapter has been published as: **L.E.A. Stehouwer**, A. Tosato, D. Degli Esposti, D. Costa, M. Veldhorst, A. Sammak, G. Scappucci,"Germanium wafers for strained quantum wells with low disorder", Applied Physics Letters, **123**, 9 (2023).

3.1. INTRODUCTION

Strained germanium quantum wells in silicon-germanium heterostructures (Ge/SiGe) have become the leading platform for quantum computation with hole spin qubits [44]. Single-hole spin qubits and singlet-triplet qubits can be universally controlled [66, 85, 86], four-qubit logic has been executed [87], and quantum dot systems have been scaled to crossbar arrays comprising 16 quantum dots [88]. Furthermore, the demonstration of a hard superconducting gap in Ge [89] motivates the pursuit of coherent coupling of high fidelity Ge spin qubits using crossed Andreev reflection for achieving two-qubit gates over micrometer distances [90, 91]. While single-spin qubits have been operated with fidelity as high as 99.99% [92], and rudimentary error correction circuits have been executed [93], quantum coherence limits the operation of larger systems. Although Ge can be isotopically enriched to remove dephasing due to hyperfine interaction [94], which can also be achieved by strong confinement [95], hole spin qubits are highly sensitive to charge noise, strain fluctuations, and other types of disorder that can affect the spin-orbit interactions [45, 96–98]. In addition to optimizing the semiconductor-dielectric interface in qubit devices, further improving the crystalline quality of strained quantum wells [56] appears as a key step to obtain a quieter environment for Ge quantum dots.

In the absence of suitable SiGe wafers for high-quality and uniform epitaxy, strained Ge quantum wells are commonly deposited on $Si_{1-x}Ge_x$ strain-relaxed buffers (SRBs) with high Ge composition ($x \approx 0.7-0.8$) [44]. Starting epitaxy from a Si wafer, Ge-rich SiGe SRBs are obtained by composition grading either in a forward-graded process [71] or in a reverse-graded process after the deposition of a thick strain-relaxed Ge layer [43, 99]. In both cases, the large lattice mismatch between the Si substrate and the Ge-rich SiGe SRB causes a dense misfit dislocation network, with associated threading dislocations that propagate through the quantum well. Moreover, such misfit dislocation network drives significant local strain fluctuations inside the Ge quantum well [100], thus challenging the scalability of semiconductor qubits. In Ge/SiGe heterostructures used to host qubits, the threading dislocation density (TDD) is in the range $\approx 10^6 - 10^7$ cm^{-2} [43, 85]. It is not surprising that Si/SiGe heterostructures have smaller TDD ($\approx 10^5$ cm^{-2}) because the Si-rich SiGe SRBs have less lattice mismatch to the Si substrate due to the smaller Ge composition ($x \approx 0.2-0.3$). In this Letter we depart from Si wafers and investigate Ge/SiGe heterostructures grown directly on Ge wafers, mitigating the complication of a large lattice-mismatch between Ge-rich SiGe and Si wafers. As a result, we show a significant enhancement of the crystal quality of the heterostructure, as well as a drastic improvement in the disorder properties of the two-dimensional hole gas (2DHG) that it supports.

3.2. STRUCTURAL CHARACTERISATION

Schematics in Figs. 3.1(a) and (b) compare heterostructures on a Ge wafer with our control reverse-graded heterostructures on a Si wafer [60], the same that supported a four qubit quantum processor and a 16 quantum dot crossbar array [87, 88]. The 100 mm Ge wafers are prepared for epitaxy by an *ex-situ* HF-dip etch followed by *in-situ* bake at 800 °C. The heterostructure is grown in a high-throughput reduced-pressure chemical vapor deposition tool from high-purity germane and dichlorosilane. The SiGe SRB is ~2.5 μm

thick and obtained by forward step grading of the Si content $(1-x = 0.07, 0.13, 0.17)$. This approach mirrors the common approach in Si/SiGe heterostructures where the Ge content is forward-graded starting from a Si wafer. Like our previous heterostructures [43], the SiGe SRB is deposited at 800 °C and the growth temperature is reduced to 500 °C for the final 200 nm of SiGe below the quantum well and for all the layers above to achieve sharp quantum well interfaces. Importantly, by growing on Ge wafers we avoid the overtensile strain arising from the difference in the thermal expansion coefficients between Ge epilayers and Si substrates [99]. Consequently, to achieve an in-plane strain (ϵ) in the Ge quantum well similar to our previous heterostructures [43, 60], here we increase the final Ge content x in the $Si_{1-x}Ge_x$ SRB to 0.83 (the supplementary material) compared to 0.8 in Refs. [43, 60]). The thickness of the Ge quantum well (16 nm) and of the SiGe barrier on top (55 nm) are nominally the same compared to Ref. [60] for a meaningful comparison of the electrical transport properties.

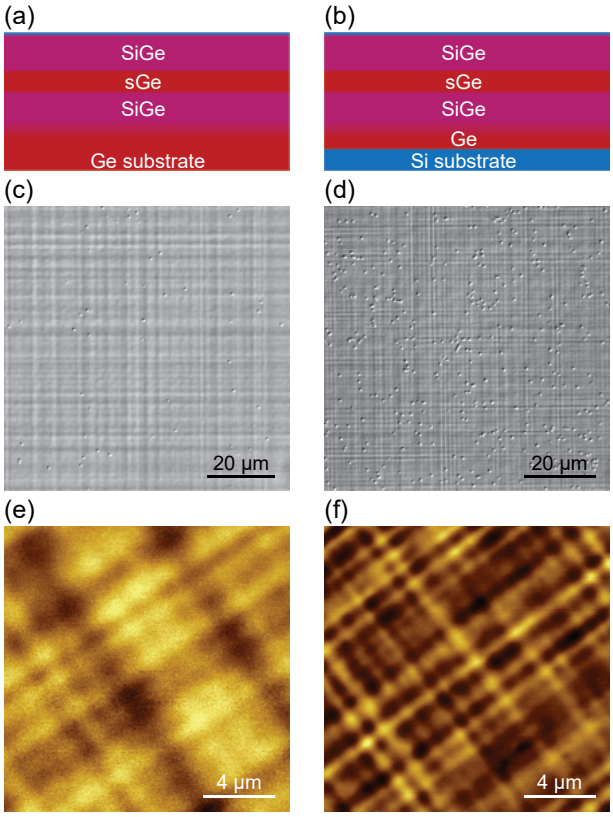

Figure 3.1: (a) Schematic of a Ge/SiGe heterostructure on a Ge wafer and (b) on a Si wafer. The strained Ge (sGe) quantum wells are grown with the same lattice parameter to SiGe strain-relaxed buffers (SRB). (c) and (d) Comparative optical microscope images of the heterostructures in (a) and (b) after threading dislocation decoration. The images are aligned to the ⟨110⟩ crystallographic axes. (e) and (f) Comparative atomic force microscopy images of the heterostructures in (a) and (b). The images were taken with an alignment of about 45 degrees to the ⟨110⟩ crystallographic axes.

Figure 3.1(c) and (d) show comparative images by Nomarski microscopy of the heterostructures on a Ge and on a Si wafer after decorating the threading dislocations by *in-situ* HCl vapor etching [76]. We quantify the TDD by counting the number of decorated threading dislocations from multiple images taken across the wafer. Changing substrate from Si to Ge improves the TDD almost an order of magnitude, from $(5.3 \pm 0.3) \times 10^6$ cm^{-2} to $(6 \pm 1) \times 10^5$ cm^{-2}. Consequently the average TD separation $(1/\sqrt{\text{TDD}})$ becomes much longer, from ~ 4.3 µm to ~ 13 µm. Comparative atomic-force microscopy images in Figs. 3.1(e) and (f) show the typical cross hatch pattern arising from the strain-releasing misfit dislocation network within the SiGe SRB on Ge and Si wafers, respectively. The root mean square surface roughness of both heterostructures is similar at ~1.5 nm. However, the heterostructure grown on a Ge wafer shows cross-hatch undulations with a longer wavelength and weaker high-frequency components of the Fourier spectrum (the supplementary material). This observation supports the intuition that the Ge-rich SiGe SRB has a less dense network of misfit dislocations when grown on a Ge wafer, as the lattice mismatch with the substrate is smaller compared to when it is grown on a Si wafer.

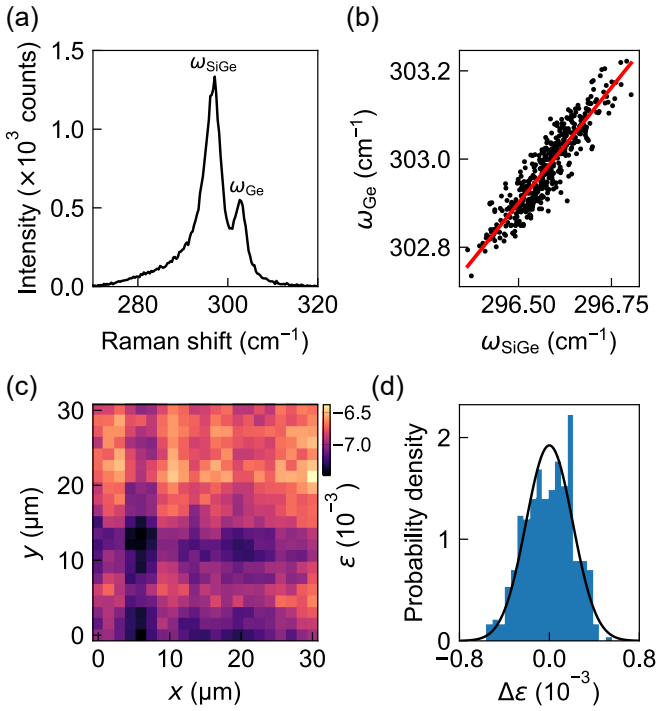

Figure 3.2: (a) Typical intensity spectra as a function of the Raman shift for a Ge/SiGe heterostructure on a Ge wafer. The positions of the Raman peaks from the Ge-Ge vibration modes in the strained Ge quantum well and in the SiGe layer are marked as ω_{Ge} and ω_{SiGe}, respectively. (b) Distribution of Raman peak positions of the Ge-Ge modes obtained by analyzing Raman spectra over an area of 30×30 µm^2 and linear fit (red). (c) Raman strain map, corresponding to the ω_{Ge} Raman shifts in (b). The map is aligned to the $\langle 110 \rangle$ crystallographic axes. (d) Strain fluctuations from the Raman map in (c) and normal distribution fit (black). Counts are normalized such that the area under the curve integrates to one.

We further characterize the heterostructure on the Ge wafer by scanning Raman spectroscopy over an area of 30×30 μm^2, much larger than the length scale of the cross-hatch pattern features. In particular, we determine the in-plane strain in the quantum well ϵ and analyze the origin and bandwidth of its fluctuations. The representative spectrum in Fig. 3.2(a) is obtained with a 633 nm red laser and shows two clear Raman peaks originating from the Ge-Ge vibration modes in the strained Ge quantum well (ω_{Ge}) and in the SiGe layer (ω_{SiGe}). The distribution of these Raman shifts in Fig. 3.2(b) shows a strong correlation, with a slope $\Delta\omega_{\mathrm{Ge}}/\Delta\omega_{\mathrm{SiGe}} = 1.05 \pm 0.02$. Comparing to predictions by Eq. 5 in Ref. [101], we argue that the distribution of the Raman shift in the Ge quantum well is mainly driven by strain fluctuations in the SiGe SRB (expected $\Delta\omega_{\mathrm{Ge}}/\Delta\omega_{\mathrm{SiGe}} \sim 0.83$), rather than compositional fluctuations ($\Delta\omega_{\mathrm{Ge}}/\Delta\omega_{\mathrm{SiGe}} \sim 0.25$). Figure 3.2(c) shows the Raman strain map of the Ge quantum well calculated using $\epsilon = (\omega_{\mathrm{Ge}} - \omega_0)/b^{\mathrm{Ge}}$, where $\omega_0 = 299.9$ cm^{-1} is the Raman shift for bulk Ge and $b^{\mathrm{Ge}} = -440$ cm^{-1} is the Ge phonon strain shift coefficient [102]. We identify signatures of the cross-hatch pattern, with regions featuring higher and lower strain around a mean strain value $\bar{\epsilon} = (-6.9 \pm 0.2) \times 10^{-3}$. This is similar to the compressive strain measured in our Ge quantum wells on a Si wafer [43], validating our heterostructure design and comparative analysis. The statistics of the lateral strain map are shown in Fig. 3.2(d). The strain fluctuations $\Delta\epsilon$ around the average $\bar{\epsilon}$ follow a normal distribution with a standard deviation of 2×10^{-4}. The bandwidth of the strain fluctuations is reduced when compared to the strain fluctuations from the heterostructure on a Si wafer [100], pointing to a more uniform strain landscape.

3.3. ELECTRICAL CHARACTERISATION

The structural characterization highlights the improvement in crystal quality when growing a Ge-rich SRB on a Ge wafer instead of a Si wafer. Next, we show how a better and more uniform crystalline environment improves the disorder properties of the 2DHG. We fabricate six Hall-bar shaped heterostructure field effect transistors (H-FETs) on a 2×2 cm^2 coupon from the center of the 100 mm wafer with a similar process as in Ref. [60] We accumulate a 2DHG inside the Ge quantum well by applying a negative DC gate voltage (V_{g}) to the top gate of the H-FETs and we increase the density p in the 2DHG above the percolation density (p_{p}) by making V_{g} more negative. We use standard four-probe low-frequency lock-in techniques for mobility-density and magnetotransport characterization of all devices in a dilution refrigerator equipped with a cryo-multiplexer [79] ($T = 70$ mK measured at the mixing chamber).

Figure 3.3(a) shows the density-dependent mobility curve (solid line), obtained by averaging over the six H-FETs, together with the standard deviation (shaded region). We observe a tight distribution over the entire density range, indicating a very uniform disorder potential landscape. The mobility increases steeply with increasing density, due to increasing screening of the remote impurity charges, most likely at the semiconductor-dielectric interface. At higher densities ($p > 5 \times 10^{10}$ cm^{-2}), the mobility increases less rapidly, signaling the relevance of scattering from impurities within or in the proximity of the quantum well [103]. We observe a maximum mobility μ_{max} in the range of $3.3 - 3.6 \times 10^6$ cm^2/Vs over the six investigated H-FETS (Fig. 3.3(a), inset), from which we extract an average $\mu_{\mathrm{max}} = (3.4 \pm 0.1) \times 10^6$ cm^2/Vs at a saturation density $p_{\mathrm{sat}} = (1.65 \pm 0.02) \times 10^{11}$cm^{-2}, corresponding to a long mean free path of 23 μm. Figure 3.3(b) shows the

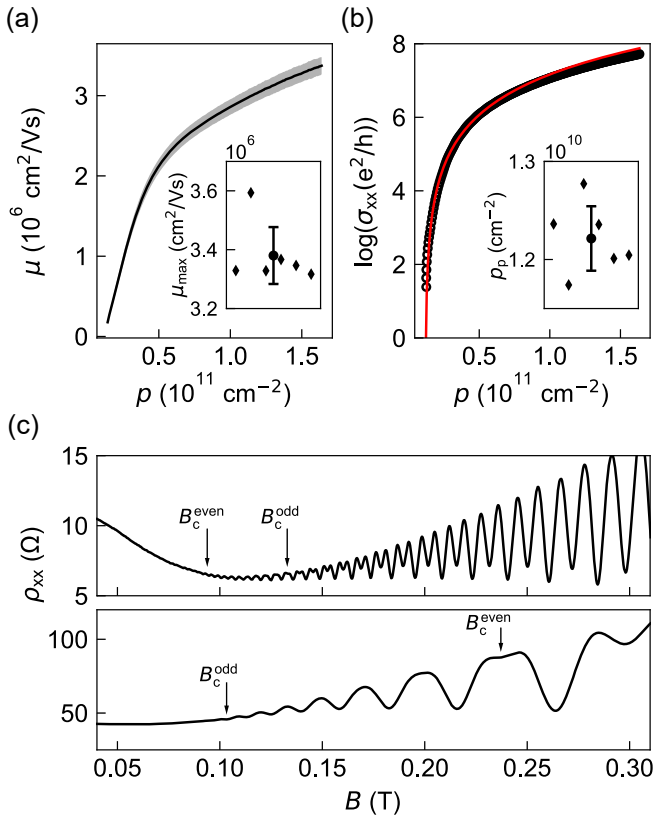

Figure 3.3: (a) Mobility μ mean (black) and standard deviation (shaded) as a function of density p obtained from measurements at $T = 70$ mK of six Hall bar devices from the same wafer. The inset shows the maximum mobility μ_{max} from all the devices and average value ± standard deviation (black). (b) Conductivity σ_{xx} as a function of p (circles) for one device and fit to the percolation theory in the low density regime (solid red line). The inset shows the percolation density p_p from all the devices and average value ± standard deviation (black). (c) Longitudinal resistivity ρ_{xx} as a function of perpendicular magnetic field B measured at a density of 1.5×10^{11} cm^{-2} (upper panel) and 6×10^{10} cm^{-2} (lower panel). B_c^{even} and B_c^{odd} indicate the critical magnetic fields for resolving even and odd filling factors, corresponding to the cyclotron and the spin gap, respectively.

longitudinal conductivity σ_{xx} as a function of density p for a representative H-FET. We extract the percolation density p_p from fitting to percolation theory [82], $\sigma_{xx} \propto (p - p_p)^{1.31}$. The inset shows p_p for the six H-FETs, from which we extract an average percolation density $p_p = (1.22 \pm 0.03) \times 10^{10}$ cm^{-2}.

Compared to our control heterostructures on a Si wafer supporting qubits [60, 87], the maximum mobility is more than 15 times larger and the percolation density is more than 1.5 times smaller. We speculate that this significant improvement, throughout the whole density range, is associated with the suppression of short-range scattering from dislocations within the quantum well. Furthermore, the mobility has not yet saturated indicating that it is still limited by long-range scattering from impurities at the dielectric interface, leaving room for further improvement. In fact, our maximum mobility, repro-

ducible across multiple devices, is less than the value $\mu = 4.3 \times 10^6$ cm^2/Vs measured on a single H-FET in Ge/SiGe grown on a Si wafer [104], likely because the dielectric interface in our samples is much closer to the channel (55 nm compared to 100 nm in Ref. [104]).

The low level of disorder is confirmed by high-quality magnetotransport characterization observed in all devices. Figure 3.3(c) shows representative magneto-resistivity curves from an H-FET at fixed densities of 1.5×10^{11} cm^{-2} (upper panel) and 6×10^{10} cm^{-2} (lower panel). The measurements were performed by keeping V_g constant and sweeping the perpendicular magnetic field B. For each longitudinal resistivity (ρ_{xx}) curve we extract the pair of critical magnetic fields for resolving the cyclotron and the spin gap, $\{B_c^{even}, B_c^{odd}\}$, corresponding, respectively, to even and odd filling factors $\nu = hp/eB$ in the Shubnikov –de Haas oscillations minima. Due to the very small Landau level broadening at high density, the cyclotron gap (see upper panel of Fig. 3.3(c)) is resolved already at very low critical fields and the spin gap only a few oscillations later, $\{B_c^{even}, B_c^{odd}\} = \{0.08, 0.13\}$ T. However, at low density the order is reversed and the spin gap is resolved earlier than the cyclotron gap, $\{B_c^{even}, B_c^{odd}\} = \{0.24, 0.095\}$ T (see lower panel of Fig. 3.3(c)). This is typical to 2DHGs in Ge/SiGe and occurs when the spin gap is more than half of the cyclotron gap, due to the increased perpendicular g-factors of holes at low density [104–106].

The combination of these two aspects, the very low level of disorder and the increasingly large spin gap at low density, makes the canonical methods [107, 108] for extracting the effective mass m^* and single-particle lifetime τ_q not straightforward throughout the investigated density range and will be pursued in a further study. However, we may still estimate the quantum mobility $\mu_q = e\tau_q/m^*$ without making assumptions on m^* and τ_q using the expression $\mu_q = (1 + \sqrt{B_c^{odd}/B_c^{even}})/2B_c^{odd}$ (the supplementary material). With this analysis, we obtain a maximum quantum mobility in the range of $7.7-9.1 \times 10^4$ cm^2/Vs over the six investigated H-FETS (the supplemental material), from which we extract an average maximum $\mu_q = (8.4 \pm 0.5) \times 10^4$ cm^2/Vs at saturation density. This value should be considered as a conservative estimate of μ_q, as the onset of Shubnikov –de Haas oscillations in our high-quality samples might be limited by small density inhomogeneities at low magnetic field [109]. The maximum μ_q is over three times larger than that of our control heterostructures on a Si wafer [60, 87], and approximately two times larger compared to the heterostructures on a Si wafer in Ref. [104]. These results highlight the significantly improved short-range scattering in 2DHGs when the Ge-rich SiGe SRB is grown on a Ge substrate, setting a benchmark for holes in group IV semiconductors.

3.4. DISCUSSION

In summary, we challenged the mainstream approach to deposit Ge/SiGe heterostructures on Si wafers and instead, we started epitaxy on a Ge wafer. We demonstrate a more uniform crystalline environment with fewer dislocations and in-plane strain fluctuations compared to control heterostructures supporting a four-qubit quantum processors. Future investigations using X-ray diffraction spectroscopy to map the complete strain tensor [100] could provide insights into the local strain modifications and fluctuation caused by nanostructured metallic gates. The disorder properties of the 2DHG are also greatly improved, with reproducible ultra-high mobility, very low percolation density, and high quantum mobility. Considering these heterostructures on Ge wafers as a proof of princi-

ple, the electrical transport metrics are likely to further improve by routine optimization of the heterostructure design and chemical vapor deposition process. We anticipate immediate benefit of using these heterostructures for improved uniformity and yield in large quantum dot arrays. Future studies on charge noise and qubit performance may also provide insight in possible improved quantum coherence. Furthermore, it would be of significant interest to explore whether suppressing the dislocation network in the SiGe SRB could improve the performance of superconducting microwave resonators integrated atop the heterostructure, towards the development of hybrid superconductor-semiconductor architectures.

3.5. SUPPLEMENTARY

3.5.1. SECONDARY ION MASS SPECTROSCOPY

Secondary ion mass spectroscopy (SIMS) was carried out to determine the chemical composition of the Ge/SiGe heterostructure on the Ge substrate. Supplementary Fig. 3.4 overlays the Ge (red), Si (blue), O (green), and C (yellow) signals. The data confirms the chemical composition $x = 0.83$ of the $Si_{1-x}Ge_x$ buffer and barrier surrounding the Ge quantum well. The oxygen and carbon concentrations far from the surface are below the detection limit. The rising O and C signals near the surface are routine in SIMS and should be considered an artifact of the measurement.

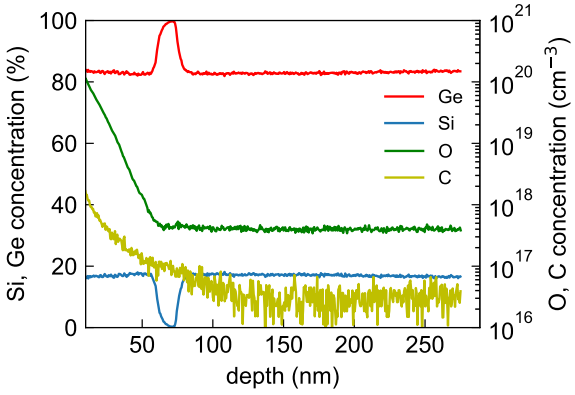

Figure 3.4: Secondary ions mass spectroscopy of Ge/SiGe heterostructures on a Ge wafer, showing Si (blue), Ge (red), O (green), C (yellow) concentration depth profiles

3.5.2. ATOMIC FORCE MICROSCOPY

We analysed the cross-hatch patterns shown in Figs. 3.1(e) and (f) in the main text by performing a 2D Fourier transform using Gwyddion [110]. The results are shown in supplementary Figs. 3.5(a) and (b) for the heterostructure grown on a Ge wafer and Si wafer, respectively. A comparison of the two images shows that the dominant frequencies are spaced closer together in the 2D Fourier transform of the heterostructure on a Ge substrate than those in the heterostructure on the Si substrate. This confirms that using a Ge wafer as a substrate results in a longer wavelength of the cross-hatch pattern compared to when a Si wafer is used, a consequence of the reduced misfit dislocation network present in this heterostructure.

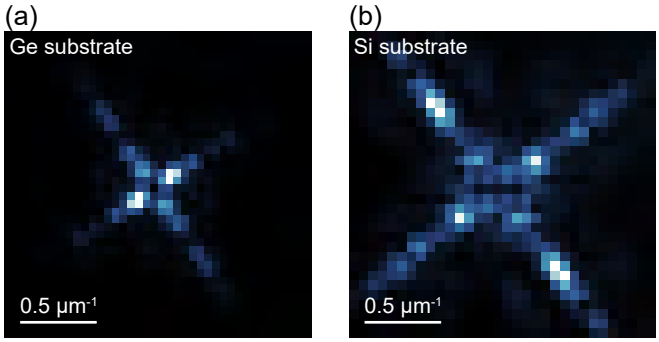

Figure 3.5: (a) 2D Fourier transform of AFM image in Fig. 1(e) in the main text for heterostructures on a Ge wafer. (b) 2D Fourier transform of AFM image in Fig. 1(f) in the main text for heterostructures on a Si wafer.

3.5.3. QUANTUM MOBILITY

In these Ge/SiGe quantum wells on Ge wafers, the combination of the very low level of disorder and the increasingly large spin gap makes an estimate of the effective g-factor g^* and effective mass m^* challenging from the analysis of the thermal activation of the resistivity minima in the Shubnikov -de Haas oscillations corresponding to the cyclotron and spin gap. The same applies to the standard analysis [107] for extracting the single-particle lifetime τ_q, which measures the time for which a momentum eigenstate can be defined even in the presence of scattering [111], and the associated quantum mobility $\mu_q = e\tau_q/m^*$. However, just like the classical mobility is typically measured without knowing the effective mass m^* or the scattering time τ_t, we may also estimate the quantum mobility without a direct measurement of m^* and τ_q. Assuming that Landau levels have a Gaussian broadening $\Gamma = \hbar/2\tau_q$ [111] that increases as $\sqrt{B}$, where B is the perpendicular magnetic field, Refs. [43, 104] show that:

$$g^* = \frac{2m_e}{m^*} \frac{\sqrt{B_c^{\text{even}}}}{\sqrt{B_c^{\text{even}}} + \sqrt{B_c^{\text{odd}}}} \tag{3.1}$$

where B_c^{even} and B_c^{odd} are the critical magnetic fields for resolving the cyclotron and the spin gap, corresponding, respectively, to even and odd filling factors $\nu = hp/eB$ in the

Shubnikov–de Haas oscillations minima of the magnetoresistivity. Evaluating the level broadening at $B = B_c^{odd}$ yields:

$$\Gamma = g^* \mu_B B_c^{odd} \tag{3.2}$$

where the Bohr magneton $\mu_B = e\hbar/2m_e$. Expressing the level broadening in terms of quantum mobility yields:

$$\Gamma = e\hbar/2m^* \mu_q. \tag{3.3}$$

By inserting g^* from Eq. 3.1 and Γ from Eq. 3.3 into Eq. 3.2, we obtain an expression for quantum mobility that is independent of m^* and $g*$:

$$\mu_q = \frac{1 + \sqrt{B_c^{odd}/B_c^{even}}}{2B_c^{odd}}. \tag{3.4}$$

We apply this analysis to the magnetoresistivity curves at saturation density for all six heterostructures field effect transistors and show in Supplementary Fig. 3.6 the obtained quantum mobility values and the average with standard deviation (black).

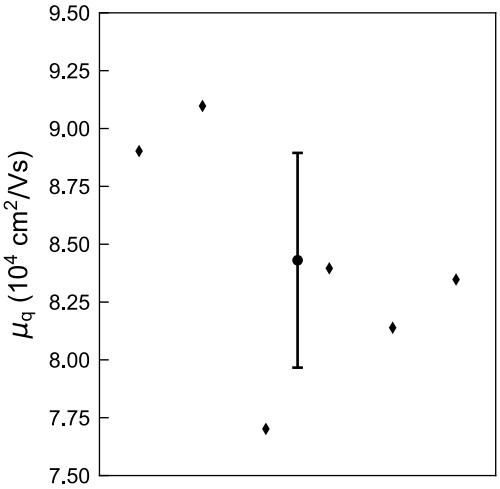

Figure 3.6: Quantum mobility for Ge/SiGe on Ge substrates measured at saturation density for all the six heterostructure field effect transistors.

4

REDUCING DISORDER IN GE QUANTUM WELLS BY USING THICK SIGE BARRIERS

We investigate the disorder properties of two-dimensional hole gases in Ge/SiGe heterostructures grown on Ge wafers, using thick SiGe barriers to mitigate the influence of the semiconductor-dielectric interface. Across several heterostructure field effect transistors we measure an average maximum mobility of $(4.4 \pm 0.2) \times 10^6$ $\mathrm{cm}^2/\mathrm{Vs}$ *at a saturation density of* $(1.72 \pm 0.03) \times 10^{11}$ cm^{-2}*, corresponding to a long mean free path of* (30 ± 1) $\mu\mathrm{m}$*. The highest measured mobility is* 4.68×10^6 $\mathrm{cm}^2/\mathrm{Vs}$*. We identify uniform background impurities and interface roughness as the dominant scattering mechanisms limiting mobility in a representative device, and we evaluate a percolation-induced critical density of* $(4.5 \pm 0.1) \times 10^9$ cm^{-2}*. This low-disorder heterostructure, according to simulations, may support the electrostatic confinement of holes in gate-defined quantum dots.*

This chapter has been published as: D. Costa, **L.E.A. Stehouwer**, Y. Huang, S. Martí-Sánchez, D. Degli Esposti, J. Arbiol, G. Scappucci, "Reducing disorder in Ge quantum wells by using thick SiGe barriers", Applied Physics Letters, **125**, 222104 (2024).

4.1. INTRODUCTION

Holes confined in strained Ge quantum wells are a promising platform for quantum computation with gate-defined quantum dots [44]. Beneficially, the low effective mass [45, 106] allows the definition of quantum dots using large electrodes [112] and the sizeable spin-orbit coupling enables local qubit control that is fully electrical and fast [67]. Recent progress in size and functionality of planar Ge qubit devices include the shared control of a 16 semiconductor quantum dot crossbar array [88], a four qubit germanium quantum processor [87], singlet-triplet qubits at low magnetic fields [85], sweet-spot qubit operation [69], and hopping-based universal quantum logic [68]. All these demonstrations used Si as a substrate for the growth of Ge/SiGe heterostructures.

Previous work [74] has shown how moving from Si to Ge wafers, however, enables better Ge-rich SiGe strain-relaxed buffers (SRBs) because of the smaller lattice mismatch between substrate and strained Ge quantum well. These SRBs on a Ge wafer have a low threading dislocation density of $(6 \pm 1) \times 10^5$ cm^{-2}, nearly one order of magnitude improvement compared to control SRBs on Si wafers [43]. The associated reduction in short range scattering allows for an improvement of the electrical performance of the two-dimensional hole gas (2DHG) in the quantum well, reaching a mobility of $(3.4 \pm 0.1) \times 10^6$ cm^2/Vs [74].

In this Letter, we further explore the potential of Ge/SiGe heterostructures on Ge wafers by growing a thicker SiGe barrier to mitigate disorder from the semiconductor-dielectric interface. By combining Hall transport measurements and scattering theory, we demonstrate an improved mobility and percolation density, setting a benchmark for group IV semiconductors, whilst giving insights into the remaining sources of disorder. Schrödinger–Poisson simulations of quantum confined energy levels indicate that this heterostructure is suitable for hosting gate-defined hole quantum dots.

4.2. STRUCTURAL AND TRANSPORT CHARACTERISATION

We grow a Ge/SiGe heterostructure on a Ge wafer by reduced-pressure chemical vapor deposition, following the same growth protocol described in Ref. [74]. The epitaxial stack comprises a $Si_{0.17}Ge_{0.83}$ SRB by step grading, a compressively strained Ge quantum well, and a $Si_{0.17}Ge_{0.83}$ barrier passivated by a thin Si cap. Here, we increase the $Si_{0.17}Ge_{0.83}$ barrier thickness from 55 nm [74] to 135 nm. We fabricate Hall-bar shaped heterostructure field effect transistors (H-FETs) for magnetotransport characterization by four-probes low-frequency lock-in techniques, as described in Ref. [43]. Figure 4.1(a) shows a high angle annular dark field (HAADF) scanning transmission electron microscopy (STEM) image of the active layers of the H-FET, with no visible defects or dislocation. From the image in Fig. 4.1(b) we estimate a quantum well width $w = 16$ nm and a characteristic length-scale 4τ of both the top and bottom interface of 2 nm, by fitting the intensity profile to a sigmoid model [42, 80] (see the supplementary material). However, the applicability of this model may be limited since we observe a slight accumulation of Si (or depletion of Ge) at both top and bottom interfaces of the quantum well, manifesting as darker lines in the HAADF-STEM image and therefore dips in the contrast profile.

We characterize disorder in this heterostructure by magnetotransport measurements across nine H-FETs in a dilution refrigerator equipped with a cryo-multiplexer [79] (tem-

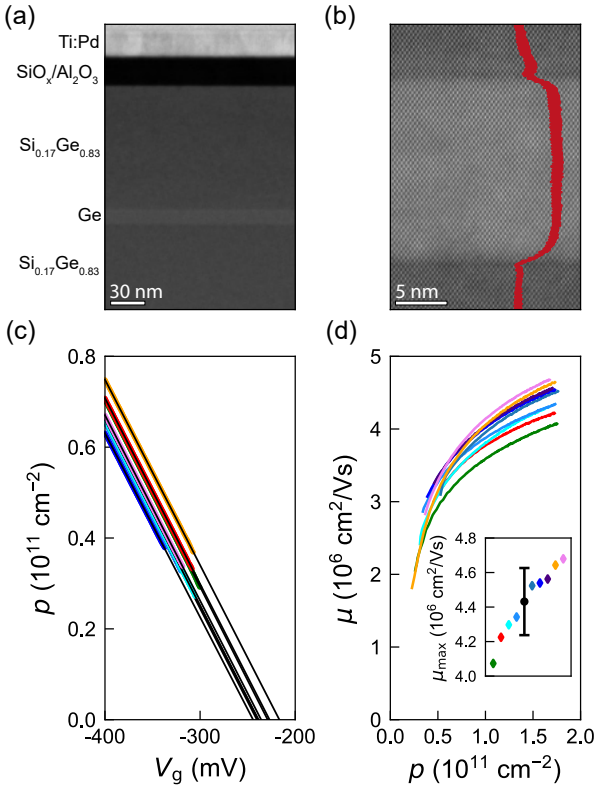

Figure 4.1: (a) HAADF-STEM image of the active layers of the Ge/SiGe heterostructure field effect transistor. The 16 nm strained Ge quantum well is grown coherently on a $Si_{0.17}Ge_{0.83}$ strain-relaxed buffer. A 135 nm $Si_{0.17}Ge_{0.83}$ barrier separates the quantum well from the dielectric stack. The dielectric stack comprises a thin native silicon oxide layer followed by a 30 nm Al_2O_3 film obtained by atomic layer deposition at 300 °C. (b) Close-up image of the Ge quantum well with a superimposed average of the intensity profile (red curve). (c) Hall density p as a function of gate voltage V_g for 9 heterostructure field effect transistors from the same wafer (colored lines) and corresponding linear fits (black lines). (d) Hole mobility μ as a function of Hall density p for the same heterostructure field effect transistors (colored lines) and distribution of maximum mobility μ_{max} (inset). Maximum mobility from all the devices (diamonds), average value, and standard deviation (black) are shown.

perature $T = 100$ mK measured at the mixing chamber). Applying a negative gate voltage V_g capacitively induces a 2DHG and controls the carrier density p in the quantum well as shown in Fig. 4.1(c). From the observed linear p-V_g relationships we obtain a capacitance per unit area C of (65.5 ± 0.3) nF/cm^2 averaged across the H-FETs. The very small standard deviation (less than 0.5%) indicates highly uniform thickness and dielectric properties of the SiGe barrier and the SiO_2/Al_2O_3 layer on top. Furthermore, we extract the gate voltages V_0 for which the density extrapolates to zero (Fig. 4.1(c), black solid lines) and obtain an average value of (-233.8 ± 8.4) mV. Since C is uniform throughout the devices, the tight distribution of V_0, with a standard deviation of 3.6%, is an indication of the very low disorder of the electrostatic potential landscape in the channel. Figure 4.1(d) shows

the density-dependent mobility μ. Whilst all devices achieve a similar saturation density p_{sat} of $(1.72 \pm 0.03) \times 10^{11}$ cm^{-2}, which is consistent with the uniform C, we do observe differences in the lowest measurable Hall density, which is 2.27×10^{10} cm^{-2} for the orange curve. These differences might arise from different contact resistances at low density across the devices. As a general trend, the mobility increases over the whole range of investigated density for all H-FETs. We observe a maximum mobility of $(4.4 \pm 0.2) \times 10^6$ cm^2/Vs averaged across the 9 H-FETs (Fig. 4.1(d), inset) and measured at p_{sat}, corresponding to an average mean free path of (30 ± 1) µm. The largest mobility measured within the distribution is 4.68×10^6 cm^2/Vs, which represents a 9% improvement over the previously highest reported hole mobility in Ge/SiGe heterostructures [104], setting a benchmark for group IV semiconductors. While the heterostructures in Ref. [104] had a dislocation density twice as high, in the 10^6 cm^{-2} range, from being grown on a Si wafer, they exhibited less Si-Ge interdiffusion in the active region possibly due to a lower growth temperature (below 500 °C) compared to our heterostructures.

4.3. EVALUATION OF SCATTERING MECHANISMS

To gain insights into the scattering mechanisms in these high-mobility strained Ge quantum wells, we analyze in Fig. 4.2 the mobility-density curve from the H-FET with the largest measured density range (orange curve, also plotted in Fig. 4.1(d)). We use Boltzmann transport theory at $T = 0$ K and calculate the mobility of the 2DHG in the Born approximation, taking into account the wavefunction of a finite potential well, the gate screening effect, and the local field correction following Ref. [113] (see the supplementary material). The fit to the theory (dashed-dotted black curve) shows good agreement with the experimental data and was calculated considering the contribution to the scattering rate from both uniform background charged impurities (BI) and interface roughness (IR). These individual contributions are shown as dashed black lines (BI) and dotted black lines (IR) in Fig. 4.2, and were obtained using a background impurity concentration of $N_b = 3.8 \times 10^{13}$ cm^{-3} and a surface roughness characterized by a typical height of $\Delta = 10$ Å and lateral size of $\Lambda = 28$ Å. To investigate how relevant is the disorder induced by the semiconductor-dielectric interface, we further evaluate the scattering rate contributed by remote charged impurities (RI). The mobility limited by RI has a quasi-cubic dependence (see the supplementary material) with the distance between the semiconductor-dielectric interface and the 2DHG in the quantum well, which is approximated by the SiGe barrier thickness. This suggests that if RI were the dominant scattering mechanism, increasing the barrier thickness from 55 nm (dashed orange line, from Ref. [74]) to 135 nm (solid orange line) would result in more than one order of magnitude increase in mobility. However, the mobility increased by a factor of ≈ 1.6, from which we conclude that the dominant scattering mechanisms for this H-FET with a thick SiGe barrier are BI at low density and IR at high density, respectively.

We further investigate disorder in the low-density regime by analyzing, for the same H-FET, the density-dependent conductivity σ_{xx} to determine the percolation density p_p. The common method of extracting p_p is to fit the longitudinal conductivity σ_{xx} to the relationship $A(p - p_p)^\alpha$ [114, 115], with coefficient A and p_p as fitting parameters [82] and exponent α fixed to the theoretical value of 1.31 from percolation theory in 2D [116]. Two aspects of fitting percolation density, however, require attention: firstly, there are

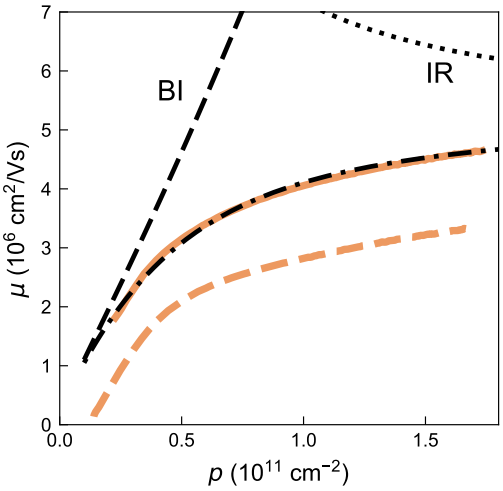

Figure 4.2: Mobility μ as a function of density p from a representative heterostructure field effect transistor with a 135 nm thick SiGe barrier. The dashed-dotted black curve is a theoretical fit to the data considering scattering from a uniform background of charged impurities (BI) and interface roughness (IR). The individual contributions from BI and IR are shown as dashed black curve and dotted black curve, respectively. The dashed orange curve is from a similar heterostructure with a thinner SiGe barrier of 55 nm [74].

studies that consider the exponent α as a free fitting parameter [104, 117]. Secondly, since the theory is only valid in the low-density regime around p_p, a meaningful estimate of p_p should account for its dependence on the density range Δp over which the fit is performed [60, 64]. We systematically address these aspects by performing the following series of percolation fits: for a given value of α, we fix the lower boundary of Δp to the minimum measured Hall density of 2.27×10^{10} cm^{-2} and gradually increase the upper bound until it encompasses the full range under consideration.

We assess the quality of the obtained percolation fits using the R-squared method and in Fig. 4.3(a) show $\log(1-R^2)$ across the portion of the $\alpha - \Delta p$ plane investigated. The local minima are positioned along a continuous curve $\vec{s}\,(\alpha, \Delta p)$ (white dashed line), which identifies the region of best fit to the experimental data and crosses the theoretical 2D case of $\alpha = 1.31$ at a low $\Delta p = 2 \times 10^{10}$ cm^{-2} (red circle). In Fig. 4.3(b), we show the obtained p_p values across the $\alpha - \Delta p$ plane and we use the curve $\vec{s}\,(\alpha, \Delta p)$ to refine the selection of p_p for a more reliable evaluation. The corresponding p_p values are shown in Fig. 4.3(c) as a function of displacement $\Delta\vec{s}$ along $\vec{s}\,(\alpha, \Delta p)$ and relative to the position of best fit for the theoretical 2D case (red circle). The fitted p_p shows an upper bound of about 8.5×10^9 cm^{-2} for positive $\Delta\vec{s}$ at $\alpha = 1.15$, whereas for negative displacements $\Delta\vec{s}$, i.e. $\alpha > 1.31$, p_p may become arbitrarily small, and even take negative, and therefore unphysical, values for $\alpha > 1.5$. For the 2D theoretical case of a percolation-induced metal-insulator transition, characterized by a fixed universal exponent $\alpha = 1.31$, p_p assumes a value of $(4.5 \pm 0.1) \times 10^9$ cm^{-2}, with the experimental data and corresponding very good fit shown as a reference in Fig. 4.3(d).

Having demonstrated the merits of a thick SiGe barrier for obtaining a very low-

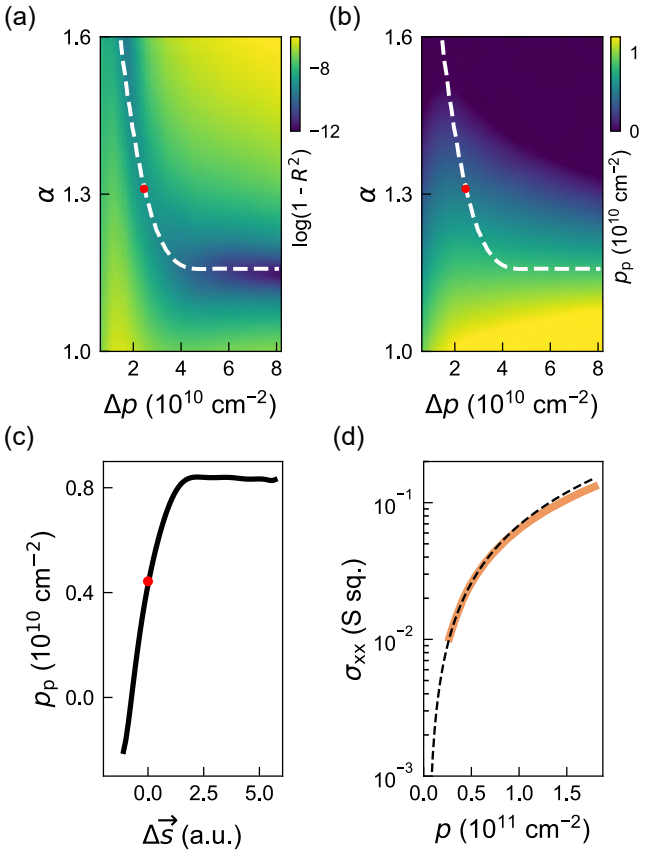

Figure 4.3: (a) Map of $\log(1-R^2)$ as a function of variables α and Δp, where R^2 is the coefficient of determination obtained by fitting the density-dependent conductivity $\sigma_{xx}(p)$ from the device in Fig. 4.2 to the theoretical model $A(p-p_p)^\alpha$. Both A and the percolation density p_p are free fitting parameters, while Δp is the density range over which the data is fitted, starting from the minimum measured density. The dashed white curve $\vec{s}(\alpha,\Delta p)$ follows the local minima of $\log(1-R^2)$. For $\alpha = 1.31$, which is the critical exponent expected from percolation theory in 2D, the local minimum is found at $\Delta p = 2\times10^{10}$ cm^{-2} (red dot). (b) Corresponding map of the fitted p_p as a function of α and Δp, with superimposed dashed white curve $\vec{s}(\alpha,\Delta p)$ and red dot as in (a). (c) Values of p_p as a function of the displacement $\Delta\vec{s}$ along the curve $\vec{s}(\alpha,\Delta p)$, relative to the position of the red dot. (d) Experimental $\sigma_{xx}(p)$ curve (orange) and best fit to percolation theory in 2D (dashed black line). α and Δp are fixed to the values identifying the red dot in (a).

disordered 2DHG, we now assess the practicality of this design choice for confining holes in gate-defined quantum dots. We perform 2D Schrödinger–Poisson simulations using the NEXTNANO software package and show in Fig. 4.4(a) the edge of the first heavy-hole band (HH_0). The top interface of the quantum well is positioned at $z = 135$ nm and the gate stack (a plunger and two barrier gates with dielectric in between) is visible for $z < 0$ nm. Following calculations of the confined energy levels for the heavy-hole and light-hole states, we show in Fig. 4.4(b) that under appropriate voltages applied to the gates (−0.58 V and −0.4 V for plunger and barriers, respectively), only the first heavy-hole

state is occupied in the quantum well. This supports the feasibility of fabricating quantum dots on this heterostructure.

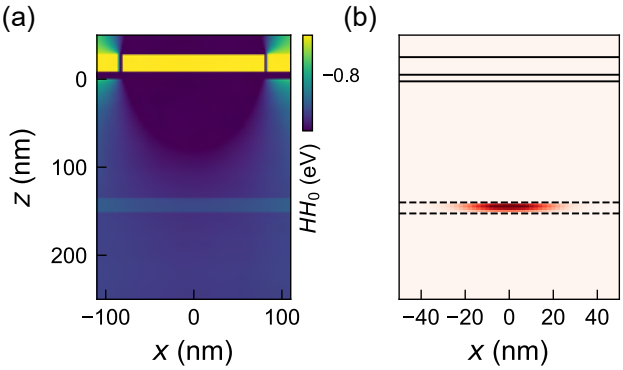

Figure 4.4: (a) Simulated ground state heavy hole (HH) band edge (HH_0) as a function of the x and z coordinates. The strained Ge quantum well is positioned 135 nm below the gate stack ($z < 0$). The plunger gate and the barrier gates are 160 nm and 30 nm wide, respectively. All gates are 30 nm thick. (b) Hole population of the HH ground state, showing a quantum dot-like confinement.

4.4. CONCLUSION

In summary, we investigate Ge/SiGe heterostructures on Ge wafers and demonstrate an improved disorder in the Ge quantum well by using a thick SiGe barrier. The electrical performance of the 2DHG is limited by uniform background impurities and interface roughness and shows very high mobility and low percolation density, which we assessed with a critical evaluation of the fitting procedure. Additional insights into the structural and electrical properties of the heterostructure may be gained by using electron tomography to reconstruct the quantum well interface roughness and alloy disorder in three dimensions [118], and by evaluating the single-particle lifetime and quantum mobility [119] from magnetotransport measurements. The high mobility reported recently in Ge/SiGe heterostructures with similar SiGe barrier thickness and alloy composition[104], despite their higher dislocation density because grown on a Si wafer, is very encouraging. These results suggest that much further improvement in the Ge/SiGe heterostructure on Ge wafers could be also achieved by purifying both Si and Ge gas precursors to suppress background contamination and by eventually lowering the growth temperature of the quantum well and barriers below 500 °C to suppress the Si and Ge interdiffusion at the quantum well interfaces. We predict that quantum confinement of holes in gate-defined quantum dots is feasible in this heterostructure and we estimate that dots of about $1/\sqrt{p_\mathrm{p}} \approx 150$ nm in size, informative about the average distance between impurities or other traps, could be essentially disorder-free. On the path to better performing spin-qubits, further measurements of charge noise in quantum dots will give insights into the dynamics of charge fluctuations that are not probed by magnetotransport experiments.

4.5. SUPPLEMENTARY

4.5.1. SCANNING TRANSMISSION ELECTRON MICROSCOPY

We evaluate the thickness of the quantum well w and the sharpness of the top and bottom interfaces by fitting the intensity profile of the high angle annular dark field (HAADF) scanning transmission electron microscopy (STEM) image in Fig. 4.1(b) of the main text with a sigmoid function:

$$I(x) = \frac{1}{1+e^{\frac{x_{\text{top}}-x}{\tau_{\text{top}}}}} + \frac{1}{1+e^{\frac{x-x_{\text{bottom}}}{\tau_{\text{bottom}}}}}, \tag{4.1}$$

In this function, x_{top} and x_{bottom} are the inflection points of the sigmoid, defining the positions of the top (Ge→SiGe) and bottom (SiGe→Ge) interfaces of the quantum well, and τ_{top} and τ_{bottom} are the their characteristic lengths. The thickness of the quantum well w is given by the distance between x_{top} and x_{bottom}, the parameter 4τ corresponds to the length over which the intensity profile changes from 0.12 to 0.88 of the asymptotic value.

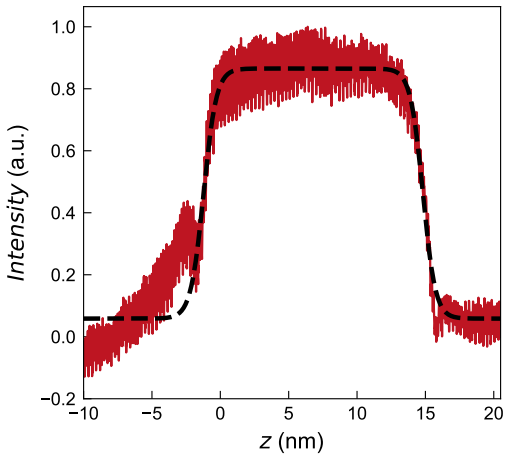

Figure 4.5: Averaged intensity profile of the HAADF-STEM image of the heterostructure active layers (red curve) with a Sigmoid fit to extract characteristic dimensions of the QW (dashed black curve).

For the intensity profile and fit reported in Fig. 4.5, we find a quantum well thickness w of (16.04 ± 0.03) nm and a top and bottom interface sharpness 4τ of (1.88 ± 0.06) nm and (1.83 ± 0.05) nm, respectively. The quantum well thickness is similar to previously grown Ge/SiGe heterostructures on Si or Ge wafers [60, 74]. The intensity profile of the top and bottom interfaces shows Si accumulation (or Ge depletion) that makes the intensity profile deviate from a simple sigmoid model. Further insights may be gained by advanced electron microscopy [118] or atom probe tomography [42] characterization.

4.5.2. SCATTERING THEORY AND FIT OF MOBILITY-DENSITY CURVES

The hole mobility of Ge/SiGe quantum wells is calculated using Boltzmann transport theory at $T = 0$ K. The relevant material parameters are provided below. The in-plane effective hole mass in Ge is $m = 0.055m_0$ where m_0 is the free electron mass, while the out-of-plane effective hole mass in Ge is $m = 0.22m_0$ [45, 106], specifically applicable for the scenario of a compressively strained Ge quantum well embedded in strain-relaxed $Si_{0.17}Ge_{0.83}$. The overall quantum degeneracy is $g = 2$ (comprising a spin degeneracy of $g_s = 2$ and a valley degeneracy of $g_v = 1$, given the large splitting between heavy and light hole bands [43]). The dielectric constant for germanium is $\epsilon = 16$ and the thickness of the quantum well is $w = 16$ nm. The thickness of the top SiGe barrier is $d = 135$ nm. The thickness of the Al_2O_3 oxide layer on top of the SiGe barrier is $d_o = 30$ nm. The valence band offset (representing the potential barrier height) between the strained Ge and the strain-relaxed SiGe barrier is $V_0 = 150$ meV [43]. The lattice constant of Si (Ge) is 5.4 Å (5.7 Å). The thickness of the lower SiGe barrier is $L_{buf} = 1.5$ μm, i.e. much greater than the top barrier and effectively irrelevant for this discussion.

In the calculation of mobility, we use the wavefunction of a finite potential well and take into account both the gate screening effect and the local field correction [113]. The mobility is evaluated using the Born approximation

$$\frac{1}{\tau} = \frac{4m}{\pi\hbar^3}\int_0^{2k} \frac{\mathrm{d}q}{\sqrt{4k^2-q^2}}\left(\frac{q}{2k}\right)^2 \langle|U(q)|^2\rangle, \tag{4.2}$$

where $U(q)$ is the screened potential of a given scattering source. The scattering rate contributed by uniform background charged impurities reads

$$\frac{1}{\tau_{BI}} = \frac{N_b}{k_F}\frac{2\pi\hbar}{m}\left(\frac{2}{g}\right)^2 f_b(s), \tag{4.3}$$

where N_b is the background impurity concentration and $k_F = \sqrt{4\pi p/g_s g_v}$ is the Fermi wavelength. $f_b(s)$ is a dimensionless function given by

$$f_b(s) = \int_0^1 \frac{x\,dx}{\sqrt{1-x^2}(x/s+1)^2} \tag{4.4}$$

$$= \begin{cases} \frac{s^2}{s^2-1} - \frac{s^2\sec^{-1}(s)}{(s^2-1)^{3/2}}, & s \geq 1, \\ \frac{s^2}{s^2-1} + \frac{s^2\ln\left(\sqrt{s^{-2}-1}+s^{-1}\right)}{(1-s^2)^{3/2}}, & s < 1. \end{cases} \tag{4.5}$$

where s is the screening parameter, equal to $q_{TF}/2k_F$, with

$$q_{TF} = \left[g_s g_v (m/m_0)/\epsilon\right]\left(e^2 m_0/4\pi\epsilon_0\hbar^2\right). \tag{4.6}$$

For Ge/SiGe quantum wells, the numerical value of the screening parameter is $s^2 \approx 0.67/p$, where p is in units of 10^{11} cm^{-2}. This means that the screening is weaker in Ge/SiGe hole systems, compared with $s^2 \approx 116/n$ in Si/SiGe electron systems and $s^2 \approx 1.5/n$ in GaAs/AlGaAs electron systems. In the strong screening limit $s \gg 1$, we have $f_b(s) \approx 1$; while in the weak screening limit $s \ll 1$, we have $f_b(s) \approx -s^2 \ln s$.

Using an infinite potential well wavefunction, we then calculate the interface roughness (IR) scattering rate

$$\frac{1}{\tau_{\mathrm{IR}}} = \frac{2\pi^4\hbar}{m}\left(\frac{m}{m_z}\right)^2 \frac{\Delta^2\Lambda^2}{w^6} f_{\mathrm{i}}(s, a_{\mathrm{IR}}), \tag{4.7}$$

where Δ is the typical height and Λ is the lateral size of the interface roughness. The dimensionless function is given by

$$f_{\mathrm{i}}(s, a_{\mathrm{IR}}) = \int_0^1 \frac{2x^4 e^{-x^2 a_{\mathrm{IR}}^2}\, dx}{\sqrt{1-x^2}(x+s)^2}, \tag{4.8}$$

where $a_{\mathrm{IR}} = k_F\Lambda$. In the strong screening limit $s \gg 1$ we have

$$f_{\mathrm{i}}(s \gg 1, a_{\mathrm{IR}}) \approx \begin{cases} \frac{3\pi}{8s^2}, & a_{\mathrm{IR}} \ll 1, \\ \frac{3\sqrt{\pi}}{4s^2 a_{\mathrm{IR}}^5} & a_{\mathrm{IR}} \gg 1. \end{cases} \tag{4.9}$$

In the weak screening limit $s \ll 1$ we have

$$f_i(s \ll 1, a_{\mathrm{IR}}) \approx \begin{cases} \frac{\pi}{2}, & a_{\mathrm{IR}} \ll 1, \\ \frac{\sqrt{\pi}}{2a_{\mathrm{IR}}^3}, & a \gg 1,\ s a_{\mathrm{IR}} \ll 1. \end{cases} \tag{4.10}$$

The finite-potential-well wave function modifies the above expression by a factor of $\tilde{E}^2$ given by

$$\tilde{E} \approx 1 - \frac{4}{\pi\tilde{V}^{1/2}} + \frac{12}{\pi^2\tilde{V}} + \mathcal{O}\left(\tilde{V}^{-\frac{3}{2}}\right), \tag{4.11}$$

where $\tilde{E} = E/E_0$ and $\tilde{V} = (V_0 - E_{\mathrm{F}})/E_0$. E and E_0 are the finite- and infinite-potential-well ground state energies, respectively. V_0 is the potential barrier. In our case of a 16 nm Ge quantum well around a hole density $p = 1\times10^{11}$ cm^{-2}, we have $\tilde{V} \approx 22$, which corresponds to $\tilde{E} \approx 0.77$. The relevant parameters extracted from the mobility fit through the BI (dashed black line) and IR (dotted black line) models are $N_{\mathrm{b}} = 3.8\times10^{13}$ cm^{-3}, $\Delta = 10$ Å, and $\Lambda = 28$ Å.

To further inspect the scattering mechanisms, we also explore the scattering rate contributed by remote charged impurities, which reads

$$\frac{1}{\tau_{\mathrm{RI}}} = n_{\mathrm{r}}\frac{2\pi\hbar}{m}\left(\frac{2}{g}\right)^2 f_{\mathrm{r}}(s, a_{\mathrm{RI}}), \tag{4.12}$$

where n_{r} is the remote impurities concentration. $f_{\mathrm{r}}(s, a_{\mathrm{RI}})$ is a dimensionless function given by

$$f_{\mathrm{r}}(s, a_{\mathrm{RI}}) = \int_0^1 \frac{2x^2 e^{-2a_{\mathrm{RI}}x}\, dx}{\sqrt{1-x^2}(x/s+1)^2}, \tag{4.13}$$

where $a_{\mathrm{RI}} = 2k_{\mathrm{F}}d$. For far away impurities $a_{\mathrm{RI}} \gg 1$ such that $s a_{\mathrm{RI}} \gg 1$, we have $f_{\mathrm{r}}(s, a_{\mathrm{RI}}) \approx (2a_{\mathrm{RI}}^3)^{-1}$. In the regime where $a_{\mathrm{RI}} \gg 1$ and under the condition of weak screening with $s \ll$

1 and $sa_{\mathrm{RI}} \ll 1$, the function $f_{\mathrm{r}}(s, a_{\mathrm{RI}})$ can be approximated as s^2/a_{RI}. For our case $d_{\mathrm{o}} \ll d$ such that remote impurities are relatively close to the gate, and $sa_{\mathrm{RI}} = q_{\mathrm{TF}}d = 17.6 \gg 1$ for $d = 135$ nm ($q_{\mathrm{TF}}d = 7.2 \gg 1$ for $d = 55$ nm), so we have the following expressions for the scattering rate with gate screening [113]

$$\frac{1}{\tau_{\mathrm{RI}}} = \frac{\pi\hbar n_r}{8mk_{\mathrm{F}}^3 d^3}\left(1 + \frac{d^3}{(2d_{\mathrm{g}} - d)^3} - \frac{2d^3}{d_{\mathrm{g}}^3}\right)\left(\frac{2}{g}\right)^2, \tag{4.14}$$

where $d_{\mathrm{g}} = d + d_{\mathrm{o}} + w/2$ is the distance from the gate to the center of the quantum well. The mobility μ_{RI} has therefore a quasi-cubic dependence with the thickness of the top SiGe barrier d. This strong dependence allows to evaluate the relative contribution of remote impurities to scattering compared to the other mechanism. If remote impurities were the primary scattering mechanism, increasing the barrier thickness from 55 nm [74] to 135 nm would have resulted in a more than eightfold increase in mobility. Instead, the mobility increased by a factor of 1.6 in the heterostructure with the 135 nm thick SiGe barrier, pointing to a marginal role of remote impurities as scattering limiting mechanism.

4.5.3. CONDUCTIVITY-DENSITY CURVES

In Fig. 4.6 we show the conductivity density curves for all nine heterostructure field effect transistors. The orange curve, measured to the lowest density, was used for the percolation density analysis in Fig. 4.3 of the main text.

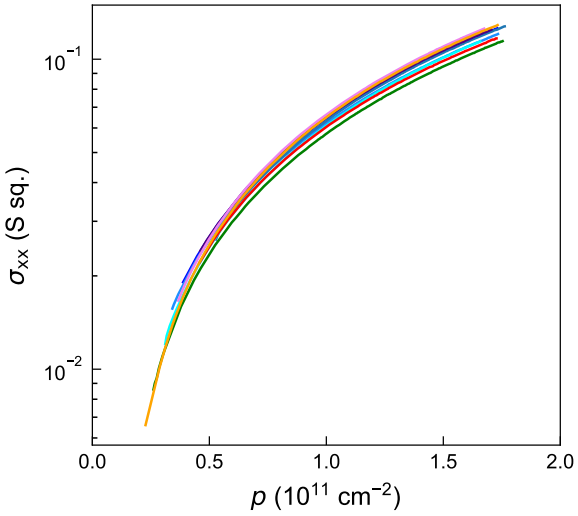

Figure 4.6: Longitudinal conductivity σ_{xx} as a function of Hall density p for the nine investigated heterostructure field effect transistors (colored lines).

5

EXPLOITING STRAINED EPITAXIAL GERMANIUM FOR SCALING LOW-NOISE SPIN QUBITS AT THE MICROMETRE SCALE

Disorder in the heterogeneous material stack of semiconductor spin qubit systems introduces noise that compromises quantum information processing, posing a challenge to coherently control large-scale quantum devices. Here, we exploit low-disorder epitaxial strained quantum wells in Ge/SiGe heterostructures grown on Ge wafers to comprehensively probe the noise properties of complex micron-scale devices comprising of up to ten quantum dots and four rf-charge sensors arranged in a two-dimensional array. We demonstrate an average charge noise of $\sqrt{S_0} = 0.3(1)$ $\mu\text{eV}/\sqrt{\text{Hz}}$ *at 1 Hz across different locations on the wafer, providing a benchmark for quantum confined holes. We then establish hole-spin qubit control in these heterostructures and extend our investigation from electrical to magnetic noise through spin echo measurements. Exploiting dynamical decoupling sequences, we quantify the power spectral density components arising from the hyperfine interaction with* ^{73}*Ge spinful isotopes and identify coherence modulations associated with the interaction with the* ^{29}*Si nuclear spin bath near the Ge quantum well. We estimate an integrated hyperfine noise amplitude* σ_f *of 180(8) kHz from* ^{73}*Ge and of 47(5) kHz from* ^{29}*Si, underscoring the need for full isotopic purification of the qubit host environment.*

This chapter has been published as: **L.E.A. Stehouwer**, C.X. Yu, B. van Straaten, A.Tosato, V. John, D. Degli Esposti, A. Elsayed, D. Costa, S.D. Oosterhout, N.W. Hendrickx, M. Veldhorst, F. Borsoi, G. Scappucci, “Exploiting strained epitaxial germanium for scaling low-noise spin qubits at the micrometre scale", Nature Materials, (2025).

5.1. INTRODUCTION

Recent progress with semiconductor spin qubits [120] has enabled proof-of-principle quantum processors [68, 121–124] with error rates below the 1% threshold predicted to enable quantum error correction [125]. However, millions of highly coherent qubits need to be integrated to achieve a realistic quantum advantage [126]. One avenue to improve quantum performance at scale is by advancing material synthesis and fabrication processes to identify and mitigate the dominant noise sources [127]. In the mature superconducting quantum technology, understanding of noise [61] has advanced and shifted from studying single, isolated components to highly integrated and densely connected quantum systems. For example, Google's Sycamore device [17] has served as a test bed for studying correlated noise in a 39-qubit superconducting quantum processor [128], extrapolating the relevant noise models, and exploring the effectiveness of error correction against correlated noise. In contrast, noise in semiconductor quantum systems has been predominantly studied in isolated components, such as single-charge transistors or individual spin qubits [48, 54, 56–58, 60, 129, 130], with recent efforts beginning to explore correlations [55] beyond nearest neighbors [131, 132]. Operating large and highly connected spin qubit systems, in fact, requires a stringent level of electrostatic uniformity. This uniformity is challenged by the disorder introduced by complex semiconductor materials, gate-stacks, and interfaces, which collectively shape the potential landscape of coupled quantum dots.

Recently, Ge/SiGe heterostructures with exceptionally low disorder have been developed by using Ge wafers as substrates for epitaxy, achieving an order-of-magnitude improvement in both dislocation density and two-dimensional hole gas mobility [74] compared to those grown on Si wafers [44] and used for hole spin qubits [67–69, 85, 87]. Here, we exploit such advancements in the semiconductor material stack to comprehensively study and benchmark the noise properties of holes in germanium. We probe simple systems, such as double quantum dots with sensors on the side, as well as more complex spin qubit devices, integrating ten quantum dots and four sensors in two dimensions. By employing a variety of tools, we assess statistically the noise power spectral density within the same and across different devices on a wafer, measuring under different hole filling conditions. By adopting a single spin as a noise probe at three different qubit sites in a device, we distinguish and quantify the contribution of the three major noise mechanisms in natural germanium qubits: charge noise coupling via spin-orbit interaction and hyperfine interactions with the ^{73}Ge and ^{29}Si nuclear spins baths.

5.2. CHARGE NOISE IN MINIMAL QUANTUM DOT LINEAR ARRAYS

We begin by characterizing charge noise properties in small quantum dot linear arrays using the flank [54, 56, 129, 134, 135] and the Coulomb peak tracking (CPT) [57, 129] methods, inferring the noise spectrum from about 50 μHz to 100 Hz. Here, we focus on two nominally identical devices (device 1 and 2) fabricated on the same Ge/SiGe heterostructure on a Ge wafer detailed in Ref. [74], which supports a two-dimensional hole gas with a high maximum mobility of $3.4(1) \times 10^6$ cm^2/Vs and a low percolation density of $1.22(3) \times 10^{10}$ cm^{-2}. The threading dislocation density is $6(1) \times 10^5$ cm^{-2}, nearly an order of magnitude lower than for growth of Ge quantum wells with similar strain [74]

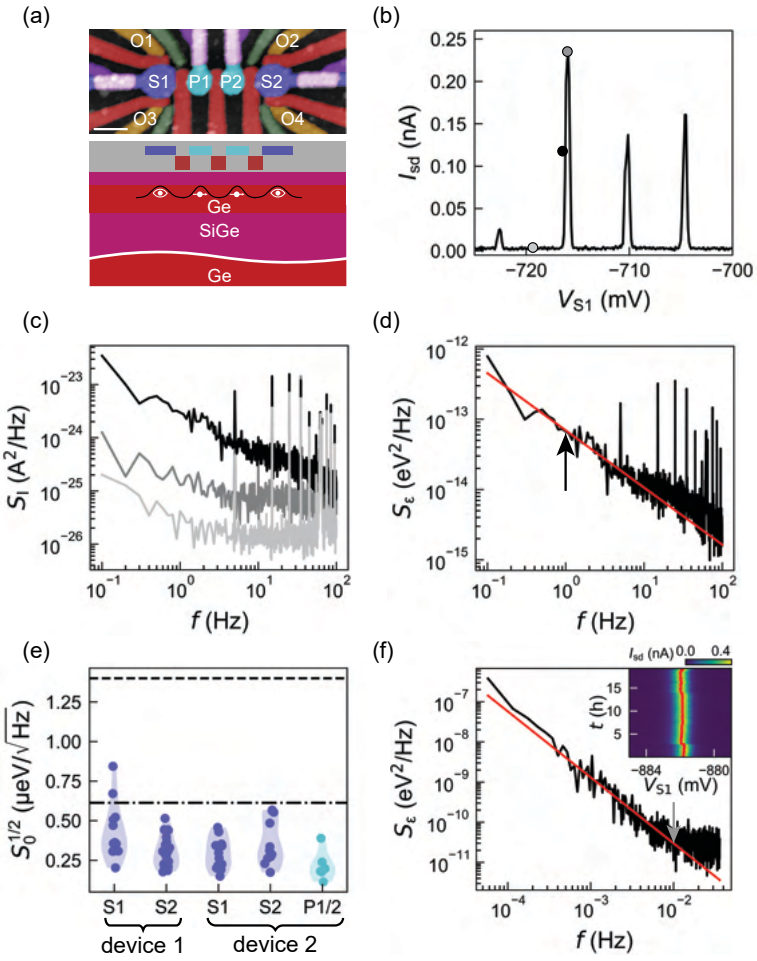

Figure 5.1: **Charge noise in minimal quantum dot linear arrays.** (a) False-coloured atomic force microscopy image (top panel) of a device lithographically identical to the measured ones. The device comprises ohmic contacts (orange) and sensor (dark blue), plunger (light blue), barrier (red, green), and screening gates (purple). The scale bar is 100 nm. The side view schematic cutting through the sensor and plunger gates illustrates the confining electrostatic potential within the Ge/SiGe heterostructure grown on a Ge wafer. (b) Current I_{sd} as a function of sensor voltage V_{S1} of device 2. Black, grey, and light grey circles mark, respectively, the flank, top, and blockade region of a Coulomb peak for the measurement of current fluctuations. (c) Correspondent current power spectral density S_I, with lines coloured to match positions in (b). (d) Representative charge noise power spectral density S_ϵ from the flank of the Coulomb peak at $V_{S1} = -716.2$ mV. The fit to S_0/f^α (red line) using a fitting range between 0.1 and 10 Hz yields a charge noise $\sqrt{S_0}$ at 1 Hz (black arrow) of 0.23(1) μeV/$\sqrt{\text{Hz}}$. (e) Distributions of $S_0^{1/2}$ from charge noise spectrum measurements as in (d) for different hole occupancies. Data points are presented as fitted values of $S_0^{1/2}$. The distribution of $S_0^{1/2}$ are represented by violin plots (shaded regions). Measurements are reported for the sensor and plunger gates from device 1 and 2. As a comparison, dashed and dash-dotted lines are values from Ref. [133] and Ref. [60], respectively. (f) Charge noise spectrum (device 2, sensor S1) extracted from ≈ 18 hour Coulomb peak tracking (inset). The fit to S_0/f^α (red line) using a fitting range between 50 μHz and 10 mHz yields a charge noise of 5.5(9) μeV/$\sqrt{\text{Hz}}$ at 10 mHz (grey arrow). The uncertainty is 1 s.d. from the fit. In the inset, the red line tracks the voltage positions of the Coulomb peak.

starting from a Si wafer. This improvement is due to the reduced lattice mismatch between the substrate and the epitaxial strained Ge quantum well, which is more than four times smaller for Ge wafers compared to Si wafers [39].

As shown in Fig. 5.1(a), the devices comprise two inner quantum dots (under P1, P2) and two charge sensors at the edges (under S1 and S2), spanning a total distance of about 430 nm. Figure 5.1(b) shows a representative Coulomb peak series measured in transport on sensor S1 of device 2. Figure 5.1(c) illustrates the power spectral density S_I of the current fluctuations as a function of frequency f, probed at the top (grey), at the flank (black), and in the blockade region (light grey) of a Coulomb peak (Methods). Measurements performed at the flank yield the larger S_I, indicating that the noise floor of our setup, probed with the relevant impedance of the load, is sufficiently low to measure the charge noise from the device [60].

We convert the current power spectral density measured at the flank into an energy scale using the slope of the Coulomb peak and its lever arm (here ≈ 0.18 eV/V, see Supplementary Fig. 5.5). Figure 5.1(d) shows a representative charge noise power spectral density and the associated best fit to the function S_0/f^α (red line), with $\sqrt{S_0}$ the charge noise amplitude at 1 Hz (black arrow in Fig. 5.1(d)). The approximate $1/f$ trend of the noise spectrum points towards an ensemble of two-level fluctuators (TLFs) with a wide range of activation energies [54, 61]. However, we note that, under specific voltage configurations, we observe spectra that deviate from a simple $1/f$ trend (see Supplementary Figs. 5.6-5.9), which could suggest the strong coupling to a single or a few dominating TLFs [54, 61].

We build up statistics by iterating this protocol for different hole occupancies, various single-hole transistors, and two different devices. We estimate an average charge noise value of $\sqrt{S_0}$ of 0.3(1) μeV/$\sqrt{\text{Hz}}$ and α of 0.9(2). Additionally, we also probe the systems under P1 and P2, by forming a quantum dot in the multi-hole regime under one of the plunger gates, obtaining comparable charge noise values (dark vs. light blue dots in Fig. 5.1(e)). As highlighted in Fig. 5.1(e), the average charge noise value estimated in this work compares favourably to what was reported for previous Ge/SiGe heterostructure implementations. Our value is ≈ 2 times lower compared to Ge quantum wells buried at the same depth of about 55 nm ($\sqrt{S_0}$ = 0.6 μeV/$\sqrt{\text{Hz}}$ [60]) grown on a silicon substrate and a factor of ≈ 5 lower than what measured for shallow Ge quantum wells ($\sqrt{S_0}$ = 1.4 μeV/$\sqrt{\text{Hz}}$ positioned 22 nm from the dielectric interface [133]).

To further corroborate this result, we extend the characterisation towards lower frequencies by using the CPT method, where the sensor gate voltage is repeatedly swept across a small voltage range around a Coulomb peak [129]. We track the Coulomb peak position in time (inset of Fig. 5.1(f) for sensor 1 of device 2 and Methods), and, from the fluctuations in its position, we extract the charge noise power spectral density S_ϵ (Fig. 5.1(f)). We determine the value at f = 10 mHz (grey arrow) by fitting the data to S_0/f^α and find a value of $\sqrt{S_{f=10\,\text{mHz}}}$ = 5.5(9) μeV/$\sqrt{\text{Hz}}$. When we extrapolate the $1/f^\alpha$ trend towards 1 Hz, we find α = 1.64(5) and $\sqrt{S_0}$ = 0.26(1) μeV/$\sqrt{\text{Hz}}$. The extracted α-value of 1.64(5) from the CPT experiment differs with the one from the flank method (α = 0.9(3)), possibly due to the presence of drift noise [54], which we are able to measure due to the long duration (≈18 hours) of the CPT measurement. $\sqrt{S_0}$ is in good agreement with the average charge noise of 0.3(1) μeV/$\sqrt{\text{Hz}}$ from the flank method, confirming our understanding of the system and the reduced noise level in this heterostructure.

5.3. CHARGE NOISE IN A MICRON-SCALE 2D QUANTUM DOT ARRAY

The improvement in the heterostructure disorder metrics enables exploration and tuning of larger quantum dot architectures. We probe a two-dimensional (2D) quantum dot array fabricated on the same heterostructure grown on a Ge wafer. We focus on the device shown in Fig. 5.2(a), comprising ten quantum dots arranged in a 3-4-3 configuration and with four rf-charge sensors at the periphery. A similar device design fabricated onto a Si substrate has been recently exploited for studying hopping spin qubit gates in a sparse occupancy [68]. However, here we operate the array in the dense regime, with each quantum dot hosting either one, three, or five holes. The outermost charge sensors are 1.5 μm apart, a distance that is comparable to the length scale of strain and compositional fluctuations of the heterostructure [74]. This spacing is therefore suitable for investigating the uniformity of noise on a large scale.

We begin our investigation by performing CPT experiments on the four rf-charge sensors. Figure 5.2(b) shows an exemplary measurement performed on the south sensor SS (see Supplementary Fig. 5.10 for the other sensors), which allows us to probe charge fluctuations over a frequency range from 1 mHz to 100 mHz. The corresponding charge noise power spectral density in Fig. 5.2(c) is calculated from the Coulomb peak position fluctuations over time, in line with the transport measurements in Fig. 5.1(f) (Methods). By fitting the data with S_0/f^α, we determine the charge noise values $\sqrt{S_{f=10\,\mathrm{mHz}}}$ at a frequency of $f = 10$ mHz (see black arrows in Fig. 5.2(c)) and report them in Fig. 5.2(d) for the four sensors. The averaged noise across the sensors in this larger array is 6 $\mu\mathrm{eV}/\sqrt{\mathrm{Hz}}$, comparable to the value of 5.5(9) $\mu\mathrm{eV}/\sqrt{\mathrm{Hz}}$ measured in the smaller linear arrays (dash-dotted line in Fig. 5.2(d)) and an exponent $\alpha = 1.21(5)$. These findings suggest that the heterostructure maintains low noise levels both within the same device and across different devices. Moreover, a comparison with the best value ($\approx 20\,\mu\mathrm{eV}/\sqrt{\mathrm{Hz}}$) obtained with CPT measurements on quantum dots defined on a Ge/SiGe heterostructure grown on a silicon substrate [57] (dashed line in Fig. 5.2(d)) shows a reduction in the noise amplitude by a factor of $\gtrsim 3$.

We also take the step to directly characterise the noise of the inner quantum dots, previously unexplored. We focus on the stability of the outermost quantum dots Q4 and Q7, and probe the susceptibility of noise to local perturbations of the electrostatic environment induced by different charge occupancy and into possible screening effects [135].

As shown in Fig. 5.2(e) for quantum dot Q4, we repeatedly sweep the plunger gate, each time loading the first hole into the quantum dot. We keep track of the transition voltage as shown by the red line in Fig. 5.2(e) (see Supplementary Fig. 5.11 for further analysis). We quantify the voltage power spectral density S_V (Fig. 5.2(f)) and estimate the voltage noise at a frequency of $f = 10$ mHz by fitting to S_0/f^α. Because of the complexity in determining with accuracy the lever arm of the plunger gates to the quantum dots in this regime, we maintain the metric of the charge noise in voltage, rather than in energy. In Fig. 5.2(g) we plot the voltage noise as a function of charge filling up to the eighth hole for quantum dots Q4 (black dots) and Q7 (red dots). We do not observe a clear trend of the voltage noise as a function of hole filling, rather we note that the voltage noise fluctuates largely between hole fillings, with average values at $f = 10$ mHz of 60(50) $\mu\mathrm{V}/\sqrt{\mathrm{Hz}}$ and

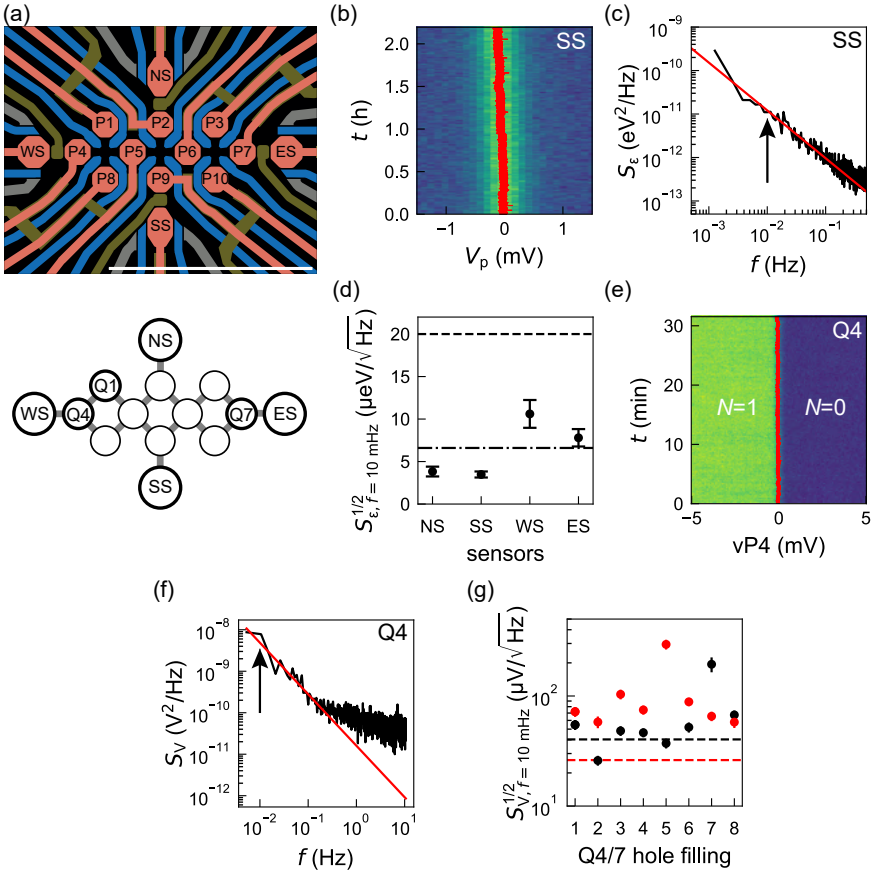

Figure 5.2: **Charge noise in a micron-scale 2D quantum dot array.** (a) Schematic of the gate layout of the quantum dot array, hosting 10 quantum dot qubits under plunger gates P1-P10 arranged in a 3-4-3 configuration. Quantum dots are read out by nearby charge sensors NS, ES, SS, WS. The scale bar is 1 µm. The inter-connectivity of the array is shown below. The quantum dots investigated are shown as circles with a thick black line. (b) Coulomb peak tracking for the south sensor of the device. (c) Charge noise power spectral density of the south sensor calculated from the Coulomb peak position fluctuations over time in (b) with S_0/f^α fit between 1 and 100 mHz (red line) and arrow indicating the charge noise at a frequency of 10 mHz. (d) Charge noise from the four sensors and benchmark to CPT experiment in Fig. 1(f) (dash-dotted line) and in Ref. [57] (dashed line) at the same frequency (10 mHz). Data are the fitted values to $S^{1/2}_{\epsilon, f=10\,\mathrm{mHz}}$, with error bars indicating the 1 s.d. of the fit. (e) Repeated loading of the first hole on Q4 by sweeping the virtualised plunger gate (vP4). The red line estimates the $N = 0$ to $N = 1$ charge state transition position. (f) Calculated voltage power spectral density from (e) with the extracted noise at 10 mHz (black arrow) from the linear S_0/f^α fit between 10 and 200 mHz (red line). Uncertainties are 1 s.d. from the fitting procedure. (g) Extracted voltage noise at 10 mHz for the first eight holes for Q4 (red) and Q7 (black). Data are represented as fitted values to $S^{1/2}_{\mathrm{V}, f=10\,\mathrm{mHz}}$, with error bars indicating 1 s.d. of the fit. The red (black) dashed line shows the voltage noise from sensor WS (ES), used to keep track of the charge state of quantum dot Q4 (Q7).

90(70) $\mu V/\sqrt{Hz}$ for quantum dots Q4 and Q7, respectively. On average, we obtain a value $\alpha = 1.0(3)$. As a comparison, we also measure the voltage noise of the corresponding charge sensors that were used to sense the charge transitions on the quantum dots (WS for Q4, and ES for Q7) using CPT. We find that the noise of the sensors (black and red dashed line for Q4 and Q7 respectively) is qualitatively comparable to the average noise of the quantum dots.

5.4. CHARGE AND HYPERFINE NOISE IN HOLE SPIN QUBITS

We then move from electrical measurements of quantum dot properties to coherent spin experiments to exploit the spin degree of freedom as a sensitive noise probe of the local host environment. We begin by demonstrating coherent operations of spin qubits in this Ge/SiGe heterostructure grown on a Ge wafer. We focus our attention on the spin qubit pair confined in the double quantum dot system Q1-Q4. Figure 5.3(a) illustrates the associated charge stability diagram, obtained by sweeping the two virtual plungers vP4 and vP1 [68]. The map reveals well-defined charge regions corresponding to different occupations centered around the $(n_{Q4}, n_{Q1}) = (1, 3)$ charge state (with n_{Qi} indicating the number of carriers confined in quantum dot i) regime in which this pair is operated. A magnetic field is applied to Zeeman split the spin states via a one-axis solenoid magnet that is nominally parallel to the sample plane.

We control the qubit pair by pulsing the voltages through the charge stability map. Starting at point I of Fig. 5.3(a), we prepare a two-hole S(0,4) singlet state, then ramp adiabatically to the center of the (1, 3) charge state (point M) preparing a $|\uparrow\downarrow\rangle$ state with an unpaired spin in each quantum dot. Here, we then perform qubit manipulation via electric dipole spin resonance (EDSR), after which we readout the qubit state in R using Pauli spin blockade (PSB). Parallel spin states ($|\downarrow\downarrow\rangle$ and $|\uparrow\uparrow\rangle$) are blocked and mapped into the (1, 3) charge state, while antiparallel spin states ($|\uparrow\downarrow\rangle$ and $|\downarrow\uparrow\rangle$) are transferred into the (0, 4) charge state, resulting in the so-called parity readout (Supplementary Fig. 5.12) [37, 136, 137].

We proceed by calibrating the single-qubit gate parameters of each qubit to then exploit Carr-Purcell-Meiboom-Gill (CPMG) sequences to probe the power spectral density of the noise affecting the qubits [48, 138–142]. Figure 5.3(b) illustrates EDSR resonant control of Q1 through a microwave burst applied to the plunger P1 at a magnetic field of of 117.5 mT for a varying driving frequency (top) and a varying driving time at the resonant condition (bottom). The Q1 and Q4 Larmor frequencies $f_{LQ1} = 826.4$ MHz and $f_{LQ4} = 954.5$ MHz map to effective g-factors of 0.503 and 0.577, respectively. By taking into account the pronounced anisotropy of the g-tensor of planar germanium quantum dots [143, 144], we estimate a misalignment angle between the magnetic field direction and the substrate plane of $\approx 3°$ (Methods). Although minimal, the deviation from a perfect in-plane configuration has implications on the sources of noise that affect the qubit.

Our hole spin qubits are, in fact, hosted in a Ge quantum well, which has a natural relative abundance of 7.7 atomic % of the ^{73}Ge isotope, which contains a non-zero nuclear spin. The resulting fluctuating Overhauser field couples to the hole spin states via a hyperfine interaction of the Ising type that is highly anisotropic with the magnetic field direction [145, 146]. Following the procedure described in Ref. [69], we quantify the contribution to the qubit decoherence arising from both charge and hyperfine noise by

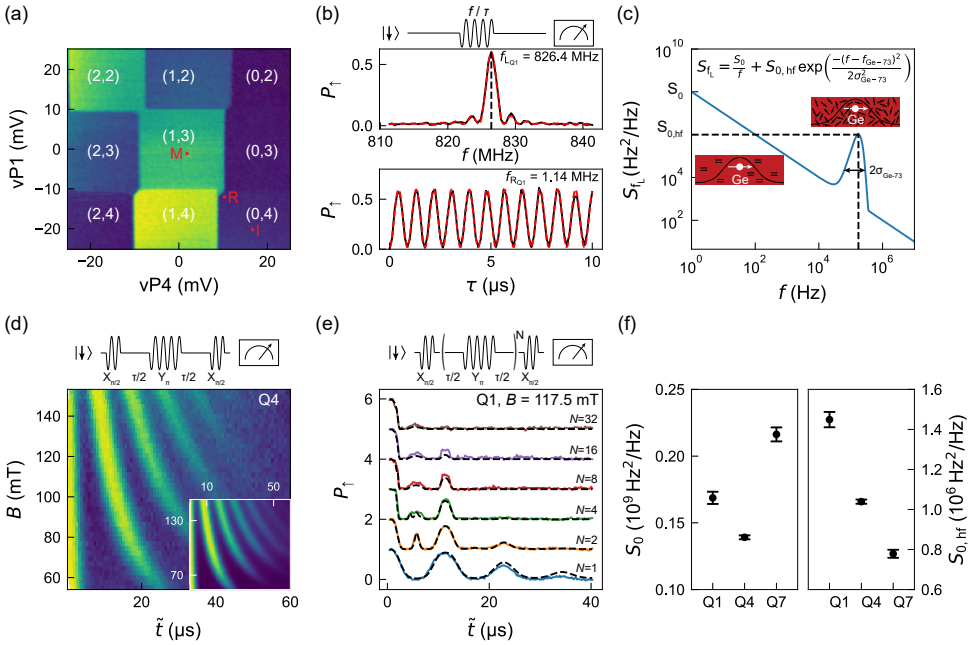

Figure 5.3: **Charge and hyperfine noise characterisation using spin echo measurement protocols.** (a) Charge stability diagram for qubit pair Q1-Q4 obtained by sweeping the two virtual plungers vP4 and vP1. Labels I, M, and R indicate approximate virtual plunger gate voltages associated with the initialisation, manipulation and read-out stages, respectively. (b) Exemplary Q1 EDSR spectroscopy (top panel) and Rabi oscillations (bottom panel) at $B = 117.5$ mT. Larmor ($f_{L_{Q1}}$) and Rabi frequencies ($f_{R_{Q1}}$) are extracted by fitting the data, as discussed in the Methods. Data (best fit) is shown as a black (red dashed) trace. (c) Model of the power spectral density affecting the hole spin qubits. The model consists of a $1/f$ contribution and a Gaussian peak arising from the hyperfine interaction with the ^{73}Ge non-zero nuclear spin. The insets show the coupling of the hole spin qubit to two-level fluctuators (on the left) and to a bath of spinful nuclei (on the right). (d) CPMG-1 experiment for a range of magnetic fields B measured on qubit Q4. Schematic of the pulse scheme on the top panel. The time axis is defined as $\tilde{t} = \tau + t_\pi$, where the finite time of the Y_π pulse ($t_\pi = 1/(2f_R)$) is taken into account. We normalise the measured signal between 0 and 1 to facilitate the fitting procedure of the model of (c). The inset shows the best-fit to the normalised data using the noise model following Ref. [69]. Data and fit show excellent agreement. (e) Normalised CPMG-N pulse sequences (schematic on top) for $N = 1, 2, 4, 8, 16$, and 32 Y_π pulses for qubit Q1 at $B = 117.5$ mT. The black dashed line is the best fit from the noise model in (c) to the data. Each trace is shifted vertically by one unity for clarity. (f) Extracted S_0 and $S_{0,hf}$ parameters for qubits Q1, Q4, and Q7 obtained from the data shown in (d), (e) and in Supp. Fig. 5.13. Data are represented as fitted values to S_0 and $S_{0,hf}$, with error bars 1 s.d. from the fit.

modeling the spectral noise affecting the Larmor frequency (S_{f_L}) with a S_0/f contribution and a Gaussian peak at the precession frequency of the ^{73}Ge nuclear spins ($f_{\mathrm{Ge-73}} = \gamma B$, with the expected gyromagnetic ratio $\gamma = 1.48\,\mathrm{MHz/T}$), as displayed in Fig. 5.3(c). We then perform a wide series of CMPG-N experiments, consider the filter function associated with each sequence, and estimate the noise spectral density by varying the number of refocusing Y_π pulses N, the time in between two pulses and the magnetic field amplitude.

We begin with a CPMG-1 experiment as a function of the magnetic field on qubit Q4. The resulting map in Fig. 5.3(d) manifests a clear collapse-and-revival pattern as a function of time, also known as hole-spin echo envelope modulations [147, 148], that is dependent on the magnetic field. This phenomenon arises from the sharp noise component at $f_{\mathrm{Ge-73}} \propto B$ that can be partially filtered only at times of $n/f_{\mathrm{Ge-73}}$ with n being an integer [69, 149]. Similar patterns have already been observed for GaAs qubits, and the detailed understanding of the qubit interactions with the ^{69}Ga, ^{71}Ga and ^{75}As nuclear spins has enabled protocols that allowed their coherence times to be improved by up to five orders of magnitude [150, 151].

The inset of Fig. 5.3(d) illustrates the fit to the data considering the noise model shown in Fig. 5.3(c), which allows us to estimate the noise component at 1 Hz (S_0), the amplitude of the hyperfine spectral peak ($S_{0,\mathrm{hf}}$), together with its frequency spread ($\sigma_{\mathrm{Ge-73}}$). Details of the analysis are discussed in the Methods, while extended measurements and fits as a function of the magnetic field for Q1 are detailed in Supplementary Fig. 5.13.

We extend the noise characterisation using CPMG-N pulse sequences for $N = 1$, 2, 4, 8, 16, and 32 Y_π pulses. The results accompanied by fits at a fixed magnetic field of $B = 117.5$ mT ($B = 138$ mT) are shown in Fig. 5.3(e) (Supplementary Fig. 5.13) for qubit Q1. Using the same approach, we also probe qubit Q7 (see Supplementary Fig. 5.13) that is located ≈ 850 nm from Q4.

Figure 5.3(f) displays the extracted values of S_0 and $S_{0,\mathrm{hf}}$ for the three qubits in a fixed magnetic field of $B = 117.5$ mT, resulting in an average value of S_0 equal to $0.17(3) \times 10^9$ $\mathrm{Hz^2/Hz}$. While nuclear spin effects could in principle also contribute to the low-frequency noise spectrum due to slow nuclear diffusion [152, 153], we find it more plausible to associate the low frequency component S_0/f to charge noise in the device. The extracted value of S_0, in fact, can be converted to a voltage noise level and compared with our findings on the electrical noise. We assume a spatially homogeneous distribution of uncorrelated fluctuators, and exploit knowledge of the g-factor susceptibility to voltage variations in all the surrounding gates [154]. Considering traps under the gates the most dominant, uncorrelated noise sources, we can estimate the resulting overall g-factor susceptibility of the hole spin qubits as $\frac{\Delta g}{\Delta V} = \sqrt{\sum_i (\frac{\delta g}{\delta V_i})^2} \approx 6.7 \cdot 10^{-4}\,\mathrm{mV^{-1}}$, with $\delta g/\delta V_i$ the susceptibility of the g-factor g to a voltage variation on each gate i of the twelve barrier and ten plunger gates controlling the array. The associated Larmor qubit fluctuations result then into $\frac{\Delta f_L}{\Delta V} = \frac{1}{h}\frac{\Delta g}{\Delta V}\mu_B B$, which for B = 117.5 mT, is $\approx 1.1\,\mathrm{MHz\,mV^{-1}}$. We can then derive an effective voltage power spectral density value at 1 Hz of

$$S_V = \frac{S_0}{(\frac{\Delta f_L}{\Delta V})^2} = 140(30)\,\mu\mathrm{V^2/Hz}, \tag{5.1}$$

that results in to an effective voltage noise of $\sqrt{S_V} = 12(1)\,\mu\mathrm{V}/\sqrt{\mathrm{Hz}}$. This represents a two-fold improvement with respect to what measured for a single qubit in Ref. [69] for a

germanium quantum well buried at the similar depth but grown on a silicon substrate. Moreover, assuming a $\propto 1/f$ framework, the value at 10 mHz (120(10) $\mu V/\sqrt{Hz}$) lies within the range of what detected from direct quantum dots measurements (80(60) $\mu V/\sqrt{Hz}$), supporting our hypothesis.

The hyperfine noise values extracted from the three different qubits are in the same order of magnitude as in Ref. [69] for qubits that are not operated on a hyperfine sweet spot (e.g. not in a configuration with the magnetic field pointing in the substrate plane), with qubit to qubit variations that are amplified by the large anisotropy in the sensitivity to hyperfine noise. Exploiting the extracted noise parameters, we estimate an integrated hyperfine noise amplitude of $\sigma_f = 180(8)$ kHz, which sets an approximate upper bound for the hyperfine-limited dephasing time of $T_2^* = 1.25(5)\,\mu s$, qualitatively similar to what measured experimentally in the range of $1-2\,\mu s$ [154] (Methods). Performing a similar analysis on the low-frequency component, we predict a charge noise-limited dephasing time of $T_2^* = 3.7(3)\,\mu s$ at 117.5 mT, and 44(4) μs at 10 mT (Methods).

As, in practice, both noise components act on the qubits at the same time, we further use the model to validate the observed dependence of T_2^H (envelope decay) with the magnetic field, which, in the investigated magnetic field range, manifests a monotonic increase (shown for Q1 and Q4 in Supplementary Fig. 5.14). Our analysis suggests that for a magnetic field below ≈ 150 mT the dominant noise source is the hyperfine interaction with the ^{73}Ge bath. Coupling of the qubit to charge noise through spin-orbit interaction sets the boundary for T_2^H at higher magnetic field, with a crossover point that exhibits an optimal T_2^H of ≈ 40 μs. The reduced charge-noise limited coherence times above the crossover is due to the proportionality of the qubit frequency fluctuations with the magnetic field through the g-factor ($\Delta f_L \propto B$) [68, 69, 149].

5.5. HYPERFINE INTERACTION WITH ^{29}SI NUCLEI

Because the hole's wavefunction is electrostatically confined near Ge/SiGe interface [45, 155], the interaction with the spinful ^{29}Si nuclei in the barrier may potentially introduce an additional noise source affecting coherence.

As the gyromagnetic ratio of the ^{29}Si nuclei (8.465 MHz/T) is much higher than that of the ^{73}Ge nuclei (1.48 MHz/T), the suppression and revival in the coherence may be visible at a much shorter time scale in a CPMG experiment. To isolate this possible decoherence mechanism, we perform a narrow-band noise measurement using a CPMG-64 sequence on qubit Q7 for three magnetic fields, as shown in Fig. 5.4(a). In addition to the collapse of the coherence at $\approx 2\,\mu s$ due to the hyperfine interaction with the ^{73}Ge isotopes, we also observe a less pronounced dip between 1 and 1.5 μs. We extract the time associated with this dip ($\tilde{t}_{dip}$) and convert it into a frequency $f_{dip} = (2n-1)/2\tilde{t}_{dip}$ (with n indicating the harmonic). We then calculate f_{dip} for $n = 2$ for the three magnetic fields and use a linear fit to find a gyromagnetic ratio of 8.6(9) MHz/T, which agrees with the expected 8.465 MHz/T for ^{29}Si (Fig. 5.4(b)). We also find qualitative agreement when we expand our noise model with an additional Gaussian peak associated with the ^{29}Si nuclear spins (Methods), confirming that the qubit coherence is also influenced by the interaction with the ^{29}Si nuclear spin bath. From the fit of the three traces, we obtain the average parameters of $S_{0,hf}^{Si-29} = 9(1)\cdot 10^3\,Hz^2/Hz$ and $\sigma_{Si-29} = 99(20)$ kHz, which results in an

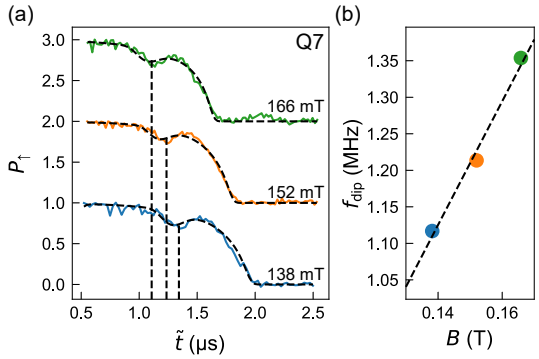

Figure 5.4: **Influence of ^{29}Si nuclear spin on qubit coherence.** (a) Collapse and revival of the qubit Q7 spin state during a CPMG-64 measurement protocol for a magnetic field of 138 (blue), 152 (orange), and 166 (green) mT. The dashed black line shows the best fit when taking into account a second gaussian peak in the noise model from the ^{29}Si non-zero nuclear isotopes. Each trace is shifted upwards by one unit for clarity. A dip in the coherence is observed between 1 μs and 1.5 μs and is attributed to the interaction with the ^{29}Si nuclear spins present in the SiGe barriers. (b) Frequency f_{dip} converted from the time of the dip in (a). From the linear fit we extract a gyromagnetic ratio of 8.6(9) MHz/T which agrees with the expected 8.465 MHz/T for ^{29}Si.

integrated hyperfine noise amplitude σ_f of 47(5) kHz and a ^{29}Si-limited dephasing time of $T_2^* = 4.8(7)$ μs (Methods).

Given the precision of the noise model to fit the data of Figs. 5.3(d),(e) and Fig. 5.4(a), we estimate an upper limit on the Hahn decay time T_2^{H} for the ideal case of perfect isotopic purification of both germanium and silicon. To do so, we set the Ge-73 hyperfine noise amplitude $S_{0,\text{hf}} = 0$ Hz^2/Hz and calculate the qubit coherence considering only the extracted average low-frequency contribution associated to charge noise, S_0 of 0.17(3) × 10^9 Hz^2/Hz. We obtain a T_2^{H} of around 0.4 ms at a small magnetic field of 10 mT, and of 36 μs for 117.5 mT, vs. the experimentally detected measurements of 25 μs and 36 μs for Q1 and Q4 respectively (see Supplementary Fig. 5.14). This shows the potential high gain in coherence when isotopically purifying the Ge quantum well as well as the surrounding SiGe barrier layers, and operating the qubits at smaller magnetic fields.

5.6. CONCLUSIONS

We build a comprehensive understanding of noise in low-disorder Ge/SiGe heterostructures grown on Ge wafers by using a variety of tools applied to increasingly complex devices. Canonical characterisation using the flank method in the multi-hole regime shows a low charge noise of 0.3(1) μeV/$\sqrt{\text{Hz}}$ at 1 Hz, consistently across six quantum dots from two different devices. This value is a significant improvement over previous generations of Ge/SiGe heterostructure and sets a benchmark for quantum confined holes in semiconductors [57, 60, 133]. Previous studies of strained Ge/SiGe transistors on Si wafers [156, 157], as well as Si/SiGe transistors [158] and quantum dots [56], have linked charge noise to electrically active dislocations originating below the quantum well. Based on these findings, we speculate that charge noise in Ge/SiGe heterostructures grown on Ge wafers may be lower and more uniform than in those grown on Si wafers, due to the sig-

nificantly reduced density of threading dislocations. Additionally, the reduced topography of the cross-hatch pattern [74, 100] may lead to a more uniform semiconductor-dielectric interface, further improving charge noise uniformity. Furthermore, as we scale the device in size and complexity, CPT measurements in the multi-hole regime show charge noise that is, on average, uniform across a length scale of 1.5 µm within the same device and comparable to the smaller devices. However, when the voltage noise is probed as function of hole occupancy, we observe large fluctuations associated with the specific hole filling. This observation hints to a complex behaviour, where each charge configuration, corresponding to different applied voltages, possibly induces a different coupling to the noise environment surrounding the quantum dot.

We then demonstrate that quantum dots in Ge/SiGe heterostructures on Ge wafers can effectively support qubits. We perform CPMG pulse sequences on three separate qubits and decouple the electrical noise from the magnetic noise by exploiting a theoretical model. We use the extracted parameters to quantify their contribution to decoherence in a range of magnetic fields and to make a prediction of the coherence time expected for a nuclear spin-free heterostructure. Lastly, we use a CPMG-64 protocol to measure the modulation of coherence due to the non-zero nuclear spin from the ^{29}Si isotope present in the SiGe barriers surrounding the Ge quantum well. This finding points towards a non-negligible overlap of the hole wave function with ^{29}Si, possibly related Si-Ge mixing at the quantum well top Ge→Si-Ge heterointerface, as observed by transmission electron microscopy in similar quantum wells [159].

Our study presents a framework for systematic charge and magnetic noise characterization in spin qubit devices and offers a starting point for future investigations of noise correlation to understand the challenges of error correction schemes in noisy intermediate scale spin qubit devices. Furthermore, our findings motivate the optimization of the Ge/SiGe interface and the complete isotopic purification of the SiGe barrier layers surrounding the Ge quantum well. Achieving nuclear spin-depleted, isotopically enriched ^{70}Ge/^{28}Si^{70}Ge quantum wells with residual ^{73}Ge and ^{29}Si below 0.01% is possible using centrifuge-separated $^{70}GeH_4$ and $^{28}SiH_4$ gas precursors [160]. Maintaining the chemical purity of these gas precursors throughout the supply chain [64] will be crucial to preserving low disorder and minimizing charge noise in future isotopically-enriched Ge spin qubit devices.

5.7. METHODS

5.7.1. HETEROSTRUCTURE GROWTH

The Ge/SiGe heterostructure material is grown using reduced-pressure chemical vapour deposition in an ASMI Epsilon 2000 reactor. Starting from a Ge wafer a 2.5 µm strain relaxed $Si_{(1-x)}Ge_x$ buffer is grown at a temperature of 800 °C with a final Ge concentration of 83% using three grading steps ($1-x = 0.07, 0.13, 0.17$). We lower the growth temperature to 500 °C for the growth of the final 200 nm of the SiGe buffer layer, the 16 nm Ge QW, the 55 nm SiGe barrier layer, and the sacrificial passivated Si cap layer.

5.7.2. DEVICE FABRICATION

The four quantum dot devices are fabricated with multiple layers of Ti/Pd and platinumgermanosilicide ohmic contacts. These are defined by electron beam lithography and created by thermally diffusing Pt at a temperature of 400 °C. A first layer of Ti/Pd (3/17 nm) barrier gates are separated from the heterostructure by a 7 nm Al_2O_3 insulating oxide grown using atomic layer deposition. A second layer of Ti/Pd (3/37 nm) plunger gates are created and separated by 5 nm of Al_2O_3 from the first layer of barrier gates. Details for the fabrication of the '3-4-3' device can be found in Ref. [68].

5.7.3. FLANK METHOD ELECTRICAL CHARACTERIZATION OF QUANTUM DOTS

We cool down multi-hole quantum dots defined underneath the charge sensor or plunger gates of a device in a Leiden cryogenic dilution refrigerator operating at a mixing chamber base temperature of 70 mK. To measure the charge noise using the flank method, we first set a source-drain bias of 0.1 mV across the device and subsequently tune the surrounding gates until we measure a current of 1 nA through the device. We define a multi-hole quantum dot underneath a sensor or plunger gate by fine tuning the barrier gates surrounding the gate of interest until we observe a spectrum of Coulomb peaks. We then measure the current I_{sd} on the left flank of the Coulomb peak where the slope $|dI_{sd}/dV_{sd}|$ of the Coulomb peak is the largest at a rate of 2 kHz for a duration of 100 s using a Keithley DMM6500 multimeter. To calculate the current power spectral density S_I, we first split each 100 second current trace into 10 segments of 10 seconds each, and subsequently average over the current power spectral densities ($S_I = 1/N \sum_{i=1}^{N} S_I^i$) that we evaluate from each segment. For each Coulomb peak that we analyse, we convert the current power spectral density S_I into charge noise power spectral density S_ϵ using [56]

$$S_\epsilon = \frac{a^2 S_I}{|dI_{sd}/dV_S|^2}, \tag{5.2}$$

where a is the lever arm extracted from the analysis of the corresponding Coulomb diamond.

5.7.4. COULOMB PEAK TRACKING

On sensor 1 of device 2, we perform an 18 hour CPT experiment tracking the current I_{sd} through a quantum dot while continuously sweeping across the quantum dot using its plunger gate. For the four charge sensors of the '3-4-3' device we track the reflected signal of each charge sensor for 2 hours when sweeping the sensor plunger gate voltage. We extract the position of the Coulomb peak by fitting each Coulomb peak to a hyperbolic secant function

$$y = \frac{a}{\cosh^2(b(x - x_0))} + c, \tag{5.3}$$

where y reflects the measured signal, x the sensor's plunger gate voltage, x_0 the position for which the Coulomb peak is maximum, and a, b, and c are free fitting parameters. To calculate the voltage power spectral density S_V from the Coulomb peak fluctuations, we split them into 10 equal segments and for each segment we calculate the voltage power spectral density from a Fourier transformation. We find the charge noise power spectral

density S_ϵ (see Fig. 5.3(c)) using the evaluated lever-arm of each sensor and using

$$S_\epsilon = a^2 S_V. \tag{5.4}$$

5.7.5. VOLTAGE NOISE ESTIMATION ON SINGLE HOLE QUANTUM DOTS

To estimate the voltage noise of the quantum dots where we know the exact hole occupancy we repeatedly load a hole into a dot by continuously sweeping the plunger gate voltage under which the quantum dot is defined. We keep track of the voltage for which a hole loads into a dot by fitting each voltage sweep to a sigmoid function given by

$$y = \frac{a}{1+\exp\left(\frac{x-x_0}{\tau}\right)} + b, \tag{5.5}$$

where y reflects the measured signal, x_0 the voltage for which a hole loads into a dot, and a, b, and τ are free fitting parameters. We split the voltage fluctuations into 10 equal segments and calculate the voltage power spectral density S_V from a Fourier transform. The final voltage power spectral density is calculated from the average of the 10 segments.

5.7.6. ESTIMATION OF THE RELATIVE OUT-OF-PLANE ANGLE BETWEEN MAGNETIC FIELD AND SUBSTRATE

We consider the average effective g-factor $g_{\text{eff}} = 0.58$ of the 10 qubits [154] and assume in-plane principal g-tensor components of $g_x = -g_y = 0.04$ [68] and an out-of-plane component of $g_z = 11$ [69]. The effective g-factor can be written in term of the out of plane angle θ and the principal components

$$g_{\text{eff}} = \sqrt{g_x^2 \cos\theta^2 + g_z^2 \sin\theta^2}. \tag{5.6}$$

By inverting the equation, we estimate the most plausible misalignment angle of $\theta = 3°$.

5.7.7. EXTRACTION OF RABI AND LARMOR FREQUENCY

We extract the Larmor frequency f_L and Rabi frequency f_R by fitting the data with the following functions. For the Rabi frequency we use

$$P = A\sin\left(2\pi f_R t + \phi\right)\exp\left(-t^2/\tau^2\right) + C\,, \tag{5.7}$$

where P represents the measured up probability and t the duration of the microwave burst. The Rabi frequency f_R, decay time τ, phase ϕ, amplitude A, and offset C are free fitting parameters. The extraction of the Larmor frequency is done using

$$P = A\frac{f_R^2}{f_R^2+\Delta^2}\sin^2\left(0.5t\sqrt{f_R^2+\Delta^2}\right) + C\,. \tag{5.8}$$

Here $\Delta = f - f_L$ with f the probed frequency range during measurement. t, A, f_R, C, and f_L are free fitting parameters.

5.7.8. QUBIT NOISE MODEL

Low-frequency and hyperfine noise affecting the qubits hosted in the natural Ge/SiGe heterostructure is modeled by [69]

$$S_{f_L} = \frac{S_0}{f} + S_{0,\mathrm{hf}} \exp\left(\frac{-(f - f_{\mathrm{Ge-73}})^2}{2\sigma^2_{\mathrm{Ge-73}}}\right). \tag{5.9}$$

Here, S_0 represents the low-frequency noise component at 1 Hz and $S_{0,\mathrm{hf}}$ represents the effective strength of the hyperfine noise acting on the qubit. $f_{\mathrm{Ge-73}} = \gamma_{\mathrm{Ge-73}} B$ is the precession frequency of ^{73}Ge determined by its gyromagnetic ratio $\gamma_{\mathrm{Ge-73}} = 1.48$ MHz/T and the magnetic field B. $\sigma_{\mathrm{Ge-73}}$ represents the spread of the ^{73}Ge precession frequencies. We follow the same fitting procedure as outlined in the methods of Ref. [69] to extract S_0, $S_{0,\mathrm{hf}}$, and $\sigma_{\mathrm{Ge-73}}$.

For the fitting of the data containing influence of the ^{29}Si nuclear spin, we expand Eq. 5.9 with a second gaussian peak

$$\begin{aligned} S_{f_L} = \frac{S_0}{f} &+ S^{\mathrm{Ge-73}}_{0,\mathrm{hf}} \exp\left(\frac{-(f - f_{\mathrm{Ge-73}})^2}{2\sigma^2_{\mathrm{Ge-73}}}\right) \\ &+ S^{\mathrm{Si-29}}_{0,\mathrm{hf}} \exp\left(\frac{-(f - f_{\mathrm{Si-29}})^2}{2\sigma^2_{\mathrm{Si-29}}}\right). \end{aligned} \tag{5.10}$$

The fitting procedure is split up into a two stage process, where we first use Eq. 5.9 to find $S^{\mathrm{Ge-73}}_{0,\mathrm{hf}}$ and $\sigma_{\mathrm{Ge-73}}$. We fix these parameters and then use Eq. 5.10 to find S_0, $S^{\mathrm{Si-29}}_{0,\mathrm{hf}}$ and $\sigma_{\mathrm{Si-29}}$. The precession frequencies of $f_{\mathrm{Ge-73}}$ and $f_{\mathrm{Si-29}}$ are also fixed.

5.7.9. ESTIMATION OF THE HYPERFINE COUPLING CONSTANTS

Using the average extracted parameters of $S^{\mathrm{Ge-73}}_{0,\mathrm{hf}} = 1.1(3) \cdot 10^6\,\mathrm{Hz}^2/\mathrm{Hz}$ and $\sigma_{\mathrm{Ge-73}} = 12(1)$ kHz that describe the modeled Gaussian peak in the power spectral density at the frequency $f_{\mathrm{Ge-73}}$, we estimate an integrated noise of the Larmor frequency fluctuations of

$$\sigma_f = \sqrt{\sqrt{2\pi} \cdot S^{\mathrm{Ge-73}}_{0,\mathrm{hf}} \sigma_{\mathrm{Ge-73}}} = 180(8)\,\mathrm{kHz}. \tag{5.11}$$

This sets an approximate boundary for the hyperfine-limited dephasing time of $T_2^* = (\pi\sqrt{2}\sigma_f)^{-1} = 1.25(5)\,\mu\mathrm{s}$, qualitatively similar to what measured experimentally in the order of $1-2\,\mu\mathrm{s}$ [154].

We use the same procedure to assess the influence of the interaction with the Si-29 nuclei in the barrier to the Ge hole spin qubits. We consider the average parameters extracted from the fits in Fig. 5.4, $S^{\mathrm{Si-29}}_{0,\mathrm{hf}} = 9.0(8) \cdot 10^3\,\mathrm{Hz}^2/\mathrm{Hz}$ and $\sigma_{\mathrm{Si-29}} = 99(20)$ kHz, that leads to an integrated noise of $\sigma_f = 47(5)$ kHz and a Si-29-limited $T_2^* = 4.8(4)\,\mu\mathrm{s}$.

5.7.10. CHARGE NOISE-LIMITED T_2^*

We evaluate the charge noise-limited T_2^* using the extracted voltage noise amplitude of $\sqrt{S_V} = 12(1)\,\mu\mathrm{V}/\sqrt{\mathrm{Hz}}$ at 1 Hz and the effective g-factor susceptibility of $\frac{\Delta g}{\Delta V} = 6.7 \cdot$

$10^{-4}\,\mathrm{mV}^{-1}$. The dephasing time T_2^* can be approximated in a quasi-static configuration by [56, 65, 68]

$$T_2^* = \frac{1}{\sqrt{2}\pi\Delta f}, \tag{5.12}$$

with Δf the amplitude of the qubit frequency fluctuations due to a voltage noise with root main square amplitude of ΔV_{RMS}

$$\Delta f = \frac{\Delta g}{\Delta V}\Delta V_{\mathrm{RMS}}. \tag{5.13}$$

We compute ΔV_{RMS} over a period of time T assuming a power spectral density of S_{V}/f, and integrating the noise from a low- and high-frequency cutoff values, $f_L = T^{-1}$ and f_H, respectively

$$\Delta V_{\mathrm{RMS}} = \sqrt{\int_{f_L}^{f_H} \frac{S_{\mathrm{V}}}{f}\,df} = \sqrt{S_{\mathrm{V}} \ln \frac{f_H}{f_L}}. \tag{5.14}$$

By considering realistic values of $f_L = 1$ mHz and $f_H = 1$ MHz, we determine $\Delta V_{RMS} = 54(5)\,\mu\mathrm{V}$. We then distinguish two cases. For B = 117 mT, the resulting fluctuations leads to $\Delta f = 60(5)$ kHz and a charge-noise limited dephasing time of $T_2^* = 3.7(3)\,\mu\mathrm{s}$. For a low magnetic field of 10 mT, we obtain an increased value of $T_2^* = 44(4)\,\mu\mathrm{s}$ due to the more than tenfold reduction in Δf.

5.8. SUPPLEMENTARY

5.8.1. ELECTRON TEMPERATURE AND LEVER ARM EXTRACTION

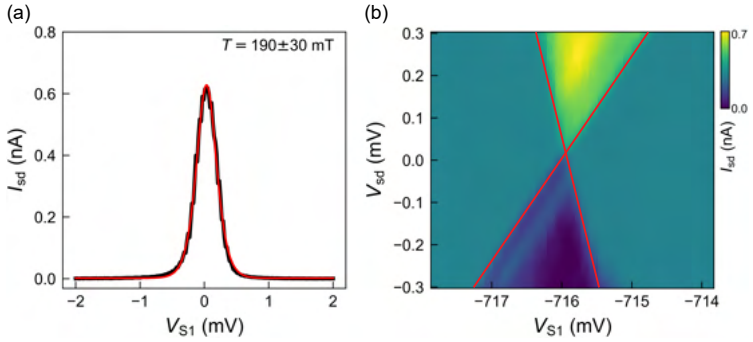

Figure 5.5: (a) Current I_{sd} as a function of sensor gate voltage V_{S1}. We make an estimation of the electron temperature by fitting (red line) using the formula $I_{sd} = a + b\cosh^{-2}\left(\frac{\alpha(V_0-V)}{2k_BT}\right)$ of the electron temperature. Here, a, b, V_0, and T are free fitting parameters, with T the estimated electron temperature. α is the lever arm corresponding to the analysed Coulomb peak. (b) I_{sd} measured as a function of quantum dot voltage V_{S1} and source drain voltage V_{sd}. We extract the lever arm from the slopes of the red lines using $\alpha = |\frac{m_s m_d}{m_s - m_d}| = 0.18$ eV/V, where m_s and m_d are the slopes of the Coulomb diamond from source and drain respectively.

5.8.2. NOISE SPECTRA FROM LINEAR ARRAYS OF SINGLE HOLE TRANSISTORS

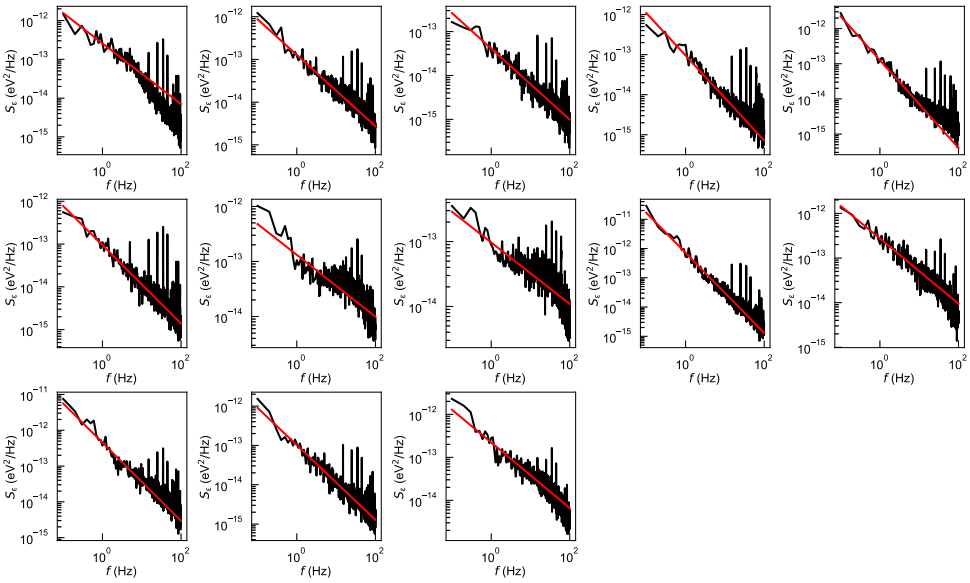

Figure 5.6: Ensemble of charge noise spectra S_ϵ taken at different Coulomb peak flanks but unknown charge occupancy to sample the distribution of charge noise levels of quantum dot sensor 1 of device 1. Each noise spectrum is fitted to S_0/f^α (red line) using a fit range between 0.1 and 10 Hz. We extract the charge noise $\sqrt{S_0}$ at 1 Hz, which is presented in Fig. 5.1(e) (device 1, S1) of the main text. Across the acquired noise spectra, we find an average charge noise of $S_0 = 0.4(1)\,\mathrm{Hz}^2/\mathrm{Hz}$ and $\alpha = 0.9(2)$. Measurement details can be found in the data repository (doi in main text).

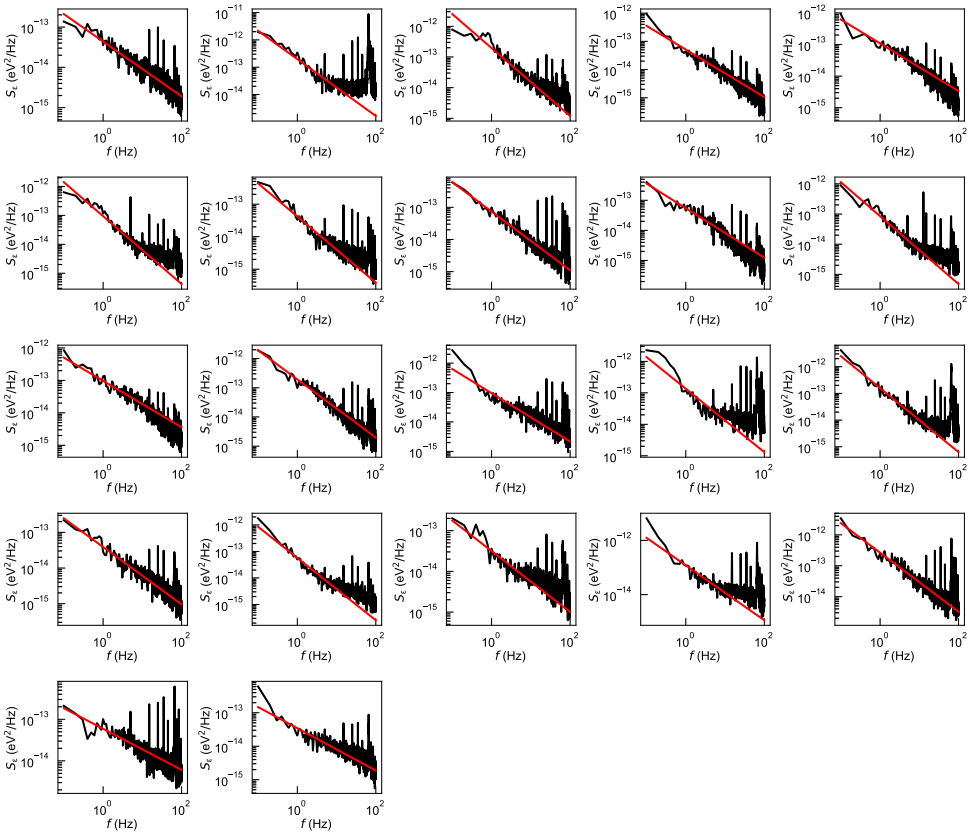

Figure 5.7: Ensemble of charge noise spectra S_ϵ taken at different Coulomb peak flanks but unknown charge occupancy to sample the distribution of charge noise levels of quantum dot sensor 2 of device 1. Each noise spectrum is fitted to S_0/f^α (red line) using a fit range between 0.1 and 10 Hz. We extract the charge noise $\sqrt{S_0}$ at 1 Hz, which is presented in Fig. 5.1(e) (device 1, S2) of the main text. Across the acquired noise spectra, we find an average charge noise of $S_0 = 0.3(1)\,\mathrm{Hz}^2/\mathrm{Hz}$ and $\alpha = 0.9(2)$. Measurement details can be found in the data repository (doi in main text).

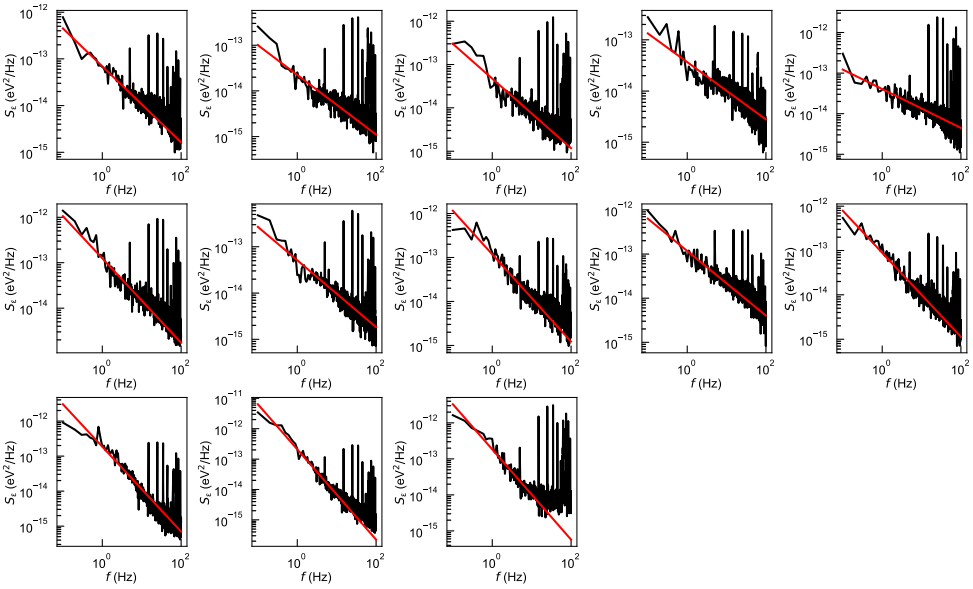

Figure 5.8: Ensemble of charge noise spectra S_ϵ taken at different Coulomb peak flanks but unknown charge occupancy to sample the distribution of charge noise levels of quantum dot sensor 1 of device 2. Each noise spectrum is fitted to S_0/f^α (red line) using a fit range between 0.1 and 10 Hz. We extract the charge noise $\sqrt{S_0}$ at 1 Hz, which is presented in Fig. 5.1(e) (device 2, S1) of the main text. Across the acquired noise spectra, we find an average charge noise of $S_0 = 0.3(1)\,\mathrm{Hz}^2/\mathrm{Hz}$ and $\alpha = 0.9(3)$. Measurement details can be found in the data repository (doi in main text).

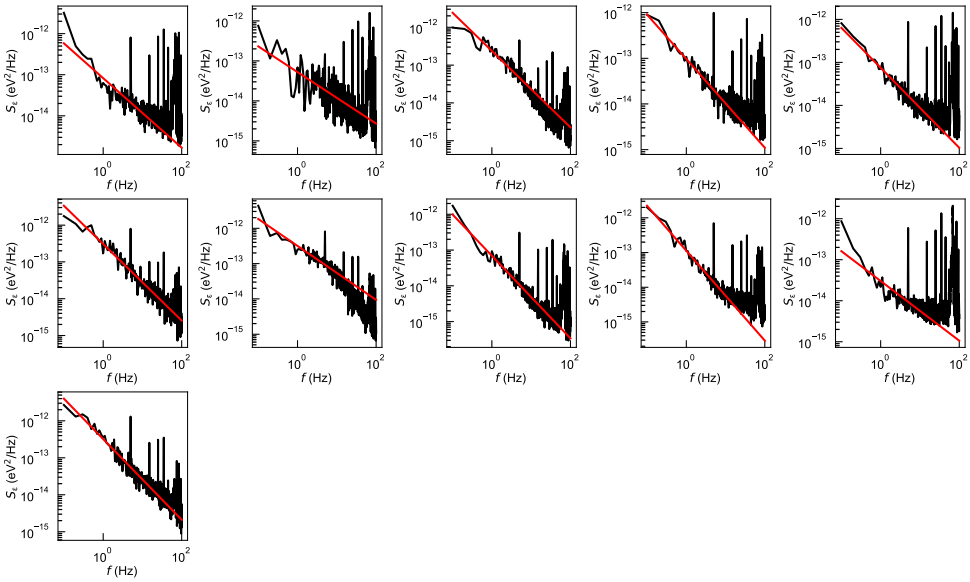

Figure 5.9: Ensemble of charge noise spectra S_ϵ taken at different Coulomb peak flanks but unknown charge occupancy to sample the distribution of charge noise levels of quantum dot sensor 2 of device 2. Each noise spectrum is fitted to S_0/f^α (red line) using a fit range between 0.1 and 10 Hz. We extract the charge noise $\sqrt{S_0}$ at 1 Hz, which is presented in Fig. 5.1(e) (device 2, S2) of the main text. Across the acquired noise spectra, we find an average charge noise of $S_0 = 0.4(1)\,\mathrm{Hz}^2/\mathrm{Hz}$ and $\alpha = 1.0(2)$. Measurement details can be found in the data repository (doi in main text).

5.8.3. CHARGE NOISE FROM SENSING DOT COULOMB PEAK TRACKING

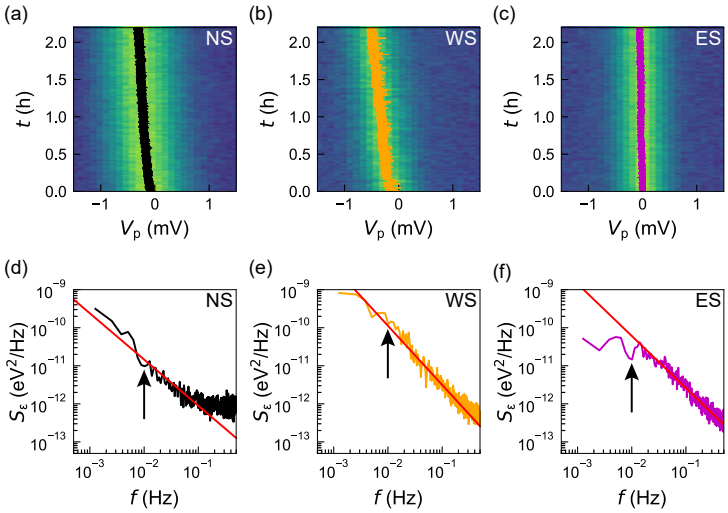

Figure 5.10: (a)-(c) two hour Coulomb peak tracking experiment of the north sensor (NS), west sensor (WS), and east sensor (ES) of the 3-4-3 device shown in Fig. 5.2(a) of the main text. The black, orange, and purple lines are the estimated Coulomb peak positions. (d)-(f) calculated charge noise power spectral densities of each sensor. We extract the charge noise at a frequency of 10 mHz (black arrow) using a linear fitting procedure (red line). For panels (d) and (e) we use a fitting range between 1 and 100 mHz, while for panel (f) we use a fitting range between 10 and 150 mHz.

5.8.4. CHARGE NOISE FROM HOLE FILLING EXPERIMENT

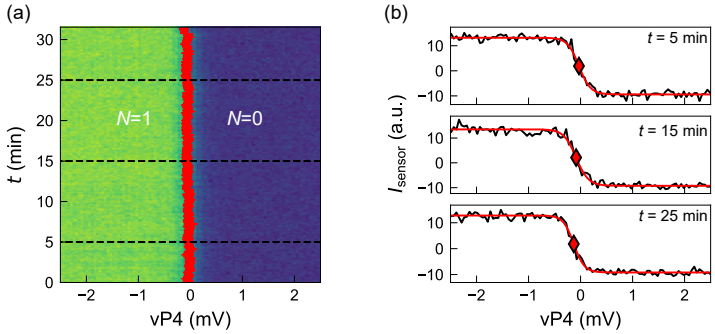

Figure 5.11: (a) Exemplary hole filling experiment on quantum dot Q4 where we repeatedly sweep over the interdot transition filling the quantum dot with a single hole. The red line shows the estimated interdot transition. (b) Line cuts of the sweep across the transition line from (a) for $t = 5$, $t = 15$, and $t = 25$ minutes. We estimate the position of the transition line by fitting each line cut to a sigmoid function (red) and finding the inflection point (red diamond).

5.8.5. SPIN STATES IN A DOUBLE QUANTUM DOT AND PARITY READOUT

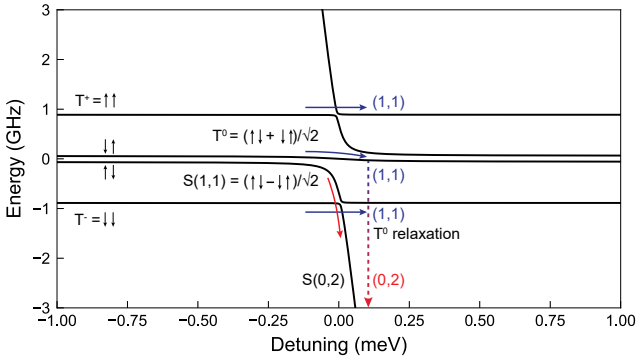

Figure 5.12: Energy levels of the spin states in a double quantum dot simulated assuming realistic experimental parameters: g-factors of 0.503 and 0.577, magnetic field of 117.5 mT, tunnel coupling t_c = 0.5 GHz, and a small relative quantization axis difference of 9°. The detuning energy axis is obtained by converting a typical detuning voltage window of 20 mV in electronvolt through a lever arm of 0.1 eV/V. The plot displays the readout mechanism of the four spin states. The two triplet parallel states are blocked when pulsing through the charge anticrossing (at zero detuning) and map to the (1,1) charge state. The antiparallel state $|\uparrow\downarrow\rangle$ is converted to the S(0,2) ground state. Finally, the $|\downarrow\uparrow\rangle$ spin state maps first to the T^0 state which relaxes to the singlet ground state S(2,0) much quicker than the typical readout time of 3 – 10 µs. The basic principles of the energy anticrossings and readout mechanism in the (1,1) to (0,2) transition also apply to the (3,1) to (0,4) transition studied in the main text.

5.8.6. CHARGE NOISE FROM SPIN-ECHO PROTOCOLS

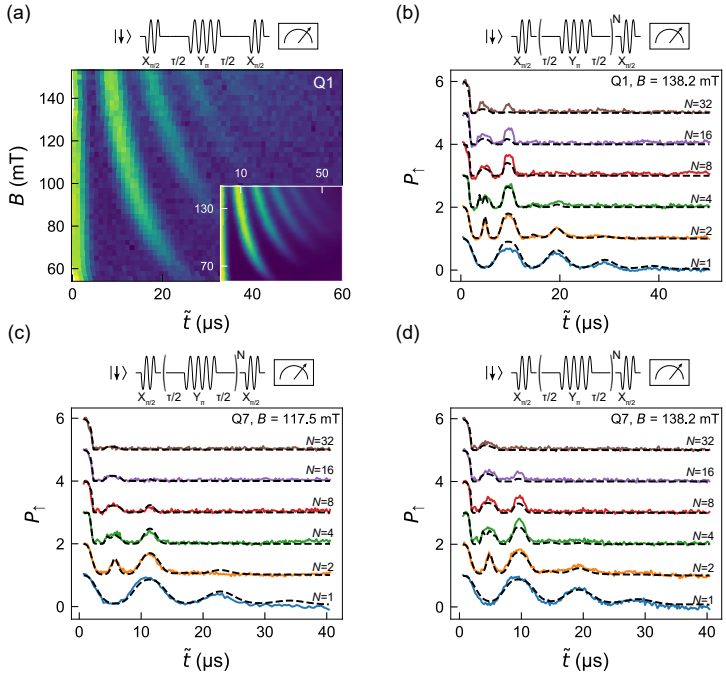

Figure 5.13: (a) CPMG-1 experiment performed on qubit Q1 for a range of magnetic fields B. The bottom right inset shows the model as presented in the Methods of the main text. (b) additional CPMG-N data taken on qubit Q1 at a magnetic field of $B = 138.2$ mT. This data, together with the data taken at $B = 117.5$ mT and presented in Fig. 5.3(e), is used to fit to the noise model of Fig. 5.3(c) to obtain an accurate estimation of the charge noise and hyperfine noise. (c)-(d) CPMG-N data taken on qubit Q7 at magnetic fields of 117.5 and 138.2 mT to estimate the charge and hyperfine noise from the fitting procedure of the noise model of Fig. 5.3(c) as presented in the main text. In panels (b)-(d) each coherence trace is offset by unity for clarity. Dotted black lines represent the estimated coherence from the noise model.

5.8.7. EXTRAPOLATION OF HAHN DEPHASING TIME IN ABSENCE OF HYPERFINE NOISE

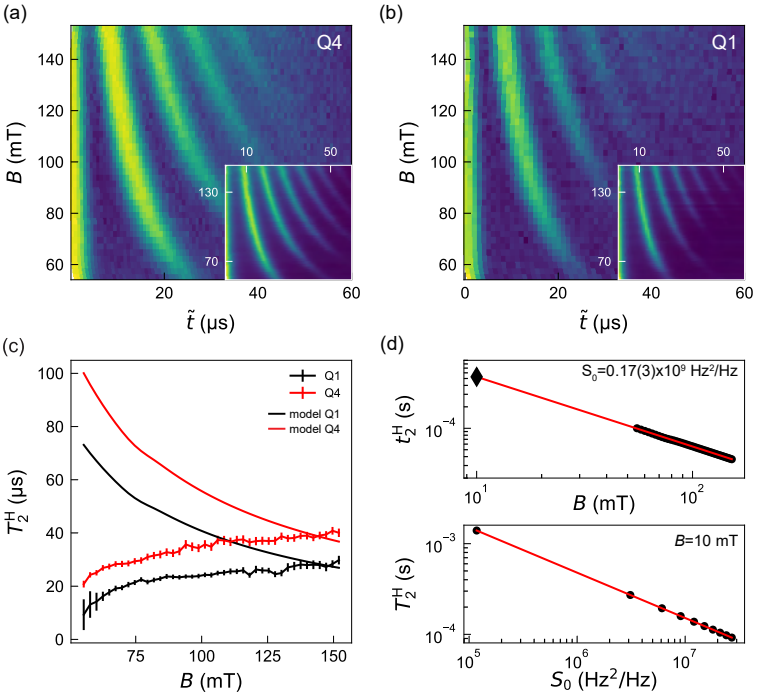

Figure 5.14: (a)-(b) Hahn echo coherence versus magnetic field and total wait time $\tilde{t}$ for qubit Q4 (panel a) and qubit Q1 (panel b). For each magnetic field B we extract the Hahn echo coherence time T_2^{H} using the fitting formula $A\exp\left(-(\tau/t_2^{\mathrm{H}})^{\alpha}\right)/(1-a_0\cos(\pi\gamma_{Ge-73}B\tau))^2+B$, where A, B, α, t_2^{H}, and a_0 are used as free fitting parameters. (c) We plot the extracted t_2^{H} as a function of magnetic field B for qubit Q1 and qubit Q4. Additionally, using the noise model from Fig. 5.3(c) of the main text, we model the coherence for qubits Q1 and Q4 when setting $S_{0,\mathrm{hf}} = 0\ \mathrm{Hz}^2/\mathrm{Hz}$ and extract the Hahn echo coherence time t_2^{H} for this idealised case. The solid lines show the extracted coherence times for qubit Q1 (black) and qubit Q4 (red). For both qubits we see a cross over point around 150 mT below which the hyperfine noise starts to dominate over the charge noise. It exemplifies the possible increase in coherence time when isotopically purifying the material stack. (d) We take the average charge noise of $S_0 = 0.17(3)\ \mathrm{Hz}^2/\mathrm{Hz}$ from the analysed qubits Q1, Q4, and Q7. Similar to (c), we set the hyperfine noise level to 0 and extract Hahn echo coherence time t_2^{H}. We extrapolate t_2^{H} to a low magnetic field of 10 mT and find a Hahn echo coherence time of around 0.4 ms. In the bottom panel we fix the magnetic field to 10 mT and investigate the behaviour of t_2^{H} as a function of charge noise S_0. The panels show how t_2^{H} could be improved towards 1 ms when addressing the two main noise sources present in the material stack being hyperfine noise and charge noise.

6

ATOMIC FLUCTUATIONS LIFTING THE ENERGY DEGENERACY IN SI/SIGE QUANTUM DOTS

Electron spins in Si/SiGe quantum wells suffer from nearly degenerate conduction band valleys, which compete with the spin degree of freedom in the formation of qubits. Despite attempts to enhance the valley energy splitting deterministically, by engineering a sharp interface, valley splitting fluctuations remain a serious problem for qubit uniformity, needed to scale up to large quantum processors. Here, we elucidate and statistically predict the valley splitting by the holistic integration of 3D atomic-level properties, theory and transport. We find that the concentration fluctuations of Si and Ge atoms within the 3D landscape of Si/SiGe interfaces can explain the observed large spread of valley splitting from measurements on many quantum dot devices. Against the prevailing belief, we propose to boost these random alloy composition fluctuations by incorporating Ge atoms in the Si quantum well to statistically enhance valley splitting.

This chapter has been published as: B. Paquelet Wuetz*, M.P. Losert*, S. Koelling*, **L.E.A. Stehouwer**, A.M.J. Zwerver, S.G.J. Philips, M.T. Mądzik, X. Xue, G. Zheng, M. Lodari, S.V. Amitonov, N. Samkharadze, A. Sammak, L.M.K. Vandersypen, R. Rahman, S.N. Coppersmith, O. Moutanabbir, M. Friesen, G. Scappucci, "Atomic fluctuations lifting the energy degeneracy in Si/SiGe quantum dots", Nature Communications, **13**, 7730 (2022).
*These authors have contributed equally

6.1. INTRODUCTION

Advanced semiconductor manufacturing is capable of integrating billions of transistors onto a single silicon chip. The promise of leveraging the same technology for large-scale integration of qubits into a fault-tolerant quantum processing unit is a key driver for developing electron spin qubits in silicon quantum dots [161]. Although these devices bear many similarities to transistors [130], qubits operate in the single electron regime [31], making them more sensitive to electrostatic disorder and noise arising from the surrounding environment. In strained silicon quantum wells, the electronically active part of the device is separated by an epitaxial SiGe barrier from the electronically noisy interface at the gate-stack, offering a quiet system with high mobility and low leakage between the gate and the quantum dots [162]. These properties make strained Si/SiGe heterostructures promising for scalable qubit tiles [163, 164] and have made it possible to define nine quantum dot arrays [165], run quantum algorithms [166] and entangle three-spin states [167] in natural silicon structures, and achieve two-qubit gate fidelity above 99% [121, 123] in isotopically purified silicon structures.

However, spin-qubits in silicon suffer from a two-fold degeneracy of the conduction band minima (valleys) that creates several non-computational states that act as leakage channels for quantum information [33]. These leakage channels increase exponentially with the qubit count [168], complicating qubit operation and inducing errors during spin transfers. Despite attempts to enhance the valley energy splitting, the resulting valley splittings are modest in Si/SiGe heterostructures, with typical values in the range of 20 to 100 μeV [166, 169–175] and only in a few instances in the range of 100 to 300 μeV [176–178]. Such variability in realistic silicon quantum dots remains an open challenge for scaling to large qubit systems. In particular, the probability of thermally occupying the excited valley state presents a challenge for spin initialization, and, in some cases, intervalley scattering may limit the spin coherence [179]. Furthermore, small valley splitting may affect Pauli spin blockade readout [163, 164]. Therefore, scaling up to larger systems of single-electron spin qubits requires that the valley splitting of all qubits in the system should be much larger than the typical operation temperatures (20 – 100 mK).

It has been known for some time that valley splitting depends sensitively on the interface between the quantum well and the SiGe barrier [180]. Past theoretical studies have considered disorder arising from the quantum well miscut angle [181] and steps in the interface [182–186] demonstrating that disorder of this kind can greatly decrease valley splitting in quantum dots. However, a definitive connection to experiments has proven challenging for a number of reasons. At the device level, a systematic characterisation of valley splitting in Si/SiGe quantum dots has been limited because of poor device yield associated with heterostructure quality and/or device processing. At the materials level, atomic-scale disorder in buried interfaces [187] may be revealed by atom-probe tomography (APT) in three-dimensions (3D) over the nanoscale dimensions comparable to electrically defined quantum dots. However, the current models employed to reconstruct in 3D the APT data can be fraught with large uncertainties due to the assumptions made to generate the three-dimensional representation of the tomographic data [188]. This results in limited accuracy when mapping heterointerfaces [189] and quantum wells [190–192]. These limitations prevent linking the valley splitting in quantum dots to the relevant atomic-scale material properties and hinder the development of accurate and

predictive theoretical models.

Herein we solve this outstanding challenge and establish comprehensive insights into the atomic-level origin of valley splitting in realistic silicon quantum dots. Firstly, we measure valley splitting systematically across many quantum dots, enabled by high-quality heterostructures with a low disorder potential landscape and by improved fabrication processes. Secondly, we establish a new method to analyse APT data leading to accurate 3D evaluation of the atomic-level properties of the Si/SiGe buried interfaces. Thirdly, incorporating the 3D atomic-level details obtained from APT, we simulate valley splitting distributions that consider the role of random fluctuations in the concentration of Si and Ge atoms at each layer of the Si/SiGe interfaces. By comparing theory with experiments, we find that the measured random distribution of Si and Ge atoms at the Si/SiGe interface is enough to account for the measured valley splitting spread in real quantum dots. Based on these atomistic insights, we conclude by proposing a practical strategy to statistically enhance valley splitting above a specified threshold as a route to making spin-qubit quantum processors more reliable — and consequently — more scalable.

6.2. MATERIAL STACKS AND DEVICES

Figure 6.1 overviews the material stack, quantum dot devices, and measurements of valley splitting. To increase statistics, we consider two isotopically purified $^{28}Si/Si_{0.7}Ge_{0.3}$ heterostructures (quantum wells A and B) designed with the same quantum well width and top-interface sharpness (see section 6.7.1), which are important parameters determining valley splitting [178, 180]. As shown in high angle annular dark field scanning transmission electron microscopy (HAADF-STEM), quantum well A (Fig. 6.1(a)) has a sharp $^{28}Si \rightarrow$ Si-Ge heterointerface at the top and a diffused Si-Ge $\rightarrow ^{28}Si$ heterointerface at the bottom, whereas in quantum well B (Fig. 6.1(b)) the growth process was optimized to achieve sharp interfaces at both ends of the quantum well. These heterostructures support a two-dimensional electron gas with high mobility and low percolation density (Supplementary Figs. 6.5 and 6.6), indicating a low disorder potential landscape, and high-performance qubits [121, 193] with single- and two-qubit gates fidelity above 99% [121].

We define double-quantum dots electrostatically using gate layers insulated by dielectrics (see section 6.7.4). A positive gate voltage applied to plunger gates P1 and P2 (Fig. 6.1(c)) accumulates electrons in the buried quantum well, while a negative bias applied to other gates tunes the confinement and the tunnel coupling between the quantum dots Q1 and Q2. All quantum dots in this work have plunger gate diameters in the range of 40-50 nm (Fig. 6.1(d) and Supplementary Table 6.1), setting the relevant lateral length scale for atomic-scale disorder probed by the electron wave function.

6.3. VALLEY SPLITTING MEASUREMENTS

We perform magnetospectroscopy measurements of valley splitting E_v in dilution refrigerators with electron temperatures of about 100 mK (see section 6.7.4). Figure 6.1(e) shows a typical charge stability diagram of a double quantum dot with DC gate voltages tuned to achieve the few electron regime, highlighted in Fig. 6.1(f). We determine the 2-electron singlet-triplet energy splitting (E_{ST}) by measuring the gate-voltage dependence

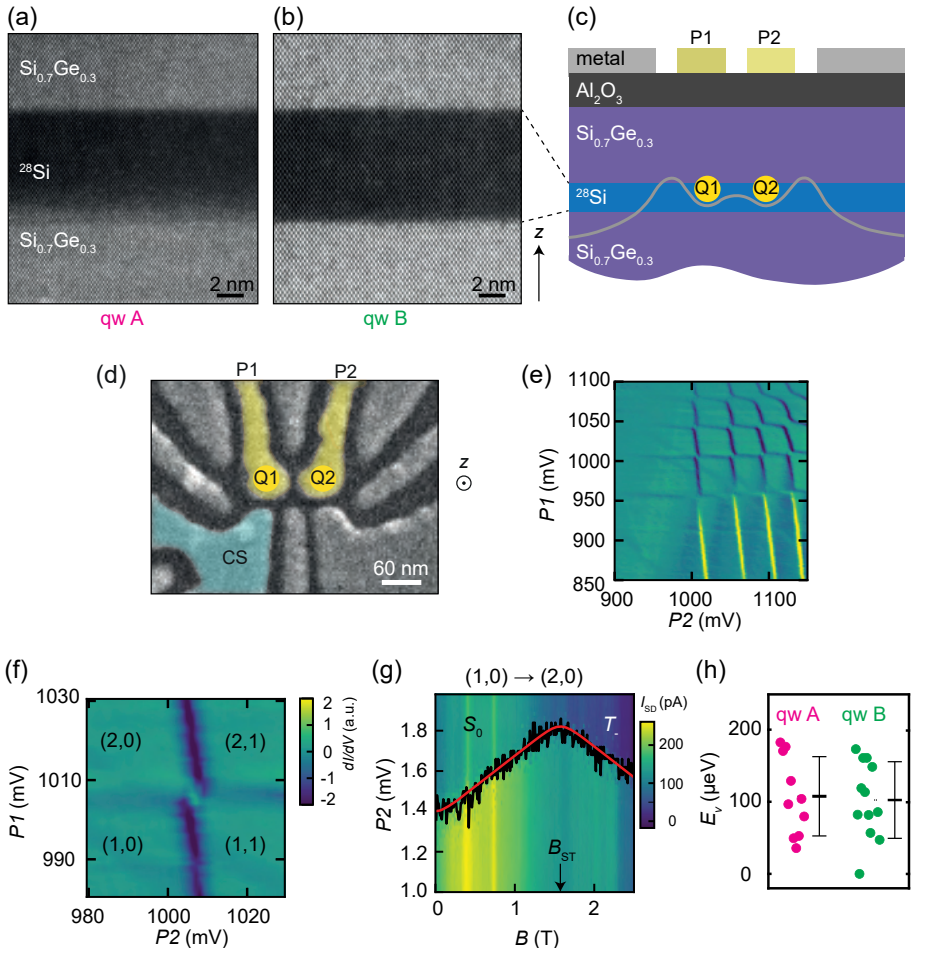

Figure 6.1: **Material stack, devices, and valley splitting measurements** (a), (b) High-angle annular dark field scanning transmission electron microscopy (HAADF-STEM) of ^{28}Si/SiGe quantum wells A and B, respectively. (c), (d) Schematic cross-section of a heterostructure with gate layout and false-coloured scanning electron microscope image of a double quantum dot, respectively. Q1 and Q2 are the quantum dots defined through confinement potentials (schematic, grey line) formed below plunger gates P1 and P2. CS is a nearby quantum dot used as a charge sensor. (e) Typical stability diagram of a double quantum dot formed by plunger gates P1 and P2 and measured by a nearby charge sensor (CS in (d)). (f) Close-up of the stability diagram in the few-electron regime. (g) Typical magnetospectroscopy of the (1,0)→(2,0) transition, used to measure singlet-triplet splittings. An offset of 1082 mV is subtracted for clarity from the gate voltage applied to P2. Black lines show the location of the maximum of the differentiated charge-sensor signal ($dI_{SD}/dP2$) of the electron charging transition. Red lines show a fit to the data, from which we extract the kink position B_{ST}. The valley splitting E_v is given by $g\mu_B B_{ST}$, where $g = 2$ is the gyromagnetic ratio and μ_B is the Bohr magneton. (h) Experimental scatter plots of the valley splittings for quantum wells A (magenta) and B (green), with thick and thin horizontal black lines denoting the mean and two-sigma error bars.

as a function of parallel magnetic field B along the (0,1) → (0,2) transition (Fig. 6.1(g)) and along the (1,1) → (0,2) transition (Supplementary Fig. 6.8). In Fig. 6.1(g), the transition

line (black line) slopes upward, because a spin up electron is added to form a singlet ground state S_0. Alternatively, a spin down electron can be added to form a T_--state, with a downward slope. A kink occurs when the S_0-state is energetically degenerate with the T_--state, becoming the new ground state of the two-electron-system. From the position of the kink (B_{ST} = 1.57 T) along the theoretical fit (red line) and the relation $E_{ST} = g\mu_B B_{ST}$, where $g = 2$ is the electron gyromagnetic ratio and μ_B is the Bohr magneton, we determine E_{ST} = 182.3 μeV for this quantum dot. E_{ST} sets a lower bound on the valley splitting, $E_v \geq E_{ST}$ [176, 194]. Due to small size, our dots are strongly confined with orbital energy much larger than E_{ST} (Supplementary Fig. 6.7), similar to other Si/SiGe quantum dots [169, 173, 177]. Therefore, we expect exchange corrections to have negligible effects [194] and here take $E_v \approx E_{ST}$.

Here we report measurements of E_v in 10 quantum dots in quantum well A and 12 quantum dots in quantum well B (Figures. 6.9-6.12) and compare the measured values in Fig. 6.1(h). We observe a rather large spread in valley splittings, however we obtain remarkably similar mean values and two-standard-deviation error bars $\overline{E_v} \pm 2\sigma$ of 108 ± 55 μeV and 106 ± 58 μeV for quantum wells A and B, respectively[1]. We argue that quantum wells A and B have similar $\overline{E_v} \pm 2\sigma$ because the electronic ground state is confined against the top interface, which is very similar in the two quantum wells.

6.4. ATOM PROBE TOMOGRAPHY

We now characterize the atomic-scale concentration fluctuations at the quantum well interfaces to explain the wide range of measured valley splittings with informed theoretical and statistical models. To probe the concentrations over the dimensions relevant for quantum dots across the wafer, we perform APT on five samples each from quantum wells A and B, with a field of view of approximately 50 nm at the location of the quantum well (see section 6.7.2). First, we show how to reliably reconstruct the buried quantum well interfaces, then we use this methodology to characterise their broadening and roughness.

Figure 6.2(a) shows a typical point-cloud reconstruction of an APT specimen from quantum well B. Each point represents the estimated position of an ionized atom detected during the experiment [188]. Qualitatively, we observe an isotopically enriched ^{28}Si quantum well, essentially free of ^{29}Si, cladded in a SiGe alloy. To probe the interface properties with the highest possible resolution allowed by APT and differently from previous APT studies on Si/SiGe [192], we represent the atom positions in the acquired data sets in form of a Voronoi tessellation [195, 196] and generate profiles on an $x-y$ grid of the tessellated data, as described in Supplementary Discussion Section 6.8.2c. A sigmoid function $[1+\exp(z-z_0)/\tau]^{-1}$ [192] is used to fit the profiles of each tile in the $x-y$ grid. Here, z_0 is the inflection point of the interface and 4τ is the interface width. As the Voronoi tessellation of the data set does not sacrifice any spatial information, the tiling in the $x-y$ plane represents the smallest lateral length scale over which we characterise the measured disorder at the interface. Note that we do not average at all over the z axis and hence maintain the inherent depth resolution of APT. We find that for tiles as small as 3 nm × 3 nm the numerical fitting of sigmoid functions to the profiles converges reliably.

[1] The quantum dots all have a similar design and hence are expected to have similar electric fields across the devices with a small influence on valley splitting under our experimental conditions

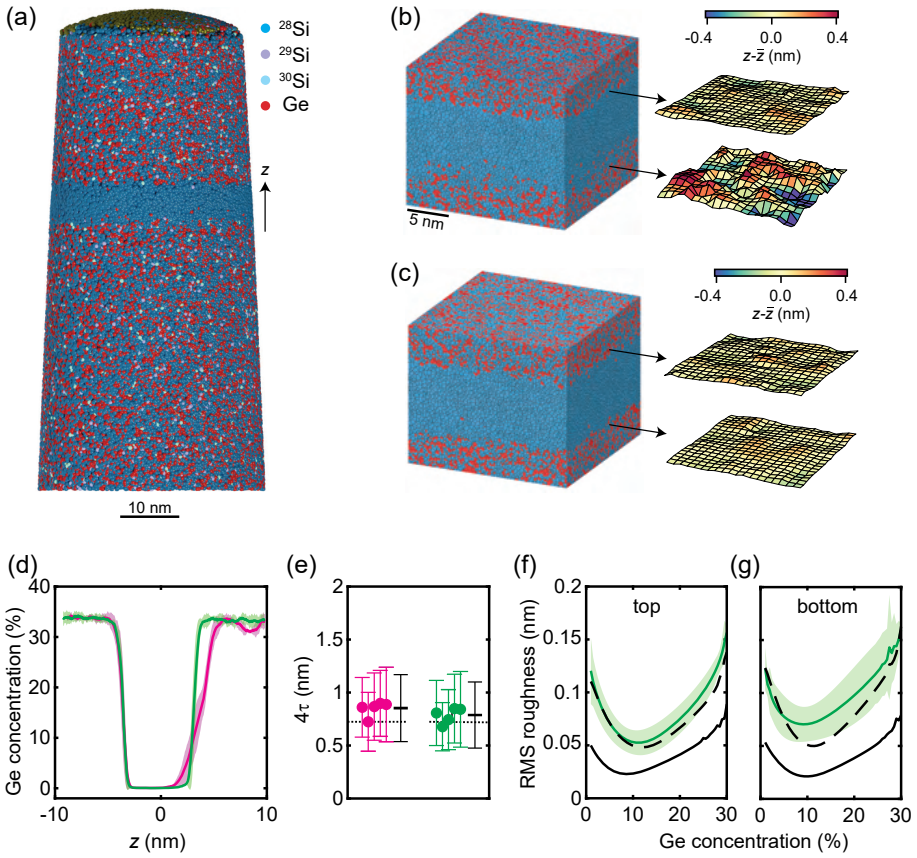

Figure 6.2: **Atom probe tomography of ^{28}Si/SiGe heterostructures.** (a) Point-cloud APT reconstruction of quantum well B, showing the ^{28}Si quantum well and surrounding SiGe barriers. Isotopic purification is confirmed by secondary ion mass spectroscopy (Supplementary Fig. 6.20). (b), (c) Voronoi tessellation of the APT reconstructions for quantum wells A and B, respectively, and extracted isosurfaces corresponding to 8% Ge concentration. $\bar{z}$ is the average position of the 8% Ge concentration across these particular samples. We limit the lateral size of the analysis to $\approx 30\,\text{nm} \times 30\,\text{nm}$, reflecting the typical lateral size of a quantum dot (Fig. 6.1(d)). (d) Average germanium concentration depth profiles across quantum wells A (magenta) and B (green). Shaded areas mark the 95% confidence interval over each of the sets of five APT samples. (e) Statistical analysis of the top interface width 4τ determined by fitting the data for quantum wells A (magenta) and B (green) to sigmoid functions. Thick and thin horizontal black lines denote the mean and two-standard-deviation error bars for the different APT samples. Dotted black lines show 4τ results from the HAADF-STEM measurements (Supplementary Fig 6.19). (f), (g) Root mean square (RMS) roughness of the concentration isosurfaces as a function of germanium concentration at the top and bottom interfaces of quantum well B (green line). Shaded areas indicate the 95% confidence interval, averaged over each set of five APT samples. The experimental data are compared to the RMS roughness of a simulated quantum well with the interface properties of (d) (dashed black line) vs. an atomically sharp quantum well (solid black line).

Although each tile contains many atoms, their size is still much smaller than the quantum dot diameter, and may therefore be considered to be microscopic. We use the sigmoid fits for each tile stack to visualise and further characterise the interfaces (Supplementary

Figs. 6.14-6.16). Importantly, Ge concentration isosurfaces as shown in Fig. 6.2(b), (c) are constructed by determining the vertical position for which each of the sigmoids reaches a specific concentration. Note, that we oversample the interface to improve the lateral resolution by making the 3 nm × 3 nm tiles partially overlap (Supplementary Discussion Section 6.8.2c).

In Fig. 6.2(d), we show the average Ge concentration profile and measurement to measurement variations from the tessellated volumes (Supplementary Discussion Section 6.8.2 b,c) of all samples for both quantum wells A and B. APT confirms HAADF-STEM results in Fig. 6.1(a),(b): quantum wells A and B have an identical sharp top interface and quantum well A has a broader bottom interface. Furthermore, the shaded colored areas in Fig. 6.2(d) reveal narrow 95% confidence levels, pointing to highly uniform concentration profiles when averaged across the wafer. Strong disorder fluctuations emerge at the much smaller tile length scale. In Fig. 6.2(e) we show for all samples of a given quantum well the interface width mean value with two standard deviations $\overline{4\tau} \pm 2\sigma$, obtained by averaging over all the tiles in a given sample. The results indicate uniformity of $\overline{4\tau}$, and further averaging across all samples of a given heterostructure ($\mu_{\overline{4\tau}}$, black crosses) yields similar values of $\mu_{\overline{4\tau}} = 0.85 \pm 0.32$ nm and 0.79 ± 0.31 nm for quantum wells A and B, consistent with our 4τ analysis from HAADF-STEM measurements (black dotted lines). However, the two-standard-deviation errors (2σ) of each data point can be up to 30% of the mean value $\overline{4\tau}$.

To pinpoint the root cause of atomic-scale fluctuations at the interface, in Fig. 6.2(f),(g) we utilize the 3D nature of the APT data sets, calculate, and compare the root mean square (RMS) roughness of the interfaces (solid green lines) as measured by APT on quantum well B to two 3D models (Fig. 6.2(f),(g)) mimicking the dimensions of an APT data set. Both models are generated with random distributions of Si and Ge in each atomic plane (see Supplementary Discussion Section 6.8.2d). The first model (solid black lines) corresponds to an atomically abrupt interface where the Ge concentration drops from ~33.5% to 0% in a single atomic layer. It hence represents the minimum roughness achievable at each isoconcentration surface given the in-plane randomness of SiGe and the method to construct the interface. The second model (dashed black lines) is generated with the experimentally determined Ge concentration profile along the depth axis (Supplementary Fig. 6.17). As shown in Fig. 6.2(f),(g), the roughness extracted from the second model fits well to the measured data, suggesting that the RMS roughness measured by APT is fully explained by the interface width and shape along the depth axis. Furthermore, as the deviation of each isosurface tile position from the isosurface's average position also matches that of the measured interfaces from the second model (Supplementary Movie 1 in Ref. [42]) the APT data are consistent with a random in-plane distribution of Ge perpendicular to the interface in all data sets of quantum well B. For 2 out of 5 samples on quantum well A that we analyzed, we observe features that are compatible with correlated disorder from atomic steps (Supplementary Fig. 6.19). In the following, the alloy disorder observed in the APT concentration interfaces is incorporated into a theoretical model. As shown below, the calculations of valley splitting distributions associated with the 3D landscape of Si/SiGe interfaces can be further simplified into a 1D model that incorporates the in-plane random distribution of Si and Ge atoms.

6.5. VALLEY SPLITTING SIMULATIONS

We begin by considering an ideal laterally infinite heterostructure with no concentration fluctuations, and we denote the average Si concentration at layer l by $\bar{x}_l$. Due to the finite size of a quantum dot and the randomness in atomic deposition, there will be dot-to-dot concentration fluctuations. We therefore model the actual Si concentration at layer l by averaging the random alloy distribution weighted by the lateral charge density in the quantum dot, giving $x_l^d = \bar{x}_l + \delta_{x_l}$, as described in Supplementary Discussion Section 6.7.5. Here, the random variation δ_{x_l} is computed assuming a binomial distribution of Si and Ge atoms. We find that these fluctuations can have a significant impact on the valley splitting.

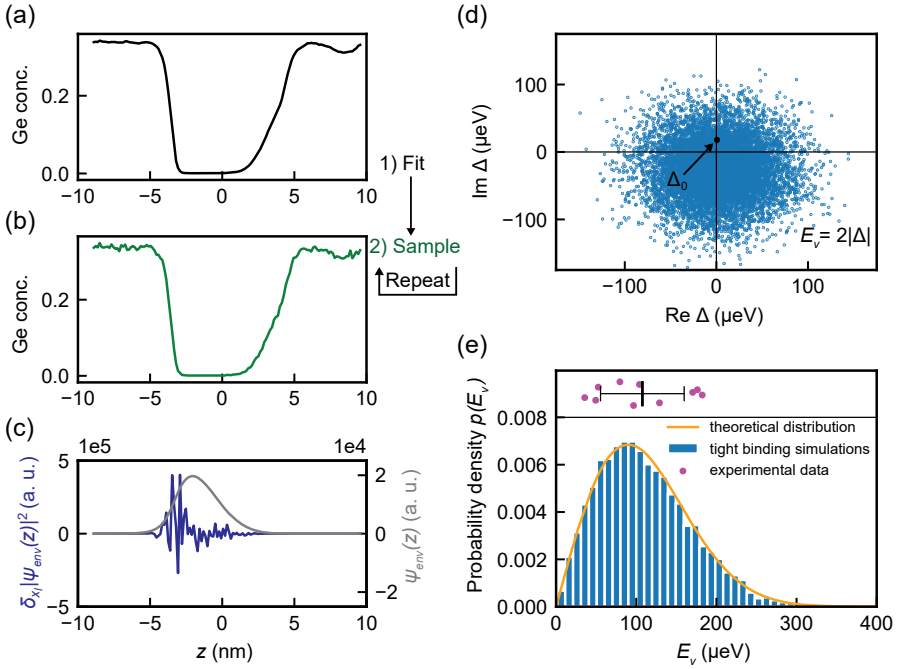

Figure 6.3: **Valley-splitting simulations.** (a) Average concentration profile obtained from APT data (quantum well A). (b), Typical, randomized Ge concentration profile, derived from (a). (c) Envelope function $\psi_{\mathrm{env}}(z)$, obtained for the randomized profile in (b) (grey curve), and the corresponding concentration fluctuations weighted by the envelope function squared: $\delta_{x_l}|\psi_{\mathrm{env}}(z_l)|^2$ (blue). Here, the wavefunction is concentrated near the top interface where the concentration fluctuations are also large; the weighted fluctuations are therefore largest in this regime. (d) Distribution of the intervalley matrix element Δ in the complex plane, as computed using an effective-mass approach, for 2,000 randomized concentration profiles. The black marker indicates the deterministic value of the matrix element Δ_0, obtained for the experimental profile in (a). (e), Histogram of the valley splittings from tight-binding simulations with 10,000 randomized profiles. The same profiles may be used to compute valley splittings using effective-mass methods; the orange curve shows a Rice distribution whose parameters are obtained from such effective-mass calculations (see section 6.7.5).

We explore these effects numerically using 1D tight-binding simulations. We begin with the averaged fitted concentration profiles obtained from the APT analysis in Fig 6.2(d), which enable us to directly measure the average Ge concentration in a given layer $\bar{x}_l$

(Fig. 6.3(a)). The variance of the concentration fluctuations is determined by the size of the quantum dot, which we assume has an orbital excitation energy of $\hbar\omega = 2$ meV and corresponding radius $\sqrt{\hbar/m^*\omega}$, as well as the average Si concentration $\bar{x}_l$. Here, m^* is the effective mass of Si. Together, $\bar{x}_l$ and the variance determine the probability distribution of weighted Si and Ge concentrations. Concentration profiles are sampled repeatedly from this distribution, with a typical example shown in Fig. 6.3(b). The valley splitting is then determined from a 1D tight-binding model [197]. The envelope of the effective mass wavefunction $\psi_{\text{env}}(z)$ is shown in Fig. 6.3(c) (grey curve) for an electron confined in the quantum well of Fig. 6.3(b). The procedure is repeated for 10,000 profile samples, obtaining the histogram of valley splittings shown in Fig. 6.3(e). These results agree very well with calculations obtained using a more sophisticated three-dimensional 20-band $sp^3d^5s^*$ NEMO tight-binding model [198] (Supplementary Discussion Section 6.7.5) and confirm that concentration fluctuations can produce a wide range of valley splittings. For comparison, at the top of Fig. 6.3(e), we also plot the same experimental valley splittings shown in Fig. 6.1(h), demonstrating good agreement in both the average value and the statistical spread. These observations support our claim that the valley splitting is strongly affected by composition fluctuations due to random distributions of Si and Ge atoms near the quantum well interfaces, even though the experiments cannot exclude the presence of correlated disorder from atomic steps in quantum dots.

Analytical methods using effective mass theory may also be used to characterise the distribution of valley splittings. First, we model the intervalley coupling matrix element [180] as $\Delta = \int e^{-2ik_0z_l} U(z)|\psi_{\text{env}}(z)|^2 dz$, where $k_0 = 0.82 \cdot 2\pi/a_0$ is the position of the valley minimum in the Si Brillouin zone, $a_0 = 0.543$ nm is length of the Si cubic unit cell, $\psi_{\text{env}}(z)$ is a 1D envelope function, and $U(z)$ is the quantum well confinement potential. The intervalley coupling Δ describes how sharp features in the confinement potential couple the two valley states, which would otherwise be degenerate. In general, Δ is a complex number that can be viewed as the sum of two distinct components: a deterministic piece Δ_0, arising from the average interface concentration profile, and a random piece $\delta\Delta$, arising from concentration fluctuations. The latter can be expressed as a sum of contributions from individual atomic layers: $\delta\Delta = \sum_l \delta\Delta_l$, where $\delta\Delta_l$ is proportional to $\delta_{x_l}|\psi_{\text{env}}(z_l)|^2$ (see section 6.7.5). To visualize the effects of concentration fluctuations in Fig. 6.3(c), we compute $\delta\Delta_l$ using the randomized density profile of Fig. 6.3(b) (blue curve). We see that most significant fluctuations occur near the top interface, where $|\psi_{\text{env}}(z_l)|$ and the Ge content of the quantum well are both large. In Fig. 6.3(d) we plot Δ values obtained for 2,000 quantum-well realizations using this effective mass approach. The deterministic contribution to the valley splitting Δ_0 (black dot) is seen to be located near the center of the distribution in the complex plane, as expected. However, the vast majority of Δ values are much larger than Δ_0, demonstrating that concentration fluctuations typically provide the dominant contribution to intervalley coupling.

The total valley splitting is closely related to the intervalley coupling via $E_v = 2|\Delta|$, and therefore exhibits the same statistical behavior. In Fig. 6.3(e), the orange curve shows the Rice distribution whose parameters are derived from effective-mass calculations of the valley splitting (see section 6.7.5), using the same concentration profiles as the histogram data. The excellent agreement between these different approaches confirms the accuracy of our theoretical techniques (Supplementary Discussion Section 3d in Ref. [42]).

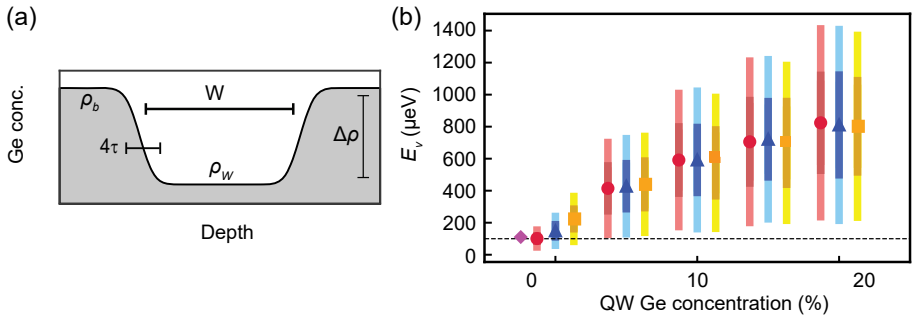

Figure 6.4: **Valley-splitting simulations.** (a), Schematic Si/SiGe quantum well with Ge concentrations ρ_W (in the well) and $\rho_b = \rho_W + \Delta\rho$ (in the barriers), with a fixed concentration difference of $\Delta\rho = 25\%$. (b), Distribution of valley splittings obtained from simulations with variable Ge concentrations, corresponding to ρ_W ranging from 0 to 20%, and interface widths $4\tau = 5$ ML (red circles), 10 ML (blue triangles), or 20 ML (orange squares), where ML refers to atomic monolayers. Here, the marker describes the mean valley splitting, while the darker bars represent the 25-75 percentile range and the lighter bars represent the 5-95 percentile range. Each bar reflects 2,000 randomized tight-binding simulations of a quantum well of width $W = 120$ ML. The magenta diamond at zero Ge concentration shows the average measured valley splitting of quantum well A. In all simulations reported here, we assume an electric field of $E = 0.0075$ V/nm and a parabolic single-electron quantum-dot confinement potential with orbital excitation energy $\hbar\omega = 4.18$ meV and corresponding dot radius $\sqrt{\hbar/m^*\omega}$.

6

6.6. DISCUSSION

Based on the results obtained above, we now propose two related methods for achieving large valley splittings (on average), with high yields. Both methods are derived from the key insight of Fig. 6.3(c): due to random-alloy fluctuations, the valley splitting is almost always enhanced when the electronic wavefunction overlaps with more Ge atoms. In the first method, we therefore propose to increase the width of the interface (4τ) as shown in Fig. 6.3(f), since this enhances the wavefunction overlap with Ge atoms at the top of the quantum well. This approach is nonintuitive because it conflicts with the conventional deterministic approach of engineering sharp interfaces. The second method, also shown in Fig. 6.4(a), involves intentionally introducing a low concentration of Ge inside the quantum well. The latter method is likely more robust because it can incorporate both deterministic enhancement of the valley splitting from a sharp interface, and fluctuation-enhanced valley splitting.

We test these predictions using simulations, as reported in Fig. 6.4(b), where different colors represent different interface widths and the horizontal axis describes the addition of Ge to the quantum well. For no Ge in the quantum well, as consistent with our experiments, we observe significant increases in the valley splitting with increasing interface width. Here, the narrowest interface appears most consistent with our experimental results (magenta marker), attesting to the sharp interfaces achieved in our devices. As the Ge concentration increases in the quantum well, this advantage is largely overwhelmed by concentration fluctuations throughout the well. A very substantial increase in valley splitting is observed for all concentration enhancements, even at the low, 5% level. Here, the light error bars represent 5-95 percentiles while dark bars represent 25-75 percentiles. At the 5% concentration level, our simulations indicate that >95% of devices should achieve valley splittings >100 μeV. This value is more than an order of magnitude larger

than the typical operation temperature of spin-qubits and is predicted to yield a 99% readout fidelity [38]. This would represent a significant improvement in qubit yield for Si quantum dots. A recent report of SiGe quantum wells with oscillating Ge concentrations provides the first experimental evidence that intentionally placing Ge in the quantum well leads to significant variability and some of the highest recorded values of valley splitting [199].

In conclusion, we argue for the atomic-level origin of valley splitting distributions in realistic Si/SiGe quantum dots, providing key insights on the inherent variability of Si/SiGe qubits and thereby solving a longstanding problem facing their scaling. We relate 3D atom-by-atom measurements of the heterointerfaces to the statistical electrical characterization of devices, and ultimately to underlying theoretical models. We observe qualitative and quantitative agreement between simulated valley splitting distributions and measurements from several quantum dots, supporting our theoretical framework. Crucially, we learn that atomic concentration fluctuations of the ^{28}Si → Si-Ge heterointerface are enough to account for the valley splitting spread and that these fluctuations are largest when the envelope of the wavefunction overlaps with more Ge atoms. Moreover, while we have only incorporated random alloy disorder into our theoretical framework so far, we foresee that APT datasets including correlated disorder, such as steps, will be used to further refine our theoretical understanding of valley splitting statistics. Since atomic concentration fluctuations are always present in Si/SiGe devices due to the intrinsic random nature of the SiGe alloy, we propose to boost these fluctuations to achieve on average large valley splittings in realistic silicon quantum dots, as required for scaling the size of quantum processors. Our proposed approaches are counter-intuitive yet very pragmatic. The interface broadening approach seems viable for hybrid qubits, which require valley splitting to be large enough to be usable but not so large as to be inaccessible. For single-electron spin qubits, which don't use the valley degree of freedom, the direct introduction of Ge in the quantum well appears better suited for targeting the largest possible valley splitting. By adding Ge to the Si quantum well in small concentrations we expect to achieve on average valley splitting in excess of 100 μeV. Based on results from scattering theories [103], we speculate that the added scattering from random alloy disorder will not be the limiting factor for mobility in current ^{28}Si/SiGe heterostructures and therefore should not compromise the low-disorder potential environment, which is important for scaling to large qubit systems. We believe that our results will inspire a new generation of Si/SiGe material stacks that rely on atomic-scale randomness of the SiGe as a new dimension for the heterostructure design.

6.7. METHODS

6.7.1. SI/SIGE HETEROSTRUCTURE GROWTH

The ^{28}Si/SiGe heterostructures are grown on a 100-mm n-type Si(001) substrate using an Epsilon 2000 (ASMI) reduced pressure chemical vapor deposition reactor equipped with a $^{28}SiH_4$ gas cylinder (1% dilution in H_2) for the growth of isotopically enriched ^{28}Si. The $^{28}SiH_4$ gas was obtained by reducing $^{28}SiF_4$ with a residual ^{29}Si concentration of 0.08% [64]. Starting from the Si substrate, the layer sequence for quantum well A comprises a 900 nm layer of $Si_{1-x}Ge_x$ graded linearly from $x = 0$ to 0.3, followed by a 300 nm $Si_{0.7}Ge_{0.3}$ strain-relaxed buffer, an 8 nm tensily strained ^{28}Si quantum well, a 30 nm $Si_{0.7}Ge_{0.3}$ barrier, and a sacrificial Si cap. The layer sequence for quantum well B comprises a 1.4 µm step-graded $Si_{(1-x)}Ge_x$ layer with a final Ge concentration of $x = 0.3$ achieved in four grading steps ($x = 0.07$, 0.14, 0.21, and 0.3), followed by a 0.45 µm $Si_{0.7}Ge_{0.3}$ strain-relaxed buffer, an 8 nm tensily strained ^{28}Si quantum well, a 30 nm $Si_{0.7}Ge_{0.3}$ barrier, and a sacrificial Si cap. In quantum well A, the $Si_{0.7}Ge_{0.3}$ strain-relaxed buffer and the Si quantum well are grown at 750 °C without growth interruption. In quantum well B the $Si_{0.7}Ge_{0.3}$ strain-relaxed buffer below the quantum well is grown at a temperature of 625 °C, followed by growth interruption and quantum well growth at 750 °C. This modified temperature profile yields a sharper bottom interface for quantum well B as compared to quantum well A.

6.7.2. ATOM PROBE TOMOGRAPHY

Samples for APT were prepared in a FEI Helios Nanolab 660 dual-beam scanning electron microscope using a gallium focused ion beam at 30, 16 and 5 kV and using a procedure described in detail in Ref. [200]. Before preparation, a 150-200 nm thick chromium capping layer was deposited on the sample via thermal evaporation to minimize the implantation of gallium ions into the sample. All APT analyses were started inside this chromium cap with the stack fully intact underneath. APT was carried out using a LEAP 5000XS tool from Cameca. The system is equipped with a laser to generate picosecond pulses at a wavelength of 355 nm. For the analysis, all samples were cooled to a temperature of 25 K. The experimental data are collected at a laser pulse rate of 200-500 kHz at a laser power of 8-10 pJ. APT data are reconstructed using IVAS 3.8.5a34 software and visualized using the AtomBlend addon to Blender 2.79b and Blender 2.92 software. For the Voronoi tessellation the reconstructed data sets were exported to Python 3.9.2 and then tessellated using the scipy.spatial.Voronoi class of SciPy 1.6.2. Note that in these analyses the interfaces are represented as an array of sigmoid functions generated perpendicular to the respective interface on 3 nm × 3 nm tiles that are 1 nm apart. This sacrifices lateral resolution to allow for statistical sampling of the elemental concentrations but preserves the atomic resolution along the depth axis that APT is known to provide upon constructing the interface as shown in Fig. 6.2(a).

6.7.3. DEVICE FABRICATION

The fabrication process for Hall-bar shaped heterostructure field effect transistors (H-FETs) involves: reactive ion etching of mesa-trench to isolate the two-dimensional electron gas (2DEG); P-ion implantation and activation by rapid thermal annealing at 700 °C; atomic layer deposition of a 10-nm-thick Al_2O_3 gate oxide; deposition of thick dielectric

pads to protect gate oxide during subsequent wire bonding step; sputtering of Al gate; electron beam evaporation of Ti:Pt to create ohmic contacts to the 2DEG via doped areas. All patterning is done by optical lithography. Quantum dot devices are fabricated on wafer coupons from the same H-FET fabrication run and share the process steps listed above. Double-quantum dot devices feature a single layer gate metallization and further require electron beam lithography, evaporation of Al (27 nm) or Ti:Pd (3:27 nm) thin film metal gate, and lift-off. For linear quantum dot arrays the gate stack consists of 3 layers of Ti:Pd metallic gates (3:17, 3:27, 3:27 nm) isolated from each other by 5 nm Al_2O_3 dielectric interlayers. The fabrication processes for quantum dot devices are further detailed in Ref. [112].

6.7.4. ELECTRICAL CHARACTERIZATION OF DEVICES

Hall-bar measurement are performed in a Leiden cryogenic dilution refrigerator with a mixing chamber base temperature $T_{\mathrm{MC}} = 50$ mK [79]. We apply a source-drain bias of 100 µV and measure the source-drain current I_{SD}, the longitudinal voltage V_{xx}, and the transverse Hall voltage V_{xy} as function of the top gate voltage V_{g} and the external perpendicular magnetic field B. From here we calculate the longitudinal resistivity ρ_{xx} and transverse Hall resistivity ρ_{xy}. The Hall electron density n is obtained from the linear relationship $\rho_{\mathrm{xy}} = B/en$ at low magnetic fields. The carrier mobility μ is extracted from the relationship $\sigma_{\mathrm{xx}} = ne\mu$, where e is the electron charge. The percolation density n_{p} is extracted by fitting the longitudinal conductivity σ_{xx} to the relation $\sigma_{\mathrm{xx}} \propto (n - n_{\mathrm{p}})^{1.31}$. Here σ_{xx} is obtained via tensor inversion of ρ_{xx} at $B = 0$. Quantum dot measurements are performed in Oxford and Leiden cryogenic refrigerators with base temperatures ranging from 10–50 mK. Quantum dot devices are operated in the few-electron regime. Further details of the 2DEG and quantum dot measurements are provided in section 6.8.1.

6.7.5. THEORY AND SIMULATIONS

The quantum-well potential at vertical position z_l is simply defined here as a linear interpolation of the conduction-band offset at the quantum-well interface: $U(z_l) = \frac{x_l^d - x_s}{x_w - x_s}\Delta E_c$, where x_l^d is the average Si concentration in layer l, x_s is the average Si concentration in the strain-relaxed SiGe barriers, x_w is the average Si concentration in the strained quantum well, and ΔE_c is the conduction band offset in the absence of fluctuations. In the effective-mass theory, the intervalley coupling matrix element can then be approximated by the sum

$$\Delta = \frac{a_0}{4}\sum_l e^{-2ik_0 z_l}\frac{x_l^d - x_s}{x_w - x_s}\Delta E_c |\psi_{\mathrm{env}}(z_l)|^2. \tag{6.1}$$

Defining the local concentration fluctuations as $x_l^d = \bar{x}_l + \delta_l$, the matrix element can then be split into its deterministic and fluctuating contributions $\Delta = \Delta_0 + \delta\Delta$, where the fluctuating term $\delta\Delta$ contains all dependence on δ_l:

$$\delta\Delta = \frac{a_0}{4}\frac{\Delta E_c}{x_w - x_s}\sum_l e^{-2ik_0 z_l}\delta_l |\psi_{\mathrm{env}}(z_l)|^2. \tag{6.2}$$

The deterministic term Δ_0 represents the matrix element of the ideal, smooth concentration profile, while $\delta\Delta$ describes the fluctuations about this value. For concentration

fluctuations δ_I defined by binomial distributions of Ge and Si atoms, the resulting valley splitting $E_v = 2|\Delta_0 + \delta\Delta|$ corresponds to a Rice distribution with parameters $\nu = 2|\Delta_0|$ and $\sigma = \sqrt{2}\sqrt{\mathrm{Var}[\delta\Delta]}$ [201]. For additional details, see the Supplementary Discussion Section 3 in Ref. [42]. All simulations and numerical calculations reported in this work were performed using Python 3.7.10 with the open-source libraries NumPy, SciPy, and Matplotlib. The 3D atomistic simulations were done using the large-scale Slater-Koster tight-binding solver NEMO3D. A spin resolved 20 band sp3d5s* nearest neighbour model was used. Strain optimization was done using a valence force field Keating model.

6.8. SUPPLEMENTARY INFORMATION

6.8.1. ELECTRICAL CHARACTERIZATION

(A). MAGNETOTRANSPORT CHARACTERIZATION OF HALL-BAR SHAPED HETEROSTRUCTURE FIELD EFFECT TRANSISTORS

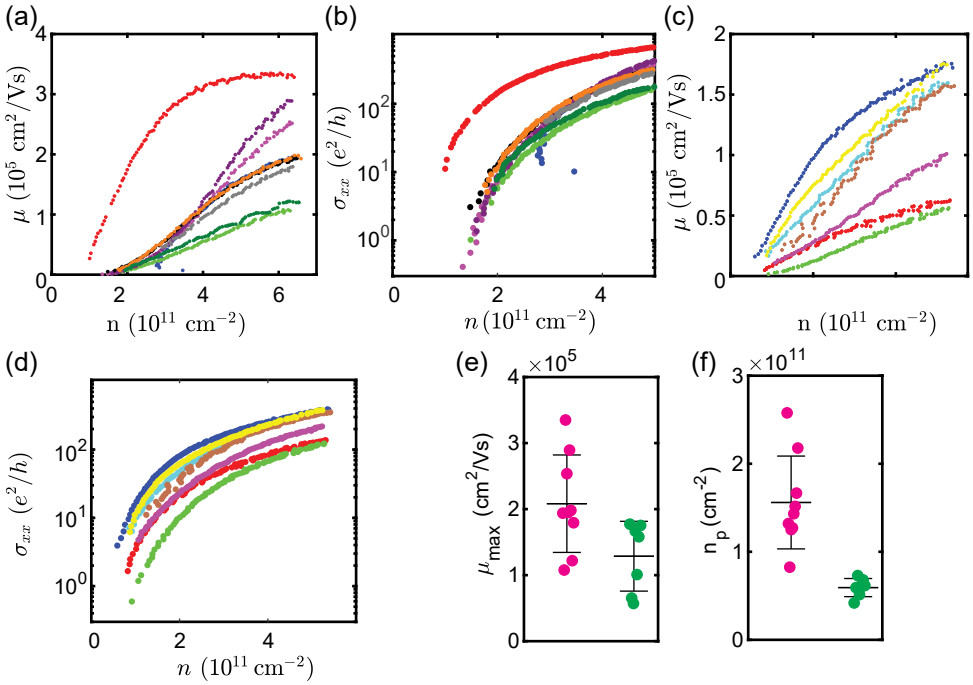

Figure 6.5: (a),(b). Mobility μ and conductivity σ_{xx} as a function of Hall density n measured for quantum well A. (c), (d) Mobility μ and conductivity σ_{xx} as a function of Hall density n measured for quantum well B. (e) Maximum mobility μ_{max} for quantum well A (magenta) and quantum well B (green) extracted from (a) and (c). Black crosses are the mean and standard deviation. For quantum well A we find $\overline{\mu_{max}} = 129.000 \pm 53.000$ cm^2/Vs and for quantum well B we find $\overline{\mu_{max}} = 208.000 \pm 74.000$ cm^2/Vs. (f) Percolation density n_p for quantum well A (magenta) and quantum well B (green) extracted by fitting the conductivity-density curves in (b) and (d) to the relationship $\sigma_{xx} \propto (n - n_p)^{1.31}$ [82]. Since this percolation theory is valid only at low densities, for each sample we chose a fitting range that goes from the lowest measured density n_{min} to a density $n_{max,fit}$ that yields the best fitting results. For the devices from quantum well A in (b) we have $n_{max,fit} = 3.2\times10^{11}$ cm^{-2}, 2.2×10^{11} cm^{-2}, 2×10^{11} cm^{-2}, 2×10^{11} cm^{-2}, 2.2×10^{11} cm^{-2}, 2.2×10^{11} cm^{-2}, 2.5×10^{11} cm^{-2}, 4×10^{11} cm^{-2}, 5.8×10^{11} cm^{-2}. For the devices from quantum well B in (d) we have $n_{max,fit} = 1.35\times10^{11}$ cm^{-2}, 1.35×10^{11} cm^{-2}, 1.6×10^{11} cm^{-2}, 1.6×10^{11} cm^{-2}, 1.6×10^{11} cm^{-2}, 1.8×10^{11} cm^{-2}, 1.35×10^{11} cm^{-2}. Black crosses are the mean and standard deviation of the percolation density. For quantum well A we find $\overline{n_p} = 1.56 \pm 0.53\times10^{11}$ cm^{-2} and for quantum well B we find $\overline{n_p} = 0.59 \pm 0.1\times10^{11}$ cm^{-2}.

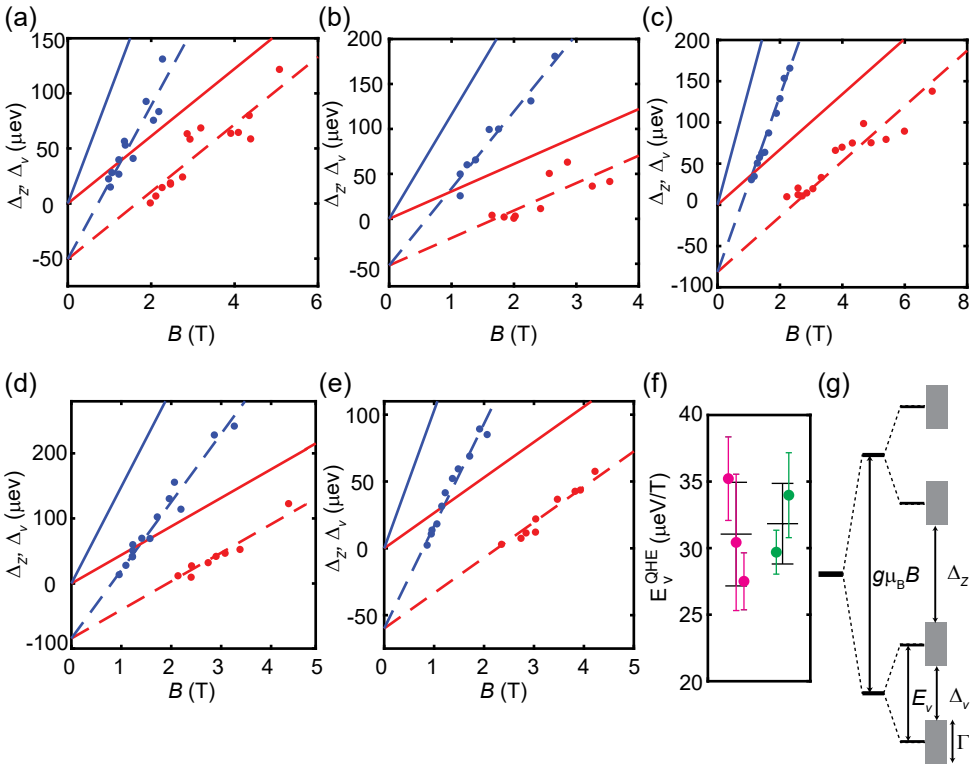

Figure 6.6: (a)-(c) Activation energy measurements of the valley gap Δ_v (red circles) and Zeeman gap Δ_Z (blue circles) as a function of the magnetic field B for three different devices from quantum well A. Δ_v is measured at the $2n-1$ quantum Hall filling factors and Δ_Z is measured at the $4n-2$ filling factors. We follow the same methodology as in Ref. [202]. The blue and red dashed lines are theoretical fits to the experimental data using the equations $\Delta_Z = g^*\mu_B B - c_B B - \Gamma$ and $\Delta_v = c_B B - \Gamma$, where g^* is the effective Landé-g-factor, μ_B is the Bohr magneton, c_B is the proportionality factor of the valley splitting with B, and Γ is the Landau level broadening induced by disorder. We obtain $c_B = 30.64 \pm 3.14$μeV/T, 30.43 ± 5.12 μeV/T, 32.46 ± 2.14 μeV/T, and $g^* = 1.74 \pm 0.16,\ 2 \pm 0.21,\ 2.36 \pm 0.12$ respectively. The blue and red solid lines correspond to the estimated Zeeman and valley energy gaps, respectively. (d), (e) Activation energy measurements and fits of the valley gap and Zeeman gap as in (a)-(c) for two devices from quantum well B. We obtain $c_B = 26.28 \pm 1.65$ μeV/T, 43.15 ± 3.19 μeV/T, and $g^* = 1.77 \pm 0.13,\ 2.54 \pm 0.17$ respectively. (f) Rate of increase of valley splitting with magnetic field E_V^{QHE} for quantum well A (magenta) and quantum well B (green) extracted from the fitting analysis of (a)-(e). We calculate E_V^{QHE} by setting $E_V^{\mathrm{QHE}} = c_B g/g^*$, thereby scaling c_B with a coefficient g/g^* that normalizes the fitted g^* to the value $g = 2$ in silicon. This normalization is a way to take into account the modest electron-electron interaction present in different devices, allowing for a comparison across different quantum wells. Black crosses are the mean and standard deviation of E_V^{QHE}. For quantum well A we find $\overline{E_V^{\mathrm{QHE}}} = 31.1 \pm 3.9$ μeV/T and for quantum well B we find $\overline{E_V^{\mathrm{QHE}}} = 31.8 \pm 3$ μeV/T. (g), Schematic drawing of a Landau level split into Zeeman and valley energy levels, showing all relevant energy separations. Shaded areas represent the single-particle Landau level broadening Γ due to disorder [202].

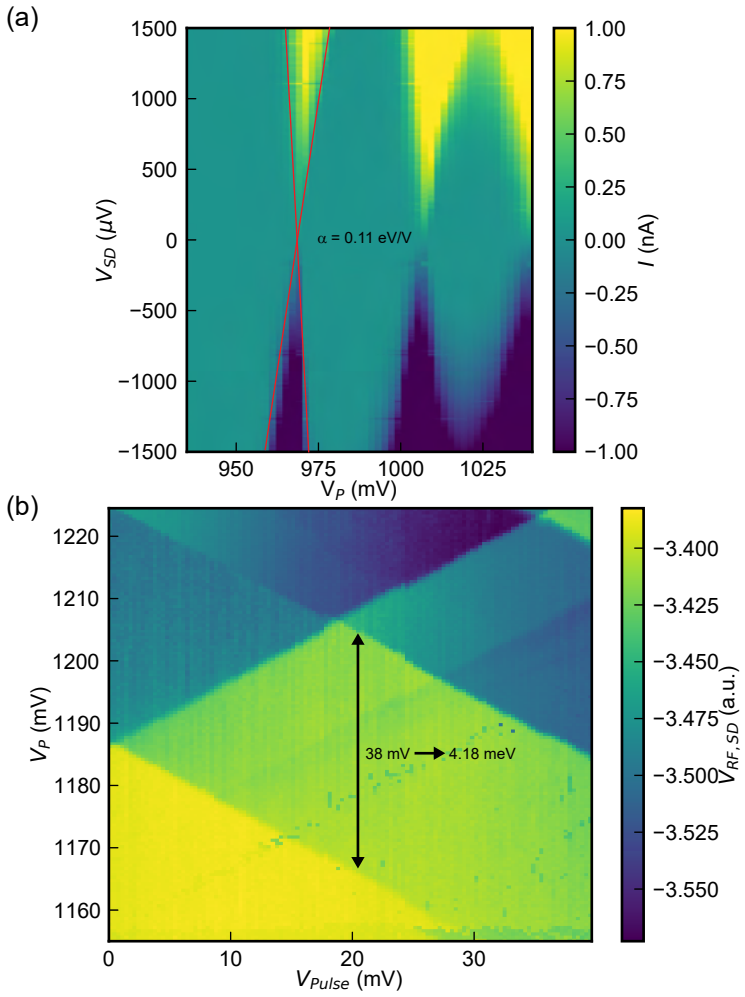

Figure 6.7: (a) Coulomb blockade measurements of QD1, device 5 (see Table S1). The current through the QD is monitored while scanning the gate voltage and the bias voltage applied between the source and the drain, resulting in Coulomb diamonds. From the leftmost Coulomb diamond (indicated by the red lines) we extract a leverarm $\alpha = 0.11$ eV/V using the method described in the supplementary information of Ref. [58]. (b) Pulsed gate spectroscopy for the same quantum dot. The time-averaged RF reflectometry signal/sensing dot response is plotted as a function of the dc gate voltage V_P and the square pulse amplitude V_{pulse} with a pulse frequency of 25 kHz, both applied to the same gate. The arrow indicates the orbital splitting, which we extract as $E_{\text{orb}} = \alpha V_{\text{orb}} = 4.18$ meV, consitent with other values reported in literature [169, 177, 203]

B. SINGLET-TRIPLET ENERGY SPLITTING IN QUANTUM DOTS

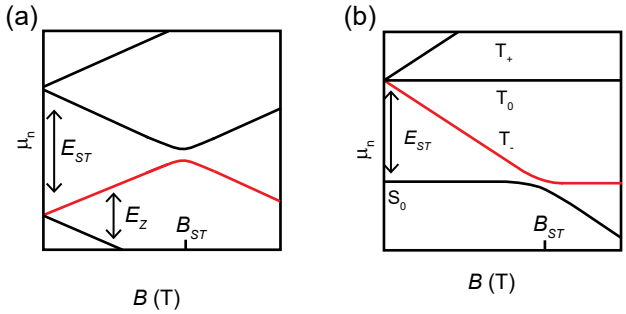

Figure 6.8: (a), Energy evolution of the ground state and first excited state in a single quantum dot as a function of the magnetic field. The red line shows the expected spin filling for the charge transition $N = 1 \rightarrow 2$. At $B = B_{ST}$ the typical kink can be observed, where the Zeeman energy E_Z is equal to the singlet-triplet splitting energy E_{ST}. (b), Energy evolution of the four lowest lying energy states in a double quantum dot as a function of the magnetic field with fixed electron number $N = 2$. The red line represents the T_- energy state measured along the (1,1) →(2,0) transition. At $B = B_{ST}$ the singlet state S_0 and the triplet state T_- are equal in energy, resulting in an anticrossing.

The singlet-triplet energy splitting is computed according to the configurations in Fig. 6.8. In the configuration in Fig. 6.8(a) the red line can be fitted to compute E_{ST} with the formula [186]:

$$V_P = \frac{1}{\alpha\beta_e} \ln \frac{e^{\frac{1}{2}\kappa B + \beta_e E_{ST}}(e^{\kappa B} + 1)}{e^{\kappa B} + e^{2\kappa B} + e^{\kappa B + \beta_e E_{ST}} + 1}, \tag{6.3}$$

where α is the lever arm converting gate voltage to energy, V_P is the gate voltage, $\kappa = g\mu_B\beta_e$ where $\beta_e = 1/k_B T_e$, g is the Lande-g-factor in silicon, μ_B is the Bohr magneton, B is the magnetic field, k_B is Boltzmann's constant, and T_e is the electron temperature [186].

In the configuration in Fig. 6.8(b) the Hamiltonian of the T− state is given by:

$$\hat{H} = \begin{pmatrix} E_{S0} & t_c \\ t_c & E_{T-} \end{pmatrix} \tag{6.4}$$

where E_{S0} is the energy evolution of the singlet state, E_{T-} is the energy evolution of the triplet minus-state, and the off-diagonal element t_c is the tunnel coupling between the (1,1)-state and the the (2,0)-state in the double quantum dot. Diagonalization of the Hamiltonian yields:

$$\mu_n(T-) = \frac{1}{2}(E_{S0} + E_{T-} + \sqrt{(E_{S0} - E_{T-})^2 + 4t_c^2}) \tag{6.5}$$

To fit the red line from Fig. 6.8(b) we use $E_{S0} = 0$ and $E_{T-} = \alpha(g\mu_B B + E_{ST})$, where α is the lever arm, g is the single particle g-factor, B is the magnetic field, and E_{ST} is the singlet-triplet splitting.

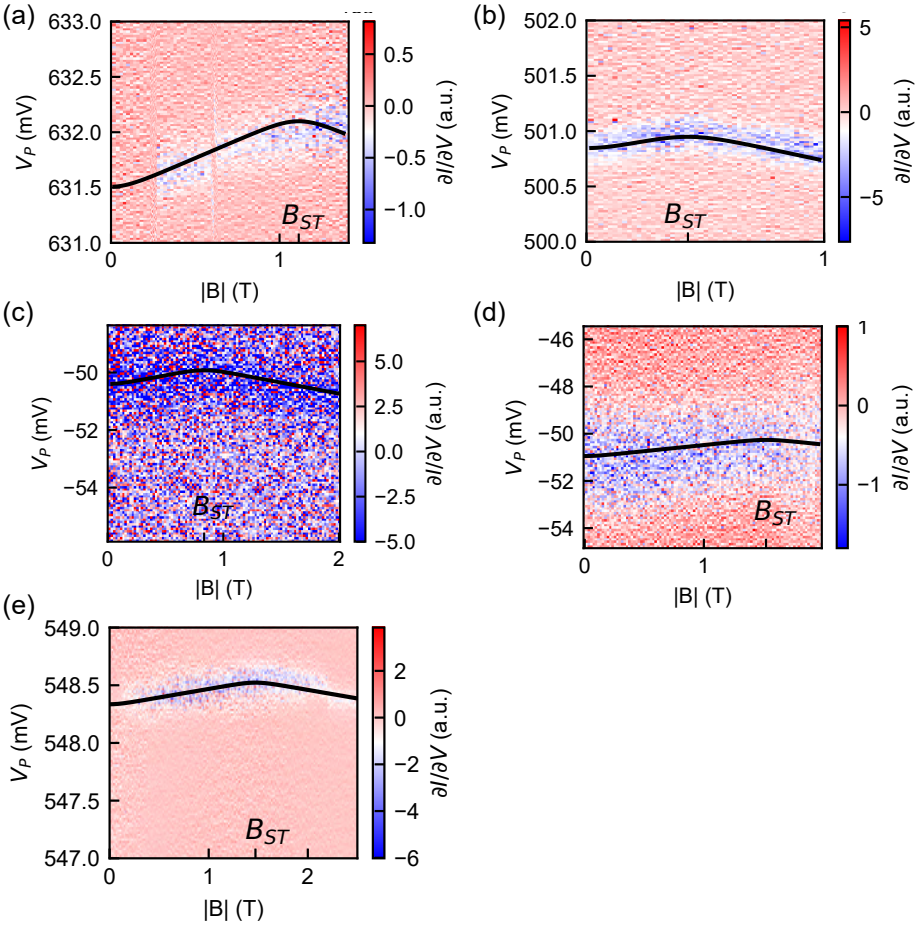

Figure 6.9: Magnetospectroscopy of quantum dots fabricated on quantum well A. V_P is the gate voltage applied to the plunger gate forming the quantum dot. (a) - (e) Magnetospectroscopy data measured along the $N = 1 \rightarrow 2$ transition of five different quantum dots on three different samples in quantum well A. The signal is measured by monitoring the derivative of the current through a nearby charge sensor. a), A charge fluctuation occurred during the measurement and to optimize the fitting routine, we shifted the data in the range 0.3-0.6 T upwards by 1 mV. (a) - (e), Due to low tunnel rates, for each gate Voltage sweep at the different magnetic fields, we determine the points with the highest derivative of the current $\frac{\partial I}{\partial V}$ through the charge sensor as the $N = 1 \rightarrow 2$ charge transition. We then use these points as the input of eq. 6.3. With this equation we can fit the charge transition as a function of the magnetic field (black curve).

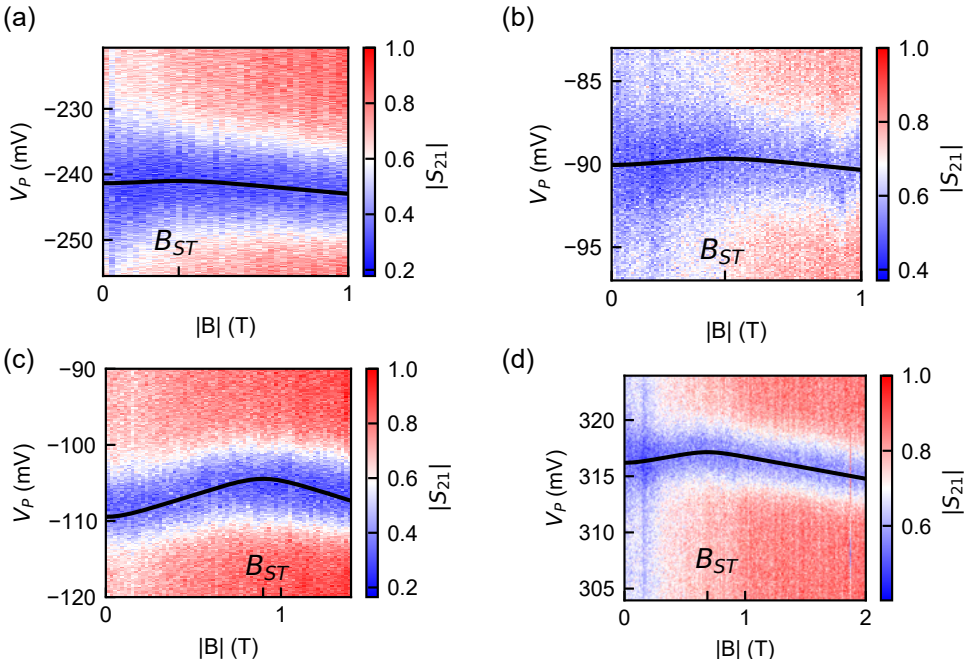

Figure 6.10: Magnetospectroscopy of quantum dots fabricated on quantum well A. V_P is the gate voltage applied to the plunger gate forming the quantum dot. (a) - (d) Magnetospectroscopy data measured along the $N = 1 \rightarrow 2$ transition of four different quantum dots on two different samples in quantum well A. The quantum dot is probed via gate-based sensing using an on-chip superconducting resonator in these measurements [204]. The magnitude of the transmitted microwave signal S_{21} through a feed line that is capacitively coupled to the resonator is plotted here. For each gate Voltage sweep at the different magnetic fields, we use a Lorentzian function to find the resonance peak of the signal. The resonance peaks then are used as input of eq. 6.3. With this equation we can fit the charge transition as a function of the magnetic field (black curve).

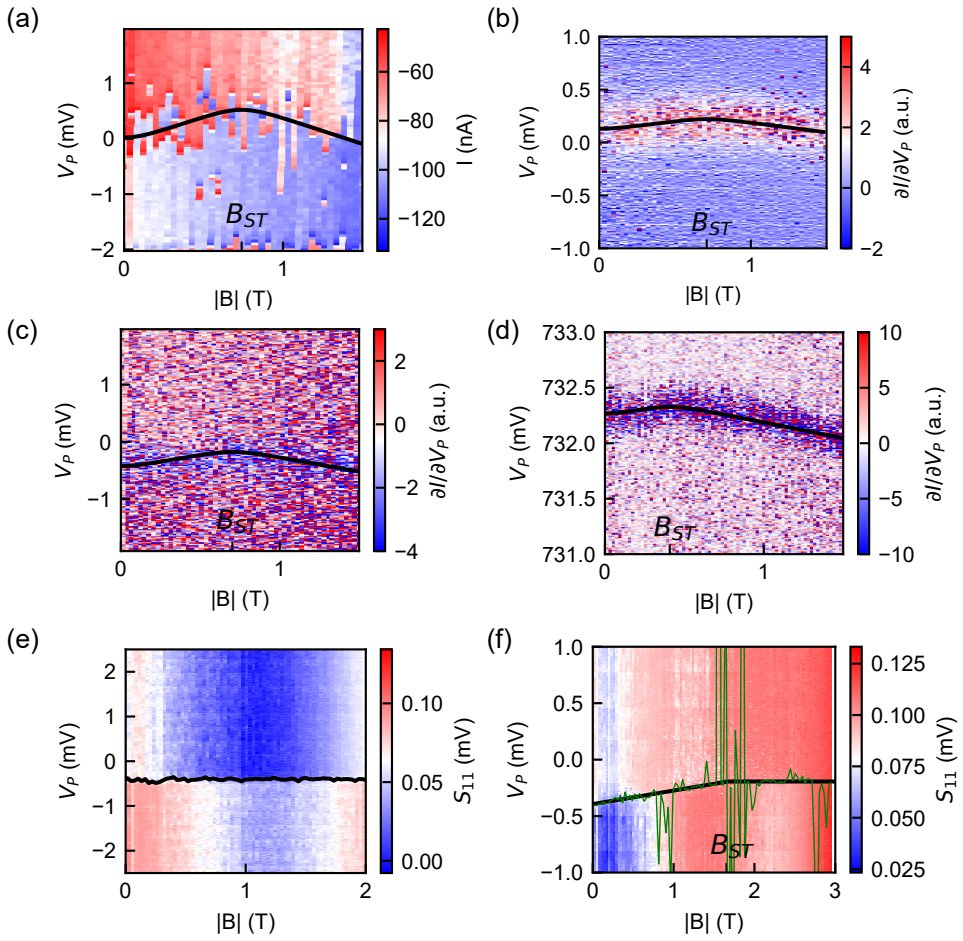

Figure 6.11: Magnetospectroscopy of quantum dots fabricated on quantum well B. V_P is the gate voltage applied to the plunger gate forming the quantum dot. For clarity, we subtract from V_P in panels (a), (b) (c), (e), and (f) an offset that depends is on the quantum dot being measured. (a) - (d) Magnetospectroscopy data measured along the $N = 1 \rightarrow 2$ transition of four different quantum dots on two different samples in quantum well B. The signal is measured by monitoring (a), the current I through a nearby charge sensor, or (b) - (d) by monitoring the derivative of the current $\frac{\partial I}{\partial V}$ through a nearby charge sensor. (a) - (d), To extract the inflection point of the electron charge transition, we fit the signal of the detuning for every magnetic field to eq. (2) from Ref. [205]. The inflection points then are used as input of eq. 6.3. With this equation we can fit the charge transition as a function of the magnetic field (black curve). (e) - (f) Magnetospectroscopy data measured along the $N = (1,1) \rightarrow (2,0)$ transition of eight different quantum dots on two different samples in quantum well B. The signal is measured by monitoring the reflected amplitude of the rf readout signal through a nearby charge sensor. To extract the inflection point of the electron charge transition, we fit the signal of the detuning for every magnetic field to eq. (2) from Ref. [205]. Here we superimpose the inflection points as green curves, to help the reader to follow the charge transitions. To extract B_{ST} we use the crossing point of two linear fits (black solid lines) along the T_- and S_0-state. On top of these samples there is a micromagnet lowering the magnetic field strength at the center of the sample by up to 0.2 T corresponding to 23 μeV which is taken as a lower bound for measurable E_{ST}.

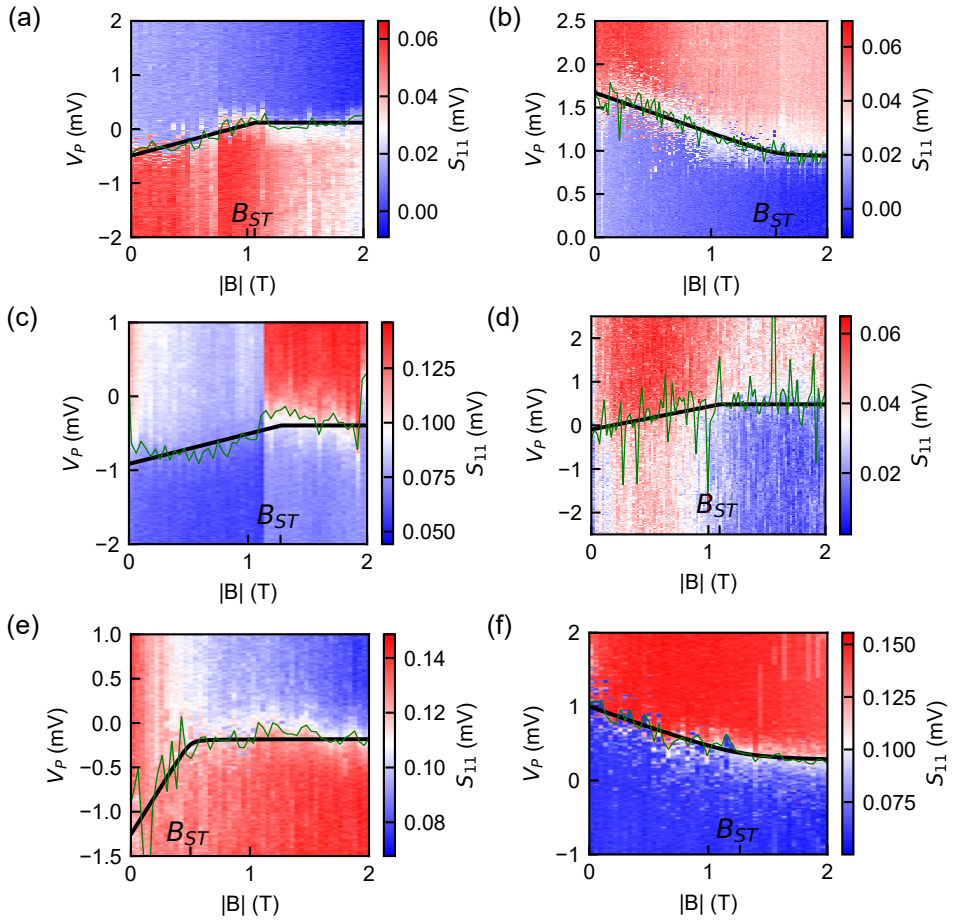

Figure 6.12: Magnetospectroscopy of quantum dots fabricated on quantum well B. V_P is the gate voltage applied to the plunger gate forming the quantum dot. For clarity, we subtract from V_P in panels (a) - (f) an offset that depends is on the quantum dot being measured. (a) - (f) Magnetospectroscopy data measured along the $N = (1,1) \rightarrow (2,0)$ transition of six different quantum dots on one sample in quantum well B. The signal is measured by monitoring the reflected amplitude of the rf readout signal through a nearby charge sensor. To extract the inflection point of the electron charge transition, we fit the signal of the detuning for every magnetic field to eq. (2) from Ref. [205]. Here we superimpose the inflection points as green curves, to help the reader to follow the charge transitions. To extract B_{ST} we use the crossing point of two linear fits (black solid lines) along the T_- and S_0-state. On top of these samples there is a micromagnet lowering the magnetic field strength at the center of the sample by up to 0.2 T corresponding to 23 μeV which is taken as a lower bound for measurable E_{ST}.

Stack	Wafer ID	database processing ID	Figure	device ID	transition	B_{ST} (T)	E_{ST} μeV	d_p (nm)
QW A	QT428	DEMO 13	6.9(a)	D1 2-dot, P2	(0,1) → (0,2)	1.11	129±1.1	50
QW A	QT428	DEMO 13	6.9(b)	D1 2-dot, P1	(0,1) → (0,2)	0.42	49.4±2.2	50
QW A	QT428	DEMO 21	6.9(c)	D2 2-dot, P1	(0,1) → (0,2)	0.83	96.6±6.3	50
QW A	QT428	DEMO 21	6.9(d)	D2 2-dot, P2	(0,1) → (0,2)	1.47	170.4±9.0	50
QW A	QT428	DEMO 15	6.9(e)	D3 2-dot, P1	(0,1) → (0,2)	1.52	176.3±13.4	50
QW A	QT428	DEMO 15	6.1(f),	D3 2-dot, P2	(0,1) → (0,2)	1.57	182.3±5.8	50
QW A	QT539	SQ19-193-1-3-03	6.10(a)	D4 2-dot, P1	(0,1) → (0,2)	0.31	35.7±5.9	50
QW A	QT539	SQ19-193-1-3-03	6.10(b)	D4 2-dot, P2	(0,1) → (0,2)	0.45	52.6±0.8	50
QW A	QT539	SQ19-193-1-3-04	6.10(c)	D5 2-dot, P1	(0,1) → (0,2)	0.9	104±1.6	50
QW A	QT539	SQ19-193-1-3-04	6.10(d)	D5 2-dot, P2	(0,1) → (0,2)	0.69	79.6±2.0	50
QW B	QT592	SQ20-20-5-25-2	6.11(a)	D1 5-dot, P4	(0,1) → (0,2)	0.74	85.7±2.0	40
QW B	QT592	SQ20-20-5-25-2	6.11(b)	D1 5-dot, P1	(0,1) → (0,2)	0.71	82.1±3.7	40
QW B	QT592	SQ20-20-5-25-2	6.11(c)	D1 5-dot, P2	(0,1) → (0,2)	0.7	81.7±10.1	40
QW B	QT553	SQ19-228-2-44-2	6.11(d)	D6 2-dot, P2	(0,1) → (0,2)	0.41	47.2±3.68	50
QW B	QT592	SQ20-20-5-18-4	6.11(e)	D1 6-dot, P3	(1,1) → (0,2)	0	0±0	50
QW B	QT592	SQ20-20-5-18-4	6.11(f)	D1 6-dot, P4	(1,1) → (0,2)	1.73	191.5±13.2	50
QW B	QT637	SQ20-205-2-12	6.12(a)	D2 6-dot, P1	(1,1) → (0,2)	1.06	123.1±8.9	40
QW B	QT637	SQ20-205-2-12	6.12(b)	D2 6-dot, P2	(1,1) → (0,2)	1.56	180.5±9.7	40
QW B	QT637	SQ20-205-2-12	6.12(c)	D2 6-dot, P3	(1,1) → (0,2)	1.1	126.8±33.6	40
QW B	QT637	SQ20-205-2-12	6.12(d)	D2 6-dot, P4	(1,1) → (0,2)	1.27	147.3±15.7	40
QW B	QT637	SQ20-205-2-12	6.12(e)	D2 6-dot, P5	(1,1) → (0,2)	0.5	57.9±13.5	40
QW B	QT637	SQ20-205-2-12	6.12(f)	D2 6-dot, P6	(1,1) → (0,2)	1.25	144.6±19.1	40

Table 6.1: Summary of quantum dot valley splitting measurements. Among all devices measured, in one case (data point $E_{ST} = 0$ μeV) we did not observe in magnetospectroscopy the signature kink associated with valley splitting. This indicates a very small valley splitting, below the lower bound of about 23 μeV set by our experimental measurement conditions. While very small valley splitting values are within the predicted theoretical distributions in the main text, previous theories [180] suggest that they could also originate from the presence of an atomic step within the quantum dot.

6.8.2. MATERIAL CHARACTERIZATION

A. ATOM PROBE TOMOGRAPHY ANALYSIS OF INTERFACES

Atom Probe analysis (APT) of the interfaces is done in 5 steps. All of them explained in detail below. First, the entire measurement is reconstructed using the standard reconstruction algorithms [188]. Second, a cube approximately representing the size of an electrically defined quantum dot in the x,y-plane and comfortably comprising the entire quantum well in the z-direction/depth-direction is extracted from the reconstructed data. This is done to have comparable sizes for each measurement, to limit the known reconstruction artefacts of APT [189] and to enable a direct comparison to simulations in step 5. Third, the three-dimensional point cloud created in the usual APT reconstruction [188] is tessellated using a Voronoi tessellation [195, 196]. The Voronoi tessellation is used for all subsequent steps. It can be viewed as a smoothing operation that "spreads out" the detected ions/atoms to a finite volume rather than representing them as zero-dimensional points. Forth, a x,y-grid is defined on the cube and for each cell of the grid a profile based on the Voronoi tessellation along the z-axis is created that is than fitted with a sigmoid

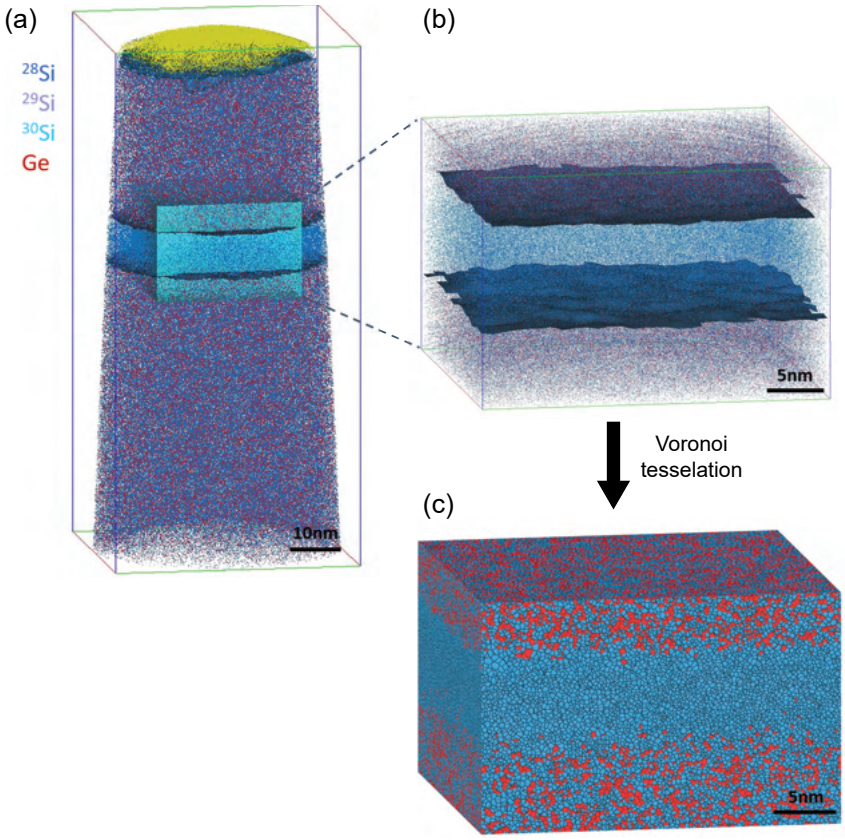

Figure 6.13: Visualization of the extraction of the cube (b) from the full data set (a) and Voronoi tessellation of the cube (c).

function. The collection of sigmoid functions is then used to represent the interface and calculate the interface positions as well as the isoconcentration surfaces. Fifth, the profile extracted from the Voronoi grid of the entire cube is used to create a model structure with the known crystal structure of SiGe and a pseudo-random distribution of Si and Ge atoms in the x-y plane, enforcing the same profile along the depths direction as given by the Voronoi grid and the same percentage of atoms in the volume as expected from the detection efficiency of the Atom Probe (here: 80 % detection efficiency of the LEAP 5000XS). These model structures interface are then compared to the measurement results. All data treatment is done in Python 3.9 using numpy 1.20.3 and scipy 1.6.3.

B. EXTRACTION OF THE CUBES AND VORONOI TESSELLATION

The cubes are manually extracted from the reconstructed volume as exemplary shown in Fig. 6.13 (a)-(b)). After a cube containing the quantum well with the approximate size of an electrically defined quantum dot (~ 30x30x20 nm) is extracted a Voronoi tessellation is performed on the point cloud representing APT data inside the cube. A result of such a tessellation in exemplary shown in Fig. 6.13 (c)).

C. CONSTRUCTION OF THE INTERFACE

Interfaces are constructed based on the Voronoi tessellated data sets. The process is depicted in Fig. 6.14. A grid is created in the x,y-plane of the tessellated data set (Fig. 6.14 (a)-(b)). For each cell of the grid a one-dimensional profile along the z-axis is generated using the tessellation. As opposed to "regular" APT data [188] where profiles are created utilizing small bins along the z-axis and concentrations are then calculated from the ions/atoms within the bin (Ref. [206] Chapter 7), the profiles on the tessellated data are created by a set of cutting planes. The process works by cutting the tessellation at each depth and use every ion/atom whose volume is cut as part of the plane and hence have it contribute to the concentration measured within that plane and at that depth.This can be viewed as a smoothing operation that spreads out the detected ions/atoms to a finite volume.

Each x,y-cell (typically 3x3 nm wide spaced 1 nm apart and hence partially overlapping) generates a profile and is then fitted using sigmoid function [192] as shown in Fig. 6.14 (c)). The sigmoid functions are then used to represent the interface in the following way:

- The inflection point of the sigmoid represents the position of the interface in each cell (Fig. 6.14 (d))
- Isoconcentration surfaces (Ref. [206] Chapter 6.3.2) are created by plotting the position where the sigmoid of each cell reaches the respective concentration

Fig. 6.15 and 6.16 show examples of the interface positions maps and isoconcentration surface maps generated in this way for the top and bottom interfaces of a QW A and a QW B sample. Note, that the data can now readily be used to calculate the average roughness and root mean square roughness in the usual way [110].

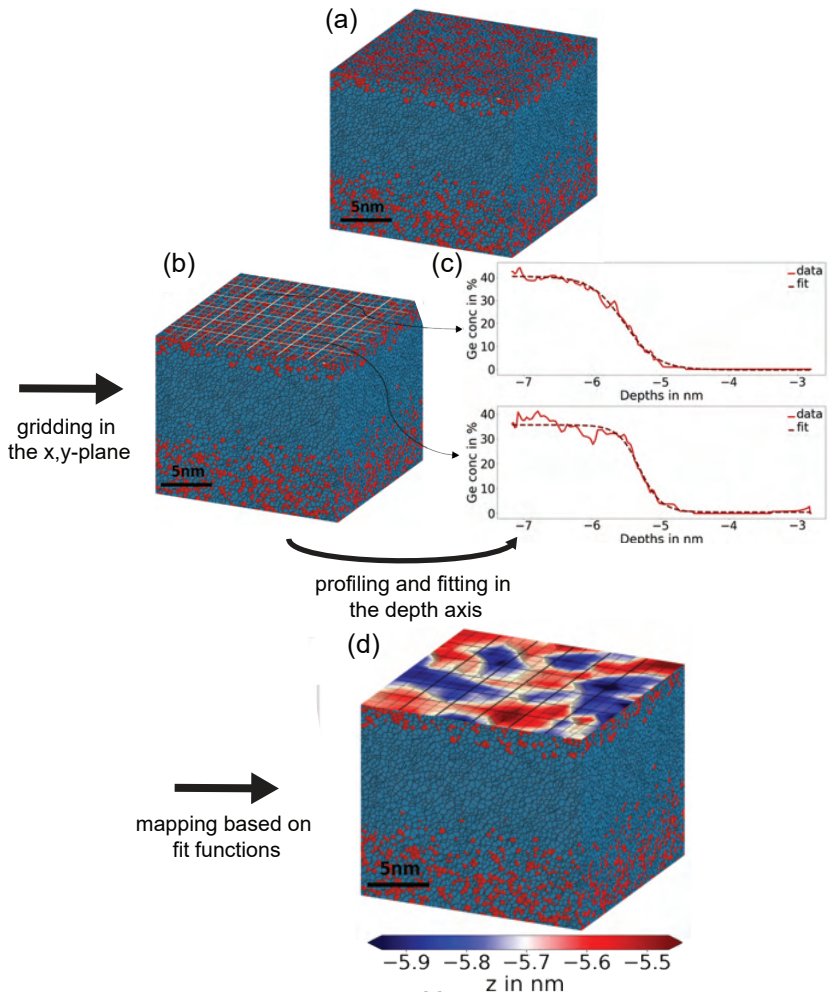

Figure 6.14: Creation of a map from the Voronoi tessellated cube (a) by applying an x,y-grid (b) and fitting of profiles along z-axis with a sigmoid function in each cell (c). The profiles can then be used to calculate the position of e.g. the 25 % Germanium isoconcentration surface (d).

D. GENERATING MODEL DATA

Model data are generated based on the known crystal properties of $Si_{66.5}Ge_{33.5}$. A crystal of the same size as the cubes extracted from the data (~ 30x30x20 nm) is generated digitally and then 20 % of the atoms in the crystal are pseudo-randomly removed to account for the detection efficiency of the LEAP5000XS system used in the APT analysis.

Along the depth axis of the cube the average measured APT profile of the Si and Ge concentration of QW A and QW B as shown in Fig. 6.2(c) is enforced. The result of the generation of such a cube for QW A and the comparison of the depth profile extracted from a cube of QWA and QW B to the average profile of QW A and QW B respectively

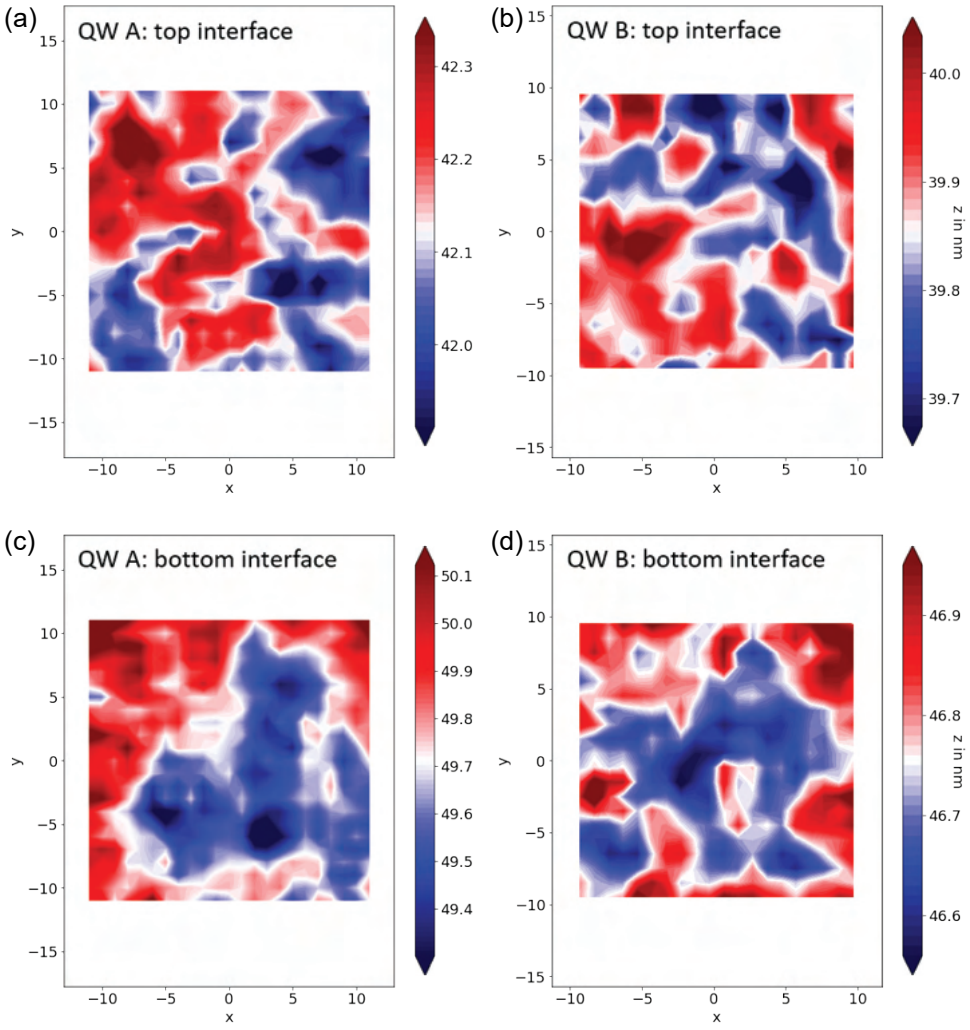

Figure 6.15: Examples of position maps of top ((a), (b)) and bottom ((c), (d)) Germanium interfaces for both Quantum wells A and B. For each cell the depth plotted on the map is extracted from inflection point the sigmoid fit to the profile extracted from the cell (Fig. 6.14 (b)-(c)).

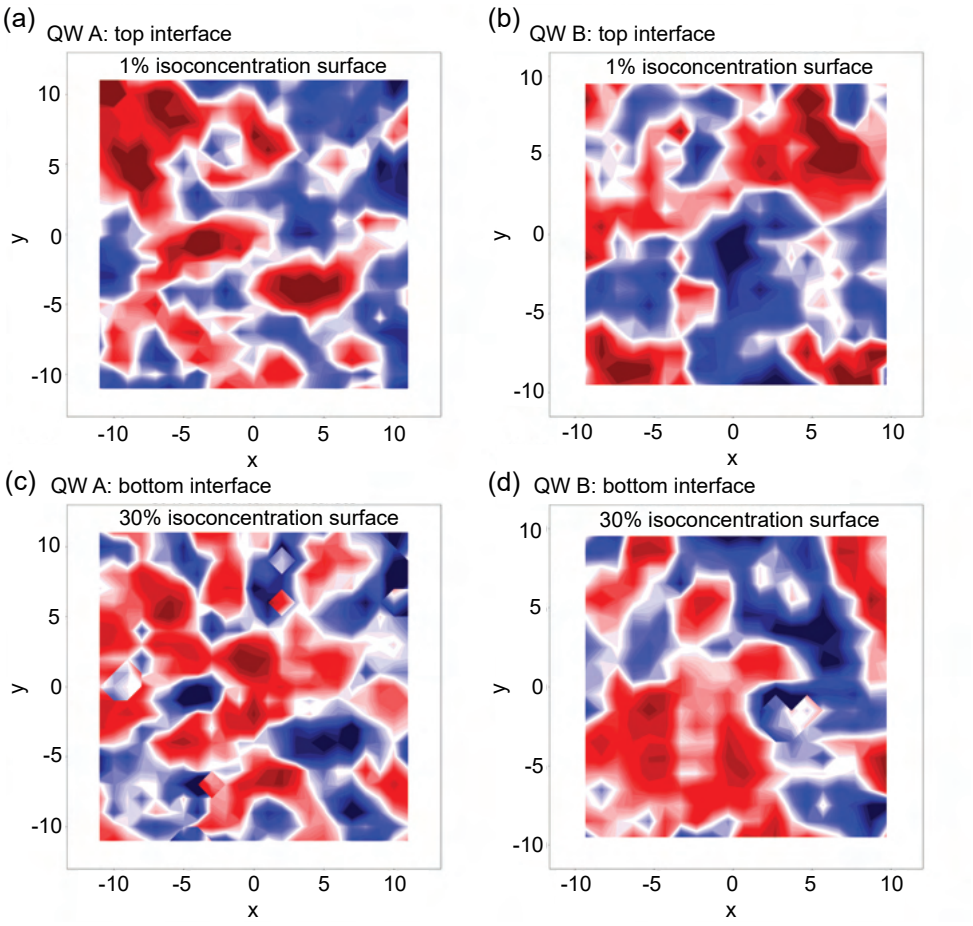

Figure 6.16: Example of Germanium isoconcentration surfaces or the top ((a), (b)) and bottom ((c), (d)) interfaces of both Quantum Wells a and B. The plots reported here show one particular isosurface, 1% in (a), (b) and 30% in c,d. Animated short clips provided as Supplementary Movies in Ref. [42] show the evolution across the interfaces of each isoconcentration surfaces, from 1-30 % Ge. As before the depth for each map can be extracted from the sigmoid fits to the profile in each cell.

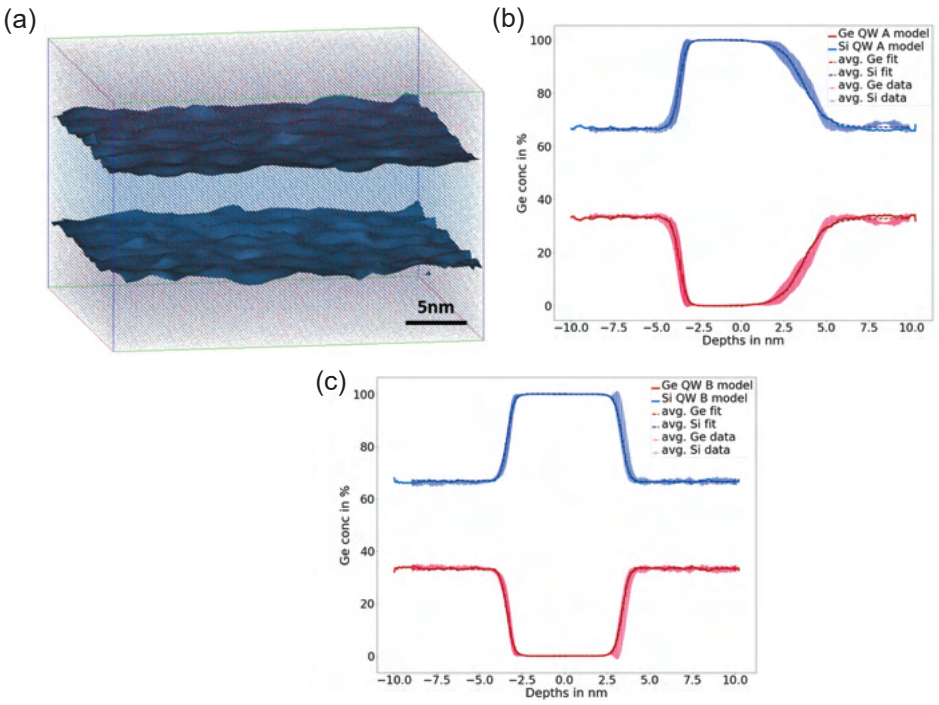

Figure 6.17: Example of a crystalline cube of QW ((a)) and a comparison of the average profiles of the measured quantum wells (see Fig. 6.2(c)) and profiles from a generated cube of Quantum Well A ((b)) and Quantum Well B ((c)).

are shown in Fig. 6.17. In Fig. 6.18 interface position maps of these model structures are shown. They should be compared to Fig. 6.15 where the same maps are extracted from measured data sets. The root mean square roughness as measured from the model is compared to the data measured from the APT data in Fig. 6.2.

Note: there is an animation in the file Supplementary_ Movie_1.m4v in Ref. [42] which shows for the top interface of quantum well B (for increasing Ge concentration) the deviation of each isosurface tile position from the isosurface's average position. There we benchmark the experimental data from our APT analysis (at each frame of the animation) against average and min-max range covered by 100 random models.

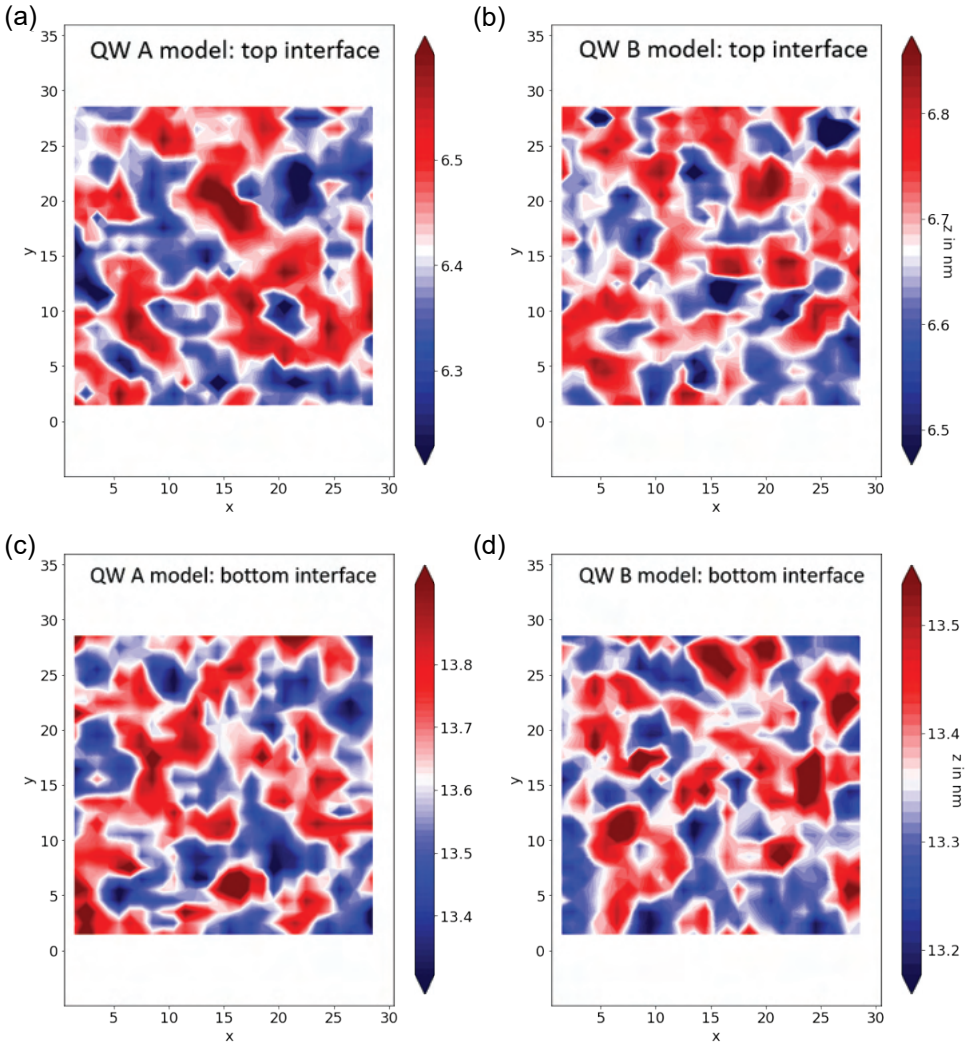

Figure 6.18: Examples of position maps of top ((a), (b)) and bottom ((c), (d)) Germanium interfaces for model data sets of both Quantum wells A and B. As in Fig. 6.15 the depth plotted on the map is extracted from the inflection point of the sigmoid fit for the profile along the depth axis generated in each cell (Fig. 6.14 (b)-(c)).

E. ATOMIC STEPS, QUANTUM WELL WIDTH, AND BOTTOM INTERFACES

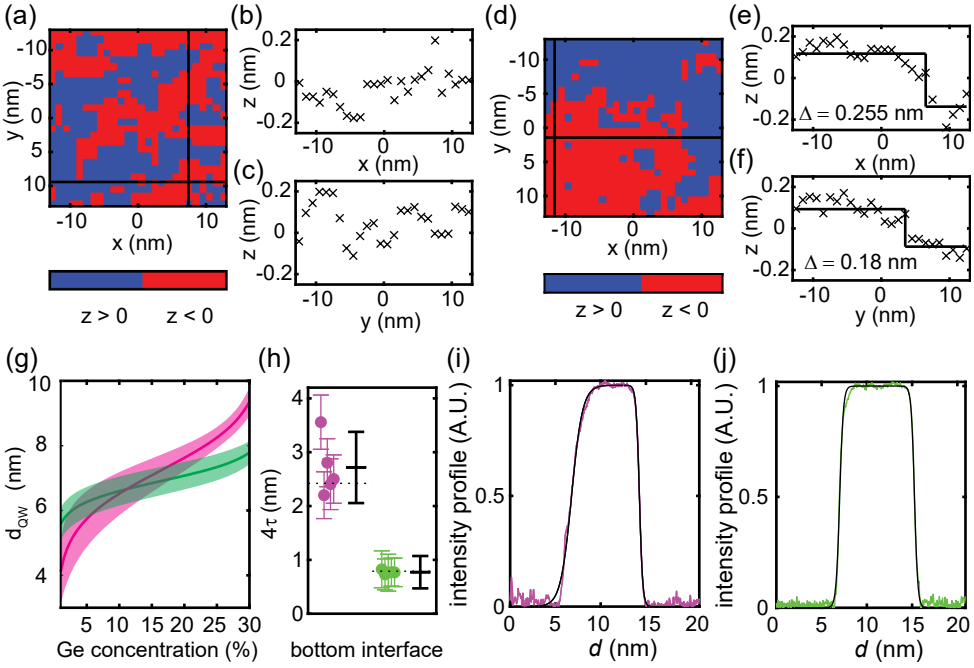

Figure 6.19: (a) 10% isoconcentration surface from a Stack A sample without step. Blue areas are below and red areas above the average height (defined as $z = 0$) of the isoconcentration surface. The black lines are the positions of the line cuts in (b) and (c). (b) line cut along the x direction of the isoconcentration surface. in (a). (c) line cut along the y-direction of the isoconcentration surface. The z-position randomly oscillates around the mean value. (d) 10% isoconcentration surface from a Stack A sample with clear spatial division of the blue and red areas. The black lines are the positions of the line cuts in (e) and (f). (e) line cut along the x-direction of (d). A step with height $\Delta = 0.255$ nm occurs at $x = 7$ nm, corresponding to approximately 2 monoatomic layers. The black line represents the Heavyside step function with the highest C and the step height is determined by taking average z-position of the line cut before and after the step. (f) line cut along the y-direction of (c). A step with $\Delta = 0.18$ nm occurs at $x = 3$ nm, corresponding to approximately 1.5 monoatomic layers. The black line represents the average z-position before and after the step. (g), Average width of quantum well A (magenta line) and B (green line) as a function of the Ge concentration of the isoconcentration surfaces. Shaded areas represent the standard deviation of the quantum wells. (h), Statistical analysis of the bottom 4τ interface widths derived from the fitting the data for quantum well A (magenta) and quantum well B (green). Black crosses are the mean and standard deviation for data from the different APT samples, highlighting the uniformity of the interfaces. (i), (j), HAADF-STEM intensity profile for stack A and B (magenta and green line, respectively) along the heterostructure growth direction (see TEMs in the main section). The black lines are fits of the data in the interface regions, using a sigmoid function.

To evaluate the presence of atomic steps from isoconcentration surfaces, we consider one-dimensional line cuts along the x- and y-axis of an isosurface. If a line cut crosses an atomic step along the isosurface, the line cut should resemble a Heavyside step function H:

$$H(x - x_s) = h_0 + \begin{cases} -a/2, & \text{for } x < x_s. \\ a/2, & \text{for } x \geq x_s. \end{cases} \tag{6.6}$$

where a is the step height, x_s is the step position and the offset h_0. To quantify the resemblance between a line cut and the step function, we determine the correlation coefficient C between the two with:

$$C = \frac{\sum_k (z_k - \bar{z})(h_k - \bar{h})}{\sqrt{\sum_k (z_k - \bar{z})^2}\sqrt{\sum_k (h_k - \bar{h})^2}} \tag{6.7}$$

where z_k are the z-values of the line cut, $\bar{z}$ is the mean value of the line cut, k is the index of the, h_k are the values of the step function, and $\bar{h}$ the mean value of the step function. If $C \geq 0.75$ we consider the linecut to represent a step. We subsequently can determine a by taking the difference between the two plateaux $\Delta = \bar{z}_{k+} - \bar{z}_{k-}$, where $\bar{z}_{k+}$ and $\bar{z}_{k-}$ are the average z-position before and after x_s, respectively.

F. SIMS AND CROSSHATCH PATTERN

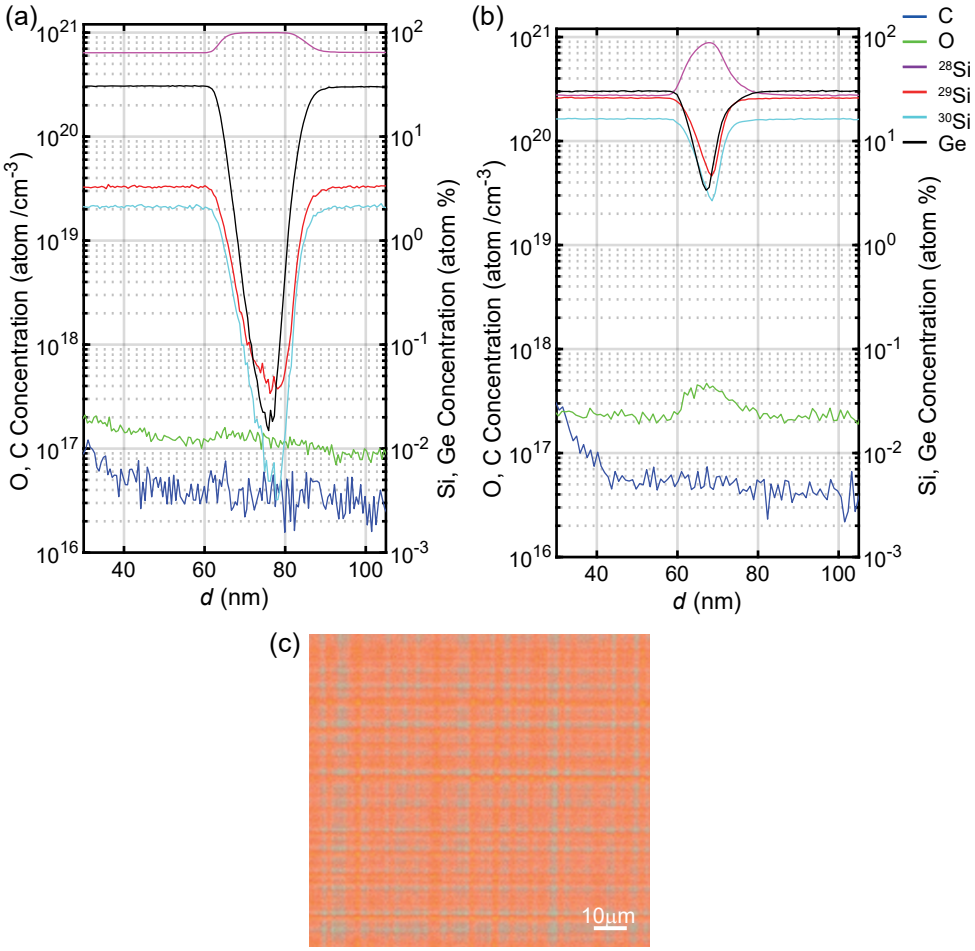

Figure 6.20: (a), (b), Depth concentration SIMS profile of quantum well A and quantum well B respectively. Analyzed elements are ^{28}Si (red), ^{29}Si (blue), ^{30}Si (purple), Ge (black), oxygen (green) and carbon (blue). In quantum well A both carbon and oxygen concentrations are below their respective detection limits of 3×10^{16} cm^{-3} and 1×10^{17} cm^{-3}. In quantum well A only carbon is below the detection limits, while there is a residual oxygen content of 4×10^{17} cm^{-3} in the quantum well. (c) typical cross-hatch pattern from the surface of the wafers.

7

ENGINEERING GE PROFILES IN SI/SIGE HETEROSTRUCTURES FOR INCREASED VALLEY SPLITTING

Electron spin qubits in Si/SiGe quantum wells are limited by the small and variable energy separation of the conduction band valleys. While sharp quantum well interfaces are pursued to increase the valley splitting energy deterministically, here we explore an alternative approach to enhance the valley splitting on average. We grow increasingly thinner quantum wells with broad interfaces to controllably increase the overlap of the electron wave function with Ge atoms. In these quantum wells, comprehensive quantum Hall measurements of two-dimensional electron gases reveal a linear correlation between valley splitting and disorder-induced single-particle energy level broadening, driven by increasing alloy scattering at the Si/SiGe interface. Benchmarked against quantum wells with sharp interfaces, we demonstrate enhanced valley splitting while maintaining a respectable electron mobility, indicating a low-disorder electrostatic potential environment. Simulations using the experimental Ge concentration profiles predict an average valley splitting in quantum dots that matches the enhancement observed in two-dimensional systems. Our results motivate the experimental realization of quantum dot spin qubits in these heterostructures.

This chapter has been published as: **L.E.A. Stehouwer**, M.P. Losert, M. Rigot, D. Degli Esposti, S. Marti-Sánchez, M. Rimbach-Russ, J. Arbiol, M. Friesen, G. Scappucci, "Engineering Ge profiles in Si/SiGe heterostructures for increased valley splitting", Nano Letters, **25**, 34 (2025).

7.1. INTRODUCTION

Spin qubit devices in gate-defined Si/SiGe quantum dots have advanced in performance, qubit count, and connectivity. Reproducible single- and two-qubit gate fidelities exceeding 99% have been achieved [121, 123, 124]. Moreover, linear array devices have scaled the number of qubits from six [37] to twelve [207], and a two-by-two qubit array has been demonstrated [208]. Coherent, high fidelity spin shuttling [209–211] and cavity-mediated iSWAP oscillations between distant spins [212] are promising achievements for connectivity beyond nearest neighbour. In addition, the fabrication of Si/SiGe spin qubits in a 300 mm semiconductor manufacturing facility [34] and the integration of multi-level interconnects with 2D spin qubit arrays [213] underscore the potential for scalable architectures. Despite this compelling progress, critical material challenges remain in the pursuit of a large-scale quantum computer.

In Si/SiGe heterostructures, a long-standing limitation has been the small and variable energy splitting between the two low-lying conduction band valleys [33, 182]. In quantum dots, the reported valley energy splittings vary between tens to hundreds of μeV [56, 162, 169–171, 176, 177, 199], even across a single chip [56, 170, 178, 186, 214]. This poses a challenge for spin qubits, because the increased leakage from the computational two-level Hilbert space affects high-fidelity initialization, control, readout, and shuttling [38, 163, 215–219].

Recent work combining experiments and theory [41, 42, 220] has established that the atomistic random alloy concentration fluctuations at the Si/SiGe interface (alloy disorder) are accountable for the measured valley splitting spread in real quantum dots. Furthermore, the valley splitting is expected to be enhanced when the electronic wavefunction overlaps with more Ge atoms. While proposed strategies like intentionally adding Ge to the Si quantum well promise increased valley splitting [41, 42], they may also worsen the electrostatic disorder, affecting electron mobility [199]. However, careful tuning of the germanium concentration profile–through adjustments in the Si quantum well thickness, interface width, and barrier composition–can strike a delicate balance between achieving high valley splitting and maintaining low disorder [80].

Here, we engineer the Ge concentration profiles of ^{28}Si/^{28}SiGe heterostructures to enhance the overlap of the electron wave function with Ge atoms in a tunable way, by growing increasingly thin quantum wells with intentionally diffused interfaces. We characterize the Ge concentration profiles by atomic-resolution scanning transmission electron microscopy (STEM), while we measure the mobility and device-averaged valley splitting energy of the two-dimensional electron gas (E_{v}) by comprehensive density-dependent magnetotransport. Benchmarking against control heterostructures with sharp interfaces [80], we can controllably increase valley splitting by up to a factor of two. Although we unambiguously observe that higher valley splitting correlates with increased alloy disorder scattering, a beneficial trade-off is achievable between enhanced valley splitting and respectable electron mobility, indicative of low electrostatic disorder. Furthermore, simulations of sample-averaged quantum dot valley splitting energy ($E_{\mathrm{v}}^{\mathrm{QD}}$) based on the experimental Ge concentration profiles, reveal a linear relationship with E_{v}. This finding provides a first insight into the long-sought connection between valley splitting in the quantum Hall regime and in quantum dots.

7.2. RESULTS AND DISCUSSION

Figures 7.1(a)-(c) show atomic-resolution high angle annular dark field (HAADF) STEM images of three ^{28}Si/^{28}SiGe heterostructures (B1–B3) having progressively thinner quantum wells with similarly broad interfaces. As a control, Fig. 7.1(d) shows ^{28}Si/SiGe heterostructure (A), with sharp interfaces as studied in [80]. Broad interfaces in heterostructures B1–B3 result from uninterrupted epitaxy at a temperature of 750 °C using only hydride precursors ($^{28}SiH_4$, GeH_4). In contrast, sharp interfaces in heterostructure A are achieved by growing the SiGe barriers at a lower temperature of 625 °C, enabled by using a different Si precursor (SiH_2Cl_2) [42, 80].

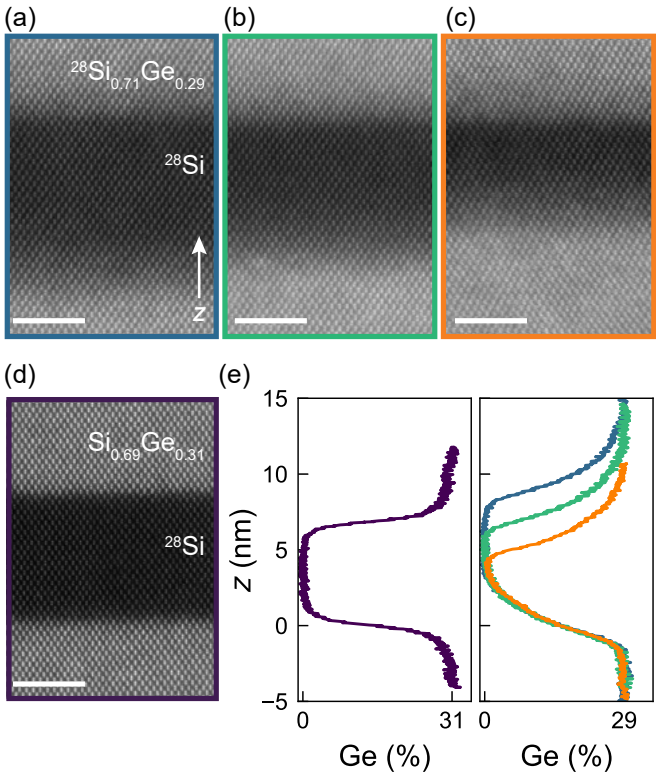

Figure 7.1: **^{28}Si/SiGe heterostructures with engineered Ge concentration profiles.** (a)-(c) HAADF-STEM images of ^{28}Si/SiGe heterostructures B1 (blue), B2 (green), and B3 (orange), with intentionally diffused quantum well interfaces. The characterisation is performed after H-FET fabrication. The quantum well and surrounding barriers feature isotopically purified ^{28}Si. We vary the quantum well width between B1–B3 from 9.5 to 5.9 nm (see also table 7.1). (d) HAADF-STEM image of control heterostructure A (purple) with sharp interfaces. Only the quantum well is isotopically purified. Scale bar is 3 nm in (a)–(d). (e) Ge concentration profiles for heterostructure A (left panel) and B1–B3 (right panel) extracted by combining SIMS data with HAADF-STEM intensity profiles (see Fig. 7.5 in the Supporting Information).

In all heterostructures, the quantum well is deposited on a SiGe strain-relaxed buffer and is separated from the dielectric interface by a 30 nm SiGe barrier (see Section 7.4.1 in the Supporting Information). Due to the different gas precursors, heterostructures

Table 7.1: **Overview of quantum well metrics.** Quantum well width w_{QW}, top interface width w_{if}^{top}, and bottom interface width w_{if}^{bottom} for heterostructures A, B1, B2, and B3 are given. The quantum well width is defined as the distance between top and bottom interface where the Ge concentration reaches 50% of its maximum value. The width of top and bottom interfaces is defined as the distance over which the Ge concentration rises from 10% to 90% of its maximum value. Uncertainty of the extracted values is assumed to be in the last reported digit. Extracted values are from heterostructures after H-FET fabrication.

	A	B1	B2	B3
w_{QW} (nm)	6.9	9.5	7.8	5.9
w_{if}^{top} (nm)	1.5	3.7	3.7	3.6
w_{if}^{bottom} (nm)	1.6	3.3	3.5	3.5

B1–B3 feature an isotopically-enriched barrier with a slightly lower Ge concentration ($^{28}Si_{0.71}Ge_{0.29}$) compared to heterostructure A ($Si_{0.69}Ge_{0.31}$). The small difference in chemical composition, and therefore band offset, is confirmed by electrical measurements of the quantum well saturation charge density [75, 106], which is smaller in B1–B3 compared to A (see Fig. 7.5 in the Supporting Information). In Fig. 7.1(e) we show the Ge concentration profiles from A (left panel) and B1–B3 (right panel) extracted from the HAADF-STEM images (see Fig. 7.5 in the Supporting Information). The right panel highlights both the reproducibility of the growth process from the overlapping bottom interfaces ($z = 0$ nm) as well as the control over the quantum well width. From the concentration profiles, we extract the quantum well width w_{QW} and the width w_{if} of the top and bottom interfaces. Table 7.1 gives a quantitative overview of the extracted parameters. We controllably reduce the quantum well width between the heterostructures B1–B3 by adjusting the quantum well growth time. Notably, the interfaces of heterostructures B1–B3 are approximately 2.4 times wider than those of heterostructure A.

We evaluate the electrical properties of the two-dimensional electron gas (2DEG) in each heterostructure by fabricating Hall-bar-shaped heterostructure field effect transistors (H-FETs) and performing magnetotransport measurements at 70 mK in a dilution refrigerator equipped with a cryo-multiplexer [79] (see Section 7.4.4 in the Supporting Information). Figures 7.2(a),(b) show the mobility-density and conductivity-density curves of a representative H-FET for each heterostructure (see Fig. 7.6 in the Supporting Information for other H-FETs). Heterostructures A, B1, and B2 show similar mobility-density curves, while heterostructure B3 shows a severe suppression of the mobility across the entire density range. In Fig. 7.2(c) we show the average extracted mobility for each heterostructure. Maximum mobility decreases from $3.8(4) \times 10^5$ cm^2/Vs in B1 to 0.58×10^5 cm^2/Vs in B3 as the quantum well becomes increasingly thinner. Compared to the control heterostructure A, B1 shows a higher average maximum mobility which we attribute to the increased growth temperature resulting in decreased background contamination. However, B1 also shows a larger spread across multiple H-FETs which is indicative of the onset of strain relaxation within the quantum well, creating additional scattering centres from dislocations [56, 80]. The severe reduction of maximum mobility in B3 is compatible with the presence of Ge throughout the thin quantum well. [103, 113, 221].

In contrast to the observed trend in maximum mobility, we do not observe a strong de-

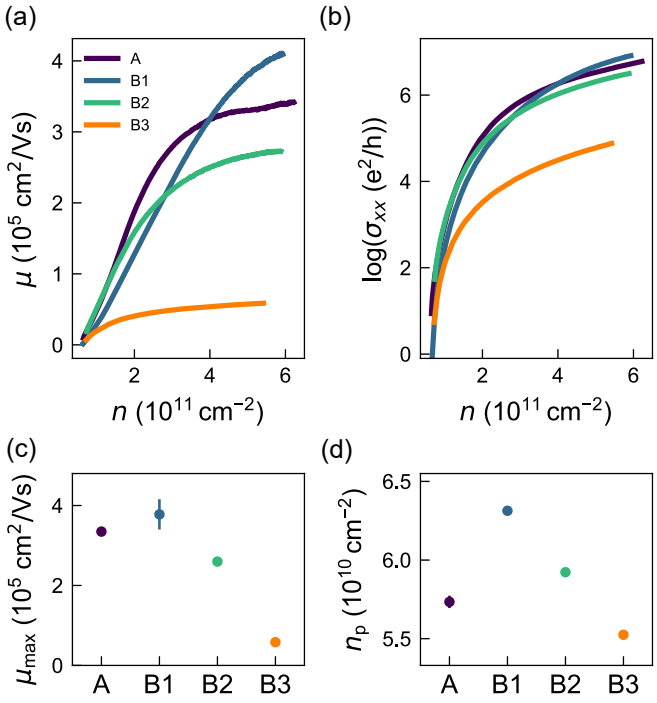

Figure 7.2: **Classical transport measurements of disorder.** (a) Mobility (μ)-density (n) curves for heterostructures A, B1, B2, and B3. (b) Conductivity (σ_{xx})-density (n) curves of the four heterostructures, from which we fit the percolation density n_p (see Section 7.4.4 in the Supporting Information). (c) Average maximum mobility μ_{max} four the four heterostructures (A1, B1–B3) from measurements of multiple devices. Error bars represent one standard deviation around the average. (d) Extracted percolation densities n_p for the four heterostructures.

pendence across different heterostructures of the percolation density n_p (Fig. 7.2(d)), obtained by fitting the conductivity curves in Fig. 7.2(b) (see Section 7.4.4 in the Supporting Information). We find similar low values of around 6.0×10^{10} cm^{-2} for all heterostructures within the constraints of the fitting procedure, which is consistent with previous arguments that alloy disorder only weakly affects the scattering rate at low density [103, 113, 221]. This observation suggests that the increased alloy disorder from the diffusion of the interfaces does not severely affect the disorder properties of the 2DEG in the low-density regime, which is relevant for quantum dots.

After assessing the electrical properties of the heterostructures, we probe valley splitting in the same H-FETs by performing activation energy measurements in the quantum Hall regime, following Ref. [202]. We focus on the first valley-split energy gap (Δ_1) at filling factor $\nu = 1$, since this gap is resolved across all heterostructures over a similar range of density n and magnetic field B, enabling meaningful comparisons. Additionally, we measure the first Zeeman-split gap (Δ_2), and first Landau gap (Δ_4), corresponding to $\nu = 2$, and $\nu = 4$, respectively. Figure 7.3 illustrates the measurement protocol with data from heterostructure B2, while measurements from all other heterostructures are shown in Figs. 7.7–7.9 in the Supporting Information. First, we measure the longitudinal

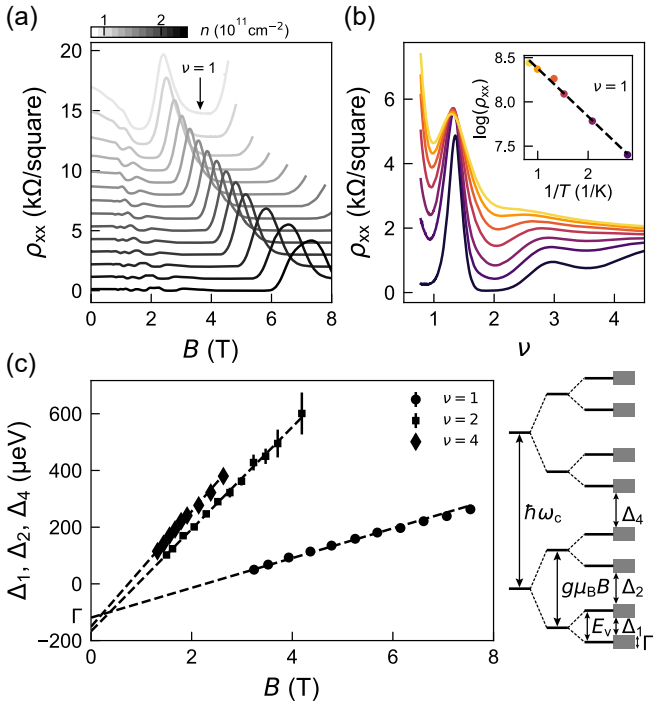

Figure 7.3: **Quantum transport measurements of valley splitting.** (a) Longitudinal resistivity ρ_{xx} of heterostructure B2 as a function of magnetic field B over a range of fixed densities n between 0.77×10^{11} cm^{-2} (light grey) and 2.46×10^{11} cm^{-2} (black) (offset for clarity). (b) Magnetotransport measurements at fixed density n (here 0.91×10^{11} cm^{-2}) and at different temperatures T, plotted against integer filling factor $\nu = nh/eB$. Different colours represent different temperatures between 70 (dark purple) and 1000 mK (yellow). The inset shows the thermally activated dependence of the oscillation minima ($\rho_{xx} \propto \exp\{(-\Delta/2k_B T)\}$) for integer filling factor $\nu = 1$ from which we extract the mobility gap Δ_1 of the first valley. These measurements are repeated for each density and the analysis for $\nu = 1, 2, 4$. (c) Mobility gaps of the first valley gap Δ_1 ($\nu = 1$), the first Zeeman gap Δ_2 ($\nu = 2$), and the first Landau gap Δ_4 ($\nu = 4$) as function of magnetic field B. The linear fits (dotted lines) are used for extracting the Landau level broadening induced disorder Γ. The side schematic shows the energy level ladder in the quantum Hall regime, including the disorder broadening Γ. Landau levels are split by energy $\hbar\omega_c$, the Zeeman levels by $g\mu_B B$, and valley levels by the valley splitting energy E_v.

resistivity ρ_{xx} at base temperature as a function of B, over a range of fixed densities n (Fig. 7.3(a)). We observe clear Shubnikov de Haas oscillations, with minima at $\nu = 1$ reaching zero, indicating a well resolved Δ_1. For each n, we repeat the measurement for different temperatures ($T = 70 - 1000$ mK) and plot in Fig. 7.3(b) ρ_{xx} as a function of filling factor ν, given by the quantum Hall relation $\nu = nh/eB$, where h is the Planck's constant and e the electron charge. As the inset shows for $\nu = 1$, we observe a thermally activated dependence of the oscillation minima ($\rho_{xx} \propto \exp\{-\Delta/2k_B T\}$). For each density, we extract the valley-split, Zeeman split and Landau mobility gaps (Δ_1, Δ_2, Δ_4 respectively), plotted in Fig. 7.3(c) as a function of magnetic field B. As in Ref. [202] , we observe striking linear relationships converging to a similar intercept, from which we estimate with confidence the disorder-induced single-particle energy level broadening [119] Γ

(Fig. 7.3(c), side panel) and the valley splitting $E_v = \Delta_1 + \Gamma$.

Following this systematic classical and quantum transport characterization, we may now investigate the key link between valley splitting and disorder, underpinned by the engineered Ge concentration profiles in the different heterostructures. In all heterostructures, E_v increases linearly with B across the investigated range (Fig. 7.4(a)). Additionally, to access the electrostatic confinement induced by the magnetic field B, the top x-axis shows the correspondingly increasing orbital energy, $E_{orb} = e\hbar B/2m^*$, where we use an in-plane effective mass of $0.2m_e$ for electrons in Si. Note that the $E_v \propto B$ relation was previously observed [202, 222] and attributed [202] to the stronger electrostatic confinement achieved for a higher density in the quantum Hall edge channel, driven by B via the quantum Hall relation $n = eB/h$ for $\nu = 1$.

Across the explored magnetic field range, we observe a clear trend in Fig. 7.4(a): all heterostructures with broad interfaces (B1–B3) show larger valley splitting compared to the control heterostructure A. Moreover, within heterostructures B1–B3, thinner quantum wells achieve larger valley splitting, validating our heterostructure design. To quantify these observations, we extract the valley g-factor, $g_v = (1/\mu_B)(dE_v/dB)$, which represents the rate of change of valley splitting with magnetic field, normalized to the Bohr magneton μ_B. Figure 7.4(b) shows g_v against Γ, revealing a striking experimental correlation, driven by the increased scattering from alloy disorder. This is further corroborated in Figure 7.4(c) by the dependence of g_v against the maximum mobility. The valley splitting in heterostructures B1–B3 may increase to more than twice the value observed in the control heterostructure A. These clear trends confirm the intuition that increasing valley splitting, which requires breaking translation symmetry, comes at the expense of a more disordered potential landscape [41, 80], qualified in our experiments either by classical or quantum transport measurements.

Next, we investigate the atomistic origin of the increased valley splitting E_v and provide a prognosis for potential gains for valley splitting in quantum dots. To this end, we calculate for each heterostructure the parameter η_1 (see Section 7.4.5 in the Supporting Information), which quantifies the overlap of the electron wave function with Ge atoms, and simulate the quantum dot valley splitting distributions and their mean value E_v^{QD} (see Fig. 7.10 in the Supporting Information). We use the extracted Ge concentration profiles of Fig. 7.1(e) as an experimental input for the simulation methods in Ref. [41] . As Fig. 7.4(d) shows, we find an unambiguous correlation between g_v and η_1, suggesting that the larger E_v measured in the 2DEG correlates with increased overlap of the electron wave function with Ge atoms, promoted in our experiments by thinner quantum wells with broad interfaces. This finding ($E_v \propto \eta_1$) mirrors the theoretical predictions for average valley splitting in alloy disorder-dominated quantum dots ($E_v^{QD} \propto \eta_1$) (see Section 7.4.5 in the Supporting Information and Refs.[41, 42]). As a consequence, the plot in Fig. 7.4(e) of simulated E_v^{QD} against experimentally measured E_v shows also a linear relationship. Here, we choose to simulate E_v^{QD} at an orbital energy E_{orb} of 1.88 meV, which is on par with measured values in quantum dots and corresponds to an experimentally accessible magnetic field of 6.5 T for the evaluation of E_v, as shown in from Fig. 7.4(a). Considering the same orbital energy ensures a meaningful comparison between the experimentally-informed simulation of E_v^{QD} and the measured E_v, although we note that confinement in qubit experiments is imposed electrostatically via top gates, while magnetic fields are

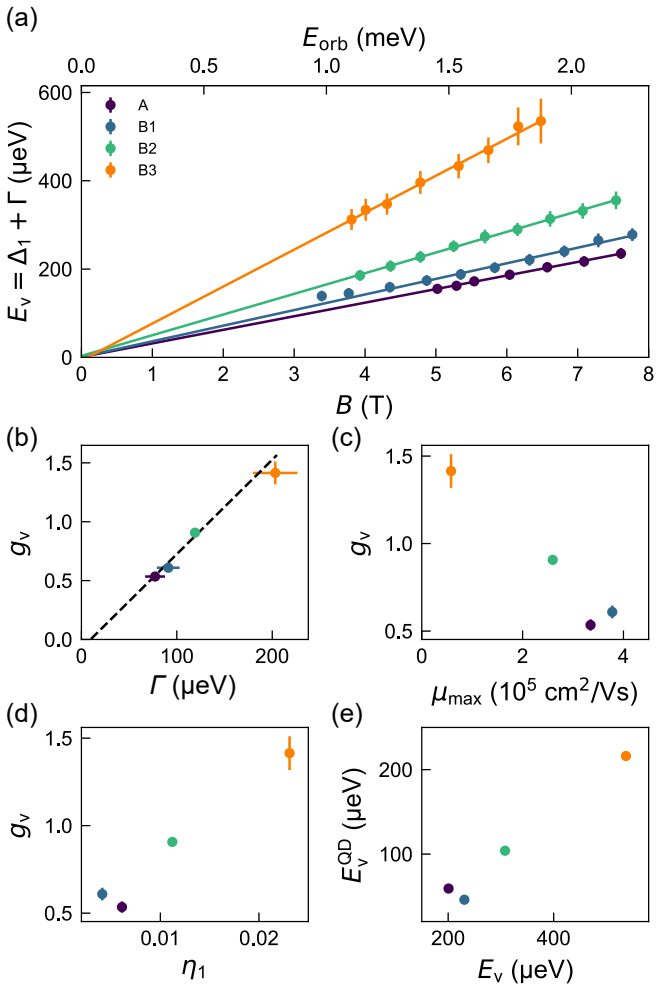

Figure 7.4: **Valley splitting correlations** (a) Valley splitting energy $E_v = \Delta_1 + \Gamma$ as a function of magnetic field B for heterostructures A, B1–B3. The corresponding orbital energy E_{orb} is shown in the top x-axis. (b) Valley g-factor g_v, from the slopes of E_v versus magnetic field B in (a), as a function of corresponding Landau level broadening-induced disorder Γ. Colour coding as in (a). (c) g_v as a function of maximum mobility μ_{max}. Colour coding as in (a). (d) g_v as a function of η_1, the overlap of the electron wave function with Ge atoms simulated using the Ge concentration profiles from Fig. 7.1(e). (d) Simulated valley splitting energy in quantum dots E_v^{QD} against the two-dimensional electron gas valley splitting E_v from Fig. 7.4(a) evaluated at a magnetic field B of 6.5 T. This magnetic field corresponds to an orbital energy of 1.88 meV (see main text), which is the same orbital energy used for the simulation of E_v^{QD}.

typically applied in-plane. While offering a first insight into the relation between the two metrics, based on these results we predict that heterostructures B1–B3 could support on average increased valley splitting in quantum dots, which is proxied by valley splitting measured in the quantum Hall regime.

7.3. CONCLUSIONS

In summary, we have engineered ^{28}Si/^{28}SiGe heterostructures to enhance the overlap of the electron wave function with germanium atoms, by growing increasingly thin quantum wells with intentionally diffused interfaces. Our comprehensive study unveils unambiguously a correlation between disorder in the two-dimensional electron gas, driven by random alloy scattering and measured with classical and quantum transport, and valley splitting, measured in the quantum Hall regime. Valley splitting is increased but so is alloy disorder. Based on simulations that take into account the experimental Ge concentration profile, we identify the overlap of the electron wavefunction with Ge atoms as the likely cause of this connection, which also propagates to calculated average values of valley splitting distributions in quantum dots.

Compared to control samples with sharp interfaces in Ref. [80], we show that a quantum well with much broader interfaces (≃3.6 nm) and similar width (≃ 7.8 nm) offers an excellent trade-off, featuring a 1.8× valley splitting increase, whilst still having respectable mobility ($> 2 \times 10^5$ cm^2/Vs) and low percolation density ($< 6 \times 10^{10}$ cm^{-2}). In contrast, thinner or thicker quantum wells either significantly degrade mobility or yield only marginal improvements in valley splitting. Future statistical studies of valley splitting in quantum dots fabricated on these new generations of heterostructures are required to confirm the valley splitting increase and assess the impact of alloy disorder in the formation of spurious quantum dots.

7.4. SUPPLEMENTARY

7.4.1. HETEROSTRUCTURE GROWTH

We grow the Si/SiGe heterostructures in an ASM Epsilon 2000 reduced pressure chemical vapour deposition reactor (RP-CVD). Each heterostructure is grown on a 100 mm n-type Si(001) wafers and begins with a step graded $Si_{1-x}Ge_x$ virtual substrate (VS) grown at 750 °C where the Ge content is graded to a final percentage of 31% in four steps ($x = 0.07, 0.14, 0.21, 0.31$). For heterostructure A, we subsequently lower the growth temperature to 625 °C to grow a $Si_{0.69}Ge_{0.31}$ strain-relaxed buffer (SRB) using dichlorosilane and germane as precursor gases. We then grow the isotopically purified ^{28}Si quantum well (800 ppm residual ^{29}Si isotopes [64, 121, 193]) using silane at a temperature of 750 °C, followed by a 30 nm thick $Si_{0.69}Ge_{0.31}$ spacer layer using the same growth conditions as the SRB. Finally, we grow a thin ^{28}Si capping layer using silane at a temperature of 750 °C.

For heterostructures B1-B3 we use use the same step graded VS as in A but subsequently continue the growth of the $^{28}Si_{0.71}Ge_{0.29}$ SRB, the ^{28}Si quantum well, the 30 nm $^{28}Si_{0.71}Ge_{0.29}$ spacer, and ^{28}Si capping layer at a growth temperature of 750 °C using silane and germane as precursor gases.

For the fabrication of the Hall bars we use the identical procedure as described in the Methods section of Ref. [80] .

7.4.2. (S)TEM

For structural characterization with (S)TEM, we prepared lamella cross-sections of the quantum well heterostructures by using a Focused Ion Beam (Helios 5UX). Atomically resolved HAADF-STEM data was acquired in a double-corrected Thermo Fisher Spectra 300 microscope operated at 300 kV.

7.4.3. ESTIMATION OF GE CONCENTRATION PROFILES

The Ge concentration profiles presented in Fig. 7.1(e) are estimated by combining HAADF-STEM data and secondary ion mass spectroscopy (SIMS) data. The atomic resolution HAADF-STEM images presented in Fig. 7.1 provide a high spatial accuracy which we make use of by extracting an intensity profile from them. SIMS provides information about the silicon-germanium composition in the barrier layers of the heterostructures. We use the SiGe composition data (see Supplementary Fig. 7.5) of the SiGe barrier layers to rescale the HAADF-STEM intensity profiles to the Ge concentration profiles.

7.4.4. H-FET MEASUREMENTS

Characterisation of the Hall bars is done in a Leiden cryogenics refrigerator with a base temperature of 70 mK. We apply a 100 μV source-drain bias and measure the current I_{sd}, longitudinal voltage V_{xx} and transverse voltage V_{xy} as a function of gate voltage V_g and perpendicular magnetic field B using four-probe low-frequency lock-in techniques. We calculate longitudinal ρ_{xx} and transverse ρ_{xy} resistivity from which we extract the Hall density n at low magnetic fields using $\rho_{xy} = B/en$, where e is the electron charge. Mobility is found using $\mu = 1/ne\rho_{xx}$. At $B = 0$ we calculate the conductivity $\sigma_{xx} = 1/\rho_{xx}$ and extract the percolation density n_p using fitting formula $\sigma_{xx} \propto (n - n_p)^{1.31}$. We measure a total of 9, 10, 10, and 8 Hall bars for heterostructures A, B1, B2, and B3 respectively.

7.4.5. VALLEY SPLITTING SIMULATIONS

In Refs. [41, 42], it was demonstrated that the expected valley splitting of a disorder-dominated quantum dot is given by

$$\bar{E}_\mathrm{v} = \frac{a_0^2 \Delta E_c}{8 a_\mathrm{dot} \Delta G} \sqrt{\sum_l \psi_\mathrm{env}^4(z_l) G_l (1 - G_l)} \tag{7.1}$$

where $a_0 = 0.543$ nm is the Si lattice constant, ΔE_c is the conduction band offset, $a_\mathrm{dot} = \sqrt{\hbar^2 / m_t E_\mathrm{orb}}$ is the dot radius, $\Delta G \approx 0.3$ is the Ge concentration offset between the quantum well and SiGe barriers, $\psi_\mathrm{env}(z)$ is an envelope function, G_l is the Ge concentration at atomic layer l, and the sum is taken over all atomic layers in the heterostructure. We use Eq. (7.1) to compute the average quantum dot valley splittings E_v^QD reported in Fig. 7.4 of the main text.

In these calculations, we determine ψ_env by diagonalizing a virtual crystal Hamiltonian

$$H_\mathrm{vc} = -\frac{\hbar^2}{2 m_l} \partial_z^2 + U_\mathrm{qw} + U_z, \tag{7.2}$$

where $m_l = 0.916 m_e$ is the longitudinal effective mass in Si. The quantum well potential is given by

$$U_\mathrm{qw}(z) = \Delta E_c \frac{G(z) - G_\mathrm{min}}{\Delta G}, \tag{7.3}$$

where G_min is the minimum Ge concentration in the quantum well, determined from the estimated Ge concentration profiles described in Sec. 3, and $G(z)$ are shown in Fig. 7.1. The conduction band offset ΔE_c is computed following Ref. [42] . The electrostatic potential is given by $U_z = -eE_z z$ for constant vertical electric field $E_z = 1$ mV/nm. While somewhat arbitrary, this E_z is consistent with prior analysis of quantum dot devices in Si/SiGe [177]. Additionally, prior simulations have indicated only a minor dependence of E_v^QD on E_z for E_z between 0 and 5 mV/nm [42, 219], especially for the narrow quantum wells considered in this work. Thus, we do not expect this choice to significantly impact our results.

Examining Eq. 7.1, we can define the dimensionless quantity

$$\eta_1 = \Delta z \sqrt{\sum_l \psi_\mathrm{env}^4(z_l) G_l (1 - G_l)}, \tag{7.4}$$

where $\Delta z = a_0/4$ is the spacing between layers in the heterostructure, such that $\bar{E}_\mathrm{v} \propto \eta_1$. This quantity captures the overlap of the quantum dot wavefunction into regions with non-zero Ge concentration and is thus a metric for the impact of alloy disorder on the system. To determine ψ_env for a Hall bar, we self-consistently solve the Schrödinger and Poisson equations. The Schrödinger-Poisson virtual crystal Hamiltonian is

$$H_\mathrm{vc}^\mathrm{sp} = -\frac{\hbar^2}{2 m_l} \partial_z^2 + U_\mathrm{qw} - e\phi(z) \tag{7.5}$$

where the electrostatic potential $\phi(z)$ is determined from Poisson's equation,

$$\partial_z^2 \phi(z) = -\frac{\rho(z)}{\epsilon} = -\frac{|\psi_\mathrm{env}(z)|^2}{\epsilon} \tag{7.6}$$

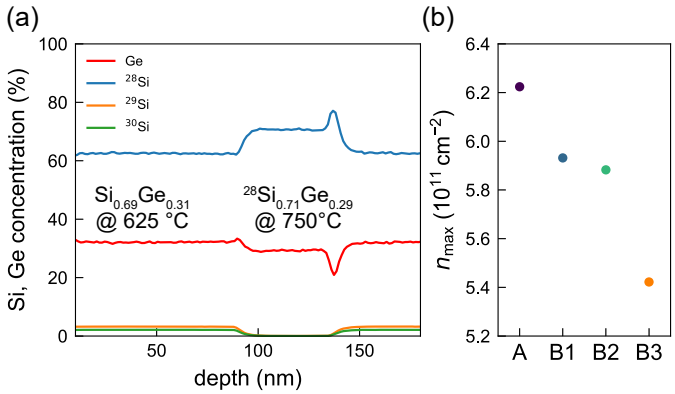

Figure 7.5: **Chemical composition and saturation density.** (a) Secondary ion mass spectroscopy (SIMS) of a test structure for the growth of SiGe with isotopically enriched ^{28}Si. The test structure consists of a layer of $^{28}Si_{0.71}Ge_{0.29}$ grown at 750 °C sandwiched between two layers of all natural $Si_{0.69}Ge_{0.31}$ grown at 625 °C. We use the same growth conditions at 750 °C of $^{28}Si_{0.71}Ge_{0.29}$ for the SiGe barrier layers in heterostructures B1, B2, and B3 of the main text. Heterostructure A uses the growth conditions of the natural $Si_{0.69}Ge_{0.31}$ at 625 °C. (b) Saturation density n_{max} for the different heterostructures. We find that B1–B3 show a lower maximum density compared to A, which we attribute to the reduced Ge composition of the barrier layers in these heterostructures. B3 shows an even lower maximum density which most likely is the result of having Ge throughout the entire quantum well in this heterostructure.

where $\epsilon = \epsilon_{Si}\epsilon_0$, and $\epsilon_{Si} = 11.4$ is the dielectric constant of Si. To bound these simulations, we choose a total electron density of 1.5×10^{11} cm^{-2}, chosen to be within the range of densities observed in the experiment, and we enforce $\partial_z \phi(z) = 0$ far below the quantum well. Again, since the overlap of the wavefunction with high-Ge layers is only weakly dependent on the vertical field in narrow quantum wells, we do not expect this choice to significantly impact our results.

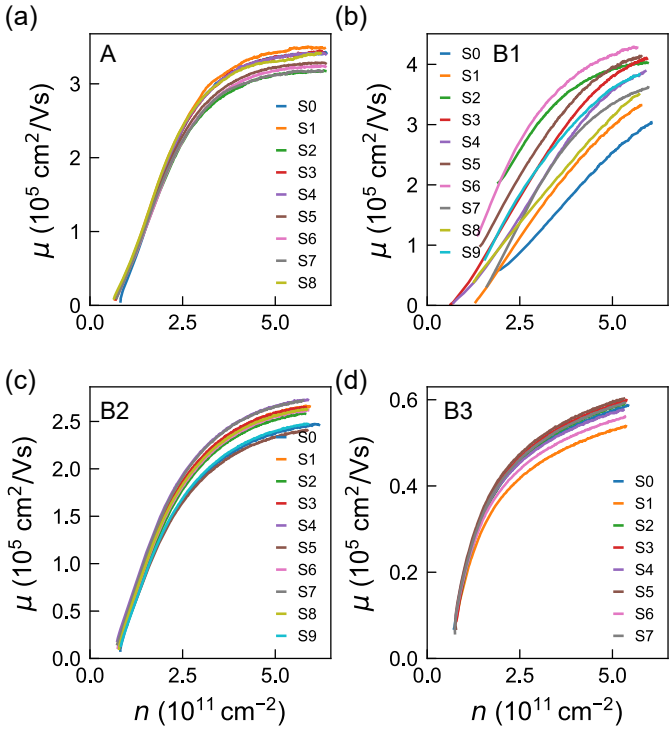

Figure 7.6: **Mobility-density characterisation.** (a)-(d) We present the mobility-density results measured across multiple H-FETs (S0-S9) on each heterostructure (A, B1-B3). Heterostructures A, B2, and B3 show uniform mobility-density curves across multiple H-FETs. B1 shows relatively less uniformity, which we attribute to possible strain-relaxation of the quantum well due to a combination of increased growth temperature of the SiGe barrier layers and a comparatively thick ^{28}Si quantum well of 9.5 nm.

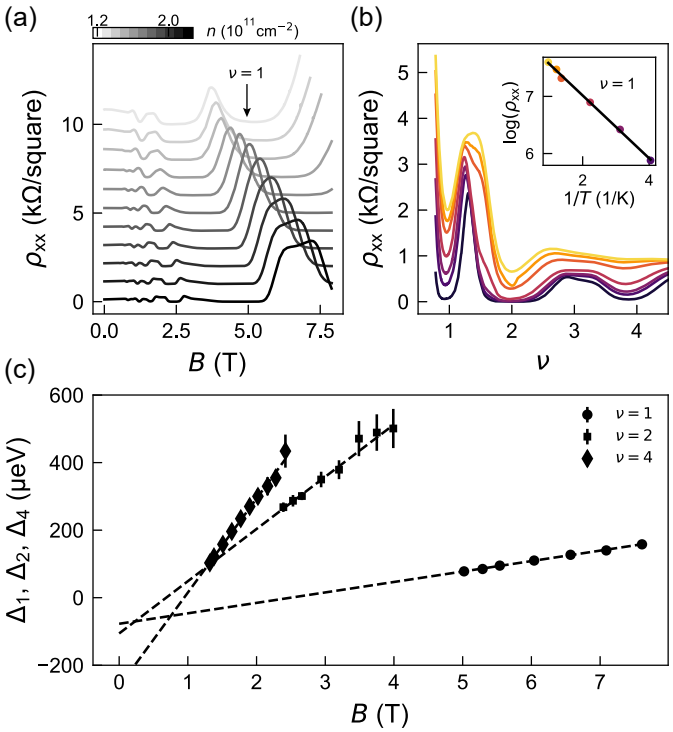

Figure 7.7: **Magnetotransport measurements for heterostructure A.** (a) We measure longitudinal resistivity ρ_{xx} as a function of magnetic field B for fixed densities n represented by the different gray colours. (b) For each density n (here 1.28×10^{11} cm^{-2}) we repeat the magnetotransport measurements at different temperatures T (70-1000 mK) and plot them against integer filling factor $\nu = nh/eB$. At each integer filling factor ν we extract the corresponding value of ρ_{xx} and find a thermally activated dependency given by $\rho_{xx} \propto \exp\{-\Delta/2k_B T\}$ (see inset), from which we extract the mobility gap Δ. Here we extract Δ_v for $\nu = 1$ corresponding to the first valley gap. (c) We plot the mobility gaps of the first valley gap Δ_v ($\nu = 1$), the first Zeeman gap Δ_z ($\nu = 2$), and the first Landau gap Δ_L ($\nu = 4$) as function of magnetic field B. From a linear fit (dotted line) we extract the Landau level broadening induced disorder Γ.

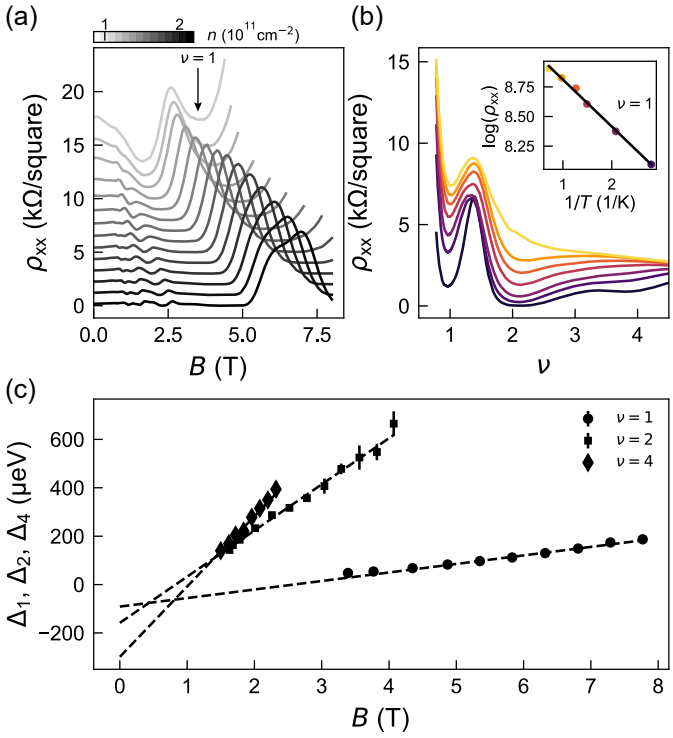

Figure 7.8: **Magnetotransport measurements for heterostructure B1.** (a) We measure longitudinal resistivity ρ_{xx} as a function of magnetic field B for fixed densities n represented by the different gray colours. (b) For each density n (here 1.05×10^{11} cm^{-2}) we repeat the magnetotransport measurements at different temperatures T (70-1000 mK) and plot them against integer filling factor $\nu = nh/eB$. At each integer filling factor ν we extract the corresponding value of ρ_{xx} and find a thermally activated dependency given by $\rho_{xx} \propto \exp\{-\Delta/2k_B T\}$ (see inset), from which we extract the mobility gap Δ. Here we extract Δ_v for $\nu = 1$ corresponding to the first valley gap. (c) We plot the mobility gaps of the first valley gap Δ_v ($\nu = 1$), the first Zeeman gap Δ_z ($\nu = 2$), and the first Landau gap Δ_L ($\nu = 4$) as function of magnetic field B. From a linear fit (dotted line) we extract the Landau level broadening induced disorder Γ.

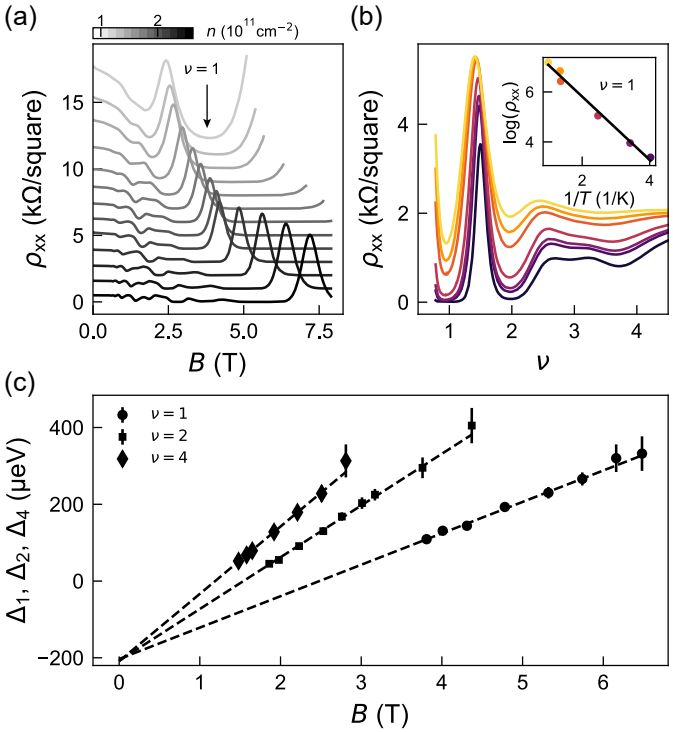

Figure 7.9: **Magnetotransport measurements for heterostructure B3.** (a) We measure longitudinal resistivity ρ_{xx} as a function of magnetic field B for fixed densities n represented by the different gray colours. (b) For each density n (here 1.21×10^{11} cm^{-2}) we repeat the magnetotransport measurements at different temperatures T (70-1000 mK) and plot them against integer filling factor $\nu = nh/eB$. At each integer filling factor ν we extract the corresponding value of ρ_{xx} and find a thermally activated dependency given by $\rho_{xx} \propto \exp\{-\Delta/2k_B T\}$ (see inset), from which we extract the mobility gap Δ. Here we extract Δ_v for $\nu = 1$ corresponding to the first valley gap. (c) We plot the mobility gaps of the first valley gap Δ_v ($\nu = 1$), the first Zeeman gap Δ_z ($\nu = 2$), and the first Landau gap Δ_L ($\nu = 4$) as function of magnetic field B. From a linear fit (dotted line) we extract the Landau level broadening induced disorder Γ.

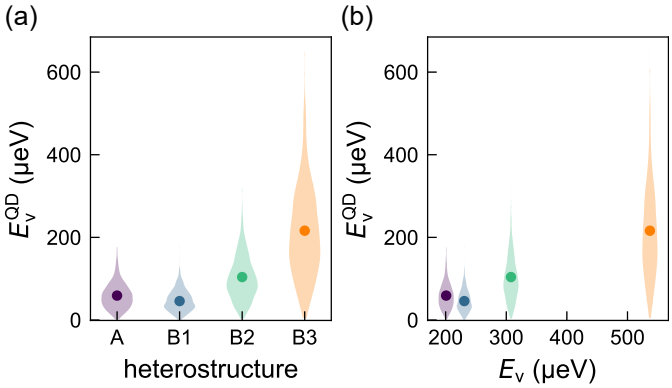

Figure 7.10: **Distribution of simulated valley splitting energies in quantum dots.** (a) Violin plots showing the distribution of simulated valley splitting energies in quantum dots as a function of heterostructure. Dots show the average valley splitting energy as reported in Fig. 4(e) of the main text. Simulations are performed at an orbital energy of 1.88 meV. (b) Violin plots showing the distribution of simulated valley splitting energies in quantum dots as a function measured valley splitting energy E_v as measured with H-FETs, extracted at a magnetic field of 6.5 T corresponding to an orbital energy of 1.88 meV.

8

Conclusions and Outlook

We shall go forward together.

Winston Churchill

8.1. CONCLUSIONS

Semiconductor spin qubits in Si/SiGe and Ge/SiGe heterostructures have seen many advancements over the past four years of my PhD. In Si/SiGe, the community has worked on progressing qubit devices from 1D arrays [37, 207] to 2D arrays [223], demonstrating high-fidelity and long-range spin shuttling [211, 224], and understanding noise correlations in dense arrays [55, 131]. Moreover, there has been a focus on fabricating Si/SiGe spin qubit devices in advanced semiconductor foundries [34, 207, 225, 226]. This is an encouraging trend, as spin qubit devices may finally start to leverage the knowledge of the semiconductor industry, an often-mentioned and sought after key advantage of semiconductor spin qubits over other types of qubit platforms. Research on Ge/SiGe based spin qubits has focused on larger 2D quantum dot devices [88, 154], operating qubits in a hyperfine sweet spot [69], and using the hopping of spins as a means of shuttling and operation [68, 227].

Underlying the above-mentioned progress has been the structural and systematic improvements made in the semiconductor heterostructure quality, a research area in which this thesis has made several contributions. In Si/SiGe, a strong focus of research has been the understanding and increasing of valley splitting. This thesis provided a foundational contribution in this regard, with chapter 6 shifting the paradigm from atomically sharp interfaces to showing the feasibility of increasing valley splitting by introducing Ge into the Si quantum well. Building upon our results, several proposals have been put forward on how to best do this in Ref. [41], with experimentalists trying to put this into practice [70, 199, 214]. In this thesis, we also contribute to this effort in chapter 7, where we effectively introduce Ge into the Si quantum well and measure increased valley splitting whilst maintaining low electrical disorder, using 2D transport characterisation.

In Ge/SiGe, the focus of heterostructure development has been to increase hole mobilities in excess of 1 million cm^2/Vs. Interestingly, this has been achieved independently by various research groups (including our own in Delft) using different approaches, such as reducing the strain in the Ge quantum wells [228, 229], using chemical purifiers on the process lines [104, 230], and positioning the quantum well further away from the surface [104, 159]. In chapter 3 we also manage to increase hole mobility excess of 1 million cm^2/Vs by starting the growth of the heterostructure from a Ge substrate, instead of the commonly used Si substrate. In chapter 4 we expand the research on the Ge/SiGe heterostructure grown from a Ge substrate by positioning the Ge QW 135 nm below the surface and study the effects on 2D transport properties. Furthermore, in chapter 5 we use quantum dot devices fabricated on a Ge/SiGe heterostructure grown from a Ge substrate and extensively characterise charge noise and hyperfine noise affecting coherence times in qubits. Next to increased hole mobilities, other advancements have been the growth of Ge/SiGe heterostructures in a semiconductor foundry environment on 300 mm silicon substrates [231] and the first demonstration of the growth of completely isotopically purified $^{70}Ge/^{28}Si^{70}Ge$ [160]. In the adoption of isotopically purified silicon and germanium precursors it will be crucial to maintain a high chemical purity of these gas precursors throughout the supply chain [64] to preserve the low disorder and minimise charge noise in future isotopically-enriched Ge spin qubit devices.

8.2. OUTLOOK

Si/SiGe and Ge/SiGe heterostructures are both at a quality level to host a small amount of spin qubits. However, looking forward, further improvements will have to be made in the pursuit to larger spin qubit devices. Ultimately, the progression of spin qubits is limited by noise and uniformity. Optimising the materials that host spin qubits can reduce noise and thereby improve the quality of spin qubits. We identify specific areas where the Si/SiGe and Ge/SiGe heterostructures can be improved.

8.2.1. SI/SIGE

Si/SiGe heterostructures have already received a lot of attention with respect to optimising the material stack. However, the limited thermal budget of the heterostructure (750 °C) does not allow for integrating a high temperature silicon oxide (900 °C). Therefore, Si/SiGe heterostructures commonly use low-temperature deposited aluminium oxide, silicon oxide, hafnium oxide, or a combination thereof. These oxides suffer from a one to two order of magnitude larger interface trap density compared to high temperature silicon oxide, resulting in a large source of charge noise. Reducing the effect of the disordered oxide or semiconductor/oxide interface on charge noise may be achieved by positioning the quantum well further away from this interface. However, deeper-buried quantum wells also limit the feasibility to effectively control the spin qubit hosted inside the quantum well and therefore a delicate balance between effective control and reduction in charge noise should be obtained. Alternatively, more research should focus into optimising the oxide itself. The mature Si/SiGe heterostructure makes it a good platform for addressing this challenge. Improving the oxides that can be used in heterostructures could be a crucial part in further lowering the noise environment for spin qubits, especially in the pursuit of scaling towards larger qubit counts.

Next to this, while in most reported Si/SiGe heterostructures the silicon quantum well is isotopically purified with ^{28}Si, this is not the case for the SiGe barrier layers surrounding the quantum well. Isotopically purifying these layers will help reducing the hyperfine interaction. Furthermore, the residual amount of ^{29}Si in the isotopically purified $^{28}SiH_4$ precursor gas can be further reduced from 800 ppm to possibly as low as 10 ppm providing an even quieter hyperfine noise environment for spin qubits.

Lastly, low and variable valley splitting still remains a limitation for spin qubits in Si/SiGe heterostructures. Attempts to increase valley splitting by engineering an increased overlap of the electron wave function with Ge atoms are being made, but it remains unclear whether the potential increase in valley splitting energy is worth the increased complexity and increased disorder. The work in chapter 7 of this thesis potentially finds a good compromise between increased valley splitting energy and disorder, but it will be crucial to further characterise these types of heterostructures with quantum dots and ultimately qubits.

8.2.2. GE/SIGE

Compared to the more mature Si/SiGe platform, Ge/SiGe heterostructures have not been subject to the same level of optimisation. For Ge/SiGe, the key objective should be the full isotopic purification of the Ge quantum well and surrounding SiGe layers to severely reduce the hyperfine interaction. So far, there has only been one report in the growth of

^{70}Ge/^{28}Si^{70}Ge [160], but no measurements of spin qubit devices on this heterostructure has been reported. The RP-CVD at TU Delft is equipped with isotopically purified ^{70}Ge and we have grown isotopically purified ^{70}Ge quantum wells. However, from 2D transport characterisation, peak mobilities were one to two orders of magnitude lower compared to the natural Ge quantum well. From SIMS analysis, it seems that the use of ^{70}Ge gives rise to increased levels of carbon and oxygen. There are only a handful of precursor bottles of isotopically $^{70}GeH_4$ in use (globally) and it seems that also other users are experiencing similar problems. It remains unclear whether this problem can be solved from using different growth conditions to reduce the incorporation of oxygen and carbon into the material or whether it will be needed to produce a chemically more pure isotopically purified $^{70}GeH_4$ gas.

Nevertheless, the Ge/SiGe material platform can also improve in other respects. The intrinsic spin orbit coupling of Ge/SiGe spin qubits makes them especially sensitive for charge noise [69]. Decreasing charge noise levels in Ge/SiGe will therefore be an important aspect to reaching longer lived qubits. In chapter 4 of this thesis we explore one approach by positioning the Ge quantum well further away from the disordered semiconductor-dielectric interface. However, no quantum dot devices have been fabricated on it and it remains unclear whether the increased SiGe barrier thickness will help to reduce charge noise. A more systematic study should be done on the effect of increasing the SiGe barrier thickness on 2D transport metrics as well as qubit metrics. It will be important to find a good trade-off between efficient charge noise reduction, and keeping effective control over the spin qubit.

In chapter 3 we show that the quality of the virtual substrate can be dramatically improved by starting growth from a Ge substrate. The improved crystal quality also gave rise to a measurable decrease of charge noise in quantum dot devices. Further improving the crystal quality of the virtual substrate could be a way to unlock even lower charge noise values. One approach could be the growth of more lightly strained Ge quantum wells, which requires a higher Ge composition in the virtual substrate. Doing this starting from a Ge substrate would require a reduced amount of lattice mismatch to be overcome, possibly reducing crystal defects. Furthermore, high-mobility lightly strained Ge quantum wells starting from a Si substrate have already been demonstrated [106].

Lastly, as Ge/SiGe are typically grown at low temperatures (400-500 °C), they are susceptible to background impurities such as oxygen and carbon. Reducing these impurities, for example by using chemical filters on the process gas precursor lines, should be a focus in the improvement of the Ge/SiGe material stack.

Both Si/SiGe and Ge/SiGe heterostructures are enticing material platforms for quantum computing. The rapid progress of spin qubits in these heterostructures in combination with adoption into semiconductor foundries could position spin qubits as the leading candidate for a large scale quantum computer. This thesis proudly provides several contributions towards this effort through careful engineering of silicon and germanium for quantum technology. It will be very exciting to see whether the true potential of spin qubits can be unlocked in the near future.

BIBLIOGRAPHY

1. Hummel, R. E. *Understanding Materials Science: History · Properties · Applications* ISBN: 9780387266916 (Springer New York, 2004).
2. Weik, M. H. The ENIAC Story. *Ordnance* **45,** 571–575. ISSN: 00304557. (2025) (1961).
3. Huff, H. R. *John Bardeen and transistor physics* in *AIP Conference Proceedings* **550** (2001), 3–32.
4. Łukasiak, L. & Jakubowski, A. History of semiconductors. *Journal of Telecommunications and information technology,* 3–9 (2010).
5. *Silicon* 1–11. ISBN: 9783662098974 (Springer Berlin Heidelberg, 2004).
6. Riordan, M. The Silicon Dioxide Solution. *IEEE Spectrum* **44,** 51–56. ISSN: 0018-9235 (Dec. 2007).
7. Planck, M. Ueber das Gesetz der Energieverteilung im Normalspectrum. en. *Annalen der Physik* **309,** 553–563. ISSN: 0003-3804, 1521-3889. (2023) (Jan. 1901).
8. Einstein, A. Über einen die Erzeugung und Verwandlung des Lichtes betreffenden heuristischen Gesichtspunkt. en. *Annalen der Physik* **322,** 132–148. ISSN: 0003-3804, 1521-3889. (2023) (Jan. 1905).
9. Feynman, R. P. Simulating physics with computers. en. *International Journal of Theoretical Physics* **21,** 467–488. ISSN: 1572-9575. (2023) (June 1982).
10. Benioff, P. The computer as a physical system: A microscopic quantum mechanical Hamiltonian model of computers as represented by Turing machines. en. *Journal of Statistical Physics* **22,** 563–591. ISSN: 1572-9613. (2023) (May 1980).
11. Elsayed, A., Van Dorpe, P. & Radu, I. *Experimental understanding of noise sources in Silicon MOS devices at cryogenic temperatures for spin qubit applications* eng. 2024.
12. Horodecki, R., Horodecki, P., Horodecki, M. & Horodecki, K. Quantum entanglement. *Rev. Mod. Phys.* **81,** 865–942 (2 June 2009).
13. Shor, P. *Algorithms for quantum computation: discrete logarithms and factoring* in *Proceedings 35th Annual Symposium on Foundations of Computer Science* (Nov. 1994), 124–134. (2023).
14. Bova, F., Goldfarb, A. & Melko, R. G. Commercial applications of quantum computing. *EPJ Quantum Technology* **8.** ISSN: 2196-0763 (Jan. 2021).
15. McArdle, S., Endo, S., Aspuru-Guzik, A., Benjamin, S. C. & Yuan, X. Quantum computational chemistry. *Reviews of Modern Physics* **92,** 015003. (2023) (Mar. 2020).
16. Grover, L. K. *A fast quantum mechanical algorithm for database search* en. in *Proceedings of the twenty-eighth annual ACM symposium on Theory of computing - STOC '96* (ACM Press, Philadelphia, Pennsylvania, United States, 1996), 212–219. ISBN: 9780897917858. (2023).

17. Arute, F. *et al.* Quantum supremacy using a programmable superconducting processor. en. *Nature* **574,** 505–510. ISSN: 1476-4687. (2024) (Oct. 2019).

18. Koch, J. *et al.* Charge-insensitive qubit design derived from the Cooper pair box. *Physical Review A* **76,** 042319. (2023) (Oct. 2007).

19. Huang, H.-L., Wu, D., Fan, D. & Zhu, X. Superconducting quantum computing: a review. en. *Science China Information Sciences* **63,** 180501. ISSN: 1869-1919. (2023) (July 2020).

20. Bloch, I., Dalibard, J. & Zwerger, W. Many-body physics with ultracold gases. *Reviews of Modern Physics* **80,** 885–964. (2023) (July 2008).

21. Cirac, J. I. & Zoller, P. Quantum Computations with Cold Trapped Ions. *Physical Review Letters* **74,** 4091–4094. (2023) (May 1995).

22. Roati, G. *et al.* Anderson localization of a non-interacting Bose–Einstein condensate. en. *Nature* **453,** 895–898. ISSN: 1476-4687. (2023) (June 2008).

23. Jaksch, D. *et al.* Fast Quantum Gates for Neutral Atoms. *Physical Review Letters* **85,** 2208–2211. ISSN: 0031-9007 (Sept. 2000).

24. Henriet, L. *et al.* Quantum computing with neutral atoms. *Quantum* **4,** 327. ISSN: 2521-327X (Sept. 2020).

25. Kitaev, A. Y. Unpaired Majorana fermions in quantum wires. *Physics-Uspekhi* **44,** 131–136. ISSN: 1468-4780. (2023) (Oct. 2001).

26. Nayak, C., Simon, S. H., Stern, A., Freedman, M. & Das Sarma, S. Non-Abelian anyons and topological quantum computation. *Reviews of Modern Physics* **80,** 1083–1159. (2023) (Sept. 2008).

27. Zhong, H.-S. *et al.* Quantum computational advantage using photons. en. *Science* **370,** 1460–1463. ISSN: 0036-8075, 1095-9203. (2023) (Dec. 2020).

28. O'Brien, J. L., Furusawa, A. & Vučković, J. Photonic quantum technologies. en. *Nature Photonics* **3,** 687–695. ISSN: 1749-4893. (2023) (Dec. 2009).

29. Pompili, M. *et al.* Realization of a multinode quantum network of remote solid-state qubits. en. *Science* **372,** 259–264. ISSN: 0036-8075, 1095-9203. (2023) (Apr. 2021).

30. Humphreys, P. C. *et al.* Deterministic delivery of remote entanglement on a quantum network. en. *Nature* **558,** 268–273. ISSN: 1476-4687. (2023) (June 2018).

31. Loss, D. & DiVincenzo, D. P. Quantum computation with quantum dots. *Physical Review A* **57,** 120–126. ISSN: 1050-2947 (Jan. 1998).

32. Hanson, R., Kouwenhoven, L. P., Petta, J. R., Tarucha, S. & Vandersypen, L. M. K. Spins in few-electron quantum dots. *Reviews of Modern Physics* **79,** 1217–1265. ISSN: 1539-0756 (Oct. 2007).

33. Zwanenburg, F. A. *et al.* Silicon quantum electronics. *Reviews of Modern Physics* **85,** 961–1019. ISSN: 0034-6861 (July 2013).

34. Neyens, S. *et al.* Probing single electrons across 300-mm spin qubit wafers. *Nature* **629,** 80–85 (2024).

35. Schäffler, F. High-mobility Si and Ge structures. *Semiconductor Science and Technology* **12,** 1515–1549. ISSN: 1361-6641 (Dec. 1997).

36. Mori, N. in *Silicon–Germanium (SiGe) Nanostructures* (eds Shiraki, Y. & Usami, N.) 26–42 (Woodhead Publishing, 2011). ISBN: 978-1-84569-689-4.

37. Philips, S. G. J. *et al.* Universal control of a six-qubit quantum processor in silicon. *Nature* **609,** 919–924. ISSN: 1476-4687 (Sept. 2022).

38. Tagliaferri, M. L. V. *et al.* Impact of valley phase and splitting on readout of silicon spin qubits. *Physical Review B* **97,** 245412. ISSN: 2469-9950 (June 2018).

39. Dismukes, J. P., Ekstrom, L. & Paff, R. J. Lattice Parameter and Density in Germanium-Silicon Alloys [1]. en. *The Journal of Physical Chemistry* **68,** 3021–3027. ISSN: 0022-3654, 1541-5740. (2024) (Oct. 1964).

40. Paul, D. J. Si/SiGe heterostructures: from material and physics to devices and circuits. *Semiconductor Science and Technology* **19,** R75–R108. ISSN: 0268-1242, 1361-6641. (2023) (Oct. 2004).

41. Losert, M. P. *et al.* Practical strategies for enhancing the valley splitting in Si/SiGe quantum wells. *Phys. Rev. B* **108,** 125405 (12 Sept. 2023).

42. Paquelet Wuetz, B. *et al.* Atomic fluctuations lifting the energy degeneracy in Si/SiGe quantum dots. *Nature Communications* **13.** ISSN: 2041-1723 (Dec. 2022).

43. Sammak, A. *et al.* Shallow and Undoped Germanium Quantum Wells: A Playground for Spin and Hybrid Quantum Technology. *Advanced Functional Materials* **29,** 1807613. ISSN: 1616-301X, 1616-3028. (2023) (Apr. 2019).

44. Scappucci, G. *et al.* The germanium quantum information route. *Nature Reviews Materials* **6,** 926–943. ISSN: 2058-8437. (2023) (Oct. 2021).

45. Terrazos, L. A. *et al.* Theory of hole-spin qubits in strained germanium quantum dots. *Physical Review B* **103,** 125201. ISSN: 2469-9969 (Mar. 2021).

46. Mi, X. *et al.* Magnetotransport studies of mobility limiting mechanisms in undoped Si/SiGe heterostructures. *Physical Review B* **92,** 035304. ISSN: 1550-235X (July 2015).

47. Wild, A. *et al.* Few electron double quantum dot in an isotopically purified 28Si quantum well. *Applied Physics Letters* **100.** ISSN: 1077-3118 (Apr. 2012).

48. Yoneda, J. *et al.* A quantum-dot spin qubit with coherence limited by charge noise and fidelity higher than 99.9%. *Nature nanotechnology* **13,** 102–106 (2018).

49. Bollani, M. *et al.* Anisotropic extended misfit dislocations in overcritical SiGe films by local substrate patterning. *Nanotechnology* **27,** 425301. ISSN: 1361-6528 (Sept. 2016).

50. Matthews, J. & Blakeslee, A. Defects in epitaxial multilayers. *Journal of Crystal Growth* **27,** 118–125. ISSN: 0022-0248 (Dec. 1974).

51. Kasper, E. & Paul, D. J. *Silicon quantum integrated circuits: Silicon-germanium heterostructure devices: Basics and realisations* (Springer Science & Business Media, 2005).

52. Liu, Y. *et al.* Role of critical thickness in SiGe/Si/SiGe heterostructure design for qubits. *Journal of Applied Physics* **132.** ISSN: 1089-7550 (Aug. 2022).

53. Hartmann, J. M., Abbadie, A. & Favier, S. Critical thickness for plastic relaxation of SiGe on Si(001) revisited. *Journal of Applied Physics* **110.** ISSN: 1089-7550 (Oct. 2011).

54. Elsayed, A. *et al.* Low charge noise quantum dots with industrial CMOS manufacturing. *npj Quantum Information* **10,** 70. ISSN: 2056-6387. (2024) (July 2024).

55. Yoneda, J. *et al.* Noise-correlation spectrum for a pair of spin qubits in silicon. en. *Nature Physics* **19,** 1793–1798. ISSN: 1745-2481. (2024) (Dec. 2023).

56. Paquelet Wuetz, B. *et al.* Reducing charge noise in quantum dots by using thin silicon quantum wells. *Nature Communications* **14,** 1385. ISSN: 2041-1723. (2023) (Mar. 2023).

57. Massai, L. *et al.* Impact of interface traps on charge noise and low-density transport properties in Ge/SiGe heterostructures. en. *Communications Materials* **5,** 151. ISSN: 2662-4443. (2024) (Aug. 2024).

58. Connors, E. J., Nelson, J., Qiao, H., Edge, L. F. & Nichol, J. M. Low-frequency charge noise in Si/SiGe quantum dots. *Physical Review B* **100,** 165305 (2019).

59. Beaudoin, F. & Coish, W. A. Microscopic models for charge-noise-induced dephasing of solid-state qubits. *Physical Review B* **91,** 165432. ISSN: 1550-235X (Apr. 2015).

60. Lodari, M. *et al.* Low percolation density and charge noise with holes in germanium. *Materials for Quantum Technology* **1,** 011002. ISSN: 2633-4356. (2023) (Jan. 2021).

61. Paladino, E., Galperin, Y., Falci, G. & Altshuler, B. 1/f noise: Implications for solid-state quantum information. *Reviews of Modern Physics* **86,** 361 (2014).

62. Scappucci, G. Semiconductor materials stacks for quantum dot spin qubits (2021).

63. Petta, J. R. *et al.* Coherent Manipulation of Coupled Electron Spins in Semiconductor Quantum Dots. en. *Science* **309,** 2180–2184. ISSN: 0036-8075, 1095-9203. (2024) (Sept. 2005).

64. Sabbagh, D. *et al.* Quantum transport properties of industrial si 28/si o 2 28. *Physical Review Applied* **12,** 014013 (2019).

65. Struck, T. *et al.* Low-frequency spin qubit energy splitting noise in highly purified 28Si/SiGe. en. *npj Quantum Information* **6,** 40. ISSN: 2056-6387. (2024) (May 2020).

66. Hendrickx, N. W. *et al.* A single-hole spin qubit. *Nature Communications* **11,** 3478. ISSN: 2041-1723. (2023) (July 2020).

67. Hendrickx, N., Franke, D., Sammak, A., Scappucci, G. & Veldhorst, M. Fast two-qubit logic with holes in germanium. *Nature* **577,** 487–491 (2020).

68. Wang, C.-A. *et al.* Operating semiconductor quantum processors with hopping spins. *Science* **385,** 447–452 (2024).

69. Hendrickx, N. *et al.* Sweet-spot operation of a germanium hole spin qubit with highly anisotropic noise sensitivity. *Nature Materials,* 1–8 (2024).

70. Gradwohl, K.-P. *et al.* Enhanced Nanoscale Ge Concentration Oscillations in Si/SiGe Quantum Well through Controlled Segregation. *Nano Letters* **25,** 4204–4210. ISSN: 1530-6992 (Mar. 2025).

71. Isella, G. *et al.* Low-energy plasma-enhanced chemical vapor deposition for strained Si and Ge heterostructures and devices. *Solid-State Electronics* **48,** 1317–1323. ISSN: 00381101. (2023) (Aug. 2004).

72. Greve, D. W., Misra, R., Strong, R. & Schlesinger, T. E. Ultrahigh vacuum/chemical vapor deposition epitaxy of silicon and germanium–silicon heterostructures. *Journal of Vacuum Science; Technology A: Vacuum, Surfaces, and Films* **12,** 979–985. ISSN: 1520-8559 (July 1994).

73. Nylandsted Larsen, A. Epitaxial growth of Ge and SiGe on Si substrates. *Materials Science in Semiconductor Processing* **9.** Proceedings of Symposium T E-MRS 2006 Spring Meeting on Germanium based semiconductors from materials to devices, 454–459. ISSN: 1369-8001 (2006).

74. Stehouwer, L. E. A. *et al.* Germanium wafers for strained quantum wells with low disorder. *Applied Physics Letters* **123** (2023).

75. Degli Esposti, D. *et al.* Wafer-scale low-disorder 2DEG in 28Si/SiGe without an epitaxial Si cap. *Applied physics letters* **120** (2022).

76. Bogumilowicz, Y. *et al.* Chemical vapour etching of Si, SiGe and Ge with HCl; applications to the formation of thin relaxed SiGe buffers and to the revelation of threading dislocations. *Semiconductor Science and Technology* **20,** 127–134. ISSN: 0268-1242, 1361-6641. (2023) (Feb. 2005).

77. Wuetz, B. P. *Silicon/silicon-germanium heterostructures for spin-qubit quantum processors* PhD thesis (Delft University of Technology, Delft, July 2022).

78. Degli Esposti, D. *Strained silicon quantum wells for spin qubits* English. Dissertation (TU Delft) (Delft University of Technology, 2025). ISBN: 978-94-6384-734-6.

79. Paquelet Wuetz, B. *et al.* Multiplexed quantum transport using commercial off-the-shelf CMOS at sub-kelvin temperatures. *npj Quantum Information* **6,** 43. ISSN: 2056-6387. (2023) (May 2020).

80. Degli Esposti, D. *et al.* Low disorder and high valley splitting in silicon. *npj Quantum Information* **10,** 32 (2024).

81. Das Sarma, S. *et al.* Two-Dimensional Metal-Insulator Transition as a Percolation Transition in a High-Mobility Electron System. *Physical Review Letters* **94,** 136401. ISSN: 1079-7114 (Apr. 2005).

82. Tracy, L. A. *et al.* Observation of percolation-induced two-dimensional metal-insulator transition in a Si MOSFET. *Physical Review B* **79,** 235307. (2023) (June 2009).

83. Volk, C. *et al.* Loading a quantum-dot based "Qubyte" register. *npj Quantum Information* **5.** ISSN: 2056-6387 (Apr. 2019).

84. Zu, H., Dai, W. & de Waele, A. Development of dilution refrigerators—A review. *Cryogenics* **121,** 103390. ISSN: 0011-2275 (2022).

85. Jirovec, D. *et al.* A singlet-triplet hole spin qubit in planar Ge. *Nature Materials* **20,** 1106–1112. ISSN: 1476-4660. (2023) (Aug. 2021).

86. Wang, C.-A. *et al.* Probing resonating valence bonds on a programmable germanium quantum simulator. *npj Quantum Information* **9.** ISSN: 2056-6387 (June 2023).

87. Hendrickx, N. W. *et al.* A four-qubit germanium quantum processor. *Nature* **591,** 580–585. ISSN: 1476-4687. (2023) (Mar. 2021).

88. Borsoi, F. *et al.* Shared control of a 16 semiconductor quantum dot crossbar array. *Nature Nanotechnology* **19,** 21–27. ISSN: 1748-3395 (Aug. 2023).

89. Tosato, A. *et al.* Hard superconducting gap in germanium. *Communications Materials* **4,** 23. ISSN: 2662-4443. (2023) (Apr. 2023).

90. Choi, M.-S., Bruder, C. & Loss, D. Spin-dependent Josephson current through double quantum dots and measurement of entangled electron states. *Physical Review B* **62,** 13569–13572. (2023) (Nov. 2000).

91. Leijnse, M. & Flensberg, K. Coupling Spin Qubits via Superconductors. *Physical Review Letters* **111,** 060501. (2023) (Aug. 2013).

92. Lawrie, W. I. L. *et al.* Simultaneous single-qubit driving of semiconductor spin qubits at the fault-tolerant threshold. *Nature Communications* **14.** ISSN: 2041-1723 (June 2023).

93. Van Riggelen, F. *et al.* Phase flip code with semiconductor spin qubits. *npj Quantum Information* **8,** 124. ISSN: 2056-6387. (2023) (Oct. 2022).

94. Itoh, K. *et al.* High purity isotopically enriched ^{70}Ge and ^{74}Ge single crystals: Isotope separation, growth, and properties. *Journal of Materials Research* **8,** 1341–1347. ISSN: 2044-5326. (2023) (June 1993).

95. Bosco, S. & Loss, D. Fully Tunable Hyperfine Interactions of Hole Spin Qubits in Si and Ge Quantum Dots. *Physical Review Letters* **127,** 190501. (2023) (Nov. 2021).

96. Bosco, S., Hetényi, B. & Loss, D. Hole Spin Qubits in Si FinFETs With Fully Tunable Spin-Orbit Coupling and Sweet Spots for Charge Noise. *PRX Quantum* **2,** 010348. (2023) (Mar. 2021).

97. Malkoc, O., Stano, P. & Loss, D. Charge-Noise-Induced Dephasing in Silicon Hole-Spin Qubits. *Physical Review Letters* **129,** 247701. (2023) (Dec. 2022).

98. Abadillo-Uriel, J. C., Rodríguez-Mena, E. A., Martinez, B. & Niquet, Y.-M. Hole-Spin Driving by Strain-Induced Spin-Orbit Interactions. *Physical Review Letters* **131,** 097002. ISSN: 1079-7114 (Sept. 2023).

99. Shah, V. A. *et al.* Reverse graded relaxed buffers for high Ge content SiGe virtual substrates. *Applied Physics Letters* **93,** 192103. ISSN: 0003-6951, 1077-3118. (2023) (Nov. 2008).

100. Corley-Wiciak, C. *et al.* Nanoscale Mapping of the 3D Strain Tensor in a Germanium Quantum Well Hosting a Functional Spin Qubit Device. *ACS Applied Materials & Interfaces* **15,** 3119–3130. ISSN: 1944-8244, 1944-8252. (2023) (Jan. 2023).

101. Kutsukake, K. *et al.* On the origin of strain fluctuation in strained-Si grown on SiGe-on-insulator and SiGe virtual substrates. *Applied Physics Letters* **85,** 1335–1337. ISSN: 0003-6951, 1077-3118. (2023) (Aug. 2004).

102. Pezzoli, F. *et al.* Phonon strain shift coefficients in $Si_{1-x}Ge_x$ alloys. *Journal of Applied Physics* **103,** 093521. ISSN: 0021-8979, 1089-7550. (2023) (May 2008).

103. Monroe, D. Comparison of mobility-limiting mechanisms in high-mobility $Si_{1-x}Ge_x$ heterostructures. *Journal of Vacuum Science & Technology B: Microelectronics and Nanometer Structures* **11,** 1731. ISSN: 0734211X. (2023) (July 1993).

104. Myronov, M. *et al.* Holes Outperform Electrons in Group IV Semiconductor Materials. *Small Science* **3,** 2200094. ISSN: 2688-4046, 2688-4046. (2023) (Apr. 2023).

105. Lu, T. M. *et al.* Density-controlled quantum Hall ferromagnetic transition in a two-dimensional hole system. *Scientific Reports* **7,** 2468. ISSN: 2045-2322. (2023) (June 2017).

106. Lodari, M. *et al.* Light effective hole mass in undoped Ge/SiGe quantum wells. *Physical Review B* **100,** 041304. (2023) (July 2019).

107. Coleridge, P. T. Small-angle scattering in two-dimensional electron gases. *Physical Review B* **44,** 3793–3801. (2023) (Aug. 1991).

108. Coleridge, P. T., Hayne, M., Zawadzki, P. & Sachrajda, A. S. Effective masses in high-mobility 2D electron gas structures. *Surface Science* **361-362,** 560–563. ISSN: 0039-6028. (2023) (July 1996).

109. Qian, Q. *et al.* Quantum lifetime in ultrahigh quality GaAs quantum wells: Relationship to $\Delta 5$ / 2 and impact of density fluctuations. *Physical Review B* **96,** 035309. ISSN: 2469-9950, 2469-9969. (2023) (July 2017).

110. Nečas, D. & Klapetek, P. Gwyddion: an open-source software for SPM data analysis. *Open Physics* **10.** ISSN: 2391-5471. (2023) (Jan. 2012).

111. Das Sarma, S. & Stern, F. Single-particle relaxation time versus scattering time in an impure electron gas. *Physical Review B* **32,** 8442–8444. ISSN: 0163-1829. (2023) (Dec. 1985).

112. Lawrie, W. *et al.* Quantum dot arrays in silicon and germanium. *Applied Physics Letters* **116** (2020).

113. Huang, Y. & Das Sarma, S. Understanding disorder in silicon quantum computing platforms: scattering mechanisms in Si/SiGe quantum wells. *Physical Review B* **109,** 125405 (2024).

114. Last, B. J. & Thouless, D. J. Percolation Theory and Electrical Conductivity. en. *Physical Review Letters* **27,** 1719–1721. ISSN: 0031-9007. (2024) (Dec. 1971).

115. Shklovskiĭ, B. I. & Éfros, A. L. Percolation theory and conductivity of strongly inhomogeneous media. *Soviet Physics Uspekhi* **18,** 845–862. ISSN: 0038-5670. (2024) (Nov. 1975).

116. Fogelholm, R. The conductivity of large percolation network samples. *Journal of Physics C: Solid State Physics* **13,** L571–L574. ISSN: 0022-3719. (2024) (Aug. 1980).

117. Kim, J.-S., Tyryshkin, A. M. & Lyon, S. A. Annealing shallow Si/SiO2 interface traps in electron-beam irradiated high-mobility metal-oxide-silicon transistors. *Applied Physics Letters* **110** (2017).

118. Paysen, E. *et al.* Three-Dimensional Reconstruction of Interface Roughness and Alloy Disorder in Ge/GeSi Asymmetric Coupled Quantum Wells Using Electron Tomography. en. *ACS Applied Materials & Interfaces* **16,** 4189–4198. ISSN: 1944-8244, 1944-8252. (2024) (Jan. 2024).

119. Das Sarma, S. & Hwang, E. H. Mobility versus quality in two-dimensional semiconductor structures. en. *Physical Review B* **90,** 035425. ISSN: 1098-0121, 1550-235X. (2024) (July 2014).

120. Burkard, G., Ladd, T. D., Pan, A., Nichol, J. M. & Petta, J. R. Semiconductor spin qubits. *Reviews of Modern Physics* **95,** 025003 (2023).

121. Xue, X. *et al.* Quantum logic with spin qubits crossing the surface code threshold. en. *Nature* **601,** 343–347. ISSN: 1476-4687. (2024) (Jan. 2022).

122. Mądzik, M. T. *et al.* Precision tomography of a three-qubit donor quantum processor in silicon. en. *Nature* **601,** 348–353. ISSN: 1476-4687. (2024) (Jan. 2022).

123. Noiri, A. *et al.* Fast universal quantum gate above the fault-tolerance threshold in silicon. en. *Nature* **601,** 338–342. ISSN: 1476-4687. (2024) (Jan. 2022).

124. Mills, A. R. *et al.* Two-qubit silicon quantum processor with operation fidelity exceeding 99%. en. *Science Advances* **8,** eabn5130. ISSN: 2375-2548. (2024) (Apr. 2022).

125. Fowler, A. G., Mariantoni, M., Martinis, J. M. & Cleland, A. N. Surface codes: Towards practical large-scale quantum computation. en. *Physical Review A* **86,** 032324. ISSN: 1050-2947, 1094-1622. (2024) (Sept. 2012).

126. Hoefler, T., Häner, T. & Troyer, M. Disentangling Hype from Practicality: On Realistically Achieving Quantum Advantage. en. *Communications of the ACM* **66,** 82–87. ISSN: 0001-0782, 1557-7317. (2024) (May 2023).

127. De Leon, N. P. *et al.* Materials challenges and opportunities for quantum computing hardware. en. *Science* **372,** eabb2823. ISSN: 0036-8075, 1095-9203. (2024) (Apr. 2021).

128. Harper, R. & Flammia, S. T. Learning Correlated Noise in a 39-Qubit Quantum Processor. en. *PRX Quantum* **4,** 040311. ISSN: 2691-3399. (2024) (Oct. 2023).

129. Kranz, L. *et al.* Exploiting a Single-Crystal Environment to Minimize the Charge Noise on Qubits in Silicon. *Advanced Materials* **32,** 2003361 (2020).

130. Zwerver, A. *et al.* Qubits made by advanced semiconductor manufacturing. *Nature Electronics* **5,** 184–190 (2022).

131. Rojas-Arias, J. *et al.* Spatial noise correlations beyond nearest neighbors in 28 Si / Si-Ge spin qubits. en. *Physical Review Applied* **20,** 054024. ISSN: 2331-7019. (2024) (Nov. 2023).

132. Donnelly, M. B. *et al.* Noise Correlations in a 1D Silicon Spin Qubit Array. *Preprint at http://arXiv.org/abs2405.03763.* (2024) (May 2024).

133. Hendrickx, N. W. *et al.* Gate-controlled quantum dots and superconductivity in planar germanium. *Nature Communications* **9,** 2835 (2018).

134. Connors, E. J., Nelson, J., Edge, L. F. & Nichol, J. M. Charge-noise spectroscopy of Si/SiGe quantum dots via dynamically-decoupled exchange oscillations. *Nature Communications* **13,** 940 (2022).

135. Spence, C. *et al.* Probing Low-Frequency Charge Noise in Few-Electron CMOS Quantum Dots. *Physical Review Applied* **19,** 044010 (2023).

136. Seedhouse, A. E. *et al.* Pauli Blockade in Silicon Quantum Dots with Spin-Orbit Control. *PRX Quantum* **2,** 010303 (1 Jan. 2021).

137. Takeda, K. *et al.* Rapid single-shot parity spin readout in a silicon double quantum dot with fidelity exceeding 99%. *npj Quantum Information* **10,** 22. ISSN: 2056-6387 (Feb. 2024).

138. Meiboom, S. & Gill, D. Modified Spin-Echo Method for Measuring Nuclear Relaxation Times. en. *Review of Scientific Instruments* **29,** 688–691. ISSN: 0034-6748, 1089-7623. (2025) (Aug. 1958).

139. Uhrig, G. S. Keeping a Quantum Bit Alive by Optimized π-Pulse Sequences. *Phys. Rev. Lett.* **98,** 100504 (10 Mar. 2007).

140. Cywi ński, Ł., Lutchyn, R. M., Nave, C. P. & Das Sarma, S. How to enhance dephasing time in superconducting qubits. *Phys. Rev. B* **77,** 174509 (17 May 2008).

141. Álvarez, G. A. & Suter, D. Measuring the Spectrum of Colored Noise by Dynamical Decoupling. *Phys. Rev. Lett.* **107,** 230501 (23 Nov. 2011).

142. Muhonen, J. T. *et al.* Storing quantum information for 30 seconds in a nanoelectronic device. en. *Nature Nanotechnology* **9,** 986–991. ISSN: 1748-3395. (2024) (Dec. 2014).

143. Jirovec, D. *et al.* Dynamics of hole singlet-triplet qubits with large g-factor differences. *Physical Review Letters* **128,** 126803 (2022).

144. Van Bree, J. *et al.* Anisotropy of electron and hole g tensors of quantum dots: An intuitive picture based on spin-correlated orbital currents. *Physical Review B* **93,** 035311 (2016).

145. Fischer, J., Coish, W. A., Bulaev, D. V. & Loss, D. Spin decoherence of a heavy hole coupled to nuclear spins in a quantum dot. *Phys. Rev. B* **78,** 155329 (15 Oct. 2008).

146. Philippopoulos, P. *Hyperfine and Spin–Orbit Interactions in Semiconductor Nanostructures.* PhD thesis (McGill University, 2020).

147. Wang, X. J., Chesi, S. & Coish, W. A. Spin-Echo Dynamics of a Heavy Hole in a Quantum Dot. *Phys. Rev. Lett.* **109,** 237601 (23 Dec. 2012).

148. Philippopoulos, P., Chesi, S., Salfi, J., Rogge, S. & Coish, W. A. Hole spin echo envelope modulations. *Phys. Rev. B* **100,** 125402 (12 Sept. 2019).

149. Lawrie, W. I. L. *Spin Qubits in Silicon and Germanium* PhD thesis (Delft University of Technology, 2022).

150. Bluhm, H. *et al.* Dephasing time of GaAs electron-spin qubits coupled to a nuclear bath exceeding 200 μs. *Nature Physics* **7,** 109–113. ISSN: 1745-2481 (Feb. 2011).

151. Malinowski, F. K. *et al.* Notch filtering the nuclear environment of a spin qubit. *Nature Nanotechnology* **12,** 16–20. ISSN: 1748-3395 (Jan. 2017).

152. Chekhovich, E. A. *et al.* Nuclear spin effects in semiconductor quantum dots. *Nature Materials* **12,** 494–504. ISSN: 1476-4660 (June 2013).

153. Rojas-Arias, J. S. *et al.* The origins of noise in the Zeeman splitting of spin qubits in natural-silicon devices. *Preprint at https://arxiv.org/abs/2408.13707* (2024).

154. John, V. *et al. A two-dimensional 10-qubit array in germanium with robust and localised qubit control* 2024. arXiv: 2412.16044 [cond-mat.mes-hall].

155. Wang, C.-A. *et al.* Modeling of planar germanium hole qubits in electric and magnetic fields. en. *npj Quantum Information* **10,** 102. ISSN: 2056-6387. (2024) (Oct. 2024).

156. Simoen, E. *et al.* Defect-Related Excess Low-Frequency Noise in Ge-on-Si pMOSFETs. *IEEE Electron Device Letters* **32,** 87–89. ISSN: 0741-3106, 1558-0563. (2025) (Jan. 2011).

157. Simoen, E. *et al. Device-Based Threading Dislocation Assessment in Germanium Hetero-Epitaxy* in *2019 34th Symposium on Microelectronics Technology and Devices (SBMicro)* (IEEE, Sao Paulo, Brazil, Aug. 2019), 1–6. ISBN: 9781728119090. (2025).

158. Hua, W.-C., Lee, M., Chen, P., Tsai, M.-J. & Liu, C. Threading dislocation induced low frequency noise in strained-Si nMOSFETs. *IEEE Electron Device Letters* **26,** 667–669. ISSN: 1558-0563. (2025) (Sept. 2005).

159. Costa, D. *et al.* Reducing disorder in Ge quantum wells by using thick SiGe barriers. *Applied Physics Letters* **125,** 222104. ISSN: 0003-6951 (Nov. 2024).

160. Moutanabbir, O. *et al.* Nuclear Spin-Depleted, Isotopically Enriched^{70} Ge/^{28} Si^{70} Ge Quantum Wells. en. *Advanced Materials* **36,** 2305703. ISSN: 0935-9648, 1521-4095. (2025) (Feb. 2024).

161. Vandersypen, L. M. & Eriksson, M. A. Quantum computing with semiconductor spins. *Physics Today* **72,** 38–45 (2019).

162. Maune, B. M. *et al.* Coherent singlet-triplet oscillations in a silicon-based double quantum dot. *Nature* **481,** 344–347. ISSN: 00280836 (2012).

163. Vandersypen, L. M. K. *et al.* Interfacing spin qubits in quantum dots and donors—hot, dense, and coherent. en. *npj Quantum Information* **3,** 1–10. ISSN: 2056-6387. (2023) (Sept. 2017).

164. Li, R. *et al.* A crossbar network for silicon quantum dot qubits. *Science Advances* **4** (2018).

165. Zajac, D. M., Hazard, T. M., Mi, X., Nielsen, E. & Petta, J. R. Scalable Gate Architecture for a One-Dimensional Array of Semiconductor Spin Qubits. *Physical Review Applied* **6,** 054013. ISSN: 2331-7019 (Nov. 2016).

166. Watson, T. F. *et al.* A programmable two-qubit quantum processor in silicon. *Nature* **555,** 633–637. ISSN: 14764687 (2018).

167. Takeda, K. *et al.* Quantum tomography of an entangled three-qubit state in silicon. *Nature Nanotechnology* **16,** 965–969. ISSN: 1748-3387 (Sept. 2021).

168. Russ, M., Péterfalvi, C. G. & Burkard, G. Theory of valley-resolved spectroscopy of a Si triple quantum dot coupled to a microwave resonator. *Journal of Physics: Condensed Matter* **32,** 165301. ISSN: 0953-8984 (Apr. 2020).

169. Zajac, D. M., Hazard, T. M., Mi, X., Wang, K. & Petta, J. R. A reconfigurable gate architecture for Si/SiGe quantum dots. *Applied Physics Letters* **106,** 223507 (2015).

170. Shi, Z. *et al.* Tunable singlet-triplet splitting in a few-electron Si/SiGe quantum dot. *Applied Physics Letters* **99,** 233108 (2011).

171. Scarlino, P. *et al.* Dressed photon-orbital states in a quantum dot: Intervalley spin resonance. *Physical Review B* **95,** 165429 (2017).

172. Ferdous, R. *et al.* Valley dependent anisotropic spin splitting in silicon quantum dots. *npj Quantum Information* **4,** 26. ISSN: 2056-6387 (Dec. 2018).

173. Mi, X. *et al.* Circuit quantum electrodynamics architecture for gate-defined quantum dots in silicon. *Applied Physics Letters* **110.** ISSN: 1077-3118 (Jan. 2017).

174. Borjans, F., Zajac, D. M., Hazard, T. M. & Petta, J. R. Single-spin relaxation in a synthetic spin-orbit field. *Physical Review Applied* **11,** 44063 (2019).

175. Mi, X. *et al.* A coherent spin–photon interface in silicon. *Nature* **555,** 599–603. ISSN: 1476-4687 (Feb. 2018).

176. Borselli, M. G. *et al.* Measurement of valley splitting in high-symmetry Si/SiGe quantum dots. *Applied Physics Letters* **98.** ISSN: 00036951 (2011).

177. Hollmann, A. *et al.* Large, Tunable Valley Splitting and Single-Spin Relaxation Mechanisms in a Si/Si_xGe_{1-x} Quantum Dot. *Phys. Rev. Appl.* **13,** 034068 (3 Mar. 2020).

178. Chen, E. H. *et al.* Detuning Axis Pulsed Spectroscopy of Valley-Orbital States in Si/SiGe Quantum Dots. *Physical Review Applied* **15,** 044033. ISSN: 2331-7019 (Apr. 2021).

179. Kawakami, E. *et al.* Electrical control of a long-lived spin qubit in a Si/SiGe quantum dot. *Nature Nanotechnology* **9,** 666–670. ISSN: 1748-3387 (Sept. 2014).

180. Friesen, M., Chutia, S., Tahan, C. & Coppersmith, S. N. Valley splitting theory of SiGe/Si/SiGe quantum wells. *Physical Review B - Condensed Matter and Materials Physics* **75,** 1–12. ISSN: 10980121 (2007).

181. Friesen, M. & Coppersmith, S. N. Theory of valley-orbit coupling in a Si/SiGe quantum dot. *Physical Review B* **81,** 115324. ISSN: 1098-0121 (Mar. 2010).

182. Friesen, M., Eriksson, M. A. & Coppersmith, S. N. Magnetic field dependence of valley splitting in realistic Si/SiGe quantum wells. *Applied Physics Letters* **89,** 2006–2008. ISSN: 00036951 (2006).

183. Kharche, N., Prada, M., Boykin, T. B. & Klimeck, G. Valley splitting in strained silicon quantum wells modeled with 2° miscuts, step disorder, and alloy disorder. *Applied Physics Letters* **90,** 092109. ISSN: 0003-6951 (Feb. 2007).

184. Gamble, J. K., Eriksson, M. A., Coppersmith, S. N. & Friesen, M. Disorder-induced valley-orbit hybrid states in Si quantum dots. *Physical Review B - Condensed Matter and Materials Physics* **88,** 1–6. ISSN: 10980121 (2013).

185. Tariq, B. & Hu, X. Effects of interface steps on the valley-orbit coupling in a Si/SiGe quantum dot. *Physical Review B* **100,** 125309. ISSN: 2469-9950 (Sept. 2019).

186. Dodson, J. P. *et al.* How Valley-Orbit States in Silicon Quantum Dots Probe Quantum Well Interfaces. *Physical Review Letters* **128,** 146802. ISSN: 0031-9007 (Apr. 2022).

187. Bennett, S. E. *et al.* Atom probe tomography characterisation of a laser diode structure grown by molecular beam epitaxy. *Journal of Applied Physics* **111,** 053508. ISSN: 0021-8979 (Mar. 2012).

188. Bas, P., Bostel, A., Deconihout, B. & Blavette, D. A general protocol for the reconstruction of 3D atom probe data. *Applied Surface Science* **87-88,** 298–304. ISSN: 01694332 (Mar. 1995).

189. Rolland, N. *et al.* New Atom Probe Tomography Reconstruction Algorithm for Multilayered Samples: Beyond the Hemispherical Constraint. *Microscopy and Microanalysis* **23,** 247–254. ISSN: 1431-9276 (Apr. 2017).

190. Koelling, S. *et al.* High depth resolution analysis of Si/SiGe multilayers with the atom probe. *Applied Physics Letters* **95,** 144106. ISSN: 0003-6951 (Oct. 2009).

191. Melkonyan, D. *et al.* Atom probe tomography analysis of SiGe fins embedded in SiO 2 : Facts and artefacts. *Ultramicroscopy* **179,** 100–107. ISSN: 03043991 (Aug. 2017).

192. Dyck, O. *et al.* Atom Probe Tomography: Accurate Quantification of Si/SiGe Interface Profiles via Atom Probe Tomography. *Advanced Materials Interfaces* **4.** ISSN: 21967350 (Nov. 2017).

193. Xue, X. *et al.* CMOS-based cryogenic control of silicon quantum circuits. *Nature* **593,** 205–210. ISSN: 1476-4687 (May 2021).

194. Ercan, H. E., Coppersmith, S. N. & Friesen, M. Strong electron-electron interactions in Si/SiGe quantum dots. *Physical Review B* **104,** 235302. ISSN: 2469-9950 (Dec. 2021).

195. Voronoi, G. Nouvelles applications des paramètres continus à la théorie des formes quadratiques. Premier mémoire. Sur quelques propriétés des formes quadratiques positives parfaites. *Journal für die reine und angewandte Mathematik (Crelles Journal)* **1908,** 97–102. ISSN: 0075-4102 (Jan. 1908).

196. Voronoi, G. Nouvelles applications des paramètres continus à la théorie des formes quadratiques. Deuxième mémoire. Recherches sur les paralléllo̊edres primitifs. *Journal für die reine und angewandte Mathematik (Crelles Journal)* **1908,** 198–287. ISSN: 0075-4102 (July 1908).

197. Boykin, T. B. *et al.* Valley splitting in low-density quantum-confined heterostructures studied using tight-binding models. *Physical Review B - Condensed Matter and Materials Physics* **70,** 1–12. ISSN: 01631829 (2004).

198. Klimeck, G. *et al.* Atomistic Simulation of Realistically Sized Nanodevices Using NEMO 3-D—Part II: Applications. *IEEE Transactions on Electron Devices* **54,** 2090–2099. ISSN: 0018-9383 (Sept. 2007).

199. McJunkin, T. *et al.* SiGe quantum wells with oscillating Ge concentrations for quantum dot qubits. *Nature Communications* **13.** ISSN: 2041-1723 (Dec. 2022).

200. Koelling, S. *et al.* (Invited) Probing Semiconductor Heterostructures from the Atomic to the Micrometer Scale. *ECS Transactions* **98,** 447–455. ISSN: 1938-5862 (Sept. 2020).

201. Aja-Fernández, S. & Vegas-Sánchez-Ferrero, G. *Statistical Analysis of Noise in MRI: Modeling, Filtering and Estimation* ISBN: 978-3-319-39933-1 (Springer International Publishing, 2016).

202. Wuetz, B. P. *et al.* Effect of Quantum Hall Edge Strips on Valley Splitting in Silicon Quantum Wells. *Phys. Rev. Lett.* **125,** 186801 (Oct. 2020).

203. Mi, X., Péterfalvi, C. G., Burkard, G. & Petta, J. R. High-resolution valley spectroscopy of Si quantum dots. *Physical review letters* **119,** 176803 (2017).

204. Samkharadze, N. *et al.* Strong spin-photon coupling in silicon. *Science* **359,** 1123–1127 (2018).

205. DiCarlo, L. *et al.* Differential Charge Sensing and Charge Delocalization in a Tunable Double Quantum Dot. *Physical Review Letters* **92,** 226801. ISSN: 0031-9007 (June 2004).

206. Larson, D. J., Prosa, T. J., Ulfig, R. M., Geiser, B. P. & Kelly, T. F. *Local Electrode Atom Probe Tomography* ISBN: 978-1-4614-8720-3 (Springer New York, New York, NY, 2013).

207. George, H. C. *et al.* 12-Spin-Qubit Arrays Fabricated on a 300 mm Semiconductor Manufacturing Line. *Nano Letters* **25,** 793–799. ISSN: 1530-6992 (Dec. 2024).

208. Unseld, F. K. *et al.* Baseband control of single-electron silicon spin qubits in two dimensions. *Nature Communications* **16.** ISSN: 2041-1723 (July 2025).

209. Noiri, A. *et al.* A shuttling-based two-qubit logic gate for linking distant silicon quantum processors. *Nature Communications* **13.** ISSN: 2041-1723 (Sept. 2022).

210. Struck, T. *et al.* Spin-EPR-pair separation by conveyor-mode single electron shuttling in Si/SiGe. *Nature Communications* **15.** ISSN: 2041-1723 (Feb. 2024).

211. De Smet, M. *et al.* High-fidelity single-spin shuttling in silicon. *Nature Nanotechnology.* ISSN: 1748-3395 (June 2025).

212. Dijkema, J. *et al.* Cavity-mediated iSWAP oscillations between distant spins. en. *Nature Physics* **21,** 168–174. ISSN: 1745-2481. (2025) (Jan. 2025).

213. Ha, S. D. *et al.* Two-Dimensional Si Spin Qubit Arrays with Multilevel Interconnects. *PRX Quantum* **6,** 030327. https://link.aps.org/doi/10.1103/sgn1-1t2d (3 Aug. 2025).

214. Marcks, J. C. *et al.* Valley Splitting Correlations Across a Silicon Quantum Well. *arXiv preprint arXiv:2504.12455* (2025).

215. Huang, P. & Hu, X. Spin relaxation in a Si quantum dot due to spin-valley mixing. en. *Physical Review B* **90,** 235315. ISSN: 1098-0121, 1550-235X. (2023) (Dec. 2014).

216. Seidler, I. *et al.* Conveyor-mode single-electron shuttling in Si/SiGe for a scalable quantum computing architecture. en. *npj Quantum Information* **8,** 100. ISSN: 2056-6387. (2024) (Aug. 2022).

217. Langrock, V. *et al.* Blueprint of a Scalable Spin Qubit Shuttle Device for Coherent Mid-Range Qubit Transfer in Disordered ${\text{Si/SiGe/SiO}}_{2}$. *PRX Quantum* **4,** 020305. (2024) (Apr. 2023).

218. Zwerver, A. *et al.* Shuttling an Electron Spin through a Silicon Quantum Dot Array. en. *PRX Quantum* **4,** 030303. ISSN: 2691-3399. (2023) (July 2023).

219. Losert, M. P. *et al.* Strategies for Enhancing Spin-Shuttling Fidelities in Si/SiGe Quantum Wells with Random-Alloy Disorder. *PRX Quantum* **5,** 040322 (4 Nov. 2024).

220. Klos, J. *et al.* Atomistic Compositional Details and Their Importance for Spin Qubits in Isotope-Purified Silicon Quantum Wells. *Advanced Science* **11.** ISSN: 2198-3844 (Sept. 2024).

221. Venkataraman, V., Liu, C. W. & Sturm, J. C. Alloy scattering limited transport of two-dimensional carriers in strained $Si_{1-x}Ge_x$ quantum wells. en. *Applied Physics Letters* **63,** 2795–2797. ISSN: 0003-6951, 1077-3118. (2025) (Nov. 1993).

222. Goswami, S. *et al.* Controllable valley splitting in silicon quantum devices. en. *Nature Physics* **3,** 41–45. ISSN: 1745-2481. (2025) (Jan. 2007).

223. Unseld, F. K. *et al.* A 2D quantum dot array in planar 28Si/SiGe. en. *Applied Physics Letters* **123,** 084002. ISSN: 0003-6951, 1077-3118. (2024) (Aug. 2023).

224. Xue, R. *et al.* Si/SiGe QuBus for single electron information-processing devices with memory and micron-scale connectivity function. en. *Nature Communications* **15,** 2296. ISSN: 2041-1723. (2024) (Mar. 2024).

225. Huckemann, T. *et al.* Industrially fabricated single-electron quantum dots in Si/Si–Ge heterostructures. *IEEE Electron Device Letters,* 1–1. ISSN: 1558-0563 (2025).

226. Koch, T. *et al.* Industrial 300 mm wafer processed spin qubits in natural silicon/silicon-germanium. *npj Quantum Information* **11.** ISSN: 2056-6387 (Apr. 2025).

227. Van Riggelen-Doelman, F. *et al.* Coherent spin qubit shuttling through germanium quantum dots. *Nature Communications* **15.** ISSN: 2041-1723 (July 2024).

228. Lodari, M. *et al.* Lightly strained germanium quantum wells with hole mobility exceeding one million. *Applied Physics Letters* **120.** ISSN: 1077-3118 (Mar. 2022).

229. Kong, Z. *et al.* Undoped Strained Ge Quantum Well with Ultrahigh Mobility of Two Million. *ACS Applied Materials I&; Interfaces* **15,** 28799–28805. ISSN: 1944-8252 (May 2023).

230. Bedell, S. W. *et al.* (Invited) Low-Temperature Growth of Strained Germanium Quantum Wells for High Mobility Applications. *ECS Transactions* **98,** 215–224. ISSN: 1938-6737 (Sept. 2020).

231. Shimura, Y. *et al.* Compressively strained epitaxial Ge layers for quantum computing applications. *Materials Science in Semiconductor Processing* **174,** 108231. ISSN: 1369-8001 (May 2024).

ACKNOWLEDGEMENTS

If you stare at the closed door, you will miss the one that is open.

Dr. Hakim

This PhD thesis would never have been completed without the amazing work of my colleagues, the support of my friends, and the love of my family. It has been a privilege to be part of the spin qubit community at QuTech. I sincerely thank all of you for the moments we shared over the past years.

Dear **Giordano**, thank you for being an amazing supervisor and promotor. When I started my PhD in your group, I initially struggled with your hands-off supervision style. However, you quickly addressed this by setting up weekly half-hour meetings, which helped me to set up projects or pivot when other projects were not working out. The quote above reminds me of several key decisions we made during my PhD, especially when the growth tool was not working—decisions that ultimately led to very successful outcomes. It has been a privilege to be one of your students, and I hope we can continue working together in the future. I will surely miss our weekly chats. **Menno**, thank you for being my promotor. While you kept your distance as a promotor, I always felt your trust in me to successfully complete my PhD. I especially want to thank you for your openness to adopting newly developed materials for your long-term projects—a risk that not many people are willing to take. **Lieven**, thank you for your kindness and approachable nature. It was a privilege to take courses from you during my Bachelor's and Master's studies, and later to work together with your students during my PhD. I also fondly remember our shared ride to the 2022 Silicon Quantum Electronics Workshop. **Max** and **Stefano**, thank you for the theory discussions we shared. It is great to see how your theoretical work is impacting the experimental efforts at QuTech.

To all members of the Scappucci-lab: thank you all for being such amazing colleagues. **Davide**, I could always come to you whenever there were issues in the lab, or when I needed more explanations about fabrication. We share many papers together, which I am very proud of. I fondly remember our trip to the QuMat summer school and our conference in Como. Especially the pasta place you found was amazing. **Amir**, we shared a lot of time together in my first year. You introduced me to the cleanroom and taught me the art of epitaxial growth. I am very grateful for everything I learned from you, and I fondly remember driving around lake Como together. **Desa**, you were the first new PhD student after I joined, and you brought a lot of new energy to the research group. You taught me a lot about debugging the electronics of the measurement setups, which became more enjoyable with every iteration. It is amazing to see that your work on the unstrained Ge QWs is taking off, and I am proud to have you as one of my paranymphs. **Asser**, you were the first postdoc to join our group after many had left. You helped me a lot with your knowledge of charge noise measurements. I love your relaxed attitude, and I enjoyed all our work and life conversations over the years. I am very honored to have you as one of my paranymphs. **Federico**, I thoroughly enjoyed interviewing you when you wanted to join the group. You are kind, very smart, and always eager to learn. Malibu and Qarpet are in safe hands with you. **Karina**, I really loved all the conversations we shared in F010 during refills. I admire your bravery in coming to the Netherlands from Australia. I hope you continue to enjoy the Dutch skies, and please let me know if you ever manage to date Stoffel Vandoorne. **Luca** and **Vladimir**, I am very honored to have taught you the art of growth. I am sure the growth tool is safe in your hands. It is incredible to see all the additional skills you both bring to the lab. **Alberto**, I admire your

independent work attitude and your inventive nature. Your working style was a bit too chaotic for me, but your great ideas led to several patents and research lines, which is very impressive. **Mario**, I wish we could have worked together more. I still open your papers on a regular basis. **Luka**, thank you for setting up a lab with cryo-multiplexers—it is still very useful! **Maia**, you helped during a very challenging and hectic phase of my PhD. It was extremely meaningful to have you as my Master's student, and I am very proud that your work resulted in a published chapter of my thesis. Good luck with your PhD in Basel; I am looking forward to seeing what you will publish in the coming years. Dear **Brian**, you were my supervisor during my Bachelor's project, then my Master's project, and we even worked together during the first few months of my PhD. I cannot tell you how grateful I am to have had you as my supervisor. You were always prepared to answer my questions and always made time for me. Working with you convinced me to do a PhD in Giordano's lab. Our relation turned into a friendship and I am very happy that we are still in contact and manage to go for dinner together, even though you live in Barcelona now.

Bruno, I cannot thank you enough for all your help. You were invaluable in bringing the growth tool back to life after nearly two years of downtime. Despite your busy schedule operating the entire EKL cleanroom, you always found time to help me leak-check the tool, install new parts, and eventually rebuild it completely. It was not always easy, but we made it work together, and in the process, I learned a lot from you—although time management was not one of those things. **Dennis**, you were always happy to help with the tool, and you have always been kind and extremely friendly. I loved listening to your diving stories and remain impressed by your welding skills. **Bianca**, thank you for all the times you lent me an access card when I had visitors or when I forgot my own (which was often the case), and **Mike**, thank you for keeping EKL running! **Paolo**, it was a pleasure getting to know you. I hope your boron-doped wafers are working well, and thank you for all the tips on where to find the best Italian food.

Francesco, **Cécile**, and **Valentin** (or **John**), you were extremely important during arguably the hardest phase of my PhD. Your extensive measurements on the 10-dot device elevated my paper to another level. It was a great pleasure to work with you, and I hope we can collaborate again in the future. **Zarije**, you were an incredibly fun office mate. I enjoyed our conference trip to Anaheim a lot, although we both did not enjoy the food too much. Good luck with your PhD—I am sure it will be very impressive. I still have not forgiven you for leaving our office. **Hanifa**, conversations with you were never boring. I admire your work on the bilayers; it always seemed impossible to me. **Floor**, although we did not interact much in the beginning of my PhD, overtime we had many very interesting conversations. You were always keen to explain qubit physics to me. You are a good singer—although sometimes a bit out of the blue. **Damien**, your love for trying new experiments is very inspiring. Good luck with those (better) EO qubits. **Dario**, continuing the research on the bilayers seems challenging, but if someone can do it, it is you. **Sasha**, thank you for all the great conversations we shared. You are passionate about your work, and the projects you take on are very ambitious! **Barnaby**, it was great fun getting to know you. You have many interesting stories, I love all your kite-surfing pictures, and those Hunt wheels are amazing. **Corentin**, your postdoc lasted as long as my PhD, and at times it seemed you were keeping Menno's lab going. Good luck in Grenoble! **Marion**, it was great getting to know you better during the Anaheim conference. Good luck with all the

shuttling projects. **Setareh**, good luck with making all the next-generation devices.

Brennan, I fondly remember doing the introduction weekend of the Master's program together. You are very knowledgeable, and your work on silicon has clearly advanced the field. **Kenji**, tracking all those qubit fidelities must have been a big project. Thank you for taking the leap with **Irene** to adopt the diffused interface material. I hope it gives you both the results you are hoping for. **Tzu-Khan**, I fondly remember getting to know you better during the SiQEW in Canada. Good luck with your career in Taiwan. **Pablo**, I admire your passion for quantum simulations. Thank you for often bringing croissants to the coffee table. **Florian**, you finally made a 2×2 device work in silicon—good luck with your next steps at Diraq. **Xiao**, it was fun to explain growth questions to you, and even more fun to show you the tool. **Tobias**, I never really understood your work, but you were very nice to interact with. **Maxim** and **Yuta**, it has been amazing to see your pioneering shuttling work. **Liza**, **Stefano**, and **Daniel**, it was great to see all your quantum simulation work on the 2×4 ladder. **Nicola**, you are an excellent candidate to take over Brennan's work. Your bus-stop device is showing extremely cool results.

Chris, you are a very funny guy, and I greatly enjoyed our early-morning chats. **Edmondo**, **Michèle**, **Tess**, **Minh**, **Patrick**, and **Daniel**, you bring many valuable theoretical insights to the experimental spin qubit groups. I am sure this will help improve spin qubits as a quantum computing platform.

Sander and **Daan**, thank you for building an amazing software framework. Your work made doing experiments so much easier. **Raymond** and **Raymond**, thank you for the electronics support. **Erik**, **Olaf**, **Jason**, and **Tom**, thank you for your support with bonding and maintaining the fridges. **Vinod**, thank you for all the times you came to flush out the turbo of the LeidenFridge. **Jelle**, **Roy**, and **Siebe**, thank you for always being willing to help out and for your patience with my questions. **Hitham**, you are making QuTech a much safer place—keep up the good work. **Nico**, thank you for making a two-euro clamp that holds together a two-million-euro tool.

Marja, thank you for your kindness and for all the times I needed last-minute shipping documents. I hope you are enjoying your well-deserved retirement. **Jenny**, **Julijana**, and **Frederieke**, I am very glad I could rely on you for my last-minute shipping documents after Marja left.

James, thank you for creating an internship for me at TNO during the COVID days. It is great to see you still around on the TU campus. **David**, your work at TNO is very valuable. I greatly enjoyed having more time to chat during the Anaheim conference—the pizza place was really great.

Nico and **Anne-Marije**, thank you for your patience during the process of joining Groove. I am very much looking forward to what we can achieve together. **Xin**, **Alice**, **Jurgen**, **Daniël**, **Achilleas**, **David**, **Davide**, and **Clair**, you make Groove a special place and I cannot wait to work with you in the future.

Lieve **Bart** en **Laurens**, het voelt nog steeds als gisteren dat ik met jullie in de collegezaal in Aachen zat. Hoewel we sindsdien onze eigen weg zijn gegaan, blijven we elkaar nog steeds met enige regelmaat zien. Ik waardeer het enorm dat we door alle jaren heen goede vrienden gebleven zijn. **Yvonne** en **Inez**, Bart en Laurens mogen zich prijzen met jullie als hun partner. Ik vind het enorm leuk dat we ook met zijn zessen weten af te spreken. Laten we de volgende keer wel een iets moeilijkere escape-room doen.

Friso, **Lars**, **Casper**, **Timo**, **Sebastiaan**, en **Hans**, het was een voorrecht om al die jaren met jullie in Delft college te mogen volgen. Ik heb enorm veel van jullie geleerd en ik mis oprecht de momenten dat we zoveel lol met elkaar hadden tijdens (werk)colleges. Het is erg mooi om te zien hoe iedereen een verschillende carrière heeft gekozen. Ik waardeer het enorm dat we ondanks alle drukke levens nog steeds de tijd vinden om met elkaar af te spreken. Het was fantastisch om jullie op mijn bruiloft te hebben. **Liset**, ik vind het heel leuk dat jij en Cathy eklaar hebben leren kennen tijdens jullie onderzoek en dat we nu vaak gezellig bij elkaar komen. Ik zal proberen mijn kookkunsten te verbeteren.

Roy, **Lisa**, **Stijn**, en **Emma**, jullie maken de 7^{e} verdieping op de Kratonkade extra leuk om te wonen. Ik hoop dat we nog vele malen bij elkaar over de vloer zullen komen.

Lieve **Co** en **Rinny**, ik kan me geen betere schoonouders wensen. Het was even slikken tijdens jullie verhoor de eerste keer dat Cathy mij aan jullie voorstelde. Ik hoop dat het inmiddels iets duidelijker is wat iemand met een natuurkunde opleiding kan doen. Jullie staan altijd klaar voor Cathy en mij en dat waardeer ik enorm. Ik hoop dat jullie nu samen van jullie welverdiende pensioen kunnen genieten. **Rick** en **Homeira**, jullie hebben mij vanaf het begin in de familie met open armen verwelkomd. Dit viel ongeveer samen met de geboorte van Sepp en het was erg mooi om jullie te zien groeien als gezin. **Sepp**, je bent een lieve jongen en je zit boordevol energie. Let maar goed op je zusje **Yara**. Lieve oma **Annie**, de (tuin)deur staat bij jou altijd open en ik vind het onwijs leuk om te zien hoe je van al je (achter)kleinkinderen kan genieten.

Lieve **Marga** en **Pieter**, het meenemen van mijn onderzoeksgroep naar de Raedt van Toezigt was voor mij een van de hoogtepunten van mijn onderzoek. Pieter, ik ben er nog steeds heel erg trots op dat jij mijn peetvader bent. Lieve **Anne**, ik ken maar weinig mensen met een groter hart dan jij. Je hebt me meer dan eens geholpen om momenten dat ik het moeilijk had en ik koester de band die we opgebouwd hebben enorm.

Lieve **Coen**, je bent een goede en lieve broer waar ik veel van heb mogen leren. Ik heb erg veel ontzag voor jouw wil om je eigen koers te varen. Het is ook onwijs leuk om je nu zo als bevlogen vader te zien. Lieve **Esther**, je bent een leuke en lieve schoonzus en jouw liefde voor Casper straalt van je af. Lieve **Casper**, je bent nog te jong om dit te begrijpen, maar ik kijk er naar uit om je te zien opgroeien. Hopelijk mag ik ooit jouw interesse voor exacte vakken weten te wekken. Leef **Sjeeetepieieie**, lieve **Esther**, je bent een geweldige zus van me, staat voor iedereen altijd klaar en 'nee' lijkt nooit onderdeel van jouw vocabulair te zijn. Ik ben benieuwd wat je volgende uitdaging gaat zijn. Het is erg leuk om te zien dat jij en **Maarten** elkaar gevonden hebben en ik wens jullie veel geluk samen. Lieve **Juliette**, je bent een lieve oudere zus. Jouw liefde voor kunst is heel inspirerend. Ik ben erg trots dat je zo zelfstandig bent en dat je je eigen plekje gevonden hebt. Lieve **oma**, het is een eer om van jouw aanwezigheid te mogen genieten tijdens mijn promotie. Mijn vroege interesse in exacte vakken is zeker ook ontstaan tijden de logeerpartijen waar we samen vliegtuigjes maakten en waar ik samen met opa **Erik** zijn ontwerpen bouwde. Ik weet zeker dat hij trots op mij zou zijn. Lieve **Huib**, je bent een lieve man en ik vind het fijn dat jij en mijn oma elkaar gevonden hebben.

Liefste **mama**, dankjewel dat je er altijd voor mij geweest bent. Je bent een geweldig lieve moeder en samen met jou het gangpad aflopen tijdens mijn bruiloft is nu al een van mijn mooiste herinneringen. Ik vond het ook enorm stoer van je dat je in je eentje mij kwam opzoeken in Canada toen ik daar een aantal maanden studeerde. Het is onwijs leuk

om te zien hoe leuk je het vindt om nu ook oma te zijn. Lieve **papa**, ik heb in grote mate aan jou te danken dat ik de keuze gemaakt heb om onderzoek te doen. Achteraf was dit een goede keuze. Wij delen veel bijzondere momenten samen, zoals samen tennislessen volgen, en de autoritten door Oostenrijk en Zwitserland. Ik ben er erg trots op dat je na een aantal moeilijke jaren je weer zo veel beter voelt.

Liefste **Cathy**, toen we elkaar net leerden kennen, twijfelde ik enorm om een PhD in het buitenland te doen. Uiteindelijk heb ik gekozen om in Nederland te blijven om onze toen nog prille relatie verder uit te zoeken. Dat was een van de beste keuzes van mijn leven. Je bent lief, zorgzaam, slim, sportief, en je hebt altijd wel een idee om iets leuks te gaan doen. Mijn PhD was voor mij niet altijd even makkelijk, zeker in het begin niet, maar ik kon altijd bij jou terecht. We zijn afgelopen jaren alleen maar naar elkaar toe gegroeid en dit jaar trouwen met jou in Italië was een hoogtepunt van mijn leven. Ik hou van je en ik kan niet wachten om de rest van mijn leven met jou door te brengen.

CURRICULUM VITÆ

Lucas Erik Adriaan STEHOUWER

05-03-1996 Born in Amsterdam, The Netherlands.

EDUCATION

2016–2019 Bachelor of Science in Applied Physics
Delft University of Technology, Delft

2019–2021 Master of Science in Applied Physics
Delft University of Technology, Delft
Thesis: Atomic insights into valley splitting in Si/SiGe quantum dots
Supervisor: dr. G. Scappucci

2021–2025 PhD. Physics
Delft University of Technology, Delft
Thesis: Engineered silicon and germanium for quantum technology
Promotor: dr. G. Scappucci
Promotor: prof. dr. ir. M. Veldhorst

AWARDS

2021 NanoFront-Casimir PhD position

LIST OF PUBLICATIONS

20. **L.E.A. Stehouwer**, A. Tosato, D. Degli Esposti, D. Costa, M. Veldhorst, A. Sammak, G. Scappucci, *Germanium wafers for strained quantum wells with low disorder*, Applied Physics Letters, **123**, 9 (2023).

19. D. Costa, **L.E.A. Stehouwer**, Y. Huang, S. Martí-Sánchez, D. Degli Esposti, J. Arbiol, G. Scappucci, *Reducing disorder in Ge quantum wells by using thick SiGe barriers*, Applied Physics Letters, **125**, 222104 (2024).

18. **L.E.A. Stehouwer**, C.X. Yu, B. van Straaten, A. Tosato, V. John, D. Degli Esposti, A. Elsayed, D. Costa, S.D. Oosterhout, N.W. Hendrickx, M. Veldhorst, F. Borsoi, G. Scappucci, *Exploiting strained epitaxial germanium for scaling low-noise spin qubits at the micrometre scale*, Nature Materials, (2025).

17. B. Paquelet Wuetz, M.P. Losert, S. Koelling, **L.E.A. Stehouwer**, A.M.J. Zwerver, S.G.J. Philips, M.T. Mądzik, X. Xue, G. Zheng, M. Lodari, S.V. Amitonov, N. Samkharadze, A. Sammak, L.M.K. Vandersypen, R. Rahman, S.N. Coppersmith, O. Moutanabbir, M. Friesen, G. Scappucci, *Atomic fluctuations lifting the energy degeneracy in Si/SiGe quantum dots*, Nature Communications, **13**, 7730 (2022).

16. **L.E.A. Stehouwer**, M.P. Losert, M. Rigot, D. Degli Esposti, S. Marti-Sánchez, M. Rimbach-Russ, J. Arbiol, M. Friesen, G. Scappucci, *Engineering Ge profiles in Si/SiGe heterostructures for increased valley splitting*, Nano Letters, **25**, 34 (2025).

15. D. Degli Esposti, **L.E.A. Stehouwer**, Ö. Gül, N. Samkharadze, C. Déprez, M. Meyer, I.N. Meijer, L. Tryputen, S. Karwal, M. Botifoll, J. Arbiol, S. V. Amitonov, L.M.K. Vandersypen, A. Sammak, M. Veldhorst, G. Scappucci, *Low disorder and high valley splitting in silicon*, npj Quantum Information **10** (1), 32 (2024).

14. S. Koelling, **L.E.A. Stehouwer**, B.P. Wuetz, G. Scappucci, O. Moutanabbir, *Three-Dimensional Atomic-Scale Tomography of Buried Semiconductor Heterointerfaces*, Advanced Materials Interfaces **10**, (2023).

13. J. Rooney, Z. Luo, **L.E.A. Stehouwer**, G. Scappucci, M. Veldhorst, H. Jiang, *Gate modulation of the hole singlet-triplet qubit frequency in germanium*, npj Quantum Information **11** (1), 15 (2025).

12. D. Costa, P. Del Vecchio, K. Hudson, **L.E.A. Stehouwer**, A. Tosato, D. Degli Esposti, M. Lodari, S. Bosco, G. Scappucci, *Buried unstrained germanium channels: a lattice-matched platform for quantum technology*, arXiv preprint arXiv:2506.04724 (2025)

11. A. Tosato, A. Elsayed, F. Poggiali, **L.E.A. Stehouwer**, D. Costa, K. Hudson, D. Degli Esposti, G. Scappucci, *QARPET: A Crossbar Chip for Benchmarking Semiconductor Spin Qubits*, arXiv preprint arXiv:2504.05460 (2025)

10. L. Lakic, W.I.L. Lawrie, D. van Driel, **L.E.A. Stehouwer**, Y. Su, M. Veldhorst, G. Scappucci, F. Kuemmeth, A. Chatterjee, *A quantum dot in germanium proximitized by a superconductor*, Nature Materials, (2025).

9. C.X. Yu, B. van Straaten, A.S. Ivlev, S.D. Oosterhout, **L.E.A. Stehouwer**, F. Borsoi, G. Scappucci, M. Veldhorst, *Optimising germanium hole spin qubits with a room-temperature magnet*, arXiv preprint arXiv:2507.03390 (2025)

8. H. Sohn, J. Jung, J. Park, H. Jang, **L.E.A. Stehouwer**, D. Degli Esposti, G. Scappucci, D. Kim, *Application of zero-noise-extrapolation-based quantum error mitigation to a silicon spin qubit*, Physical Review A **112**, 1 (2025).

7. H. Tidjani, A. Tosato, A.S. Ivlev, C. Déprez, S.D. Oosterhout, **L.E.A. Stehouwer**, A. Sammak, G. Scappucci, M. Veldhorst, *Vertical gate-defined double quantum dot in a strained germanium double quantum well*, Physical Review Applied **20**, (2023).

6. B.P. Wuetz, M.P. Losert, A. Tosato, M. Lodari, P.L. Bavdaz, **L.E.A. Stehouwer**, P. Ayim, J.S. Clarke, S.N. Coppersmith, *Effect of Quantum Hall Edge Strips on Valley Splitting in Silicon Quantum Wells*, Physical Review Letters **125**, (2020).

5. V. John, C.X. Yu, B. van Straaten, E.A. Rodríguez-Mena, M. Rodríguez, S.D. Oosterhout, **L.E.A. Stehouwer**, G. Scappucci, S. Bosco, M. Rimbach-Russ, Y. Niquet, F. Borsoi, M. Veldhorst, *A two-dimensional 10-qubit array in germanium with robust and localised qubit control*, arXiv preprint arXiv:2412.16044 (2024)

4. J. Park. H. Jang, H. Sohn, J. Yun, Y. Song, B. Kang, **L.E.A. Stehouwer**, D. Degli Esposti, G. Scappucci, D. Kim, *Passive and active suppression of transduced noise in silicon spin qubits*, Nature Communications, **16**, 78 (2025).

3. A.S. Rao, D. Buterakos, B. van Straaten, V. John, C.X. Yu, S.D. Oosterhout, **L.E.A. Stehouwer**, G. Scappucci, M. Veldhorst, *Modular Autonomous Virtualization System for Two-Dimensional Semiconductor Quantum Dot Arrays*, Physical Review X **15**, 2 (2025)

2. C. Wang, V. Johgn, H. Tidjani, C.X. Yu, A.S. Ivlev, C. Déprez, F. van Riggelen-Doelman, B.D. Woods, N.W. Hendrickx, W.I.L. Lawrie, **L.E.A. Stehouwer**, S.D. Oosterhout, A. Sammak, M. Friesen, G. Scappucci, S.L. de Snoo, M. Rimbach-Russ, F. Borsoi, M. Veldhorst, *Operating semiconductor quantum processors with hopping spins*, Science (2024)

1. G. scappucci, M. Rimbach-Russ, A. Sammak. **L.E.A. Stehouwer**, A. Tosato, *Method for manufacturing a single heterojunction semiconductor device and such a single heterojunction semiconductor device*, (2024).